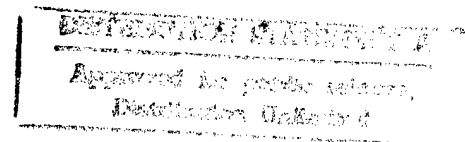


# **ACTIVE CONTROL OF COMBUSTION INSTABILITY IN A RAMJET USING LARGE-EDDY SIMULATIONS**

**Suresh Menon  
School of Aerospace Engineering  
Georgia Institute of Technology  
Atlanta, Georgia 30332-0150**

**Final Report for the Period  
September 1992 - July 1995  
Grant No. N00014-92-J-403**

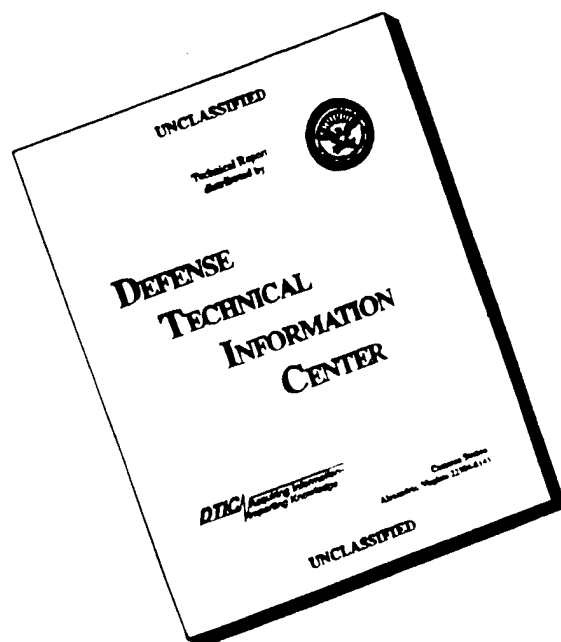


**Submitted to  
The Office of Naval Research**

**19961030 083**

**DTIC QUALITY INSPECTED 3**

# DISCLAIMER NOTICE



**THIS DOCUMENT IS BEST QUALITY AVAILABLE. THE COPY FURNISHED TO DTIC CONTAINED A SIGNIFICANT NUMBER OF PAGES WHICH DO NOT REPRODUCE LEGIBLY.**

E-16-m59

## REPORT DOCUMENTATION PAGE

Form Approved  
OMB No. 0704-0188

Public reporting burden for this collection of information is estimated to average 1 hour per response, including the time for reviewing instructions, searching existing data sources, gathering and maintaining the data needed, and completing and reviewing the collection of information. Send comments regarding this burden estimate or any other aspect of this collection of information, including suggestions for reducing this burden to Washington Headquarters Services, Directorate for Information Operations and Reports, 1215 Jefferson Davis Highway, Suite 1204, Arlington, VA 22202-4302, and to the Office of Management and Budget, Paperwork Reduction Project (0704-0188), Washington, DC 20503

1. AGENCY USE ONLY (Leave Blank)		2. REPORT DATE July 1995		3. REPORT TYPE AND DATES COVERED Final - 9/1/92 through 7/31/95	
4. TITLE AND SUBTITLE Active Control of Combustion Instability in a Ramjet Using Large-Eddy Simulations				5. FUNDING NUMBERS N00014-92-J-403	
6. AUTHOR(S) Suresh Menon					
7. PERFORMING ORGANIZATION NAME(S) AND ADDRESS(ES) Dr. Suresh Menon School of Aerospace Engineering Georgia Institute of Technology Atlanta, Georgia 30332-0150				8. PERFORMING ORGANIZATION REPORT NUMBER	
9. SPONSORING/MONITORING AGENCY NAME(S) AND ADDRESS(ES) Eric Hendricks Office of Naval Research 800 North Quincy Street Arlington, VA 22217-5000				10. SPONSORING/MONITORING AGENCY REPORT NUMBER	
11. SUPPLEMENTARY NOTES COR:					
12a. DISTRIBUTION/AVAILABILITY STATEMENT  Unlimited				12b. DISTRIBUTION CODE	
13. ABSTRACT (Maximum 200 words)  This study has developed a large-eddy simulation model for active control. The basic simulation control was extended for general applications, the simulation code was implemented on a massively parallel processor, and two active control techniques (acoustic feedback control and secondary fuel injection control) were investigated. However, the primary focus for active control in this study was on secondary fuel injection techniques, as it had been demonstrated in past experimental studies that this method was more practical. Numerical simulations of fuel injection control were carried out and, in addition, a theoretical model for secondary fuel injection control was developed along with a method to couple the theoretical model to the simulation model. Finally, to implement a robust controller, a fuzzy logic based controller for fuel injection was studied using a simplified problem geometry. To investigate the effects of three-dimensionality, full 3D LES of combustion instability was also carried out.					
14. SUBJECT TERMS  Active control, Ramjet, Fuzzy Logic, Combustion Instability, Large eddy simulation				15. NUMBER OF PAGES 162	
				16. PRICE CODE	
17. SECURITY CLASSIFICATION OF REPORT  Unclassified	18. SECURITY CLASSIFICATION OF THIS PAGE  Unclassified	19. SECURITY CLASSIFICATION OF ABSTRACT  Unclassified	20. LIMITATION OF ABSTRACT  Unlimited		



Georgia Institute of Technology  
Office of Contract Administration  
Atlanta, Georgia 30332-0420 USA

CONTRACTING SUPPORT DIVISION  
404•894•6944

Telex: 542507 GTRC OCA ATL  
Fax: 404•894•5945

January 25, 1996

Reply to: E-16-M59

Scientific Officer Code: 1221A2  
Eric Hendricks  
Office of Naval Research  
800 North Quincy Street  
Arlington, VA 22217-5000

Subject: Final Technical Report  
Project Director(s): S. Menon  
Phone No.: (404) 894-9126  
Contract No.: N00014-92-J-4030  
"ACTIVE CONTROL OF COMBUSTION INSTABILITY  
IN A RAMJET USING LARGE-EDDY SIMULATIONS"  
Period Covered: 920901 - 950731

The subject report is forwarded in conformance with the contract/grant specifications.

Should you have any questions or comments regarding this report (s), please contact the Project Director or the undersigned at 404-894-4764.

/tw

Sincerely,

Wanda W. Simon  
Reports Coordinator

Distribution:  
Addressee, 3 copies  
1 copy to: Director, Naval Research Laboratory  
2 copies to: Defense Technical Information Ctr.  
cc: ONR-RR



# **ACTIVE CONTROL OF COMBUSTION INSTABILITY IN A RAMJET USING LARGE-EDDY SIMULATIONS**

**Suresh Menon  
School of Aerospace Engineering  
Georgia Institute of Technology  
Atlanta, Georgia 30332-0150**

**Final Report for the Period  
September 1992 - July 1995  
Grant No. N00014-92-J-403**

## **1. INTRODUCTION**

This report summarizes the research carried out at Georgia Tech. Most of the achievements in this research have been described in research papers that are included in Appendix A. Here, the major highlights of this research study are summarized.

The primary objectives of this study were to

1. Carry out large-eddy simulations of combustion instability in a ramjet to understand the physics of the nonlinear processes
2. Develop, implement and demonstrate the capability of active control methods to control the combustion instability

This study has successfully achieved all the objectives of this study. The basic simulation model was extended for general applications, the simulation code was implemented on a massively parallel processor and two active control techniques: acoustic feedback control and secondary fuel injection control, were investigated. However, the primary focus for active control in this study was on secondary fuel injection technique since it had been demonstrated in past experimental studies that this method is more practical. Numerical simulations of fuel injection control was carried out and in addition, a theoretical model for secondary fuel injection control was developed along with a method to couple the theoretical model to the simulation model. Finally, to implement a robust controller, a fuzzy logic based controller for fuel injection was studied using a simplified problem geometry. To investigate the effects of three-dimensionality, full 3D LES of combustion instability was also carried out.

In the following, the development in each of the above mentioned areas is briefly summarized along with the list of relevant publications. Most of the publications noted are included in Appendix A.

## 2. PARALLEL IMPLEMENTATION OF THE LES CODE

Combustion instability in ramjets is a complex phenomenon that involve nonlinear interaction between acoustic waves, vortex motion and unsteady heat release in the combustor. To numerically simulate this phenomenon, very large computer resources (both time and memory) are required. Although current vector supercomputers are capable of providing adequate resources for simulations of this nature, the high cost and their limited availability, makes practical use of such machines less than satisfactory. To investigate the use of massively parallel systems for unsteady simulations, a large-eddy simulation model for combustion instability was implemented on the Intel iPSC/860 and a careful investigation was carried out to determine the benefits and problems associated with the use of highly parallel distributed processing machines for unsteady simulations. Results of this study along with some of the results of the simulations carried out on the iPSC/860 are discussed Weeratunga and Menon (1993).

It was demonstrated that it is possible to realize a highly scalable, distributed memory, data parallel implementation for a class of explicit time integration schemes used in unsteady combustion simulations. The geometry-tailored, two-level data partitioning strategy adapted to deal with L-shaped computational space appears to have resulted in an efficient implementation, in spite of it's added complexity. The implementation is general enough to be portable to any MIMD parallel computer that supports processor-to-processor communication primitives. This includes most of the current and emerging highly parallel MIMD computers as well as networks of workstations supporting distributed computing software such as the Parallel Virtual Machine (PVM). The MIMD parallel computers appears to provide a scalable, yet reasonably low-cost alternative to traditional vector supercomputers for simulation of unsteady flow phenomena, except in the crucial area of external I/O performance. Further improvements in the computational and the inter-processor communication performance envisaged for the future generations of the highly parallel computers will make them attractive tools for carrying out 3-D unsteady flow simulations. The additional computations associated with computing fluxes for hexahedral cells is likely to improve the computation to communication ratio over that encountered in 2-D computations and lead to enhanced scalability. However, to realize this promise, the above mentioned hardware performance improvements will have to be accompanied by rapid improvements in the external I/O performance to produce systems that are well-balanced in all relevant aspects of performance.

Subsequent to this implementation, the LES codes were ported to the currently available massively parallel systems such as: the Intel Paragon, Cray T3D, IBM SP-2 and the SGI Power Challenge. Both the 2D/axisymmetric and a full 3D LES codes were ported using both vendor supplied parallel compilers (NX on the Paragon, MPL on the SP-2, PFA on the SGI) and a system independent compiler: Message Passing Interface (MPI) that is now supported on all parallel machines. Simulations codes implemented using MPI can be ported from one machine architecture to another without any changes and thus, provides a significant flexibility. The results of these implementation and performance of the codes on these machines are summarized in a recent paper, Menon (1996). Results of the timing studies demonstrate that even when the code is highly optimized, different system hardware capability and performance must be taken into consideration when carrying out LES to minimize the execution time.

### **Relevant Publications/Presentations:**

1. Weeratunga, S. and Menon, S. (1993) "Parallel Simulation of Unsteady Combustion in a Ramjet Engine", AIAA 93-1914, presented at the 29th AIAA/ASME/ASCE/SAE Joint Propulsion Conference and Exhibit, Monterey, CA.
2. Menon, S. (1993) "Parallel Computations of Unsteady Combustion" invited seminar presented at the Sandia National Laboratory, Combustion Research Facility, September, 1993.
3. Menon, S. and Weeratunga, S. (1994) "Parallel Simulations of Combustion Instability in a Ramjet", Proc. High Performance Computing 1994 Conference, La Jolla, CA.
4. Menon, S. (1996) "Parallel Simulations of Unsteady Turbulent Flames", to be presented at the 1996 EUROSIM International Conference on HPCN Challenges in Telecomp and Telecom: Parallel Simulations of Complex Systems and Large-Scale Applications", 10-12 June, Delft, The Netherlands.

### 3. SECONDARY FUEL INJECTION CONTROL OF COMBUSTION INSTABILITY

The low frequency, large-amplitude pressure oscillations characteristic of combustion instability in a ramjet engine was numerically simulated using the LES method. Many features of the numerically simulated instability are in very good agreement with experimental observations. Simulations for different reference Mach numbers were carried out to differentiate between acoustic and coupled acoustic-convective modes. Analysis of the results showed that depending upon the flow Mach number, both the inlet duct acoustics and a coupled acoustic-vortex mode can excite the combustion instability in the combustor. Similar observations have been made in experimental studies.

Active control technique that uses secondary fuel injection as the controller was then investigated to suppress the instability. This method was chosen because previous experimental investigations have shown that this is a practical system for hot environments and also has the ability to increase the net thrust of the device. Secondary premixed fuel was injected upstream in the inlet duct and also at the base of the dump plane. The phase of the injected fuel (relative to the pressure fluctuation phase) was chosen based on cross correlation analysis and using theoretical considerations. Pulsed secondary fuel injection was investigated in more details. The results show that when the inlet duct acoustic mode is exciting the instability, the active control method decreases the rms fluctuation level of the pressure oscillation by 35 percent (10 dB) but leaves the dominant frequency unchanged. When the instability is being driven by the convective mode, active control results in a similar reduction in the fluctuation level and also completely suppresses the dominant frequency. However, two new frequencies: an inlet duct acoustic resonant mode and a convective mode, are excited that are not controlled. These results are consistent with recent experimental observations and suggest that to successfully control combustion instability for a wide range of flow conditions, a dynamically adjusting controller will be required.

#### Relevant Publications/Presentations:

- [1] Menon, S. (1992a) "Active Combustion Control of Combustion Instability in a Ramjet Combustor using Large-Eddy Simulations," *Combustion Science and Technology*, Vol. 84, pp. 51-79.
- [2] Menon, S. (1992b) "A Numerical Study of Secondary Fuel Injection Technique for Active Control of Instability in a Ramjet," AIAA Paper No. 92-0777.
- [3] Menon, S. (1994) "Secondary Fuel Injection Control of Combustion Instability in a Ramjet," *Combustion Science and Technology*, Vol. 100, pp. 385-393.

values thereby requiring adaptive controllers. Adaptive controllers based on neural network have proven successful in the experimental studies but the training required to implement the neural network was considerable. In addition, neural network based controllers have to be trained and implemented on the actual system thereby making a priori development of the control system difficult. On the other hand, fuzzy systems are based on an imprecise rule base and it is feasible that the training required to develop the rule base does not have to be as extensive as required for neural networks. Furthermore, the fuzzy control system has a possible advantage that the system could work just as well on non-linear systems that exhibit similar instability (even without training). Fuzzy controllers for combustion instability problems have not yet been investigated in detail. In the present study, the feasibility of a simple fuzzy rule based controller is investigated using a simplified reheat buzz device that exhibits the characteristics of combustion instability due to fluid motion - acoustic wave - unsteady heat release interactions.

The demonstration of fuzzy control is carried out using a device used by researchers at Cambridge University (see references in Menon and Sun, 1996) to investigate reheat buzz and to devise an active control method. In their study, various control methods were tested: unsteady mass injection, unsteady secondary fuel injection, etc. They were able to demonstrate that although unsteady mass injection was successful, unsteady secondary fuel injection provided a more robust control. Their numerical studies employed a one-dimensional model that closely mimic their experimental device. Using linearized analysis, they were able to show that the model predictions were in good agreement with their experimental data. In the present study, the same device and numerical model are employed with active control using fuzzy control algorithm to demonstrate the viability of fuzzy controllers to achieve active control.

The results (described in the draft paper Menon and Sun, 1995 in Appendix A) show that the fuzzy controller is capable of achieving adequate control using even very simple rule base. More refinements are required to adapt this controller to an actual combustor; however, the results obtained so far clearly demonstrate that this method is feasible. Note that, the rule base required for the fuzzy controller can be easily programmed into a memory chip (as demonstrated in past studies) and thus, is cost effective.

#### **Relevant Publications/Presentations:**

[1] Menon, S. and Yang V. (1993) "Some Issues Concerning Active Control of Combustion Instability in Ramjets", AIAA 93-0116, presented at the 31st Aerospace Sciences Meeting, Reno, NV.

[2] Menon, S. and Y. Sun (1996) "Fuzzy Logic Control of Reheat Buzz," to be presented at the 32nd AIAA/ASME/ASEE/SAE Joint Propulsion Conference, July 1-3, 1996, Orlando Florida.

## 5. STRUCTURE OF PREMIXED FLAMES IN DUMP COMBUSTORS

### 5.1 Effect of Curvature and Strain on the Premixed Flame Structure:

Large eddy simulations of spatially propagating premixed flames in a three-dimensional dump combustor have been conducted at relatively high Reynolds numbers. A thin flame model is used to simulate the propagating flame front and the propagation speed is estimated using the subgrid turbulence intensity. Analysis of the simulations show that various statistics, such as flame front shape factor, stretch effects, vorticity/strain rate, and strain rate/surface normal alignments, agree reasonably well with data from constant density, direct numerical simulations of passive scalar and premixed flame propagation in simpler, temporally evolving low Reynolds number flows. This suggests that the general characteristics of propagating scalars in turbulent flows are relatively independent of Reynolds number and further that these features can be captured using relatively coarse grid LES at high Reynolds numbers. However, detailed analysis showed that in spatially developing flows, there is a significant dependence on the spatial location for some statistical properties. As the flame propagates downstream the probability density of the shape factor showed a decreasing probability for cylindrical shaped flames and the strain rate/flame normal alignment showed a transition from the alignment seen in shear driven flow to alignment seen in isotropic turbulence. Strain rate (in the plane of the flame) was maximum near the flame holder (the rearward facing step) and decreases in the downstream direction with the pdf becoming more symmetric similar to isotropic flows. The implication of the observed spatial dependence for investigating flame stretch effects and therefore, flame extinction is discussed.

### 5.2 Fractal Nature of Premixed Flame:

A computational method that provides a one-dimensional stochastic representation of turbulent convection and laminar flamelet propagation in turbulent premixed flames has been used to investigate the structure and propagation characteristics of the wrinkled flame. An earlier study of the structure of the turbulent flame brush is extended and generalized to include thermal expansion (i.e., heat release). In this broader context, the issues of fractal dimension and dynamic range of fractal scaling are revisited. A new viscous length scale is identified that collapses the data and help explain the observed dependence of the fractal dimension on  $u'/S_L$ .

Here,  $u'$  is the turbulence intensity and  $S_L$  is the laminar flame speed. These and other properties of the time-varying structure of the flame brush were analyzed in order to assess the reliability of extrapolations from moderate-Re laboratory configurations to high-Re conditions.

#### **Relevant Publications/Presentations:**

- [1] Smith, T. M., Menon, S., and McMurtry, P. (1994) "The Structure of Premixed Flames in Isotropic and Shear Driven Turbulent flow Fields," AIAA 94-0677, presented at the 32nd Aerospace Sciences Meeting, Reno, NV.
- [2] Menon, S. and Kerstein, A. R. (1994) "A Computational Model to Predict the Fractal Nature of Turbulent Premixed Flames," AIAA 94-0678, presented at the 32nd Aerospace Sciences Meeting, Reno, NV.
- [3] Smith, T. M., and Menon, S. (1994a) "The Structure of Constant-Property Propagating Surfaces in a Spatially Evolving Turbulent Flow," AIAA 94-2391, presented at the 25th AIAA Fluid Dynamics Conference, Colorado Springs, CO.
- [4] Smith, T. M. and Menon, S. (1994b) "Simulation of Premixed Flame Propagation and Turbulence Interactions in a High Reynolds Number Spatially Evolving Flow", presented at the 1994 Meeting of the Division of Fluid Dynamics, American Physical Society, November 20-22, 1994, Atlanta, Georgia.
- [5] Smith, T. M., and Menon, S. (1995) "The Structure of Premixed Flames in a Spatially Evolving Turbulent Flow," submitted to *Combustion Science and Technology*.
- [6] Menon, S. (1996) "Large-Eddy Simulations of Combustion Instability in a Dump Combustor", to be presented at the Sixth International Conference on Numerical Combustion, SIAM, New Orleans, March 4-6, 1996.

## 6. FULL 3D SIMULATIONS OF COMBUSTION INSTABILITY

A full 3D code was also used to carry out a relatively coarse grid LES to evaluate importance of the 3D effects. High resolution 3D LES is not possible due to the increased computational cost; however, even the coarse grid simulations clearly show the 3D effects. A recent study (Smith et al., 1994) has shown that even when the flow field is highly 3D, the vortical structures has a tendency to roll up into coherent 2D structures. In fact, recent analysis shows that the flame structure is highly 2D even when the flow is 3D. This has some important significance, since it suggests that 2D simulations should be sufficient to simulate reacting flows. In retrospect, the good results obtained in this research clearly lends support to these results.

Here, a brief summary of these results is given. Detailed analysis of this data is still underway and will be reported in the near future. The primary objective of the 3D simulation... was to determine if the earlier axisymmetric simulations results are reliable concerning the physics of the low-frequency, large-amplitude pressure oscillation and its relationship to the vortex motion. Earlier studies (Menon and Jou, 1991) has shown that during the combustion instability a large vortex-flame structure propagates through the combustor at the dominant frequency. Analysis and comparison of these results with past experimental data showed very good agreement. For reference, Figures 1 and 2 show respectively, the computed flame structure (using axisymmetric LES) and the experimentally observed flame motion observed during combustion instability in a dump combustor. The computed vorticity contours in the dump combustor are shown in Fig. 3. As can be seen there is very good agreement between the computed flame features and the experimentally observed flame. Further analysis (in Menon and Jou, 1991 - noted above) showed that there is also good agreement between the simulated results and the experimentally measured data on the phase relationship between the pressure and axial velocity fluctuations. Since the axisymmetric simulations does not allow for the 3D vortex stretching effects, it was not possible to confirm if this feature is important. To determine this, full 3D LES was also carried out. In the following, some of the 3D results are shown and discussed.

Figures 4a through 4c show respectively, x-y planes (at quarter-span, mid span and three-quarter-span) of the flame structure during the full 3D LES. The corresponding z-component of the vorticity are shown respectively in Figs. 5a-5c. These results were obtained from a 3D LES carried out using a grid resolution of  $192 \times 64 \times 32$  with periodic boundary conditions in the spanwise (z) direction. The one-equation model for the subgrid kinetics energy is used to close the subgrid stresses and energy flux. The time sequence shown in figures 4 and 5 is for a single wavelength of the pressure oscillation. Comparison with the earlier results obtained using the axisymmetric code shows remarkable agreement in the large-scale structures and the correspondence of the flame front with these large structures. However, the 3D data is much more richer in the finer details such as the wrinkling of the flame front, and the presence of smaller vortical structures in the combustor. Significant 3D (spanwise variation) of the flame and vortical structures can be seen in these figures. However, in spite of the 3D effects seen in these figures, the large vortex-flame structure propagates through the combustor at the frequency of the instability. This characteristic behavior is quite similar to the vortex-flame propagation seen in the axisymmetric simulations carried out earlier. The vortical contours shown in Figs. 5a-5c also show significant 3D vortex stretching effects and the breakdown of the large structures near the diffuser.



The 3D nature of the flame structure in the combustor is shown in 3D perspective of the flame in Figs. 6a and 6b which show two characteristic snapshots of the flow field shown in Figs. 4 and 5.

The properties of the flame front can be analyzed as done earlier to evaluate the structure and the propagation characteristics of the flame. Some results, including comparison with the earlier 3D simulations (without heat release) are presented below for completeness. Figures 7a-7h show some of the typical results obtained in the present simulations. The data from one entire oscillation is averaged and presented. Figure 7a shows the pdf of the shape factor for the whole domain and also for four locations (separated by a distance equal to the step height) in the combustor. The shape factor was computed using the definition given before (Smith and Menon, 1995) and is the ratio of the smaller radius over the larger radius of curvature of the flame. As earlier (for no heat release), the shape factor has a maximum value close to zero (which corresponds to a cylindrical flame) with vanishing probability for saddle (-1) and spherical (+1). This suggests that even when heat release is included, the flame tends to become cylindrically shaped surface and this result agrees quite well with previous results obtained in flows without heat release. This cylindrical nature of the flame sheet is due to the intense vorticity that wraps the flame around it, increasing the curvature of the flame and the tangential strain in the plane of the flame. As shown earlier, the vorticity aligns with the intermediate principle strain rate while the normal to the flame aligns with the most compressive strain rate. Figure 7b shows the probability density for the alignment of the intermediate strain-rate with vorticity as obtained from the present simulation. The observed alignment is maintained in the entire domain.

Figure 7c shows the alignment of the three principle strain-rate with the flame normal and Figure 7d shows the alignment of the flame normal with the most compressive strain rate. These figures again corroborate the earlier (no heat release) data that the flame tends to wrap around the intense local vortical structure and forms a cylindrical shape with the orientation of the normal to the flame in the direction of the most compressive strain-rate.

Figure 7f shows the probability density for the normalized mean curvature (as defined in Smith and Menon, 1995). In order to be consistent with earlier data, the negative of the mean curvature is plotted (negative indicates that curvature concave with respect to the unburned fuel is positive). The data is quite similar to that obtained in the earlier no-heat release simulations. Figure 7g shows the probability density of the normalized tangential strain rate in the whole domain and at the chosen locations. The pdf of the tangential strain rate in the plane of the flame is normalized by the Kolomogorov time-scale and the pdf data indicates the mean strain rate is slightly positive. This is in good agreement with the earlier data and in other no-heat release studies. Mean positive straining indicates that on the whole the flame is being stretched. Finally, Fig. 7h shows the stretch probability which is a result of the curvature and tangential strain in the plane of the flame. There appears to a spatial dependence of the stretch and the mean probability is slightly positive. This means that, on the average, the laminar flame speed will be reduced by the stretch effect. The stretch effect is highest near the step and decreasing downstream. This indicates that there is a possibility of flame extinction near the step.

To directly compare the cases with and without heat release, Figures 8a-8f show some characteristic flame structure properties averaged over the whole domain. It can be seen that on

the average, both simulations show very similar results. Of particular interest is the observation that flame maintains a cylindrical shape with an alignment such that it always wraps around the vortex structures. The effect of heat release is to increase somewhat the mean tangential strain rate in the plane of the flame and hence the stretch effects.

In conclusion, the 3D LES of the combustion instability with and without heat release shows that the earlier results (obtained using axisymmetric LES) were quite accurate regarding the fundamental nature of the combustion instability in the combustor. The instability results in the formation of a large vortex-flame structure that propagates through the combustor at the instability frequency. The 3D effects are confined to the later stages of the vortex-flame evolution especially near the diffuser where the vortex breaks down. Thus, it appears that to understand the primary coupling between unsteady heat release, vortex motion and acoustic oscillation in a dump combustor, a more (computationally) cost-effective axisymmetric LES is sufficient. This result is further explained by investigating the structure of the 3D flame front and by determining the orientation of the flame-vortex structure. Results shows that in most cases, the flame tends to wrap around the most intense local vortex shape. Thus, in the near field of the dump plane, the flame wraps around the large spanwise structures (that are likely to be axisymmetric) while further downstream the flame tends to wrap around streamwise structures (that are 3D). Thus, axisymmetric LES data is likely to contain adequate physics of the flame-vortex propagation in the near field but will not be able to capture the 3D nature near the diffuser. However, since the combustion instability is known to be due to the formation of the large structures, the results obtained using axisymmetric LES can be used to understand the physics of this interaction.

## PUBLICATIONS/PRESENTATIONS UNDER THIS GRANT

The titles of the various publications and presentations under this project are re-summarized below. The papers included in the Appendix are also indicated.

- [1] Menon, S. (1992a) "Active Combustion Control of Combustion Instability in a Ramjet Combustor using Large-Eddy Simulations," *Combustion Science and Technology*, Vol. 84, pp. 51-79.
- [2] Menon, S. (1992b) "A Numerical Study of Secondary Fuel Injection Technique for Active Control of Instability in a Ramjet," AIAA Paper No. 92-0777.
- [3] Weeratunga, S. and Menon, S. (1993) "Parallel Simulation of Unsteady Combustion in a Ramjet Engine", AIAA 93-1914, presented at the 29th AIAA/ASME/ASCE/SAE Joint Propulsion Conference and Exhibit, Monterey, CA. [In Appendix A]
- [4] Menon, S. and Yang V. (1993) "Some Issues Concerning Active Control of Combustion Instability in Ramjets", AIAA 93-0116, presented at the 31st Aerospace Sciences Meeting, Reno, NV. [In Appendix A]
- [5] Menon, S. (1993) "Parallel Computations of Unsteady Combustion" invited seminar presented at the Sandia National Laboratory, Combustion Research Facility, September, 1993.
- [6] Menon, S. and Weeratunga, S. (1994) "Parallel Simulations of Combustion Instability in a Ramjet", Proc. High Performance Computing 1994 Conference, La Jolla, CA.
- [7] Menon, S. (1994) "Secondary Fuel Injection Control of Combustion Instability in a Ramjet," *Combustion Science and Technology*, Vol. 100. pp. 385-393. [In Appendix A]
- [8] Smith, T. M., Menon, S., and McMurtry, P. (1994) "The Structure of Premixed Flames in Isotropic and Shear Driven Turbulent flow Fields," AIAA 94-0677, presented at the 32nd Aerospace Sciences Meeting, Reno, NV. [In Appendix A]
- [9] Menon, S. and Kerstein, A. R. (1994) "A Computational Model to Predict the Fractal Nature of Turbulent Premixed Flames," AIAA 94-0678, presented at the 32nd Aerospace Sciences Meeting, Reno, NV. [In Appendix A]
- [10] Smith, T. M., and Menon, S. (1994a) "The Structure of Constant-Property Propagating Surfaces in a Spatially Evolving Turbulent Flow," AIAA 94-2391, presented at the 25th AIAA Fluid Dynamics Conference, Colorado Springs, CO. [In Appendix A]
- [11] Smith, T. M. and Menon, S. (1994b) "Simulation of Premixed Flame Propagation and Turbulence Interactions in a High Reynolds Number Spatially Evolving Flow", presented at the 1994 Meeting of the Division of Fluid Dynamics, American Physical Society, November 20-22, 1994, Atlanta, Georgia.

## **PUBLICATIONS/PRESENTATIONS (Cont.)**

[12] Smith, T. M., and Menon, S. (1995) "The Structure of Premixed Flames in a Spatially Evolving Turbulent Flow," submitted to *Combustion Science and Technology*. [In Appendix A]

[13] Menon, S. (1996) "Parallel Simulations of Unsteady Turbulent Flames", to be presented at the 1996 EUROSIM International Conference on HPCN Challenges in Telecomp and Telecom: Parallel Simulations of Complex Systems and Large-Scale Applications", 10-12 June, Delft, The Netherlands.

[14] Menon, S. and Sun, Y. (1996) "Fuzzy Logic Control of Reheat Buzz," to be presented at the 32nd AIAA/ASME/ASEE/SAE Joint Propulsion Conference, July 1-3, 1996, Orlando Florida.

[15] Menon, S. (1996) "Large Eddy Simulations of Combustion Instability in a Dump Combustor," to be presented at the Sixth International Conference on Numerical Combustion, SIAM, New Orleans, March 4-6, 1996.

## LIST OF FIGURES

Figure 1. Flame propagation in an axisymmetric ramjet combustor during unstable combustion. Red indicates the flame, Cyan indicates the premixed fuel and yellow indicates the burnt product.

Figure 2. Vortex-Flame evolution in a two-dimensional dump combustor during unstable combustion. Flow visualization from Smith and Zukoski (1985) shown inverted.

Figure 3. Vortex motion in an axisymmetric ramjet combustor during unstable combustion. Results for the same oscillation shown in Figure 1.

Figure 4. Flame propagation in a three-dimensional ramjet combustor during unstable combustion. Results for a full oscillation. Flame is indicated by the red regions.

(a) x-y plane at quarter-span (z) plane

(b) x-y plane at mid-span (z) plane

(c) x-y plane at three-quarter-span (z) plane

Figure 5. Vorticity contours in a three-dimensional ramjet combustor during unstable combustion. Conditions and snapshots correspond to the figures shown in Figure 4.

(a) x-y plane at quarter-span (z) plane

(b) x-y plane at mid-span (z) plane

(c) x-y plane at three-quarter-span (z) plane

Figure 6. Three-dimensional perspective of the flame structure in the three-dimensional ramjet during unstable combustion. Figures correspond to snapshots shown in Fig. 4.

Figure 7. Structure properties of the flame front in the three-dimensional ramjet combustor. Analysis involved averaging snapshots over a full unstable oscillation (shown as whole region) and also averaging locally to obtain spatial evolution information. Four axial locations (separated by a distance each of step height) is also shown. All results are for the heat release case.

(a) Probability density of the shape factor.

(b) Probability density of the alignment between the intermediate strain rate and vorticity.

(c) Probability density of the alignment between the three component of the strain rate and the flame normal for the whole domain

(d) Probability density of the alignment between the strain rate and the flame normal for the

whole domain and local regions.

(e) Probability density of the alignment of the two principle radius of curvature.

(f) Probability density of the negative mean curvature.

(g) Probability density of the normalized tangential strain rate.

(h) Probability density of the normalized stretch.

Figure 8. Structure properties of the flame front in the three-dimensional ramjet combustor. Analysis involved averaging snapshots over a full unstable oscillation. Comparison of the no-heat release and heat release cases

(a) Probability density of the shape factor.

(b) Probability density of the alignment between the intermediate strain rate and vorticity.

(c) Probability density of the alignment between the strain rate and the flame normal for the whole domain and local regions.

(d) Probability density of the normalized tangential strain rate.

(e) Probability density of the normalized negative mean curvature.

(f) Probability density of the normalized stretch.

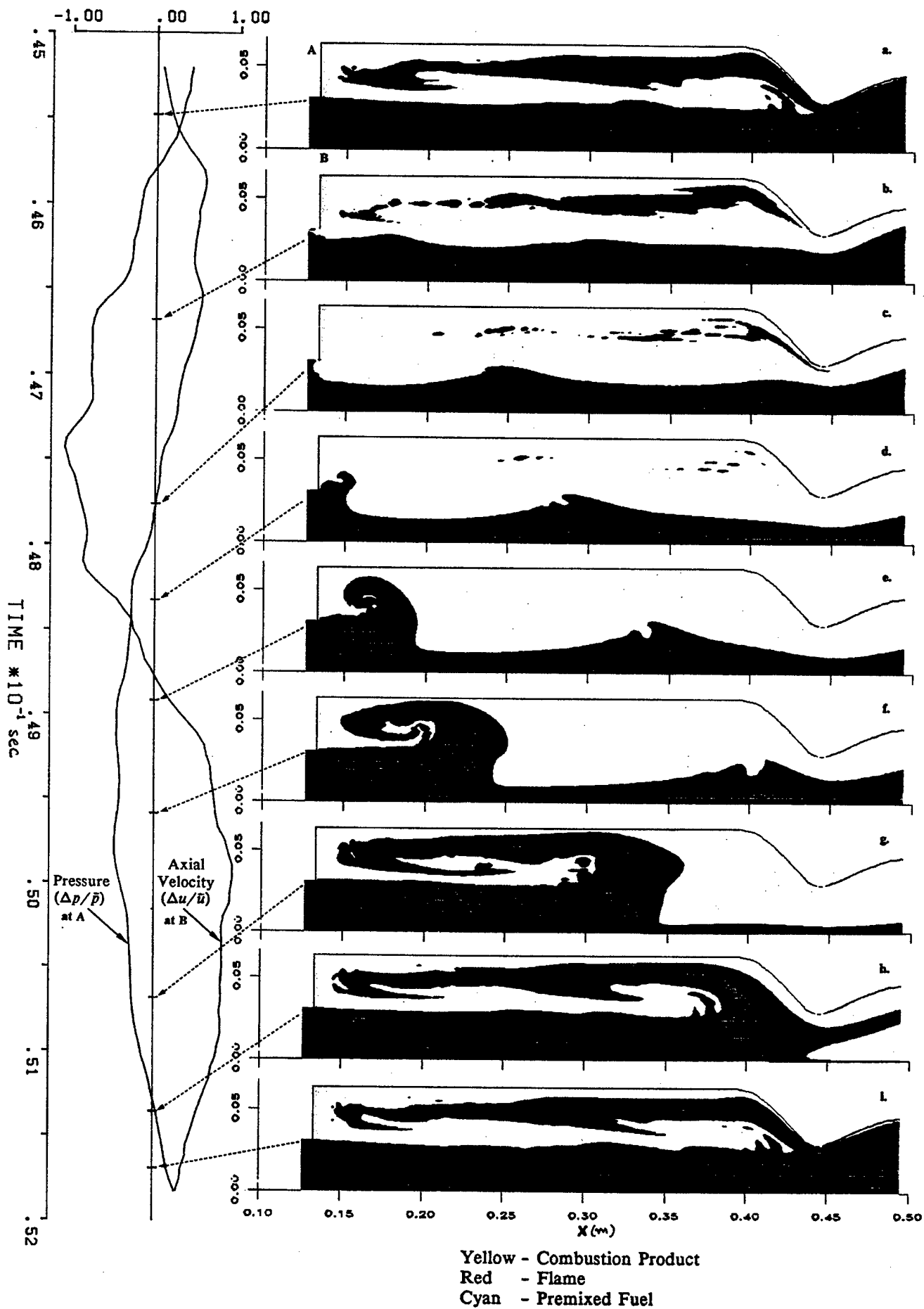


Figure 8. Flame Propagation in an Axisymmetric Ramjet Combustor During Unstable Combustion

FIGURE 1

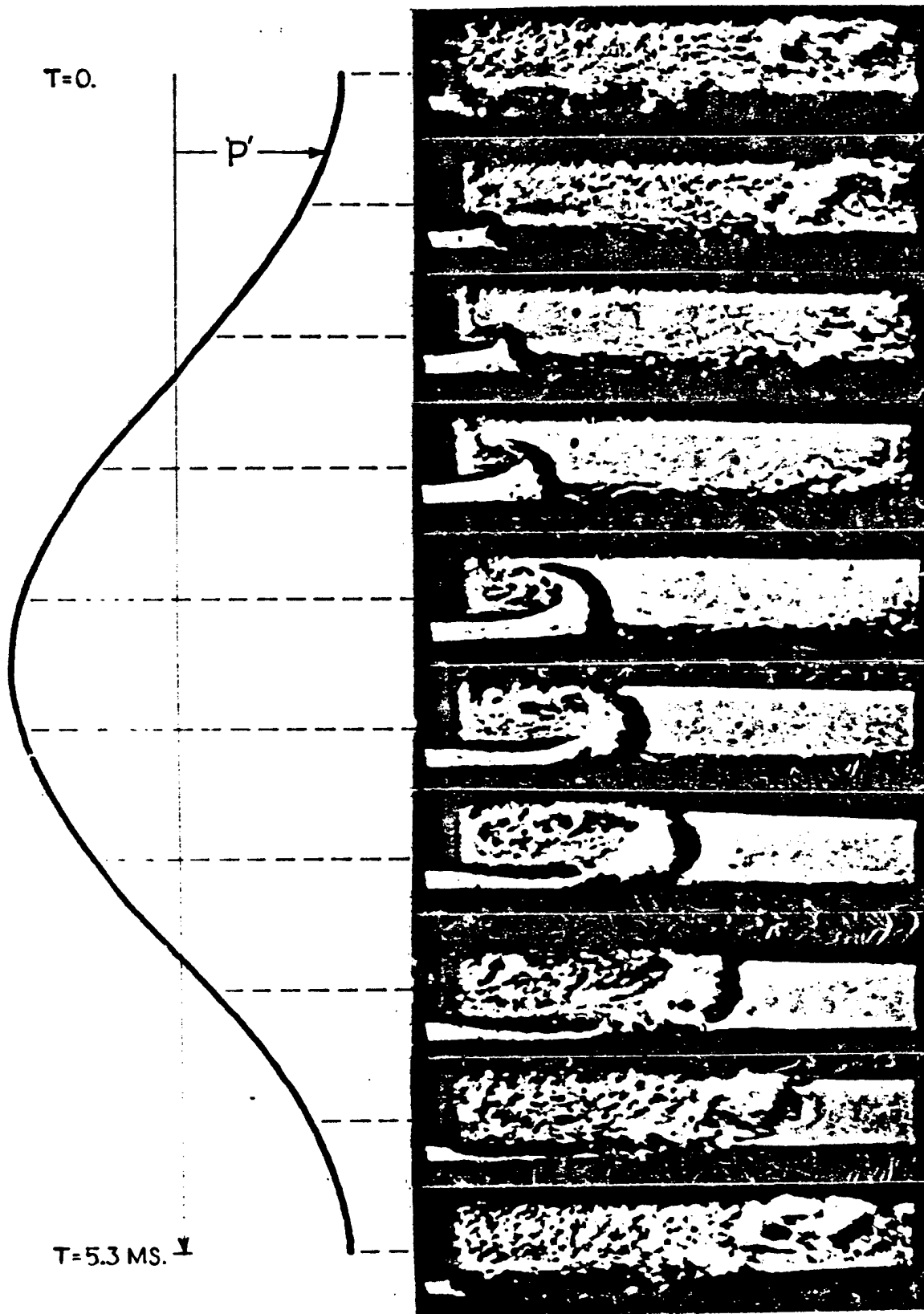


Figure 2. Vortex evolution in a two-dimensional dump combustor during unstable combustion. Flow visualization from Smith and Zukoski (1985) (Shown Inverted).

FIGURE 2



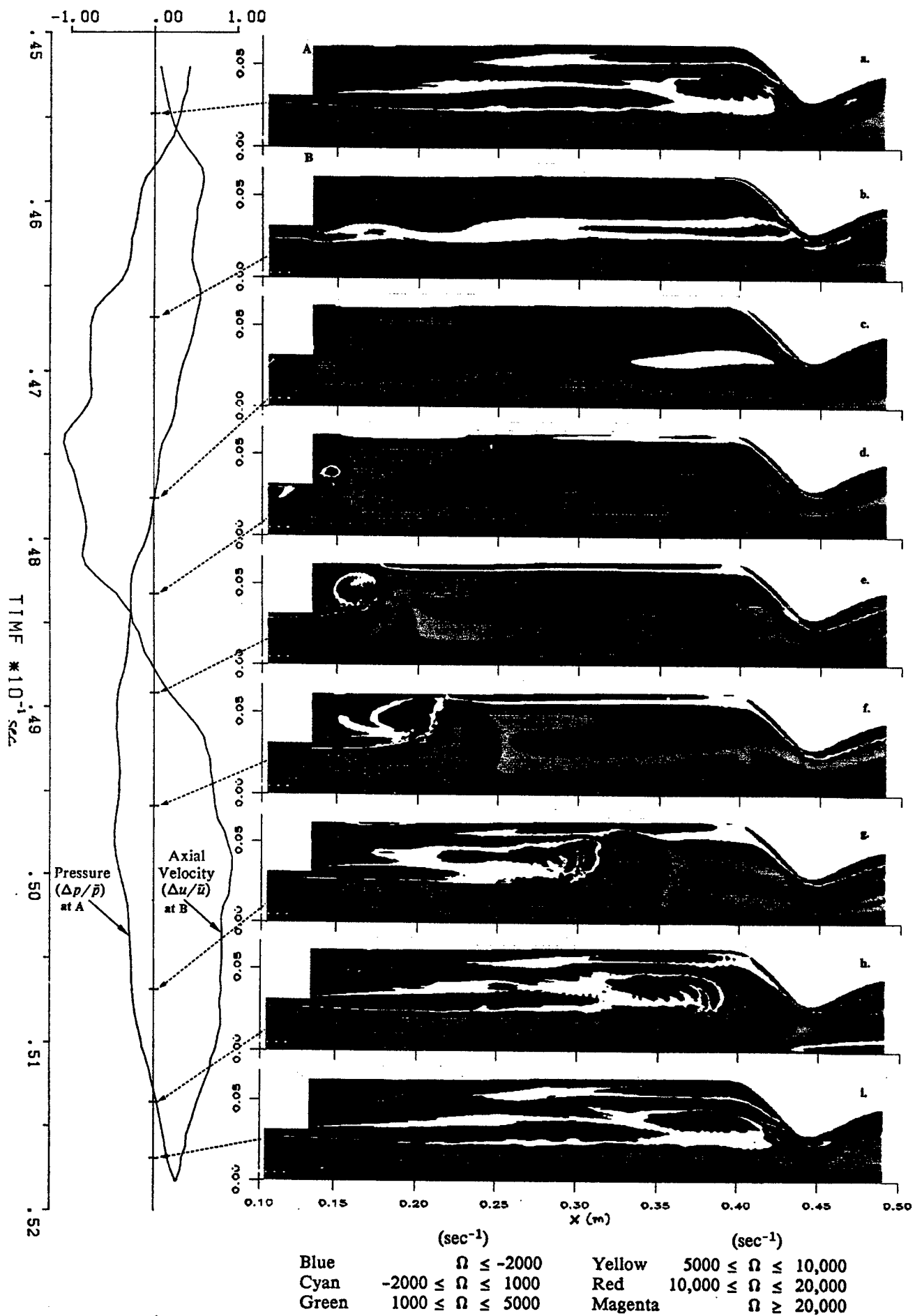
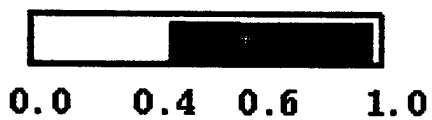
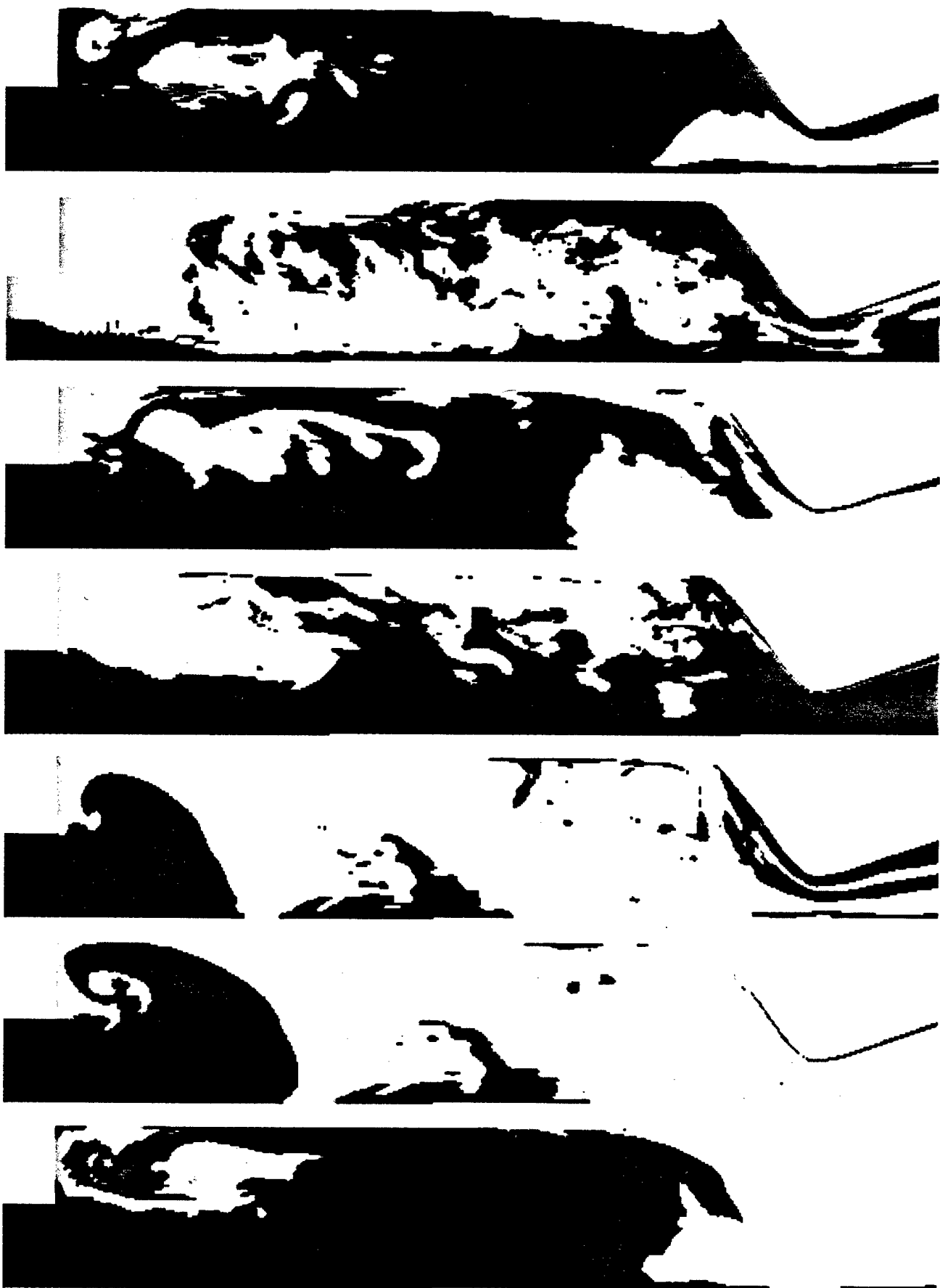


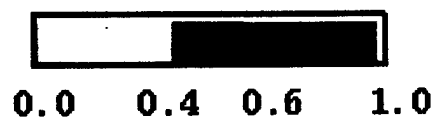
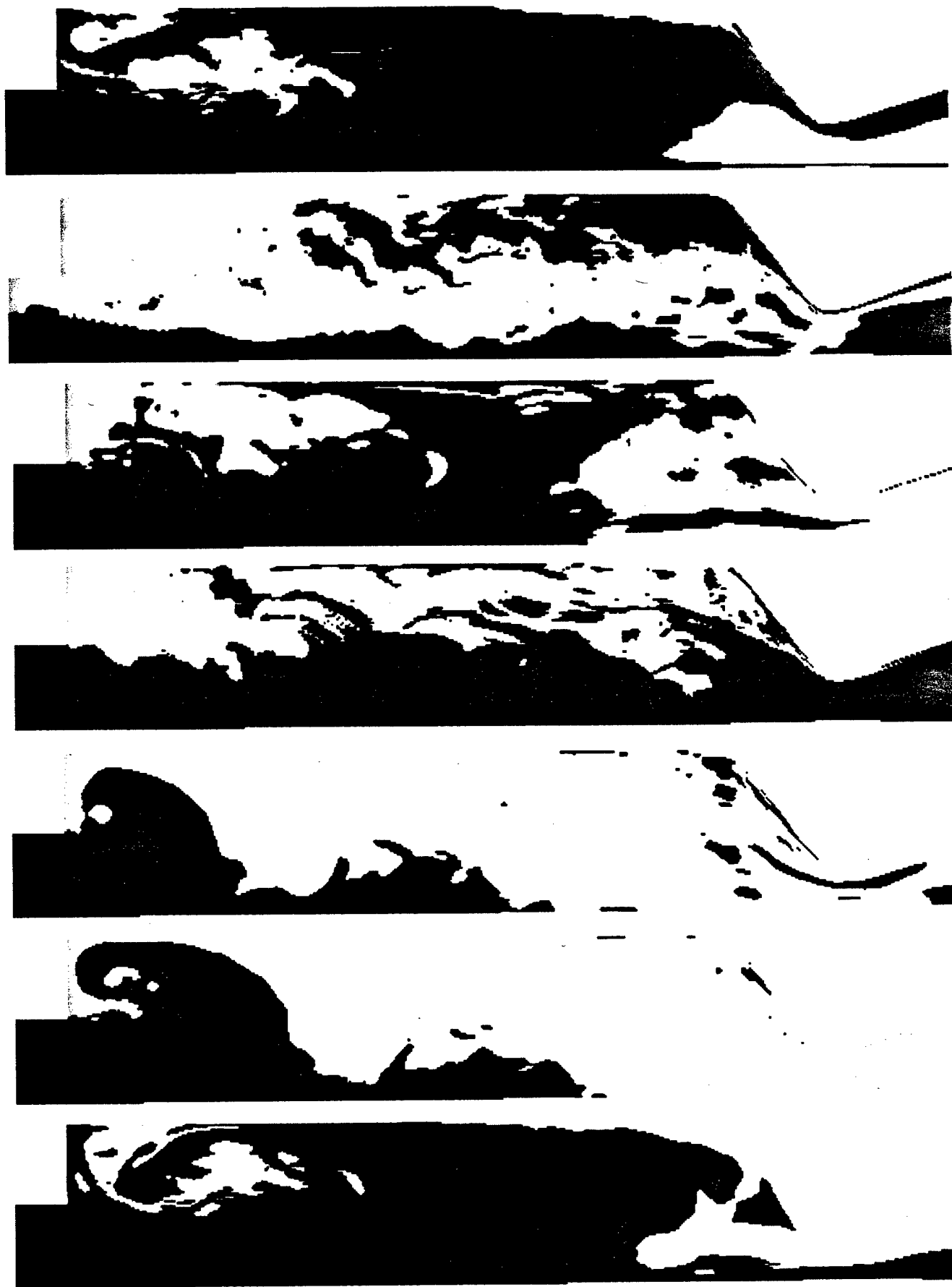
Figure 3. Vortex motion in the ramjet combustor for a cycle of unstable combustion

FIGURE 3



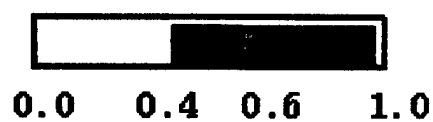
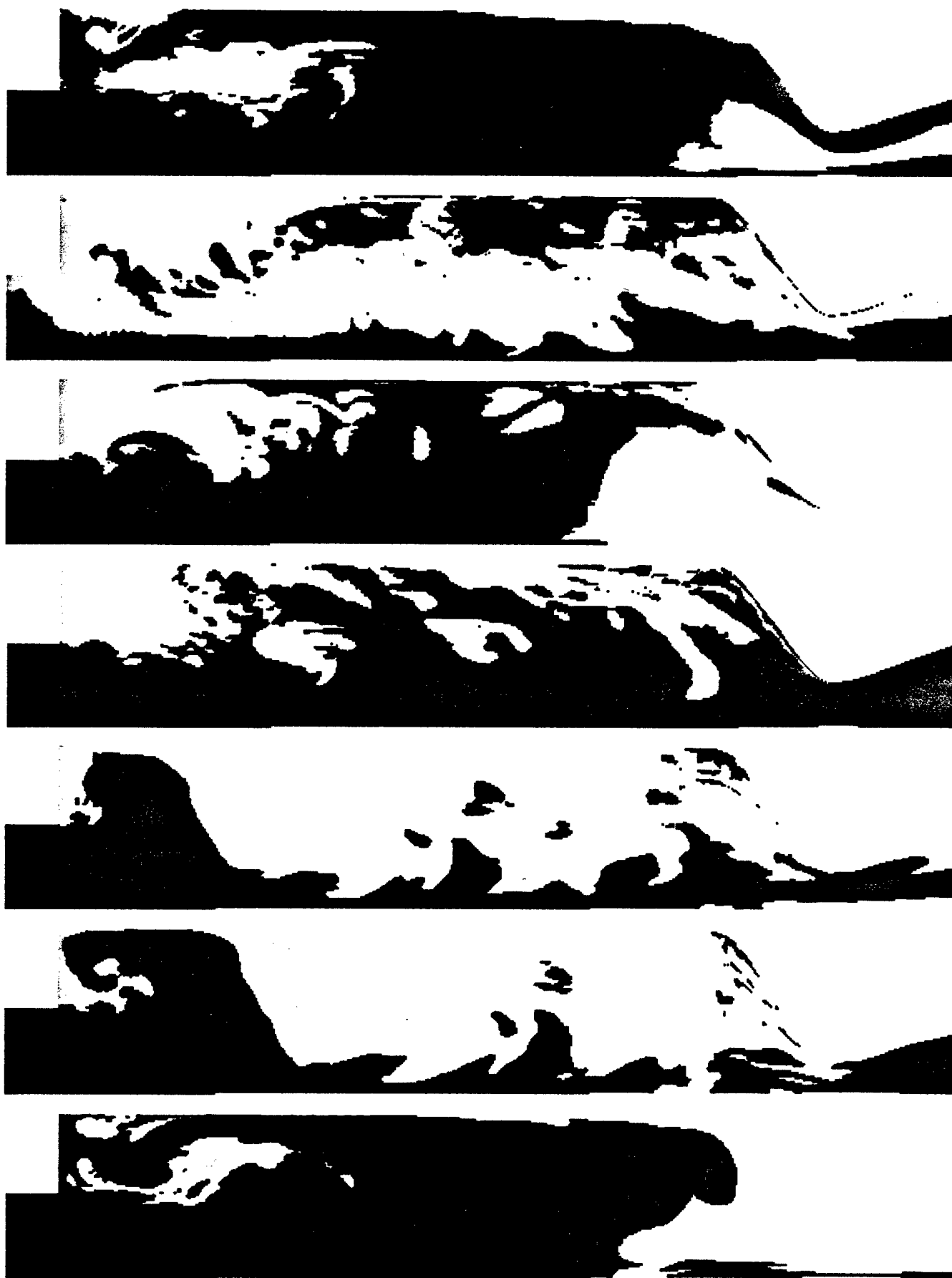
Flame propagation in the combustor of an  
axisymmetric ramjet, at  $1/4 z$  plane, at  
various time steps

FIGURE 4a



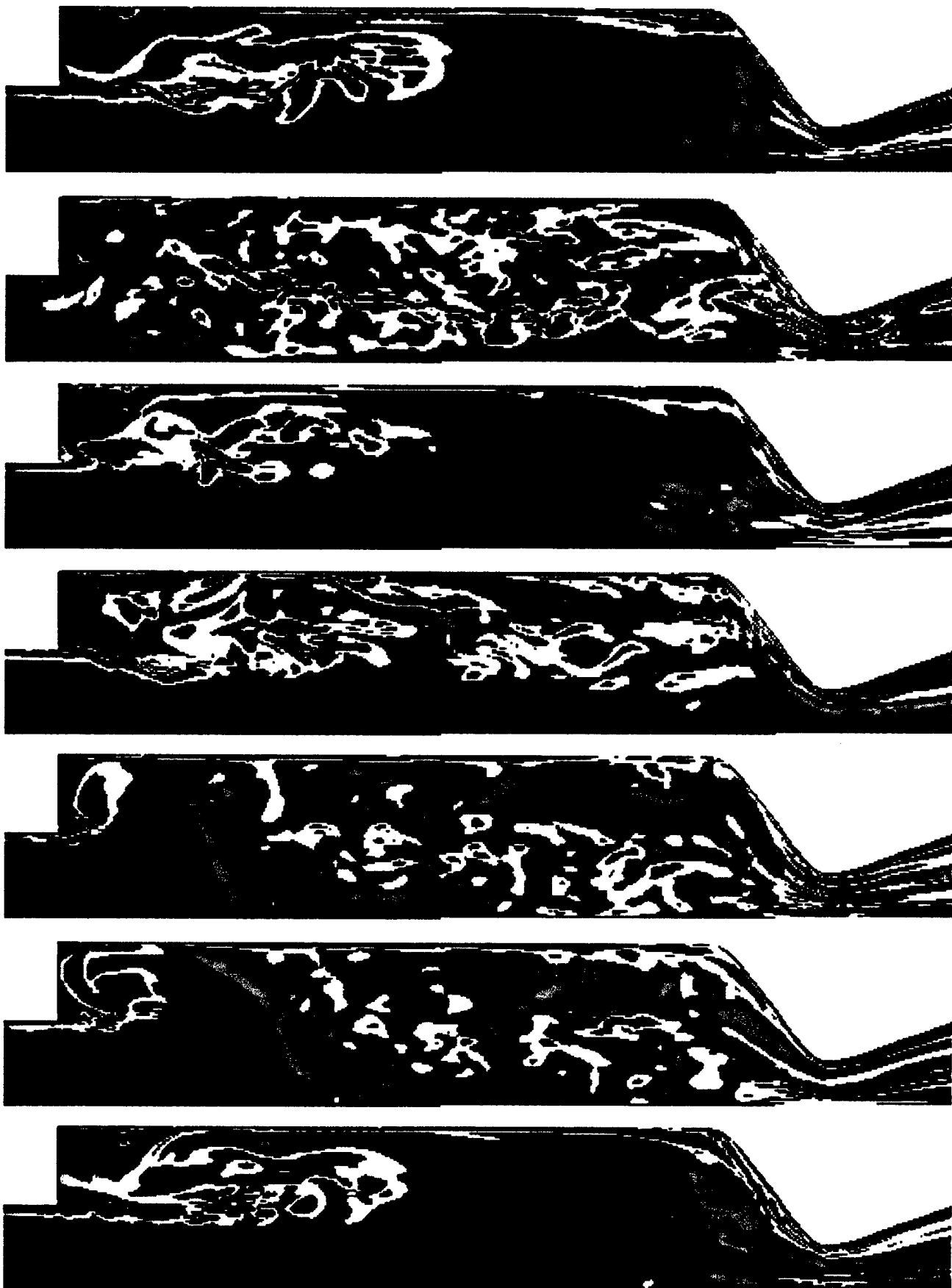
Flame propogation in the combustor of an  
axisymmetric ramjet, at  $1/2 z$  plane, at  
various time steps

FIGURE 4b



Flame propagation in the combustor of an  
axisymmetric ramjet, at  $3/4 z$  plane, at  
various time steps

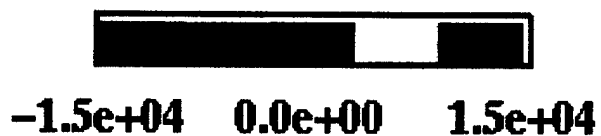
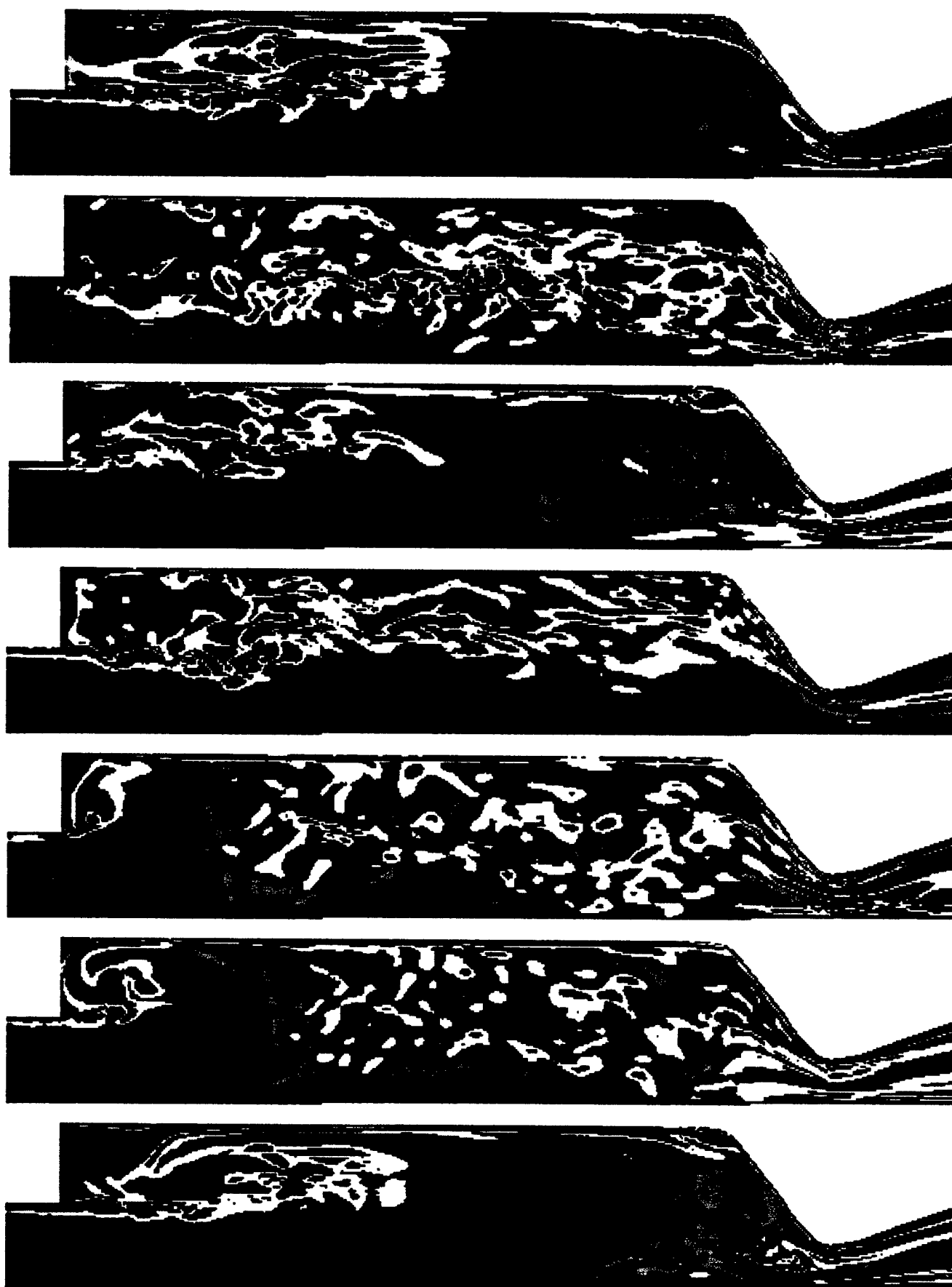
FIGURE 4c



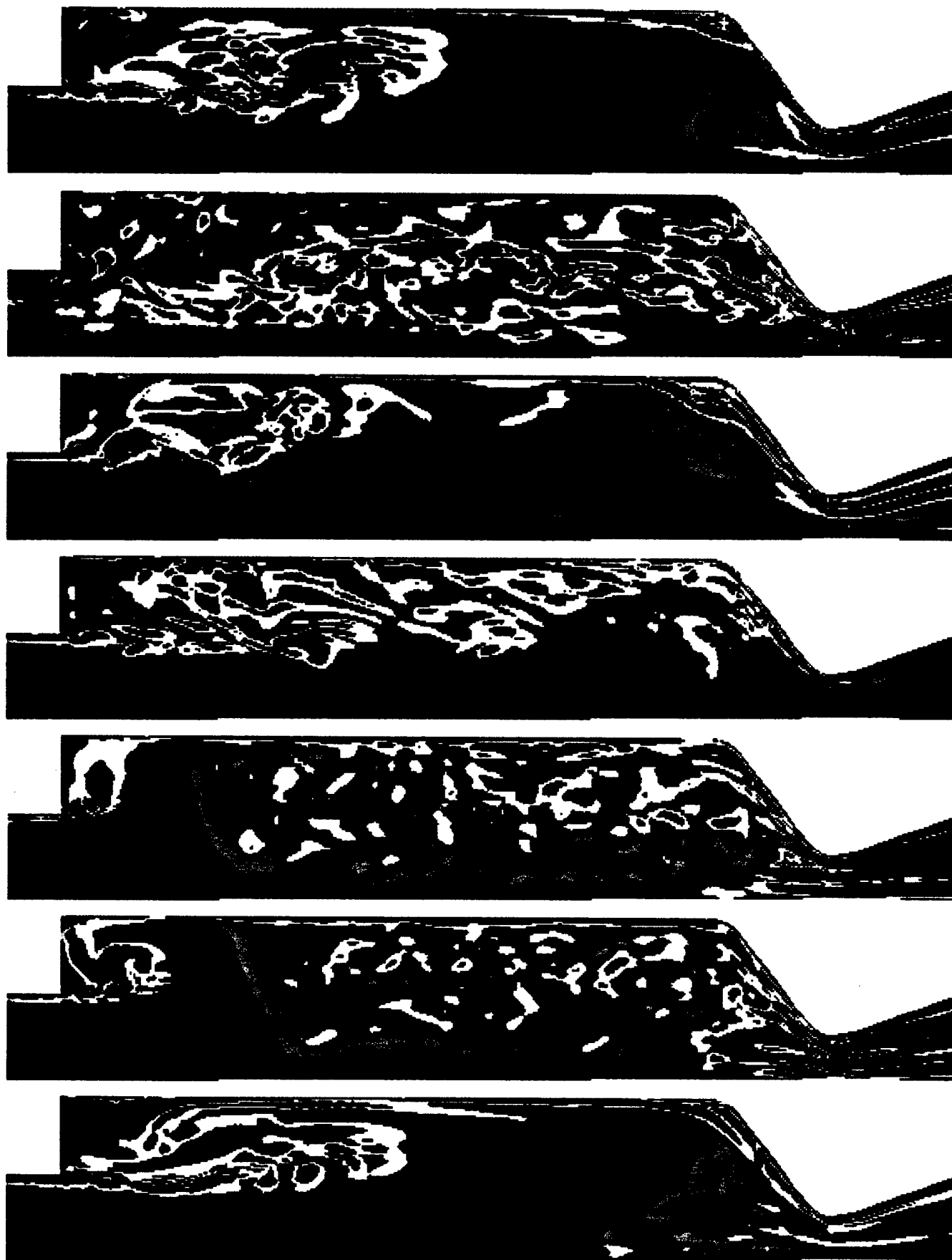
-1.5e+04    0.0e+00    1.5e+04


z component of vorticity in the  
combustor of an axisymmetric ramjet,  
at 1/4 z plane, at various time steps

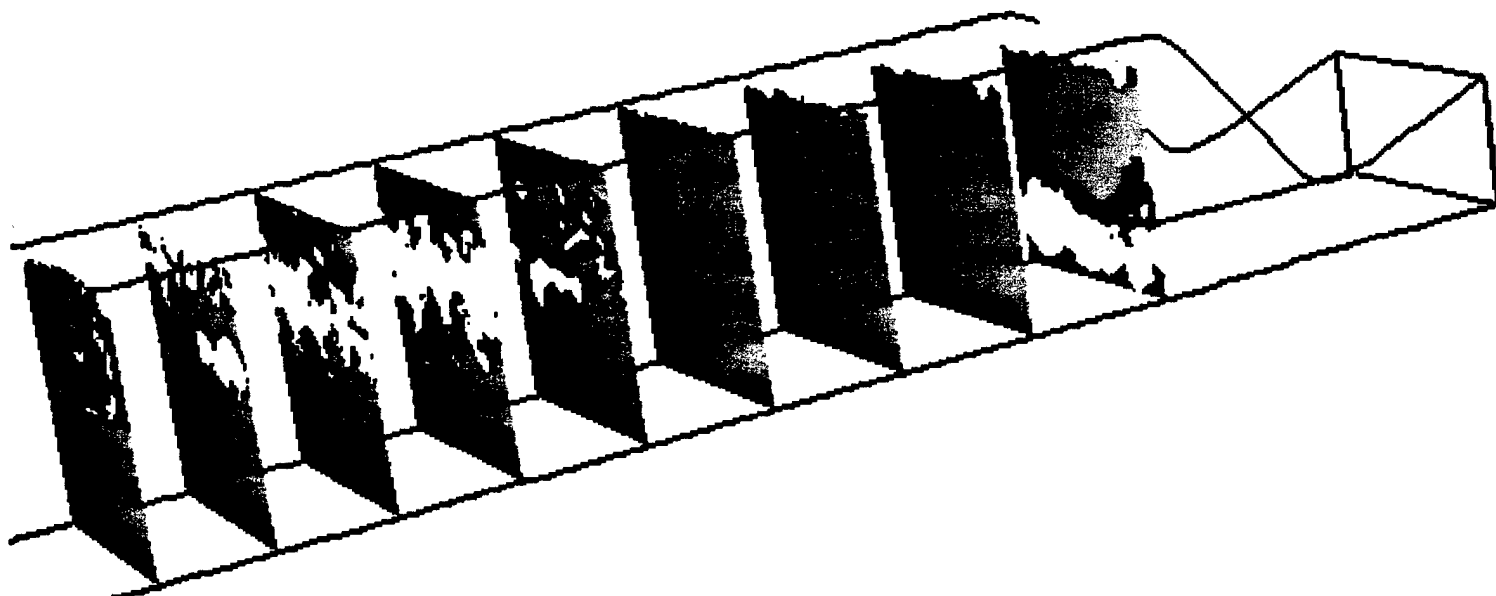
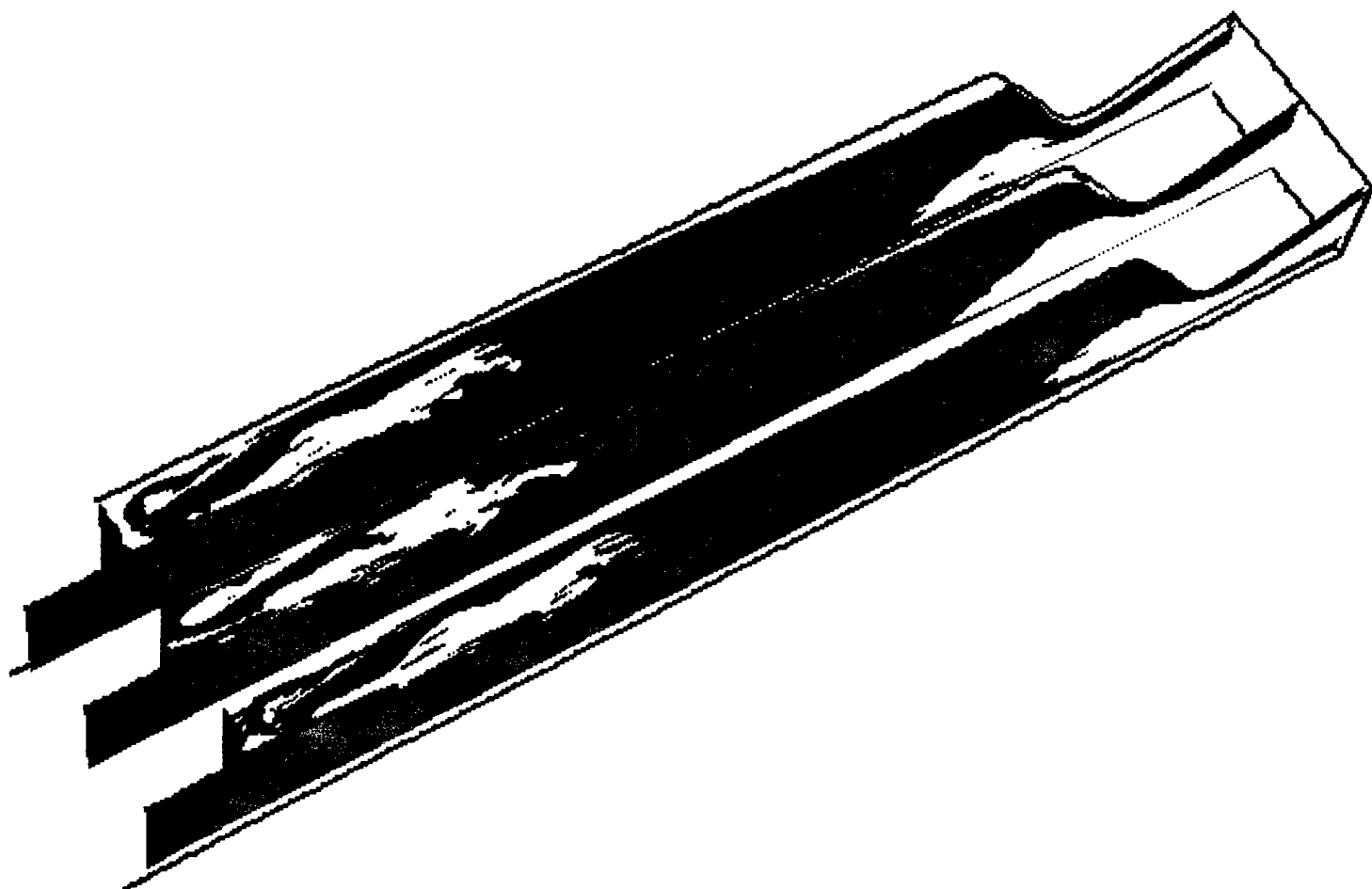
FIGURE 5a



z component of vorticity in the  
 combustor of an axisymmetric ramjet,  
 at 1/2 z plane, at various time steps  
 FIGURE 5b




 z component of vorticity in the  
 combustor of an axisymmetric ramjet,  
 at 3/4 z plane, at various time steps  
 FIGURE 5c

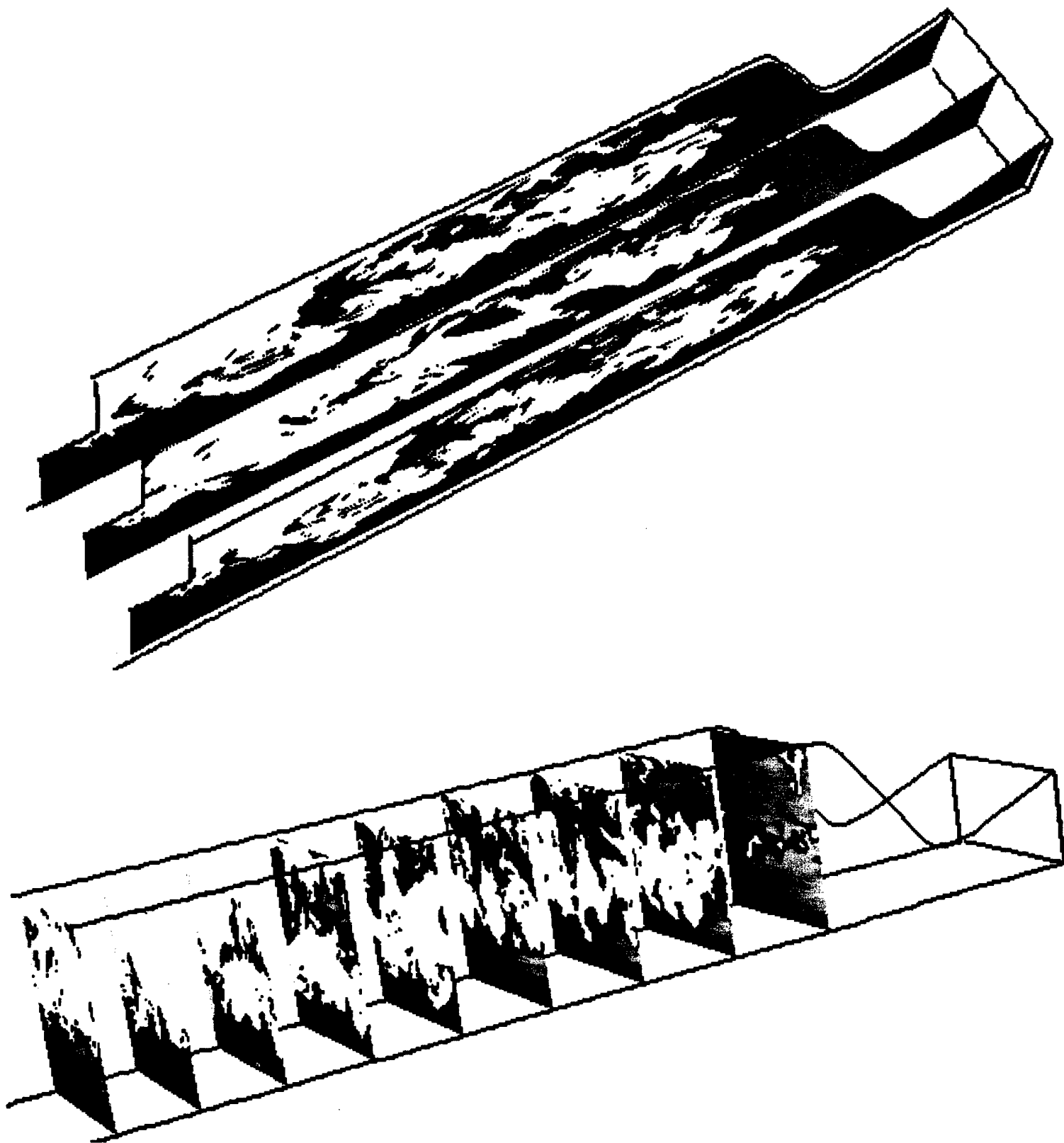


Flame propagation in the combustion chamber of an axisymmetric ramjet, at various spanwise & streamwise locations.

file : r4b150

FIGURE 6a





file : r4b170

FIGURE 66

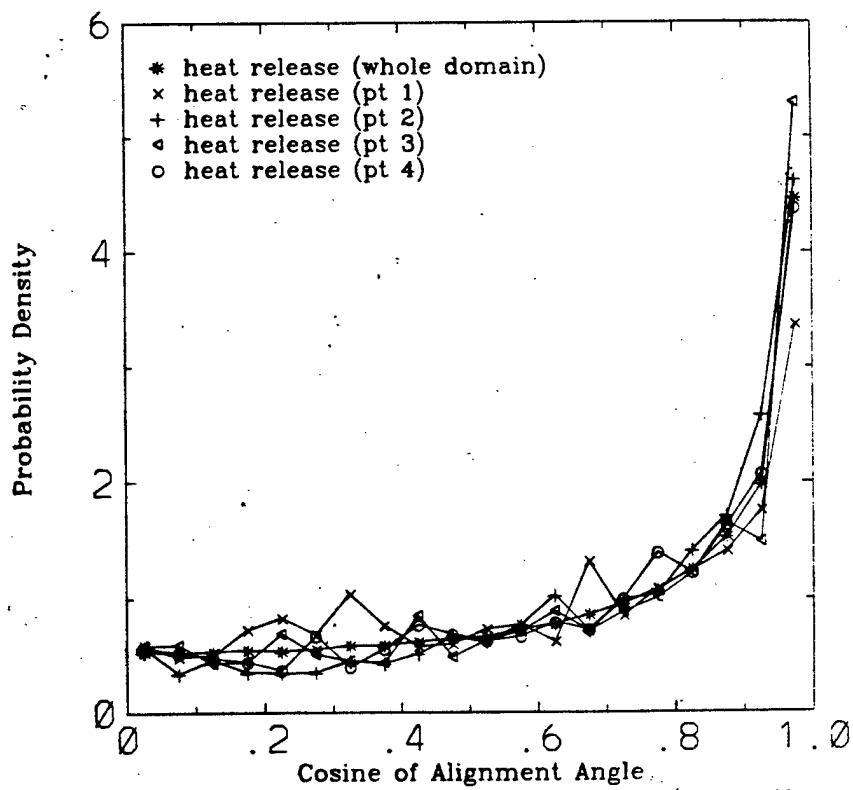
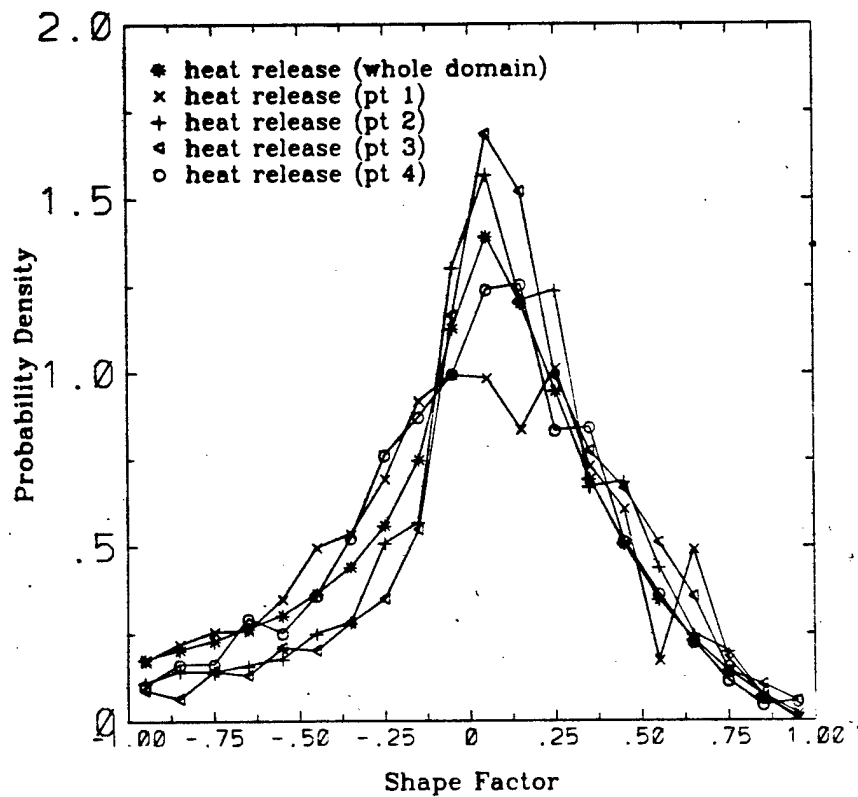
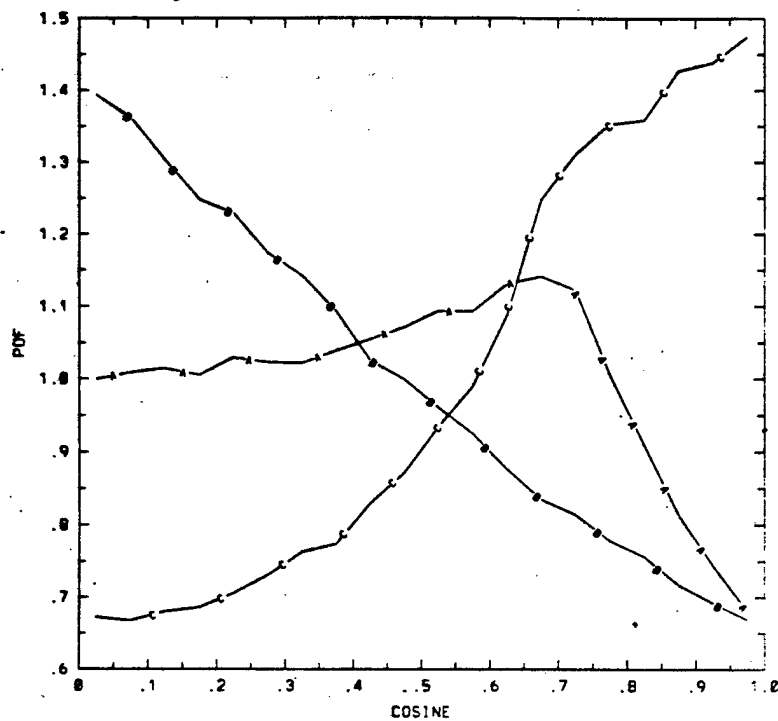
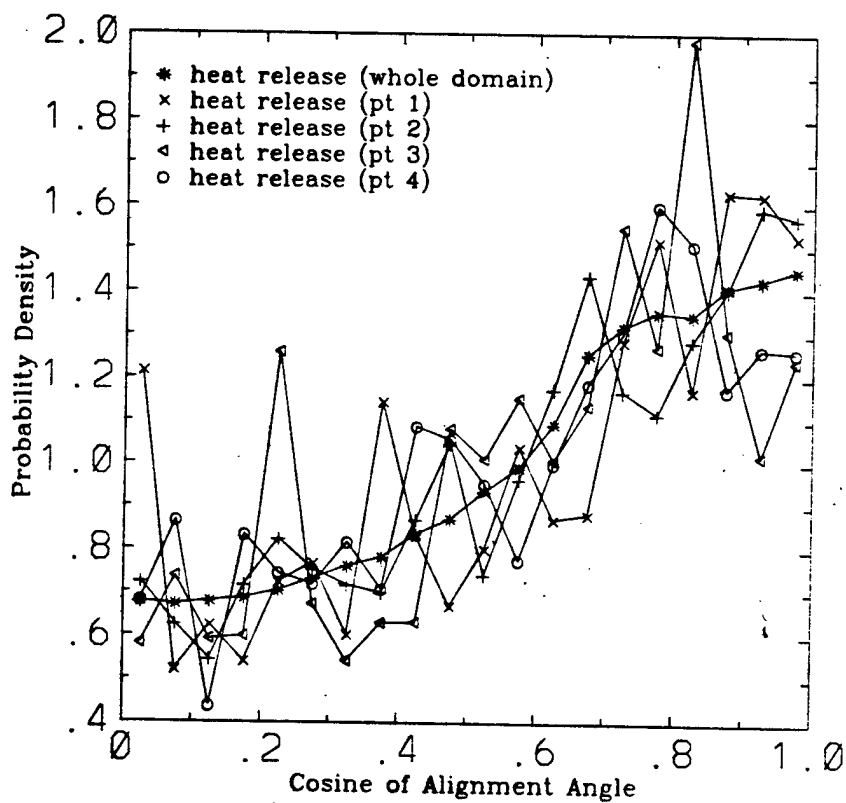


FIGURE 7

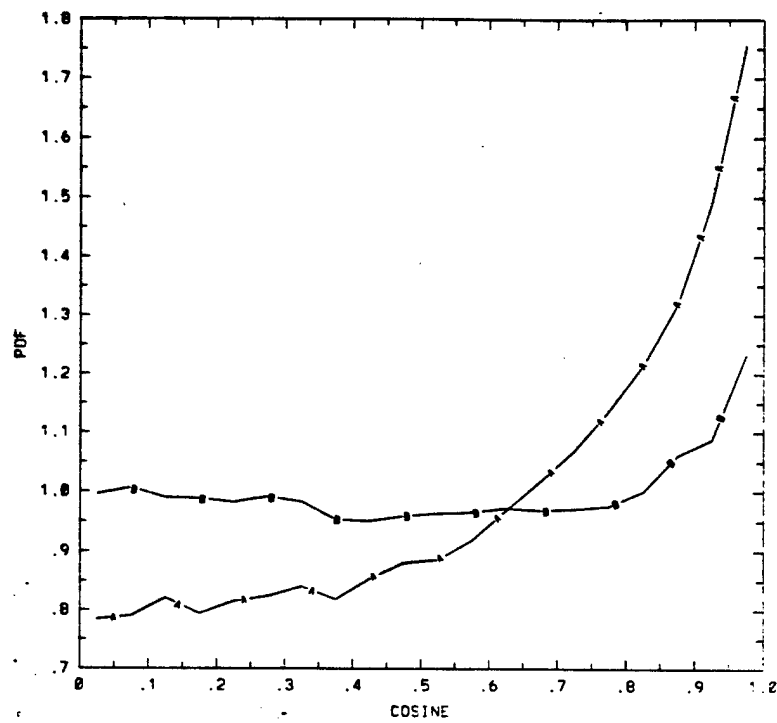


(c)

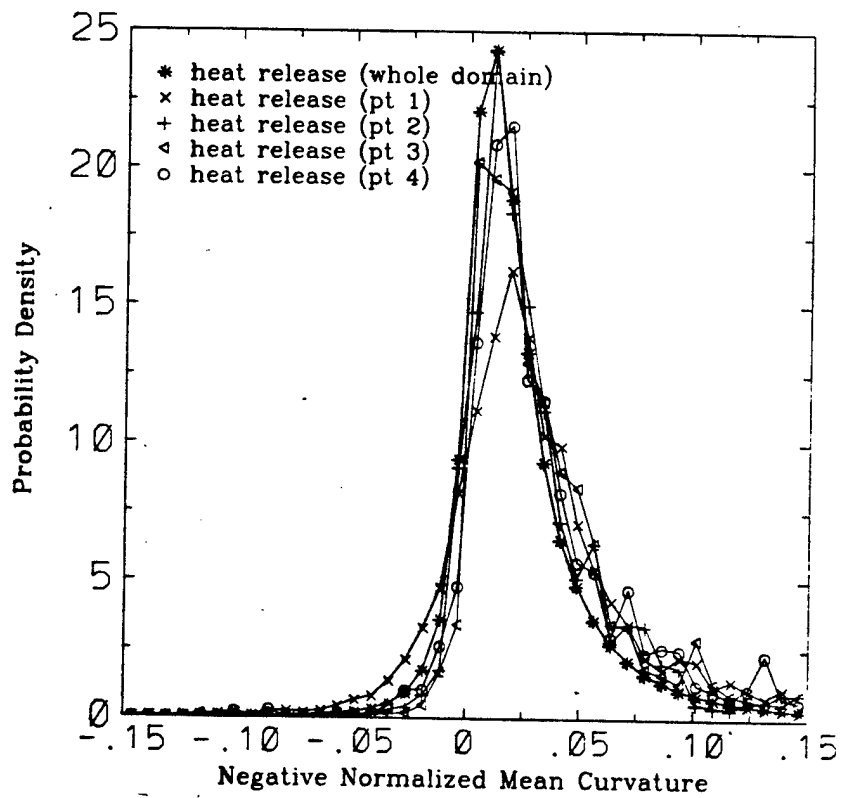


(d)

FIGURE 7

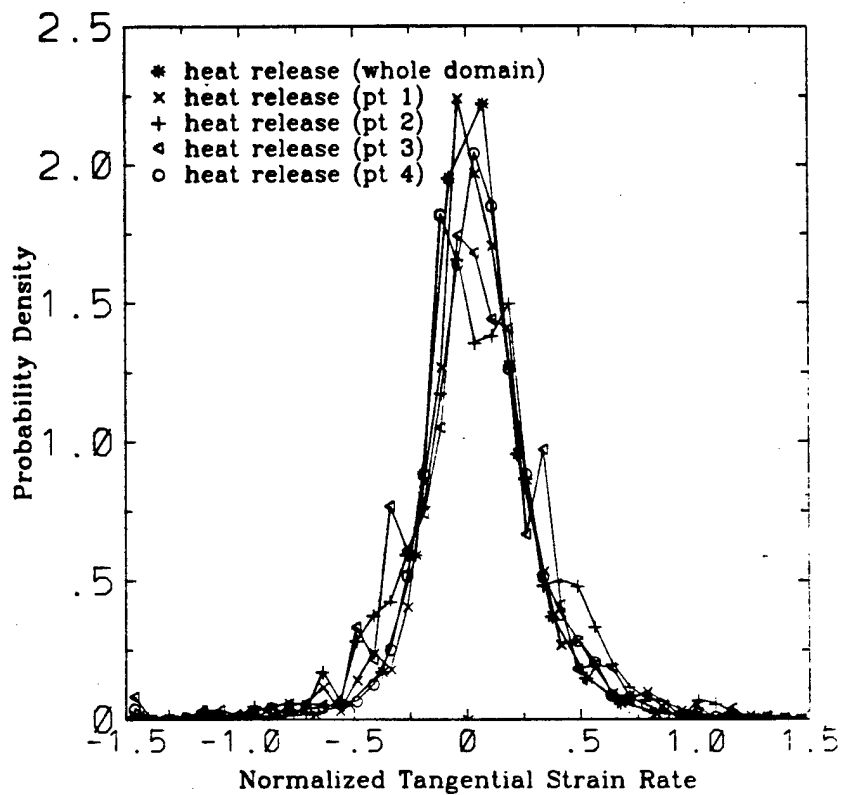


(e)

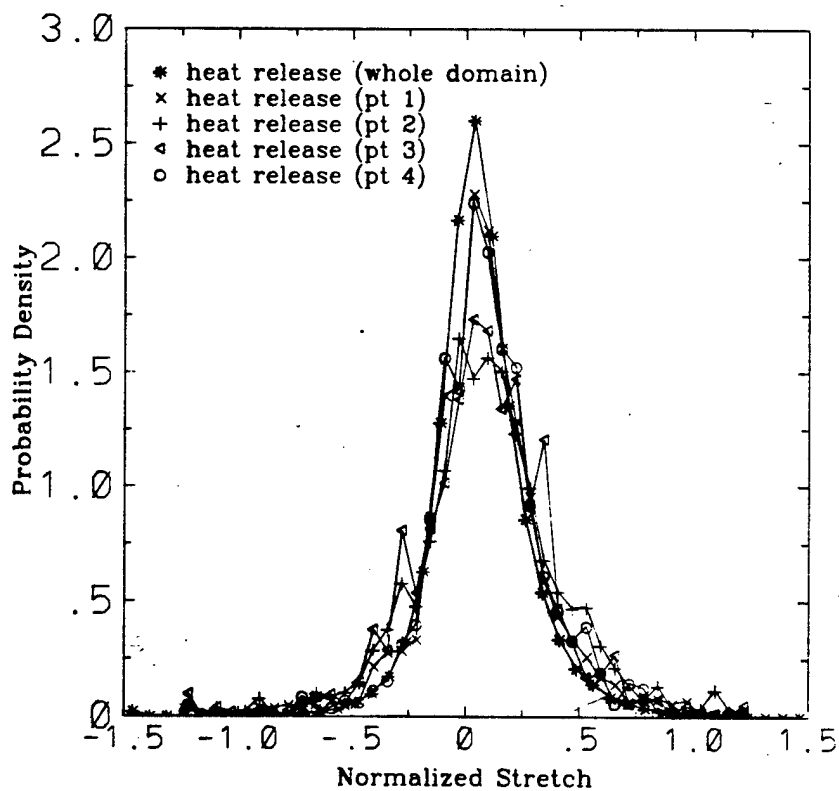


(f)

FIGURE 7



(g)



(h)

FIGURE 7

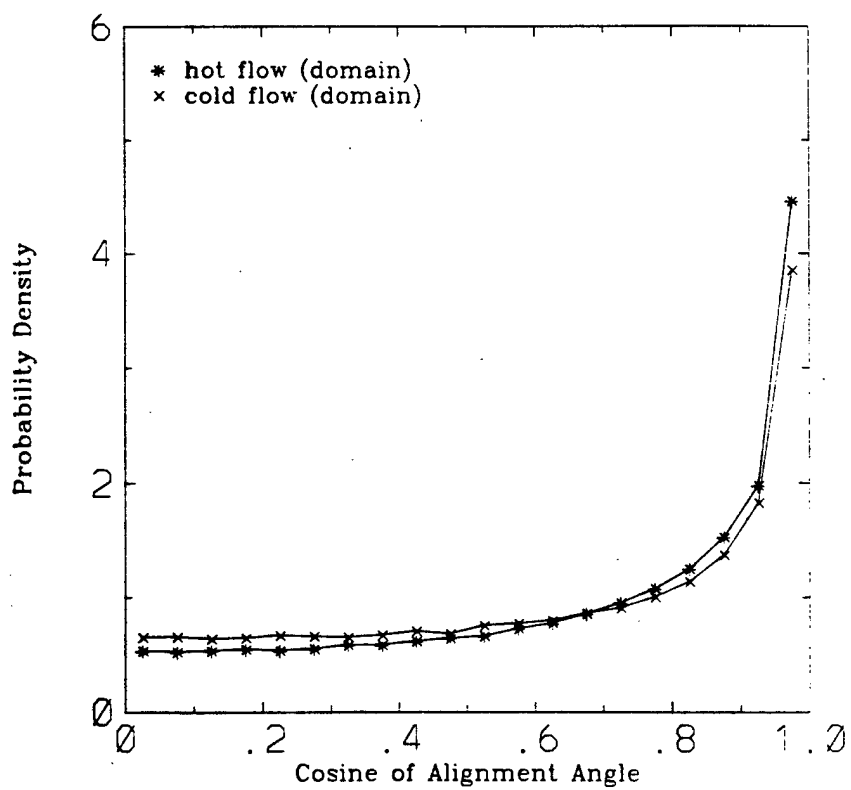
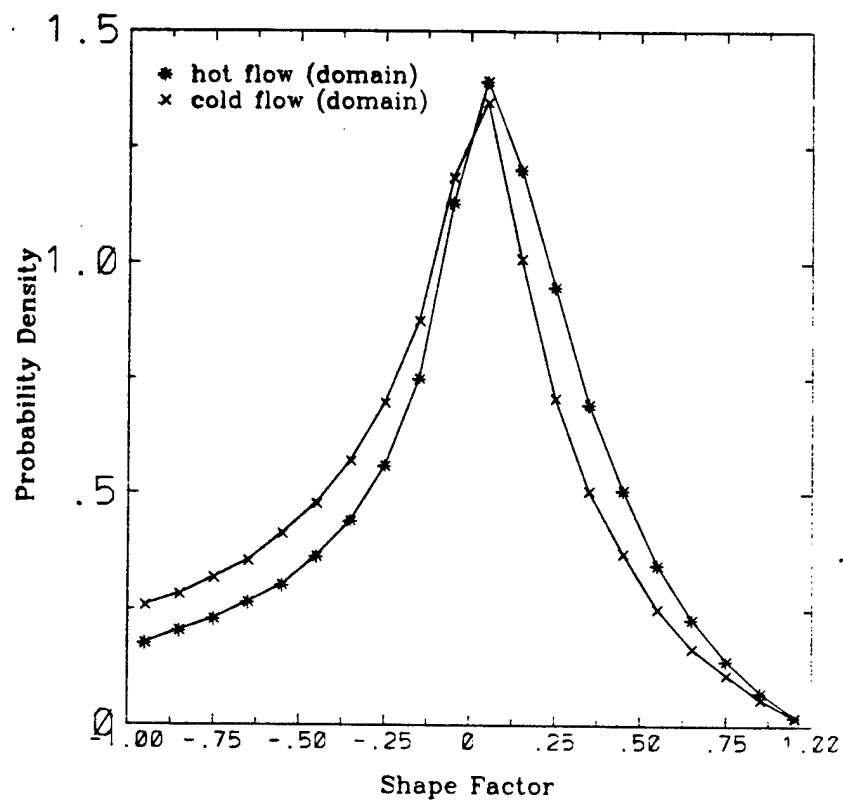
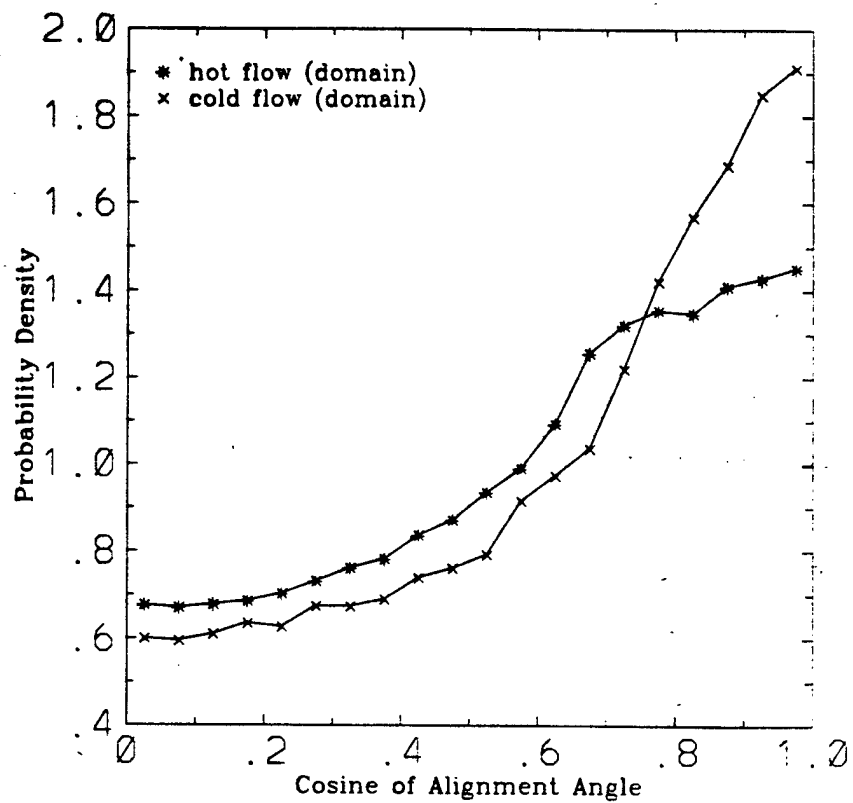
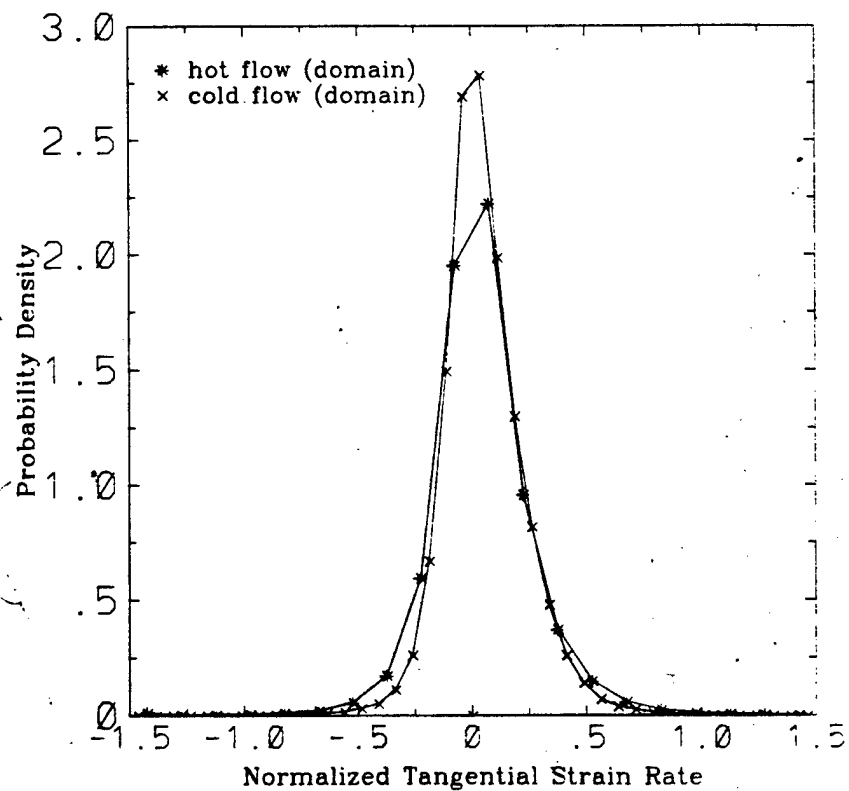


FIGURE 8

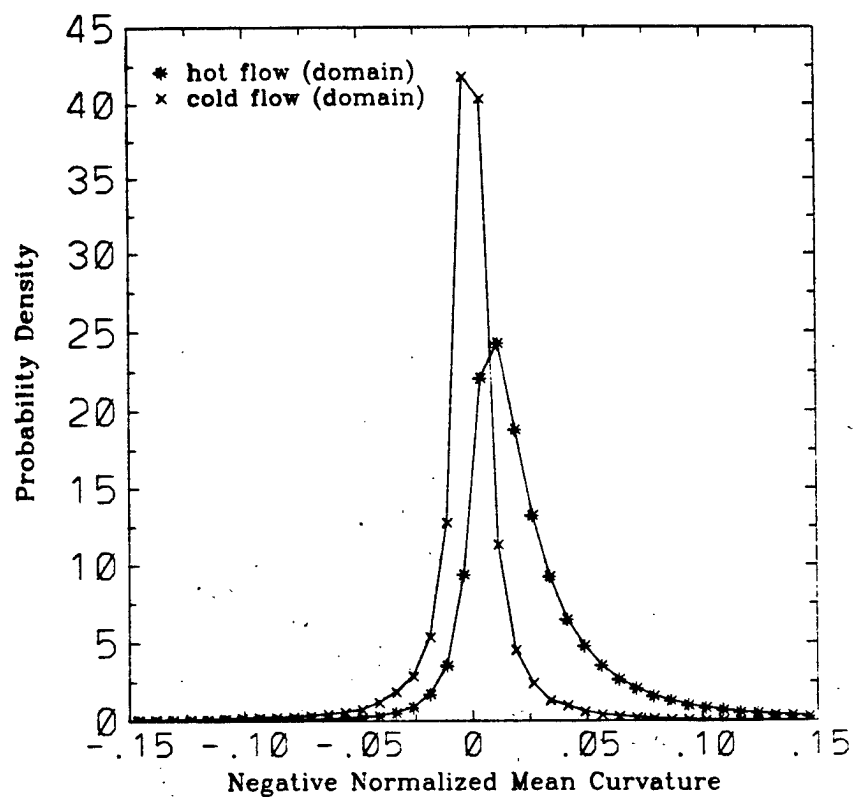


(c)

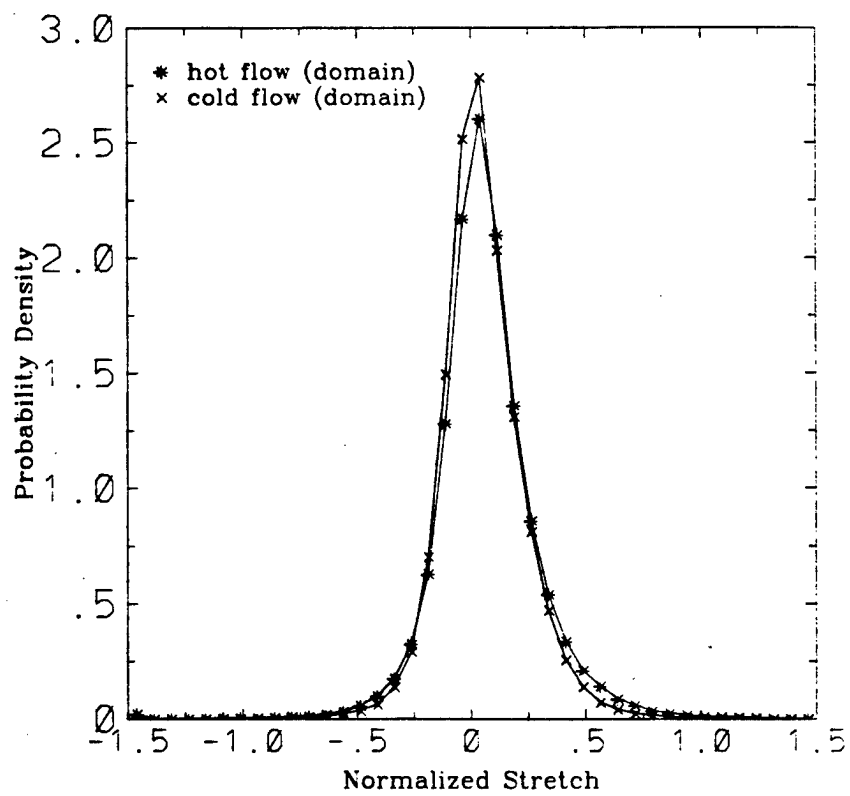


(d)

FIGURE 8



(e)



(f)

FIGURE 8



**THE STRUCTURE OF PREMIXED FLAMES  
IN A SPATIALLY EVOLVING TURBULENT FLOW**

**Thomas M. Smith  
Suresh Menon  
School Of Aerospace Engineering  
Georgia Institute Of Technology  
Atlanta, Georgia 30332-0150**

**Submitted to Combustion Science and Technology**

**June 1995**

# **THE STRUCTURE OF PREMIXED FLAMES IN A SPATIALLY EVOLVING TURBULENT FLOW**

**Thomas M. Smith  
Suresh Menon  
School of Aerospace Engineering  
Georgia Institute of Technology,  
Atlanta, Georgia 30332-0150**

## **Abstract**

Large eddy simulations of spatially propagating premixed flames in a three-dimensional dump combustor have been conducted at relatively high Reynolds numbers. A thin flame model is used to simulate the propagating flame front and the propagation speed is estimated using the subgrid turbulence intensity. Analysis of the simulations show that various statistics, such as flame front shape factor, stretch effects, vorticity/strain rate, and strain rate/surface normal alignments, agree reasonably well with data from constant density, direct numerical simulations of passive scalar and premixed flame propagation in simpler, temporally evolving low Reynolds number flows. This suggests that the general characteristics of propagating scalars in turbulent flows are relatively independent of Reynolds number and further that these features can be captured using relatively coarse grid LES at high Reynolds numbers. However, detailed analysis showed that in spatially developing flows, there is a significant dependence on the spatial location for some statistical properties. As the flame propagates downstream the probability density of the shape factor showed a decreasing probability for cylindrical shaped flames and the strain rate/flame normal alignment showed a transition from the alignment seen in shear driven flow to alignment seen in isotropic turbulence. Strain rate (in the plane of the flame) was maximum near the flame holder (the rearward facing step) and decreases in the downstream direction with the pdf becoming more symmetric similar to isotropic flows. The implication of the observed spatial dependence for investigating flame stretch effects and therefore, flame extinction is discussed.

## **1. Introduction**

A propagating surface is a reasonable representation of the flame sheet in premixed combustion when the flame thickness is much smaller than the smallest turbulent scale. The flame sheet is convected by the flow velocity while undergoing propagation normal to itself at the local propagation speed. The effect of turbulence is to wrinkle and stretch the propagating surface, thereby, changing its flame speed and possibly causing local extinction. In constant density flows,

a number of studies have been made aimed at characterizing the properties of the propagating surface such as its local curvature (which is a measure of local wrinkling) and its relation to the strain and vorticity fields in the turbulent flow. In temporally evolving flows, such as, isotropic and shear driven turbulence, Ashurst et al. (1987) showed that the vorticity vector tends to align itself in the direction of the intermediate strain rate even if the strain rate is compressive while the normal to the propagating surface aligns itself in the most compressive strain rate direction. Alignment of the surface normal with the most compressive strain rate implies that the surface is undergoing extension most of the time, and if this extension reaches a critical value for a long enough period of time, the flame extinction could occur. Further, Ashurst et al. (1987) showed that the most likely shape of the propagating surface is cylindrical in such flows and analysis of the alignment of the surface show that it is a direct result of the modification of the propagating surface by the local vortex structure. In a recent study, Smith et al. (1994) showed that similar results are obtained in forced and decaying isotropic turbulence and in temporally evolving mixing layers. These results showed that as vortices undergo stretching and the core becomes intense, the flame surface tends to wrap around on the outside of the vortex core.

Understanding the role of flame stretch (which is the combination of strain field in the plane of the flame and curvature) in quenching turbulent premixed flames is a major area of research. It is known that in laminar flames, severe stretch effects can cause extinction. Curvature and strain rate affect flame propagation differently. Locally, curvature correlates with flame speed for diffusionally neutral mixtures (Lewis number=1), however, the curvature is nearly symmetric in isotropic turbulence and therefore integrates to zero. Experiments have shown that curvature can increase the local laminar flame speed by a factor of 6.25 (Echehki and Mungal, 1990). Globally, the spatial average flame speed correlates with the tangential strain rate (Rutland and Trouvé, 1993). At this point there is no clear explanation of how flame stretch contributes towards the extinction of a turbulent premixed flame. Since flame stretch and Lewis number determine the laminar flame speed and have been shown to play a direct role in premixed flame extinction, understanding the mechanism of flame extinction in turbulent flows must first include an understanding of flame stretch effects in turbulent flows.

All the above noted studies of the properties of propagating premixed flames in turbulent flows were carried out using direct numerical simulations (DNS) of low Reynolds number, incompressible, temporally evolving flows. The evolution of the propagating surface in a spatially developing turbulent shear flow is of considerable interest since such flows form the basis of fluid dynamics/combustion coupling in realistic combustors. Of particular interest here is to determine how the correlation of the surface curvature with the vorticity field and the strain field evolves in

such flows. These issues are investigated in this paper by employing large-eddy simulations (LES) of relatively high Reynolds number flows past a rearward facing step in a rectangular channel. This configuration is typical of flame holders in combustors as in ramjet engines. Only cold flows are studied here; the effects of heat release will be discussed in a future paper.

## 2. Simulation Model

### 2.1 Equations of LES

The equations describing the conservation of mass, momentum and total energy are given by the full three-dimensional, unsteady, compressible Navier-Stokes equations. In LES, the flow variables are decomposed into the resolved scale and subgrid scale components. The large scales are computed explicitly while the effects of the subgrid scales on the large scales are modeled. Dynamics of large scale structures (which contain most of the energy) is dictated by the geometry of the flow and the Reynolds number, while the small scales (which primarily dissipate energy transferred from the large scales) are relatively unaffected by the geometry except near walls.

Following Erlebacher et al. (1987), the flow variables are decomposed into the resolved (supergrid scale) and unresolved (subgrid scale) components by a spatial filtering operation such that:  $f = \bar{f} + f''$  where the Favre filtered variable (with tilde) is defined as  $\tilde{f} = \frac{\bar{\rho}f}{\bar{\rho}}$  and the bar represents spatial filtering given by

$$\bar{\rho}f = \int_D \rho f(\bar{x}) G(\bar{x} - \bar{x}', \Delta) d^3x' \quad (1)$$

Here,  $G$  is the filter kernel,  $D$  is the domain of the flow and  $\Delta$  is a characteristic grid size. The filtering operation is normalized by requiring that

$$\int_D G(\bar{x} - \bar{x}', \Delta) d^3x' = 1. \quad (2)$$

Filtering reduces the high wave number content in the flow variables and separates the resolved scale component from the subgrid (unresolved) scales. In this study, a box filter is employed which is appropriate for finite volume schemes. Contrary to the more traditional Favre temporal averaging,  $\tilde{\tilde{f}} \neq \tilde{f}$  and in general,  $\tilde{f}'' \neq 0$ . Applying the filtering to the Navier-Stokes equations

results in the following LES equations:

$$\frac{\partial \bar{\rho}}{\partial t} + \frac{\partial \bar{\rho} \bar{u}_i}{\partial x_i} = 0 \quad (3a)$$

$$\frac{\partial \bar{\rho} \bar{u}_i}{\partial t} + \frac{\partial}{\partial x_j} [\bar{\rho} \bar{u}_i \bar{u}_j + \bar{p} \delta_{ij} - \bar{\tau}_{ij}] + \frac{\partial \tau_{ij}^{sgs}}{\partial x_j} = 0 \quad (3b)$$

$$\frac{\partial \bar{\rho} \bar{E}}{\partial t} + \frac{\partial}{\partial x_i} [(\bar{\rho} \bar{E} + \bar{p}) \bar{u}_i + \bar{q}_i - \bar{u}_j \bar{\tau}_{ij}] + \frac{\partial H_i^{sgs}}{\partial x_i} + \frac{\partial \sigma_{ij}^{sgs}}{\partial x_i} = 0 \quad (3c)$$

In the above equations,  $\rho$  is the density,  $E$  is the total energy per unit mass,  $p$  is the pressure,  $u_i$  ( $i=1,3$ ) are the velocity components,  $\tau_{ij}$  and  $q_i$  are respectively, the viscous stresses and heat conduction and  $\tau_{ij}^{sgs}$ ,  $H_i^{sgs}$  and  $\sigma_{ij}^{sgs}$  are the subgrid stresses that have to be modeled. The above equations are supplemented by the filtered equation of state  $\bar{p} = \bar{\rho} R \bar{T}$  and other relevant thermodynamic relations. The filtered viscous stresses and heat conduction terms are defined as:

$$\bar{\tau}_{ij} = \bar{\mu} \left( \frac{\partial \bar{u}_i}{\partial x_j} + \frac{\partial \bar{u}_j}{\partial x_i} \right) - \frac{2}{3} \bar{\mu} \frac{\partial \bar{u}_k}{\partial x_k} \delta_{ij} \quad (4a)$$

and

$$\frac{\partial \bar{q}_i}{\partial x_i} = -\bar{\lambda} \frac{\partial \bar{T}}{\partial x_i} \quad (4b)$$

where  $\bar{\mu}$  and  $\bar{\lambda}$  are respectively the filtered coefficient of molecular viscosity and thermal conductivity. In this study, the Sutherland's law of viscosity is used to determine molecular viscosity and  $\bar{\lambda} = \bar{\mu} C_p / \text{Pr}$ , where  $\text{Pr}$  is the Prandtl number and  $C_p$  is specific heat at constant pressure (assumed to be a constant in this study). The filtered total energy per unit volume is given by

$$\bar{\rho} \bar{E} = \bar{\rho} \bar{e} + \frac{1}{2} \bar{\rho} \bar{u}_i \bar{u}_i + \frac{1}{2} \bar{\rho} [u_i u_i - \bar{u}_i \bar{u}_i] \quad (4c)$$

Here,  $\bar{e} = C_p \bar{T}$  is the internal energy per unit mass and the last term in Eq. (4c) is a contribution due to the unresolved kinetic energy, hereafter referred to as the subgrid kinetic energy and is defined as  $k = \frac{1}{2} [u_i u_i - \bar{u}_i \bar{u}_i]$ .

The exact subgrid terms are given by;

$$\tau_{ij}^{ss} = \bar{\rho} [u_i u_j - \tilde{u}_i \tilde{u}_j] \quad (5a)$$

$$H_i^{ss} = \bar{\rho} [E u_i - \tilde{E} \tilde{u}_i] + [\overline{p u_i} - \bar{p} \tilde{u}_i] \quad (5b)$$

$$\sigma_{ij}^{ss} = [\overline{u_j \tau_{ij}} - \tilde{u}_j \bar{\tau}_{ij}]. \quad (5c)$$

In order to solve this system of equations, models must be found for the above noted subgrid terms  $\tau_{ij}^{ss}$ ,  $H_i^{ss}$ , and  $\sigma_{ij}^{ss}$ . In addition, it is necessary to obtain the subgrid turbulence intensity to evaluate the flame speed model (which is discussed in the next section). Subgrid models for compressible flows are still relatively new (Erlebacher et al. 1987, Squires and Zeman 1990, and Moin et al. 1991) and no best choice exists. In this study, we employ the one-equation model for the subgrid kinetic energy proposed by Menon (1991). The equation is given by

$$\frac{\partial \bar{\rho} k}{\partial t} + \frac{\partial (\bar{\rho} \tilde{u}_i k)}{\partial x_i} = P_k - D_k + \frac{\partial}{\partial x_i} \left( \bar{\rho} \nu_i \frac{\partial k}{\partial x_i} \right). \quad (6)$$

Here,  $P_k$  and  $D_k$  are the rate of production and dissipation of subgrid kinetic energy, respectively. An advantage of this model is that unlike in algebraic eddy viscosity models (e.g., Smagorinsky's model), the production and the dissipation of the subgrid kinetic energy need not be in equilibrium. The above model however, neglects the pressure dilatation term that appears in the original exact  $k$ -equation for two reasons. First, it is still unclear how to model the pressure dilatation in terms of the resolved flow field variables, and second, at low fluctuating Mach numbers, its influence may be negligible. The production and dissipation of the subgrid kinetic energy are modeled respectively as:

$$P_k = -C_k \tau_{ij}^{ss} \frac{\partial \tilde{u}_i}{\partial x_j} \quad (7a)$$

$$D_k = C_\epsilon \bar{\rho} \frac{k^{3/2}}{\Delta_t} \quad (7b)$$

where  $\Delta_g$  is a characteristic grid size and  $\nu_t$  is the subgrid eddy viscosity given by  $\nu_t = C_v k^{1/2} \Delta_g$ . The three constants appearing in the above equations have been prescribed as (Yoshizawa, 1993):  $C_k = 1.0$ ,  $C_\epsilon = 0.916$ ,  $C_v = 0.0854$ .

A new dynamic  $k$ -equation model is being studied (Kim and Menon, 1995; Menon and Kim, 1995) as a possible replacement to the constant coefficient model described above. The dynamic approach uses a new method for local evaluation of the coefficients so that the algebraic identity of Germano et al. (1991) is no longer necessary. The dynamic model has been shown to perform significantly better than the constant coefficient model and the Germano et al.'s eddy viscosity model for incompressible, homogeneous isotropic turbulence, Taylor-Green flow and temporal mixing layers (Menon and Kim, 1995). However, since the model is still undergoing evaluation in compressible flows, in the present study, the original form of the model, Eq. (6) is used.

The  $k$ -equation is solved simultaneously with the rest of the flow equations. With  $k$  and  $\nu_t$  determined, the subgrid stresses are evaluated as:

$$\tau_{ij}^{ss} = -2\bar{\rho}\nu_t \left( \tilde{S}_{ij} - \frac{1}{3} \tilde{S}_{kk} \delta_{ij} \right) \quad (8a)$$

where  $\tilde{S}_{ij} = \frac{1}{2} \left( \frac{\partial \tilde{u}_i}{\partial x_j} + \frac{\partial \tilde{u}_j}{\partial x_i} \right)$  is the resolved scale stress tensor and  $H_i^{ss}$  is given by

$$H_i^{ss} = -C_\epsilon \bar{\rho} \nu_t \frac{\partial \tilde{H}}{\partial x_i} = -C_\epsilon \bar{\rho} \nu_t \left( C_p \frac{\partial \tilde{T}}{\partial x_i} + \tilde{u}_j \frac{\partial \tilde{u}_j}{\partial x_i} \right) \quad (8b)$$

and  $C_\epsilon = 1/Pr_t$ .  $Pr_t$  is the turbulent Prandtl number and  $\sigma_{ij}^{ss}$  is modeled by:

$$\sigma_{ij}^{ss} = \tilde{u}_j \tau_{ij}^{ss}. \quad (8c)$$

Note that in Eq. (8a) no attempt has been made to separate the Leonard and Cross terms from the subgrid Reynolds stresses since it has been noted earlier (Speziale, 1985) that in doing so, the modeled LES equations no longer satisfy Galilean invariance. It should also be noted that third order correlation arise as a result of this modeling approach but are neglected here. To account for the subgrid kinetic energy behavior in the near wall regions explicit wall damping similar to that used by Piomelli et al. (1988) is employed. This results in the following form for the characteristic

filter width near the wall:

$$\Delta_s = \left[1 - \exp(-y^{+3} / A^{+3})\right]^{1/2} (\Delta_x \Delta_y \Delta_z)^{1/3} \quad (9)$$

where  $(\Delta_x \Delta_y \Delta_z)^{1/3}$  is the characteristic grid size based upon the local cell volume,  $A^{+} = 26$ ,  $y^{+} = y u_{\tau} / \nu$ , and  $u_{\tau}$  is the friction velocity.

## 2.2 Flame Propagation Model

To simulate the propagating surface, the thin-flame model of Kerstein et al. (1988) is used in which a progress variable  $G$  is defined that is governed by the equation :

$$\frac{\partial G}{\partial t} + \mathbf{u} \cdot \nabla G = -u_F |\nabla G| + \frac{\nu_t}{C_G} \nabla^2 G \quad (10)$$

where  $\mathbf{u}$  is the fluid velocity and  $u_F$  is the local propagation speed. This equation is solved simultaneously with the LES equations. This equation describes the convection of a level surface, described by  $G = \text{constant}$ , by the fluid velocity while simultaneously undergoing propagation normal to itself at a speed  $u_F$ . In the flow field, the value of  $G$  is in the range  $[0,1]$  and in flame front modeling,  $G$  exhibits a step function like-behavior, separating the burnt region from the unburned region.  $G$  is assigned the value of unity in the unburned region and zero in the burnt region with the thin flame identified by a fixed value of  $G$  in the range  $[0,1]$ . Since no heat release is included in the present study, any value of  $G = \text{constant}$  can be used to identify the flame front. Thus, the physical interpretation is that an evolving  $G$ -level for any level  $G$  represents the simulated propagation of the constant property surface of that level. Thus, statistics from all values of  $G = \text{constant}$  can be combined; in effect, each simulation corresponds to a family of simulations parameterized by  $G$ .

The second term on the right hand side of equation (10) does not appear in the original equation, however it was added here in order to avoid false minima from occurring in the flow. A false minima is not physically meaningful and results from a lack of resolution of the scalar field. Ashurst (1993) and Smith et al. (1994) both added a similar term to the above equation in their simulations of isotropic turbulence. The constant  $C_G = 4$  was used in all simulations reported here. It was determined by analyzing the simulation data that this term does not affect the key results of this study and further that, in most of the simulated cases, less than 10% of the grid points



exhibited this false minima.

In LES of premixed combustion,  $u_f$  is considered the turbulent flame speed  $u_t$  averaged over a characteristic volume. The turbulent flame speed is not known explicitly and must be modeled. We employ the RNG model of Yakhot (1988):

$$\frac{u_t}{S_L} = \exp \left[ \frac{(u' / S_L)^2}{(u_t / S_L)^2} \right]. \quad (11)$$

Here,  $S_L$  is the laminar flame speed and  $u' = \sqrt{2k}$  is the subgrid turbulence intensity. Thus, the solution of the one-equation model for the subgrid kinetic energy is necessary to obtain the subgrid intensity to close Eq. (11). This is another reason for the choice of the subgrid model in the present study. Yakhot (1988) found that Eq. (11) correlates quite well with various experimental observations. The laminar flame speed  $S_L$  contains information about the chemical kinetics and molecular diffusion and, once the local subgrid turbulence intensity is determined, Eq. (11) can be used to find  $u_f$  for a given fuel mixture. Equation (11) is a nonlinear equation and direct application requires an iterative procedure. Therefore, to reduce computational cost, a look-up table is first generated and then used in the simulations.

The numerical method solves the unsteady, three-dimensional compressible filtered Navier-Stokes equations, the one-equation subgrid model, and the flame propagation model using a finite-volume scheme based on the unsplit explicit MacCormack predictor-corrector method. The scheme is formally second-order accurate in space and time. Details of the algorithm are given elsewhere (Menon and Jou, 1991) and are therefore, avoided here for brevity.

### 3. Results and Discussion

To address the issues of interest here, various simulations (with different grid resolution and Reynolds number) were carried out. Grid independence studies performed earlier showed that most of the large scale features are relatively independent of the resolution used in the simulations analyzed here. However, since the flame front model is for an infinitely thin flame no grid resolution (however fine) will be able to resolve this front. Analysis of the earlier DNS data (Smith et al., 1994) showed that improved resolution would resolve the flame front more crisply; however, the statistics obtained from the simulations are not changed significantly. This is particularly true for no heat release cases where any level surface can be considered a flame front.

Two simulations are analyzed here in detail for flow past a rearward facing step in a rectangular channel with a choked downstream nozzle. Such a configuration is characteristic of ramjet dump combustors that have been studied extensively in recent years (Menon and Jou, 1991; Menon, 1992; Menon, 1995). Boundary conditions demonstrated earlier in this configuration (Menon and Jou, 1991) are used for these simulations. At the inlet, the total pressure and total temperature are specified and the transverse and spanwise components of the velocity are set to zero. One-dimensional characteristic equation for the properties carried by the backward running acoustic wave is solved for the axial velocity. Previous analysis (Menon and Jou, 1991) has shown that this type of boundary condition does not generate spurious acoustic waves at the inlet. At the combustor supersonic nozzle exit, all characteristics are outgoing and therefore, all flow variables are extrapolated. Symmetry conditions are imposed on the centerline and periodic conditions are imposed in the spanwise direction. Viscous no-slip boundary conditions are used at all the adiabatic walls of the combustor. Figure 1a shows the computational domain and Figure 1b shows the  $96 \times 48 \times 16$  grid used for these simulations. The grid is clustered near the wall and in the shear layer region in order to capture the coherent structures in the shear layer. The grid clustering near the inlet wall allows approximately 12-14 grid points in the boundary layer. The two simulations discussed here correspond to a reference inlet Mach number of .32 and Reynolds number based on step height of 5000 and 50000, respectively.

Typical features of the flow field are discussed here in order to highlight the distinguishing characteristics of this flow field. The shear layer separating from the step rolls up into spanwise coherent vortices due to shear layer instability. Figure 2a shows a constant spanwise vorticity ( $\omega_z$ ) surface in the combustor for the  $Re=50000$  simulation. Only the region between the rearward facing step and the diffuser is shown in this figure. The spanwise vortices undergo a pair/merging process as they propagate downstream and also undergo vortex stretching due to the three dimensional nature of the flow. Three dimensional effects also result in the formation of streamwise counter-rotating vortices ( $\omega_x$ ) that form in the braid region between adjacent spanwise vortices and are highly coherent rod-like structures. Figure 2b shows a constant streamwise vorticity surface for the same snapshot shown in Fig. 2a. It is well known that the formation of coherent streamwise vortices in shear layers is due to the excitation of secondary instability and the effects seen here are very similar to results obtained in low-Re DNS of temporal mixing layers (Metcalf et al, 1987). Further downstream, vortex stretching effects break down the coherent spanwise structures. Interestingly, the streamwise vortices maintain their coherence, and the braid-like structures persist all the way into the choked nozzle. The acceleration in the nozzle further stretches these structures. Near the step, the streamwise vortices are aligned in the axial (x) direction and exist in the braid region between the coherent spanwise structures. However, as the

shear layer approaches the diffuser and the spanwise structures lose their coherence, the streamwise vortices begin to orient more randomly. These randomly oriented vortex-tubes are quite similar to those seen in DNS of homogeneous isotropic turbulence (Smith et al., 1994). The implication of this transition from spanwise vorticity dominated shear flow very near the step to more randomly oriented streamwise vorticity in the farfield will be discussed in more detail below when analyzing its effects on the flame front.

The effect of this intense vorticity on the flame front is to wrinkle the surface and as a result, the flame develops regions of high curvature. Figure 2c shows a constant  $G$ -level surface in the shear layer. Since the present study is without heat release any level surface can be used to represent a flame front. For following discussion, a level surface in the range  $.45 < G < .55$  is used to represent the flame front. The influence of both spanwise and streamwise vorticity can be seen on the curvature of the surface. The flame curvature is much larger in the regions where streamwise vorticity dominates suggesting that the smaller rod like streamwise vortices tend to wrinkle the flame more efficiently.

To further understand the effects of spanwise and streamwise vorticity on the wrinkling of the flame front, two dimensional images from both simulations were analyzed. Some representative results are discussed below. Figures 3a and 3b show respectively, a 2D plane of  $z$ -vorticity magnitude (spanwise vorticity), and the subgrid kinetic energy, in the combustor region from the  $Re = 50000$  simulation. These figures are taken from the same snapshot as in the previous Fig. 2. A single  $G$  contour, again in the range  $.45 < G < .55$ , is also plotted in the figures (the dark line). These images show how the curvature of the flame front is evolving in the streamwise direction. Initially, the spanwise vortices shed at the corner of the step dominate the shear layer and the rollup process creates a highly wrinkled flame that is wrapped around the large spanwise vortices. However, as the flame/shear layer convects further downstream, two effects are at work. First, the flame propagation effect, due to the flame burning normal to itself at the local flame speed  $u_f$ , causes the negative curvature to decrease and the positive curvature (defined concave to the fresh mixture) to increase. The second effect is due to the changes in the shear layer as noted earlier in Fig. 2. As the spanwise vortices lose their coherence, their ability to wrinkle the flame front weakens and thus decreases the local burning speed. Thus, both these effects cause a reduction in the flame curvature and therefore, further downstream of the step, the flame becomes more planar in this (x-y) plane.

The subgrid kinetic energy field shown in Figure 3b demonstrates the subgrid model behavior. The subgrid model predicts that significant subgrid kinetic energy is present in the shear

layer and is closely associated with the large vortical spanwise structures. Since Eq. (11) predicts an increase in the flame speed with increase in subgrid turbulence intensity, this suggests that in regions where the flame is highly wrinkled by the structures, the flame speed is also enhanced. This observation is consistent with experimental observations (e.g., Smith and Zukoski, 1985; Yu et al., 1991) and shows that the present implementation of the subgrid model is capable of reproducing experimentally observed features in the reacting flow. Another interesting observation is that significant kinetic energy is seen near the diffuser wall. Again, it has been observed in experiments (Smith and Zukoski, 1985; Yu et al., 1991) that as the large structures breakdown intense small scale mixing occurs with an associated increase in turbulence intensity. Thus, if any unburned fuel mixture is present in these regions then significant combustion can occur. The simulation results appears to qualitatively agree with these observations.

Figures 4a-4c show respectively, the flame front and the streamwise vorticity at three different (y-z) planes as a function of axial location. The axial locations are chosen to highlight the ability of the streamwise vortices to wrinkle the flame in the (y-z) plane. Due to the formation of the counter rotating streamwise vortices the flame is drawn up between two vortex cores and the curvature is significantly increased. As the shear layer evolves downstream, initially, all the streamwise vortices are concentrated in the braid region of the shear layer (Figs. 4a and 4b) and the flame is wrinkled by this strong vorticity. However, further downstream (Fig. 4c) as the spanwise vorticity breaks down (see Figs. 2a and 3a) the shear layer becomes dominated by the more randomly oriented streamwise vorticity. These vortices occur in regions further away from the chosen  $G=\text{constant}$  level surface. Note that, in reacting flows, only a single (pre specified) level surface is identified as the flame front. Therefore, the ability of the randomly oriented streamwise vorticity to wrinkle the flame front is significantly reduced. This behavior is also indicated in the present non-reacting simulation since the chosen level surface is no longer wrinkled by the streamwise vortices further downstream (Fig. 4c). Thus, as the flame propagates downstream the flame sheet curvature is again decreased (as was seen also in Fig. 3a).

In order to quantify the observations made from the flow visualizations, probability densities (pdf's) have been calculated from a series of instantaneous snapshots. Each pdf is computed from an ensemble of twenty snapshots at time intervals of roughly 1/3 of the flow through time after the flow field has reached a quasi-stationary state. The spatial locations for the pdf's start a small distance downstream of the step corner and end at the point where the diffuser begins. This region is the true domain of the combustor. All statistics have been volume weighted to account for the variation in the cell volumes in this domain of interest. Volume weighting simply means that equal cell volumes contribute equally to the statistical quantities.

One measure of the structural shape of the surface is the ratio of the smaller principle radius of curvature to the larger one. The radii of curvature of the scalar are determined from the eigenvalues of the curvature tensor (Ashurst, 1993):

$$h_{ij} = -\frac{\partial^2 G}{\partial x_i \partial x_j} \frac{1}{g} + \frac{1}{g^3} \sum_{k=1}^3 \frac{\partial G}{\partial x_i} \frac{\partial G}{\partial x_k} \frac{\partial^2 G}{\partial x_j \partial x_k} \quad (12)$$

where  $g = |\nabla G|$ . This nine element tensor has two real eigenvalues  $h_1$  and  $h_2$  and one eigenvalue equal to zero. The ratio of the smaller radius divided by the larger, hereafter referred to as the shape factor is bounded by  $\pm 1$ . Pope et al. (1989) used this definition to characterize the shape of material surfaces in isotropic turbulence. The value -1 corresponds to a saddle point, 0 corresponds to cylindrical and +1 to spherical. The probability density of the shape factor from each of the twenty realizations, encompassing the entire combustion chamber and over a range of  $G$ ,  $.2 \leq G \leq .8$ , was calculated and an ensemble pdf was obtained. Figure 5a shows this pdf. The maximum occurs very near zero indicating a high probability of cylindrical shapes with vanishing probability for spherical or saddle points. Data from incompressible direct simulations by Ashurst et al. (1987), Pope et al. (1989), and Smith et al. (1994), obtained in simpler flow fields such as isotropic turbulence and temporally evolving mixing layers are also shown in this figure. There is very good agreement between all these widely different simulated flow fields indicating that even in the spatially evolving shear layer studied here, the probability density indicates that the propagating surface tends to be a cylindrical shaped surface. This result suggests that even though the spatially developing shear layer shows a significant transition from spanwise dominated structures near the step to streamwise dominated structures further downstream, the flame front always tends to wrap around the most intense local vortical structure. This feature is further discussed below.

Figures 3 and 4 showed that the shear layer is dominated by the (organized) spanwise structures near the step and (more randomly oriented) streamwise structures further downstream. However, we also saw that close to the step, strong counter-rotating streamwise vorticity is formed in the braid region between the spanwise structures and as a result, the local flame curvature becomes quickly controlled by these smaller streamwise vorticity (see Fig. 4). Furthermore, Figs 3 and 4 showed that these streamwise structures become more randomly oriented further downstream. Therefore, it is clear that even though, on an average, over the entire combustor volume the pdf of the shape factor shows a high probability for cylindrical shape, there is likely a local (spatial) variation in the shape factor due to the spatial evolution of the flow field. To demonstrate this spatial dependence, the probability density of the shape factor was computed at

different streamwise locations. In Fig. 5b, the shape factors computed for the entire domain and at four streamwise locations are shown. The four streamwise locations chosen are spaced apart approximately twice the step length with the first location chosen near the step. The spatial probability densities were computed from the same twenty snapshots used for the pdf of the entire domain of interest. The probability for cylindrical shape decreases in the downstream direction and increases for saddle point, while the probability for spherical shape remains nearly zero. This indicates that the ratio of curvatures (which equals the ratio of radii) is increasing in the downstream direction. This is consistent with the earlier observation that near the step the flame curvature is dictated first by the coherent spanwise structures and then by the strong streamwise vortices in the shear layer and further downstream the curvature decreases when the streamwise vortices become more randomly located (Fig. 4). A similar result was obtained when the  $Re=5000$  LES data was analyzed (and therefore, not shown).

The mean curvature is defined as  $\bar{C} = \frac{1}{2}(h_1 + h_2)$ . The mean curvature pdf for the entire domain and for the same four axial locations are shown in Fig. 6. In order to be consistent with published data, the negative of the mean curvature is plotted. The negative sign is due to the definition that curvature concave with respect to the unburned fuel is positive. The data has been normalized by the Kolmogorov length scale to compare with other published data. The pdf's are nearly symmetric having very small mean values, however, the mean value is decreasing in the downstream direction. This result is consistent with earlier observations.

As noted earlier, the cylindrical shape of the flame sheet is due to the propensity of the flame to wrap around the locally most coherent vorticity. This results in an increase in the flame curvature. In addition, tangential strain in the plane of the flame is also increased. Ashurst et al. (1987) showed that the vorticity aligns with the intermediate principle strain rate while the normal to the flame aligns with the most compressive strain rate. The principle strain rate directions are the eigenvectors obtained from the strain rate tensor. If  $\alpha, \beta$  and  $\gamma$  are the three principal strain rates, then results for incompressible flow (Ashurst et al., 1987; Smith et al., 1994) show that they appear in a ratio:  $\alpha:\beta:\gamma = 3:1:-4$ . Here, the negative sign indicates compression. However, in compressible flows, this ratio will not be satisfied if there is significant variable density effects. Figure 7a shows the alignment between the intermediate strain rate ( $\beta$ ) and the vorticity from incompressible DNS data obtained by Ashurst et al. (1987) for shear driven turbulence, from the 3D mixing layer and the forced isotropic turbulence simulation data obtained by Smith et al. (1994) and from the present  $Re = 50000$  LES simulation. High probability of alignment is expected when the flow field is organized. Thus, although all cases shown in Figure 7a exhibits similar trends,

since the temporal mixing layer is the most organized flow it shows the highest probability of alignment followed respectively, by the present LES, the shear driven turbulence and forced isotropic turbulence.

Due to the spatial evolution of the shear layer seen in the present simulations, a spatial dependence of the alignment between the vorticity and the strain field is also expected. To determine this spatial dependency, the alignment between the intermediate strain rate ( $\beta$ ) and vorticity was computed over the entire domain and at the same four locations as before and shown in Fig. 7b. The alignment decreases with increase in distance from the step and this result is again consistent with the observations noted earlier for the shape factor and the evolution of the vorticity field. As the organized structures in the shear layer breaks down into randomly oriented structures, the alignment also weakens. This trend is also consistent with the results of Ashurst et al. (1987) where it was determined that this alignment was larger in shear flows than in isotropic turbulence.

Another interesting observation can be made from the present simulations by examining the alignment between the most compressive strain rate ( $\gamma$ ) and the flame normal  $\mathbf{n} = \nabla G / |\nabla G|$  where  $\mathbf{n}$  is the unit normal in the direction of the flame propagation. Ashurst et al. (1987) examined this alignment for both shear driven turbulence and isotropic turbulence and showed that in shear driven turbulence, the alignment peaked at an angle of roughly 30 degrees, while for the isotropic case the angle was nearly zero. This can be understood by realizing that when the flame approaches a stretched vortex, its gradient is increased by the compressive strain rate and rotation thereby increasing the alignment. Clearly, this is more likely to happen in flows dominated by coherent structures such as a shear layer than in isotropic turbulence. In Fig. 8a, the results for the LES at  $Re = 5000$  are shown along with the data for shear driven turbulence (Ashurst et al., 1987) and in Fig. 8b, the data from the  $Re = 50000$  LES simulation and from the DNS of isotropic flow is shown. The low  $Re$  LES data compares well with the shear driven turbulence result of Ashurst et al. (1987) while the  $Re = 50000$  LES case compares well with the isotropic turbulence result. This is understandable when the flow fields of the LES at the two Reynolds number are examined. In the low  $Re$  case, the coherence in the shear layer is maintained nearly all the way into the diffuser (since the shear layer is more stable) while in the high  $Re$  case, breakdown of the shear layer and formation of more randomly oriented vorticity occurs before the diffuser is reached. Thus, the low  $Re$  LES data has a characteristic behavior similar to shear driven turbulence whereas the high  $Re$  LES shows similarity with the isotropic data.

The spatial evolution of the alignment between the compressive strain rate ( $\gamma$ ) and the flame normal  $\mathbf{n}$ , further explains the above observation. In Fig. 9a, this alignment pdf's over the entire

domain and at the same four streamwise locations are shown for the  $Re = 5000$  case. These results clearly demonstrate the evolution of the alignment in the downstream flow direction. The alignment resembles the shear driven pdf of Ashurst et al. (1987) near the step (where the flow field highly organized), however, further downstream there is a tendency for the alignment to transition to the behavior seen in isotropic-like flow. This is consistent with the observation that as the diffuser is approached, the coherence of the shear layer decreases and smaller more randomly oriented vortex tubes appear. However, since the low  $Re$  flow is more stable, this transition is just beginning to occur by the fourth  $x$ -location and therefore, the pdf averaged over the entire domain resembles the pdf obtained in shear driven turbulence. In the high  $Re$  case, the transition to the alignment seen in isotropic flows occurs much earlier since the breakdown of the shear layer into randomly oriented vorticity occurs much more rapidly. This is reflected in the evolution of the alignment in the downstream direction and is shown in Fig. 9b. At the first  $x$ -location, just downstream of the step, the alignment is still similar to that seen in shear flow, however, by the third and fourth  $x$ -locations, the alignment has become similar to that seen in isotropic turbulence.

The tangential strain rate (in the plane of the flame) is found by solving the relation  $\mathbf{t}_1 \cdot \bar{\mathbf{e}} \cdot \mathbf{t}_2 = \nabla \cdot \mathbf{u} - \mathbf{n} \cdot \bar{\mathbf{e}} \cdot \mathbf{n}$ , where  $\mathbf{t}_1$  and  $\mathbf{t}_2$  are two orthogonal vectors in the plane of the scalar surface and  $\bar{\mathbf{e}} = \frac{1}{2}[\nabla \mathbf{u} + \nabla \mathbf{u}^T]$  is the resolved scale strain rate tensor. The pdf of the tangential strain rate in the plane of the surface is shown in Fig. 10a. The tangential strain rate is normalized by the Kolmogorov time-scale and the pdf data indicates that the mean strain is slightly positive. The data are in good qualitative agreement with the laminar flamelet modeling of Cant et al. (1990) and the material surface curvature analysis of Yeung et al. (1990). Mean positive straining indicates that on the whole the flame is being stretched but the data also show that compression of the flame surface can occur as indicated by a non-zero probability of negative tangential strain rate as shown in Fig. 10a for the  $Re = 50000$  simulation. The pdf for the entire domain and at the four  $x$ -locations are shown in Fig. 10b. The probability density becomes more symmetric downstream, similar to isotropic flow, and the probability for high strain rates is decreased. This suggests that the flame experiences much higher strain rates near the step and the strain rate decreases downstream as the flame becomes less wrinkled.

The data from the LES can now be used to estimate the flame stretch which is defined as the rate of change of a Lagrangian flame surface element  $A$ . Mathematically, flame stretch can be expressed in terms of the local tangential strain rate, curvature and flame speed (Candel and Poinso, 1990):



$$\kappa = \frac{1}{\delta A} \frac{d(\delta A)}{dt} = \left[ \nabla \cdot \mathbf{u} - \mathbf{n} \cdot \bar{\mathbf{e}} \cdot \mathbf{n} - \frac{S_L}{R} \right]. \quad (13)$$

where  $R = 1/h_1 + 1/h_2$ , is the sum of the principle radii of curvature. Positive stretch tends to reduce the flame speed while negative stretch tends to increase it. Though the effect of flame stretch on the flame speed is not included in these calculations, examination of the flame stretch *a priori* can provide useful information. Figure 11 shows a plot of the probability density of flame stretch from the  $Re = 50000$  simulation for the entire domain and locally at the four axial locations. This figure shows that a spatial dependence does exist, which is consistent with the spatial dependence of the strain field and curvature seen earlier. The mean probability in all cases is slightly positive. This means that on average, the laminar flame speed will be reduced by the stretch effects in this flow field. The flame stretch is highest near the step (location 1) and is correlated quite well with the positive straining seen near the step (Fig. 10b). Thus, near the step, increased stretch effects will markedly reduce the flame speed and therefore, increase the possibility of flame extinction. Further downstream the stretch effect decreases and therefore, there is less likelihood of flame extinction due to stretch effects.

#### 4. CONCLUSIONS

A study of premixed flame propagation in three-dimensional spatially evolving turbulence at two different Reynolds numbers has been conducted using LES. A one-equation model for the subgrid kinetic energy is used to determine the subgrid terms in the momentum and energy equations. In addition, the same subgrid model is used to obtain an estimate for the local subgrid intensity which is required for closure of the thin flame model used to simulate the flame front. The dynamics of the separated shear layer was examined and results show that near the step, the shear layer is dominated by coherent spanwise vortices that undergo a pairing/merging process as seen in experiments and in DNS studies. Furthermore, due to the natural excitation of the secondary instability, counter-rotating streamwise vortices are formed in the braid region between the spanwise structures quite similar to the behavior seen in earlier DNS studies of temporal mixing layers (e.g., Metcalfe et al., 1987). Further downstream, the spanwise coherence is lost as the shear layer breaks down and more randomly oriented (and relatively smaller) vortical structures appear. The behavior of the turbulent flame is seen to be consistent with experimental observations and demonstrates that the present subgrid closure has the ability to qualitatively reproduce the effect of turbulence on the flame. The thin flame (here for tracking purposes is chosen to be an arbitrarily pre-specified level surface) tends to wrap around the locally most coherent structure. Thus, very close to the step, the flame is wrapped around the spanwise vortices however, further downstream,

the flame curvature is determined by the streamwise vortices.

Statistics from these simulations for the flame shape factor, the flame curvature, the vorticity/strain rate alignment, the strain rate/surface normal alignment, and the stretch rate have been compared with data from constant density DNS of passive scalar and premixed flame propagation in relatively simple flows (Pope et al., 1989, Ashurst et al. 1987, Ashurst, 1993, and Smith et al. 1994). Very good agreement with these earlier studies was obtained for most of the volume averaged statistical properties. However, a significant dependence upon the spatial location has been found for some statistical properties. The probability density of the shape factor shows a relatively decreased likelihood for cylindrical shaped flames moving downstream. This was shown to be a consequence of the inability of the randomly orientation vortices to wrinkle the flame front (which is a pre specified level surface and propagates normal to itself). An interesting result obtained from these simulations is that in the downstream direction, the strain rate/flame normal alignment shows a transition from alignment seen in shear driven turbulence to an alignment seen in isotropic turbulence. This behavior was shown to be a consequence of the breakdown of the shear layer into randomly oriented vortex tubes as the shear layer evolves in the downstream direction. In the low Re case, this behavior was less pronounced since the shear layer was more stable when compared to the high Re case.

Strain rate (in the plane of the flame) has been found to be highest near the step and decreasing in the downstream direction, the pdf becoming more symmetric, similar to isotropic flows. The flame stretch pdf calculated *a priori* showed a positive mean value at all locations examined but was highest near the corner of the step. This has important implications in flamelet modeling, for it is known that the flame stretch together with the Lewis number can greatly affect the laminar flame speed and in extreme cases may cause local extinction. The present results suggests that this more likely to occur in regions close to the step where the flame front is stretched by both the spanwise and the streamwise vorticity in the shear layer. The effect of flame stretch and thermal expansion due to heat release is currently being investigated and will be reported in the near future.

## ACKNOWLEDGMENT

This research is funded in part by the Office of Naval Research under Grant No. N00014-92-J-403. The computational resources were provided by the Numerical Aerodynamic Simulation (NAS) at NASA Ames Research Center and are gratefully acknowledged.

## REFERENCES

- Ashurst, Wm.T., Kerstein, A. R., Kerr, R. M., and Gibson, C. H., (1987) "Alignment of vorticity and scalar gradient with strain rate in simulated Navier-Stokes turbulence," *Phys. Fluids A*, Vol. 30, No. 8, pp. 2343-2353.
- Ashurst, Wm.T., (1993) "Constant-Density Markstein Flamelet in Navier-Stokes Turbulence", preprint, submitted to *Combustion, Science and Technology*.
- Candel, S. M. and Poinso, T. J., (1990) "Flame Stretch and the Balance Equation for the Flame Area," *Combustion Science and Technology*, Vol. 70, pp. 1-15.
- Cant, R. S., Rutland, C. J., and Troune, A., (1990) "Statistics for laminar flamelet modeling," Center for Turbulent Research, Proceedings of the Summer Program, pp. 271-279.
- Echekki, T. and Mungal, M. G., (1990) "Flame Speed Measurements at the Tip of a Slot Burner: Effects of Flame Curvature and Hydrodynamic Stretch," *Twenty-Third Symposium (International) on Combustion*, The Combustion Institute, pp. 451-461.
- Erlebacher, G. Hussaini, M. Y. Speziale, C. G. and Zang, T. A., (1987) "Toward the Large-Eddy Simulation of Compressible Turbulent Flows," Institute for Computer Applications in Science and Engineering, Hampton, VA, ICASE 87-20.
- Germano, M., Piomelli, U., Moin, P., and Cabot, W. H., (1991) "A Dynamic Subgrid-Scale Eddy viscosity Model," *Phys. Fluids A*, Vol. 3, pp. 1760-1765.
- Kerstein, A. R., Ashurst, W. T., and Williams, F. A., (1988) "The Field Equation for Interface Propagation in an Unsteady Homogeneous Flow field," *Phys. Rev. A* 37, pp. 2728-xx.
- Kim, W.-W. and Menon, S. (1995) "A New Dynamic One-Equation Subgrid-Scale Model for Large-Eddy Simulations," AIAA Paper No. 95-0356, 33rd Aerospace Sciences Meeting.
- Menon, S. (1992) "Active Control of Combustion Instability in a Ramjet Using Large-Eddy Simulations," *Combustion Science and Technology*, Vol. 84, pp. 53-72.
- Menon, S. (1995) "Secondary Fuel Injection Control of Combustion Instability in a Ramjet,"

*Combustion Science and Technology*, Vol. 100, pp. 385-393.

Menon, S. and Jou, W.-H. (1991) "Large-Eddy Simulations of Combustion Instability in an Axisymmetric Ramjet Combustor," *Combustion Science and Technology*, Vol. 75., pp. 53-72.

Menon, S. and Kim, W.-W. (1995) "High Reynolds Number Flow Simulations Using the Localized Dynamic Subgrid-Scale Model," submitted for presentation at the 34th Aerospace Sciences Meeting, Reno, NV.

Metcalf, R. W., Orszag, S. A., Brachet, M. E., Menon, S., and Riley, J. J. (1987) "Secondary Instability of a Temporally Growing Mixing Layer," *J. Fluid Mech.*, Vol. 184, pp. 207-243.

Moin, P., Squires, K., Cabot, W., and Lee, S., (1991) "A Dynamic Subgrid-Scale Model for Compressible Turbulence and Scalar Transport," *Phys. Fluids A*, Vol. 11, pp. 2746-2754.

Piomelli, U., Moin, P., and Ferziger, J. H., (1988) "Model Consistency in Large Eddy Simulation of Turbulent Channel Flows," *Phys. Fluids*, Vol. 31, pp. 1884-1891.

Pope, S.B., Yeung, P. K., and Girimaji, S. S., (1989) "The curvature of material surfaces in isotropic turbulence," *Phys. Fluids*, Vol. 1, pp. 2110-2018.

Rutland, C. J. and Trouvé, A., (1993) "Direct Simulations of Premixed Turbulent Flames with Nonunity Lewis Numbers," *Combustion and Flame*, Vol. 94, pp. 41-57.

Smith, T. M., Menon, S., and McMurtry, P. A., (1994) "The Structure of Premixed Flames in Isotropic and Shear Driven Turbulent Flows," AIAA 94-0677, 32nd Aerospace Sciences Meeting.

Smith, D. A., and Zukoski, E. E. (1985) "Combustion Instability Sustained by Unsteady Vortex Combustion," AIAA 85-1248.

Speziale, C. (1985) "Galilean Invariance of Subgrid Scale Stress Models in Large-Eddy Simulations of Turbulence," *J. Fluid Mechanics*, Vol. 156, pp. 55-62.

Squires, K. and Zeman, O., (1990) "On the Subgrid-Scale Modeling of Compressible Turbulence," Center for Turbulence Research, Proceedings of the Summer Program, pp. 47-59.

Yakhot, V. (1988) "Propagation Velocity of Premixed Turbulent Flame," *Combustion Science and Technology*, Vol. 60, pp. 191-214.

Yeung, P. K., Girimaji, S. S., and Pope, S. B., (1990) "Staining and Scalar Dissipation on Material Surfaces in Turbulence: Implications for Flamelets," *Combustion and Flame*, Vol. 79, pp. 340-365.

Yu, K. H., Trounev, A. and Daily, J. W. (1991) "Low-Frequency Pressure oscillations in a Model Ramjet Combustor," *J. Fluid Mechanics*, Vol. 232, pp. 47-72.

## LIST OF FIGURES

Figure 1. Three-dimensional dump combustor: a) characteristic geometry and dimensions, and b) two planes of the  $96 \times 48 \times 16$  grid (every other horizontal (y) line shown).

Figure 2. Three-dimensional isosurface of the flow field: a) spanwise vorticity, b) streamwise vorticity, and c)  $G$ -field.

Figure 3. Spanwise vorticity, subgrid kinetic energy and  $G$ -surface: a) spanwise vorticity and  $G$ -field in a  $z$ -plane, and b) subgrid kinetic energy and  $G$ -field in the same  $z$ -plane.

Figure 4. Spanwise vorticity and  $G$ -field in three  $x$ -planes: a) plane 1, b) plane 2, and c) plane 3.

Figure 5a. Probability density of the shape factor for data by Pope et al. (1989), Ashurst (1993), Smith et al. (1994), and LES at  $Re = 50000$ .

Figure 5b. Probability density of the shape factor for LES at  $Re = 50000$  over the entire domain and four  $x$  locations.

Figure 6. Probability density of negative mean curvature for LES at  $Re = 50000$  over the entire domain and four  $x$  locations.

Figure 7a. Probability density of the alignment between the intermediate strain rate and vorticity for data by Ashurst (1993), Smith et al. (1994), and LES at  $Re = 50000$ .

Figure 7b. Probability density of the alignment between the intermediate strain rate and vorticity for LES at  $Re = 50000$  over the entire domain and four  $x$  locations.

Figure 8a. Probability density of the alignment between most compressive strain rate and the flame normal for data by Ashurst et al. (1987) and LES at  $Re = 5000$  over the entire domain.

Figure 8b. Probability density of the alignment between most compressive strain rate and the flame normal for data by Ashurst et al. (1987) and LES at  $Re = 50000$  over the entire domain.

Figure 9a. Probability density of the alignment between most compressive strain rate and the flame normal for LES at  $Re = 5000$  over the entire domain and four  $x$  locations.

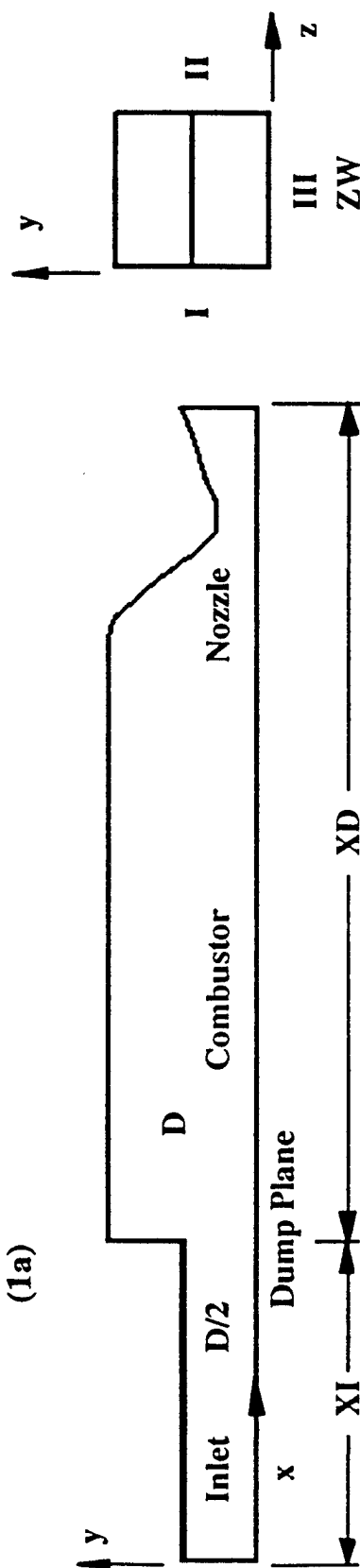
Figure 9b. Probability density of the alignment between most compressive strain rate and the flame normal for LES at  $Re = 50000$  over the entire domain and four  $x$  locations.

Figure 10a. Probability density for the tangential strain rate for data by Cant et al. (1990), Yeung et al. (1990), and Smith et al. (1994), and LES at  $Re = 50000$ .

Figure 10b. Probability density of the tangential strain rate for LES at  $Re = 50000$  over the domain and four  $x$  locations.

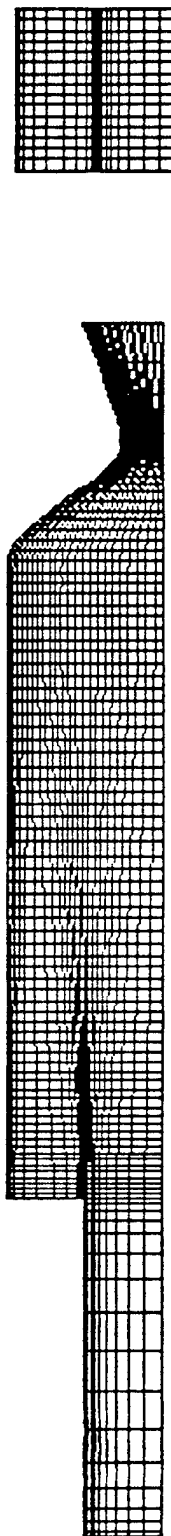
Figure 11. Probability density of flame stretch for LES at  $Re = 50000$  over the domain and four  $x$  locations.

(1a)



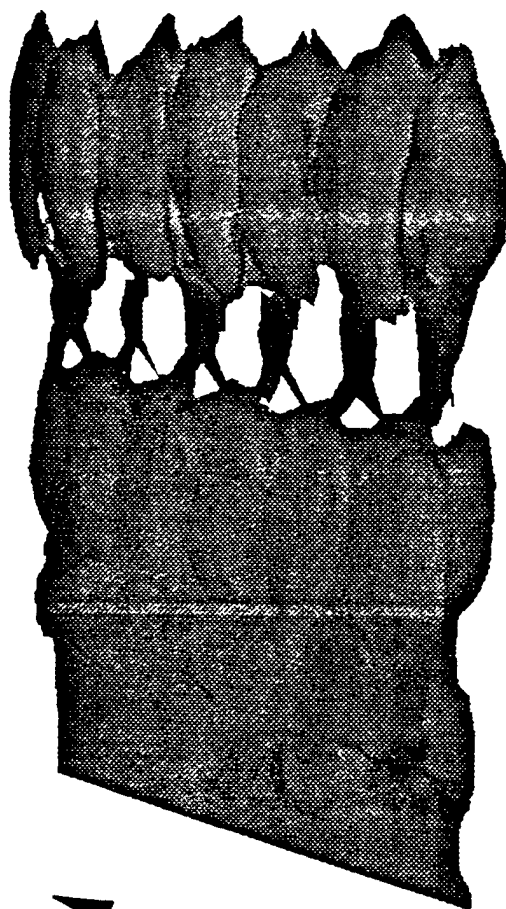
Duct Height	$D = .0635 \text{ m}$	I,II	Periodic Planes
Step Height	$H = D/2 = .03175 \text{ m}$	III	Symmetry Plane
Dump Height	$2D = .1270 \text{ m}$		
Inlet Length	$XD = .3600 \text{ m}$		
Inlet Length	$XI = .1344 \text{ m}$		
Dump Width	$ZW = .0635 \text{ m}$		

(1b)





(2a)



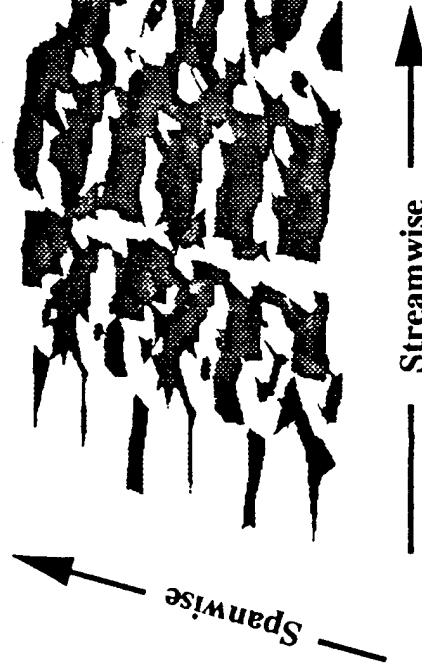
Spanwise

Streamwise

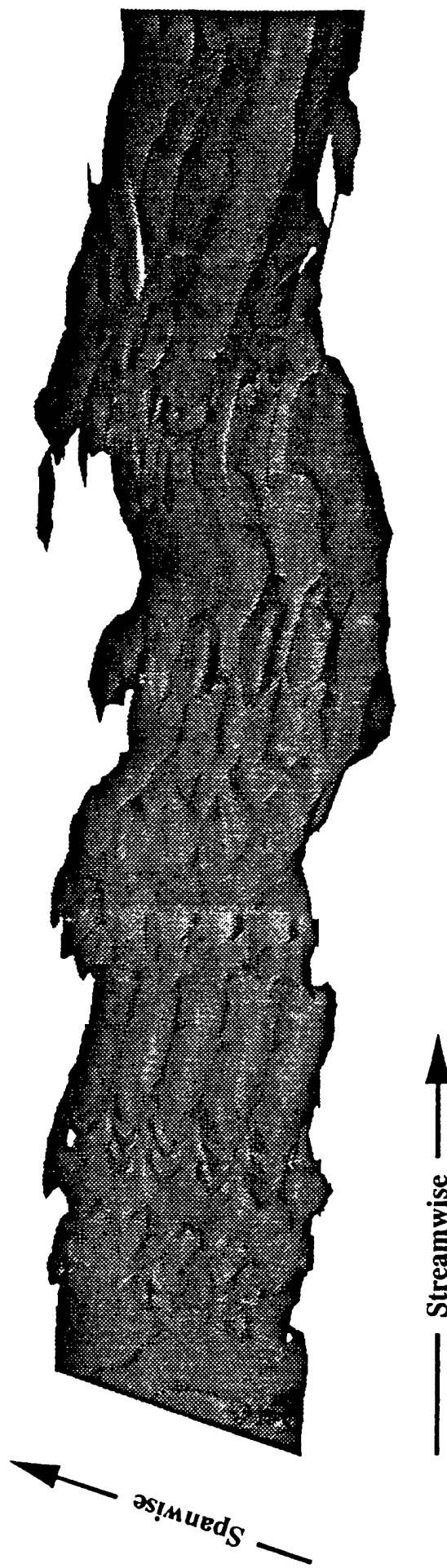




(2b)



(2c)



(3a)



-5000 15000 (1/sec)

(3b)



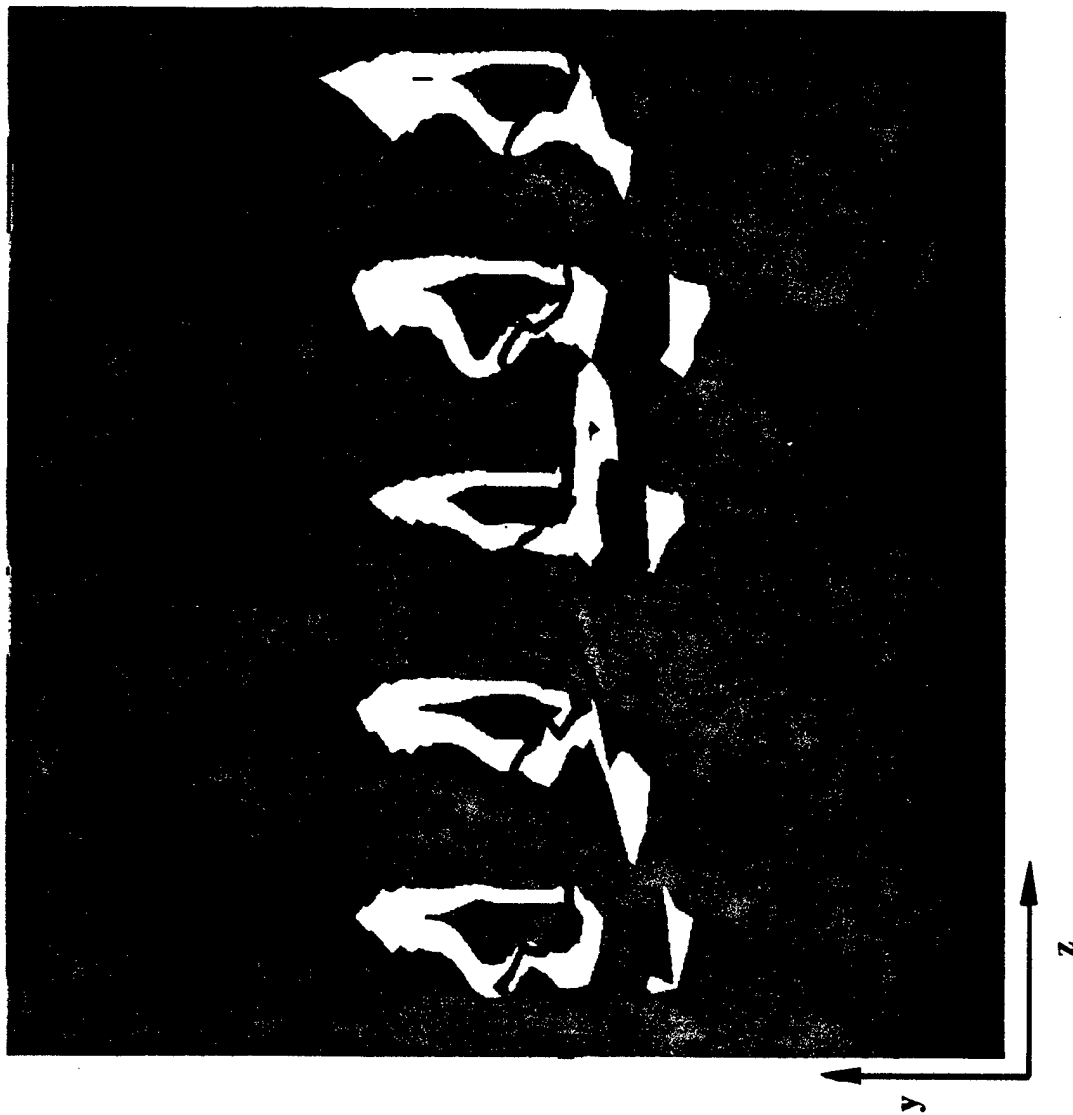
100 ( $\text{m}^2/\text{sec}^2$ )

0

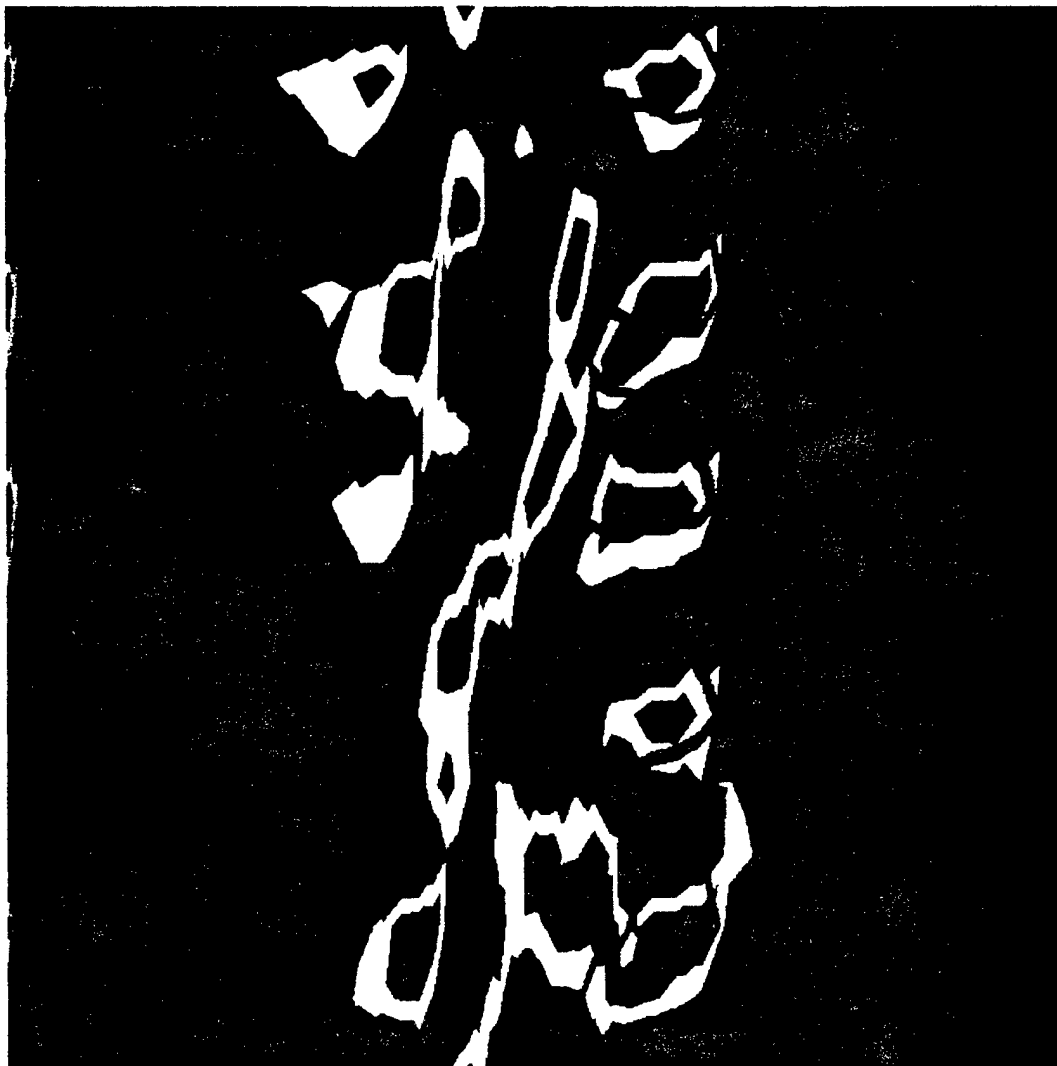
(4a)

4000 (1/sec)

-4000

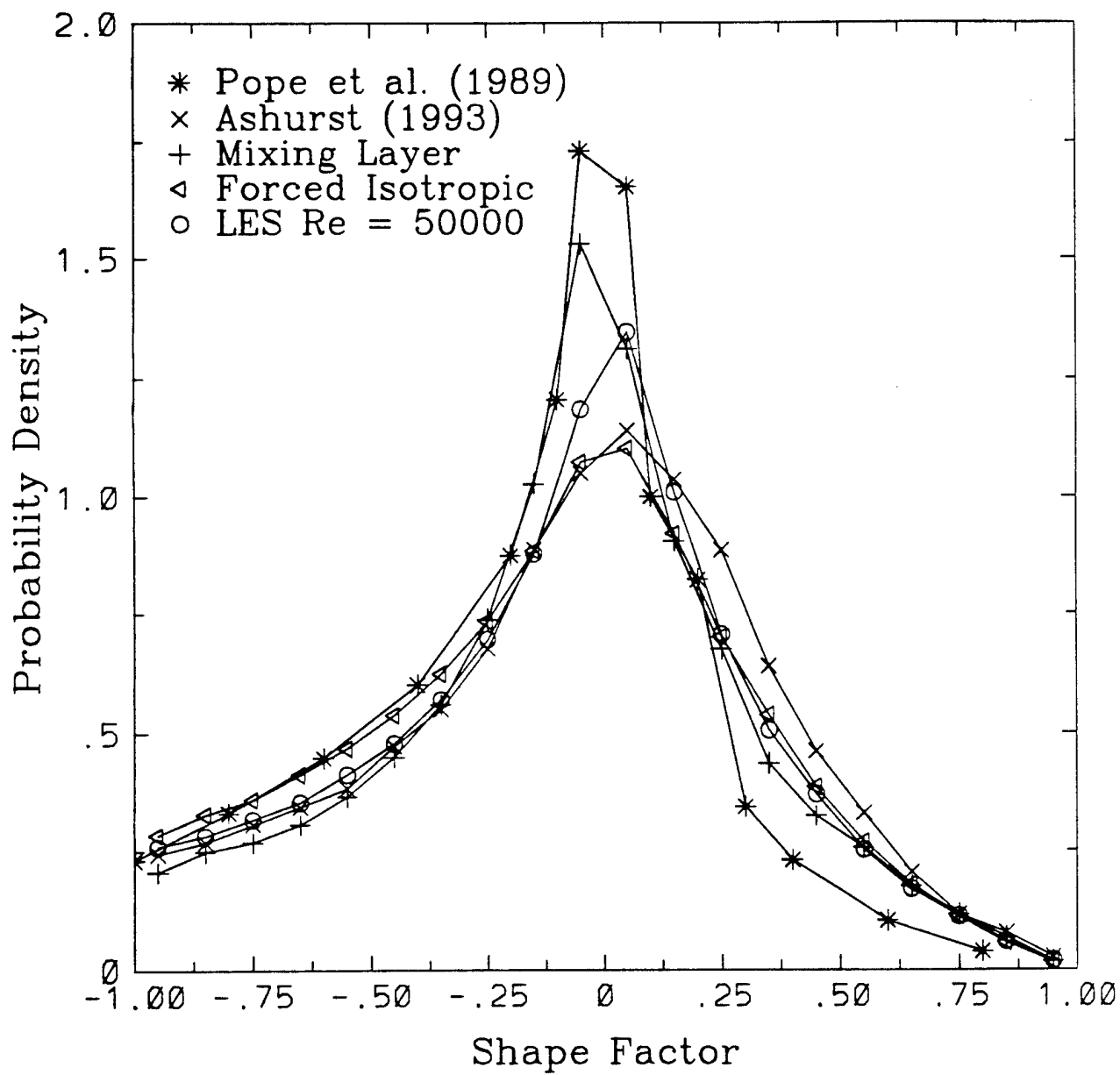


(4b)

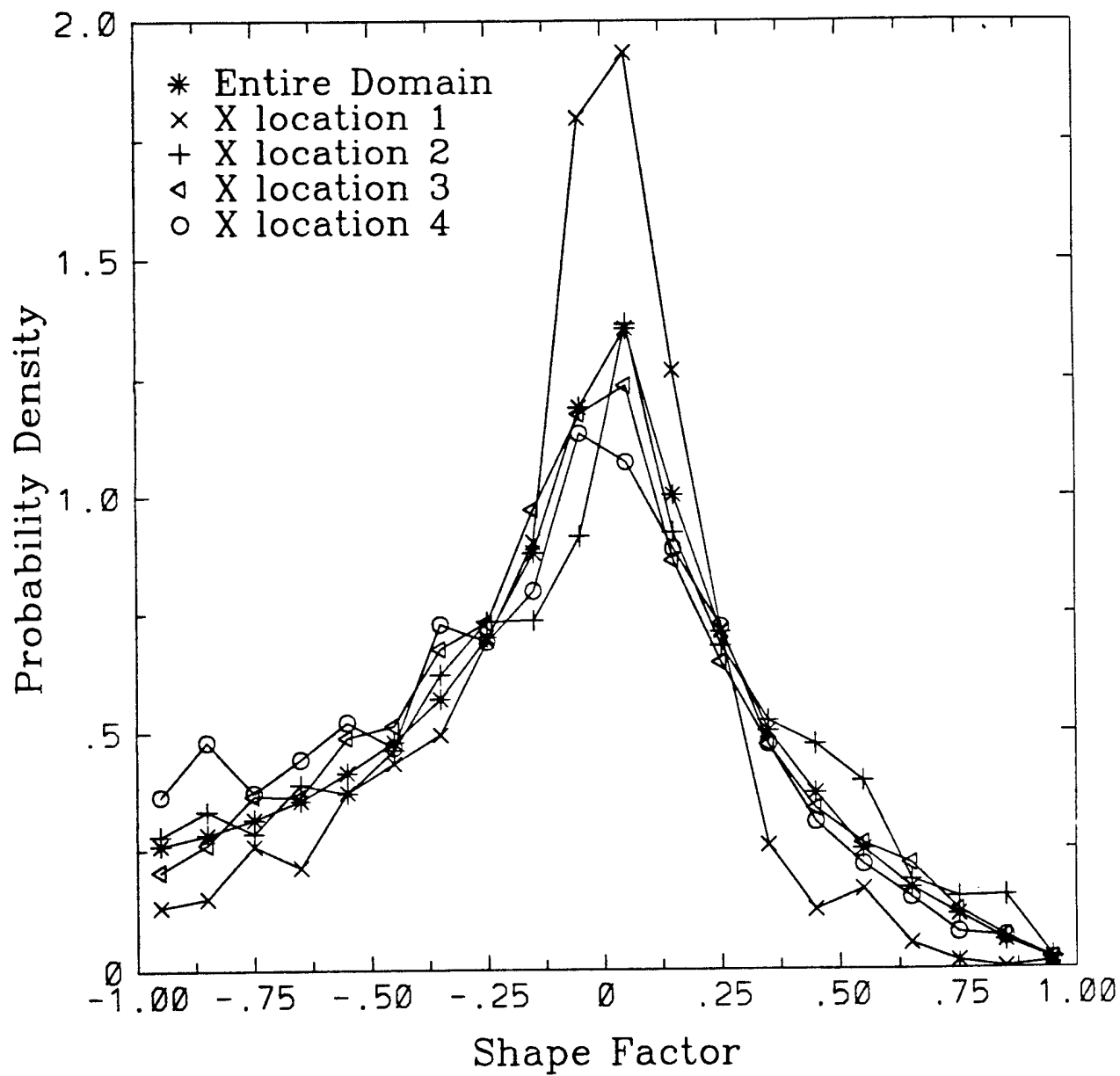


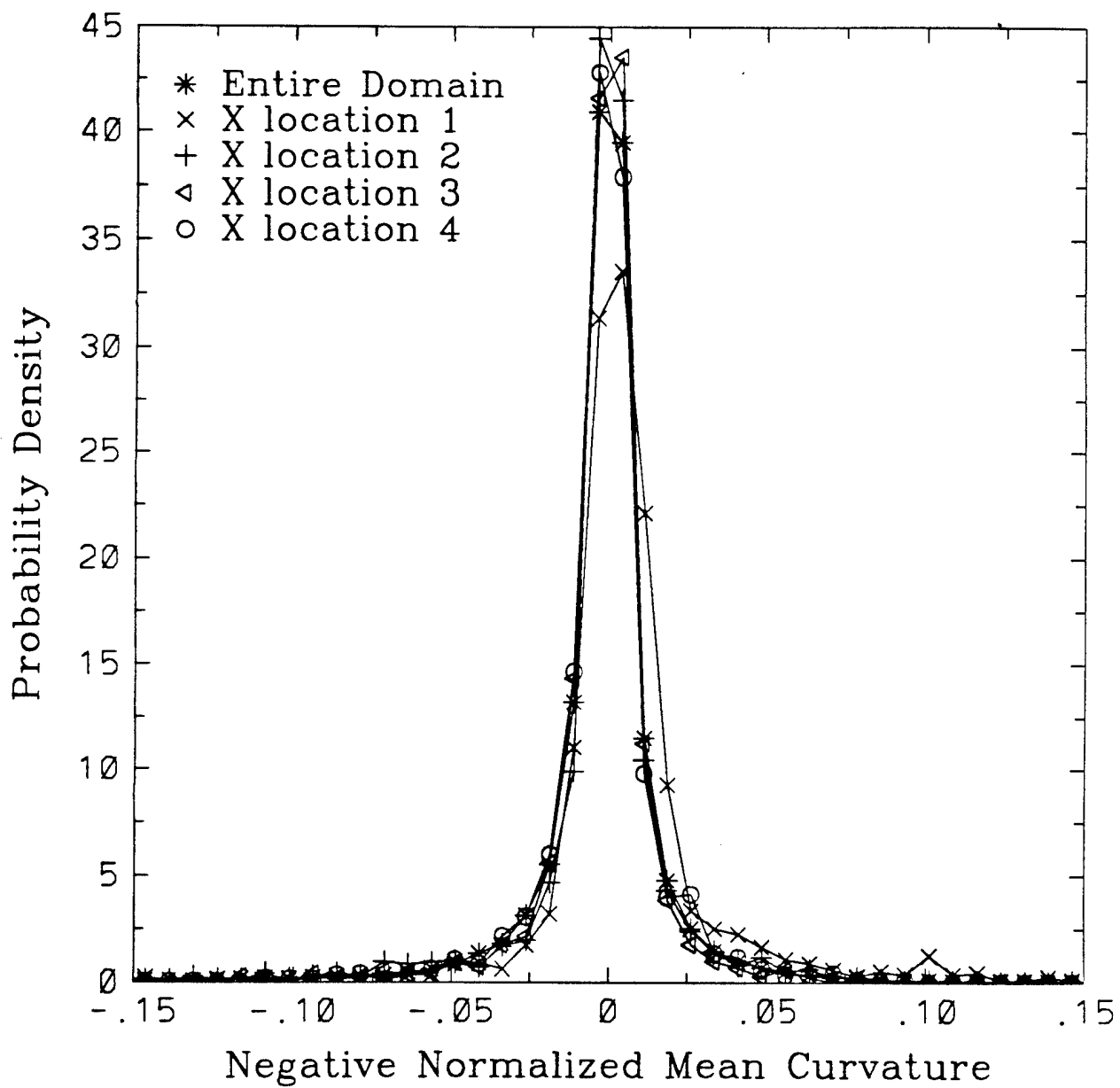
(4c)

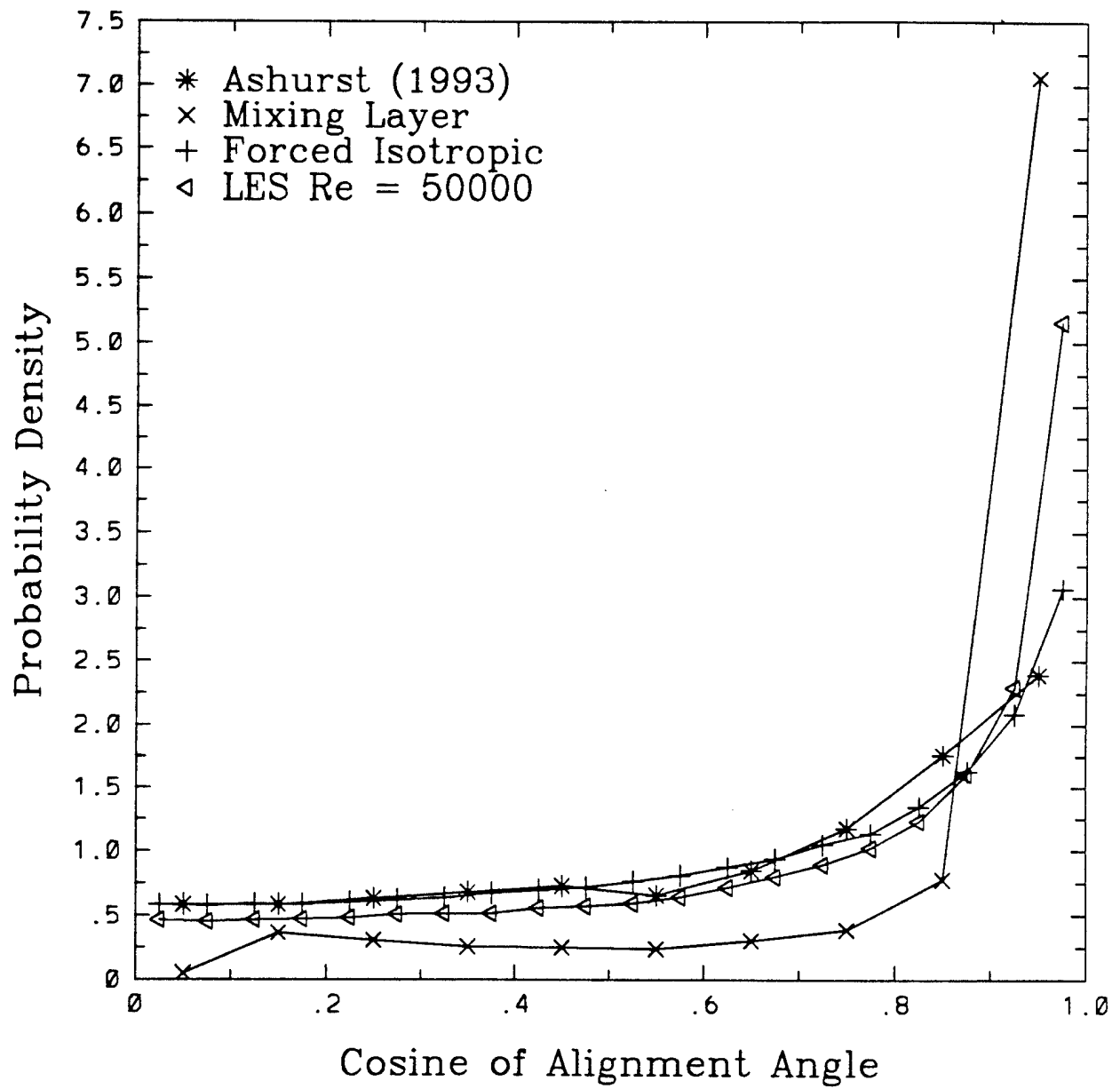


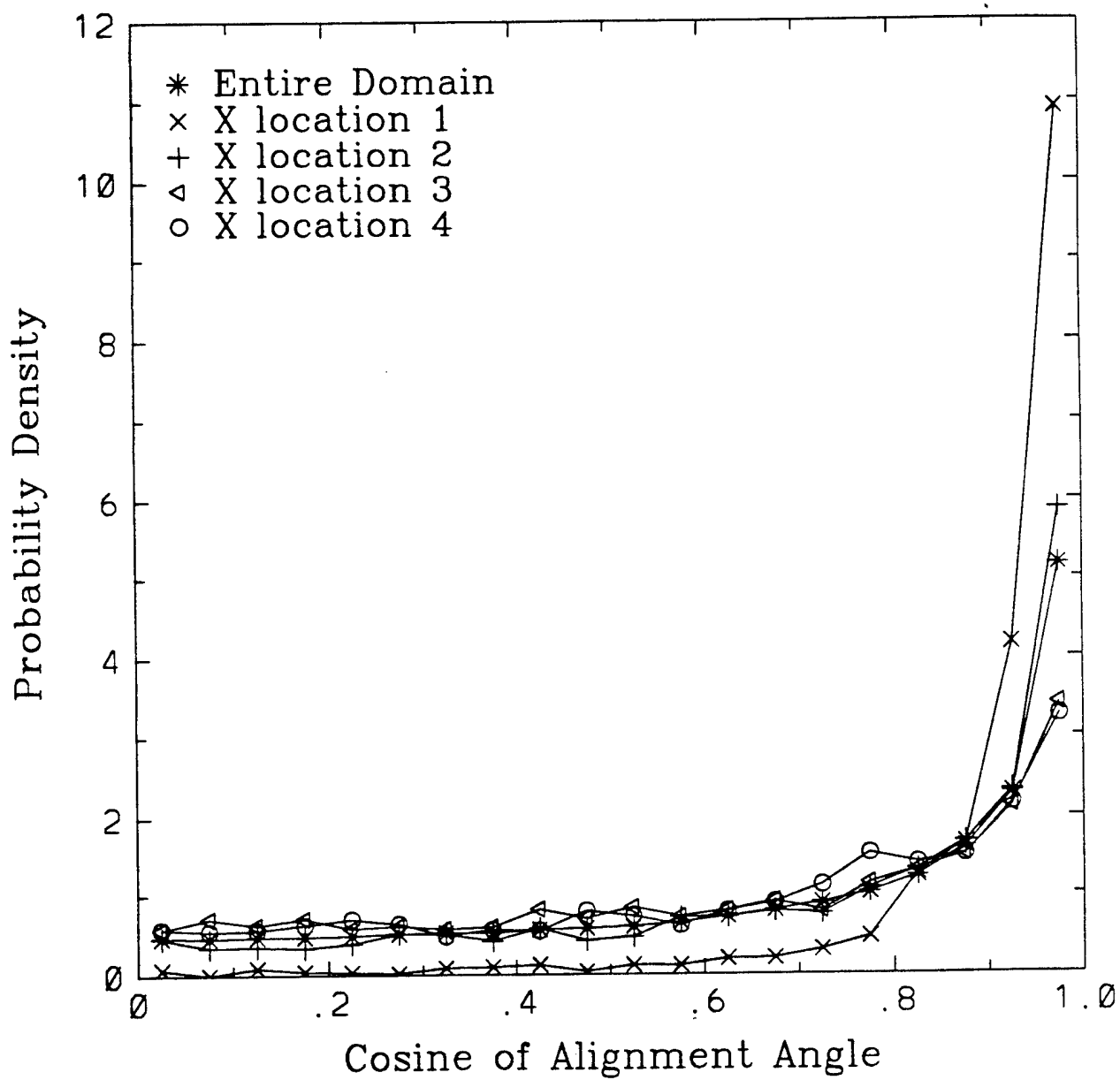


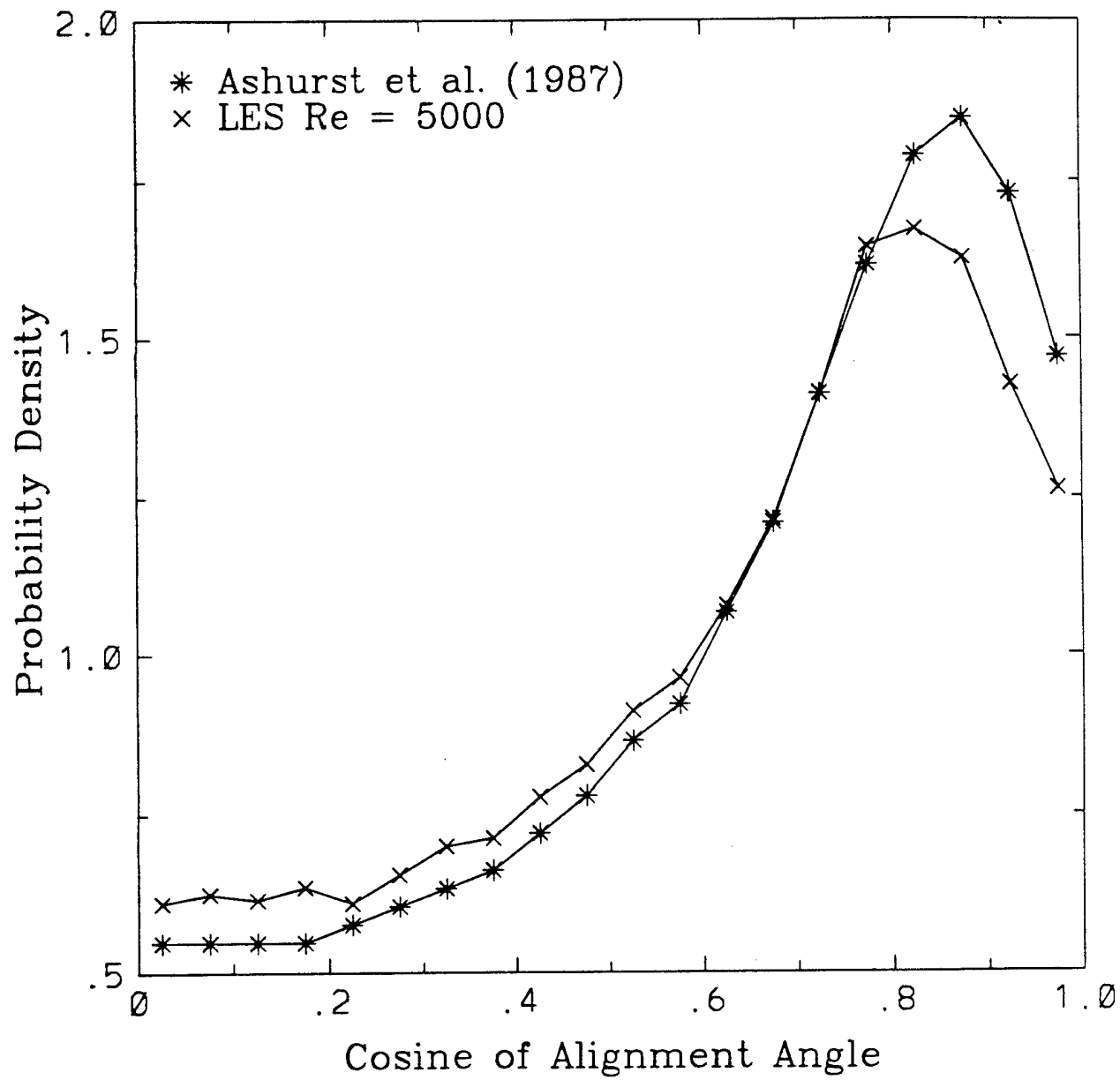


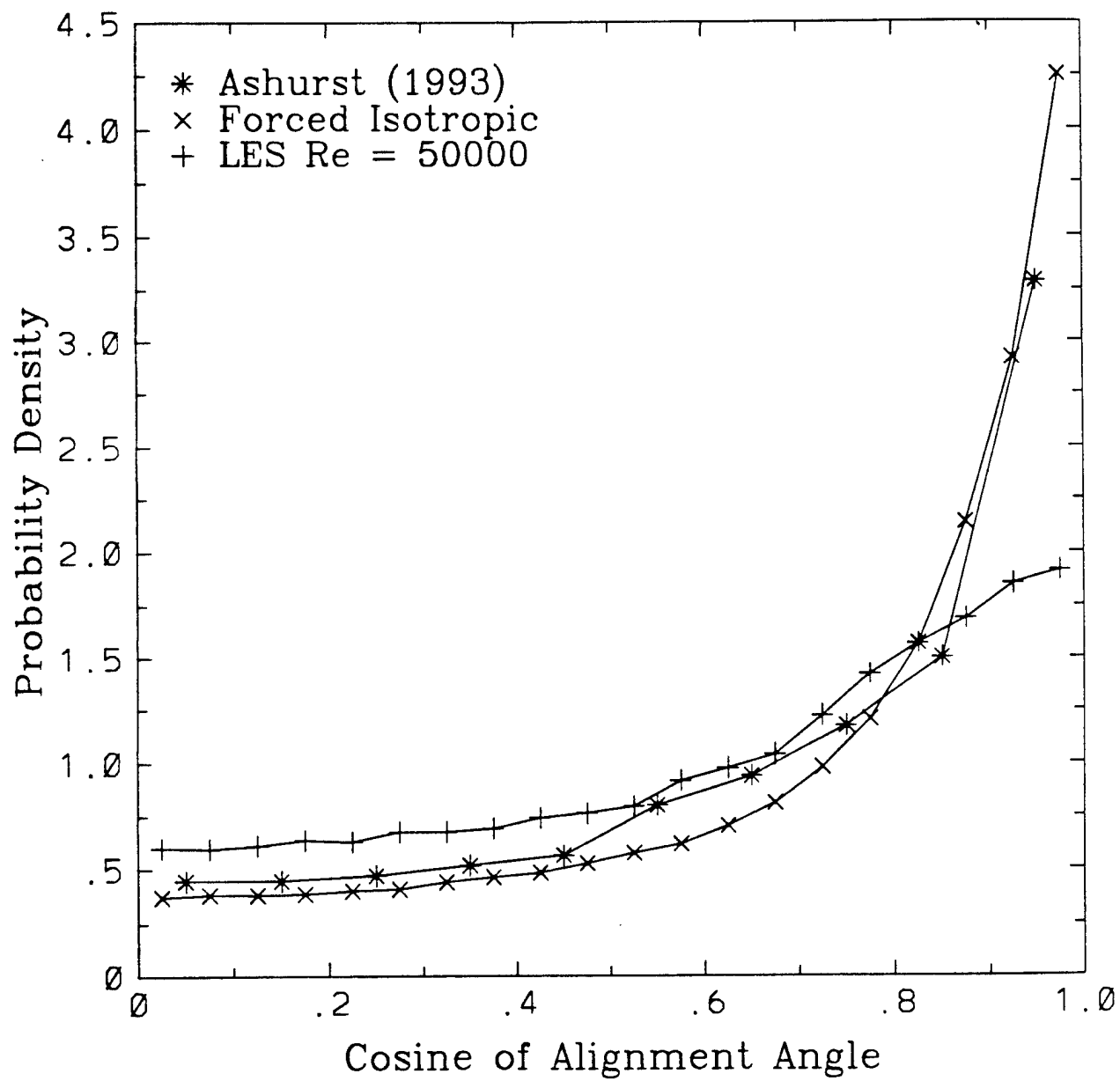


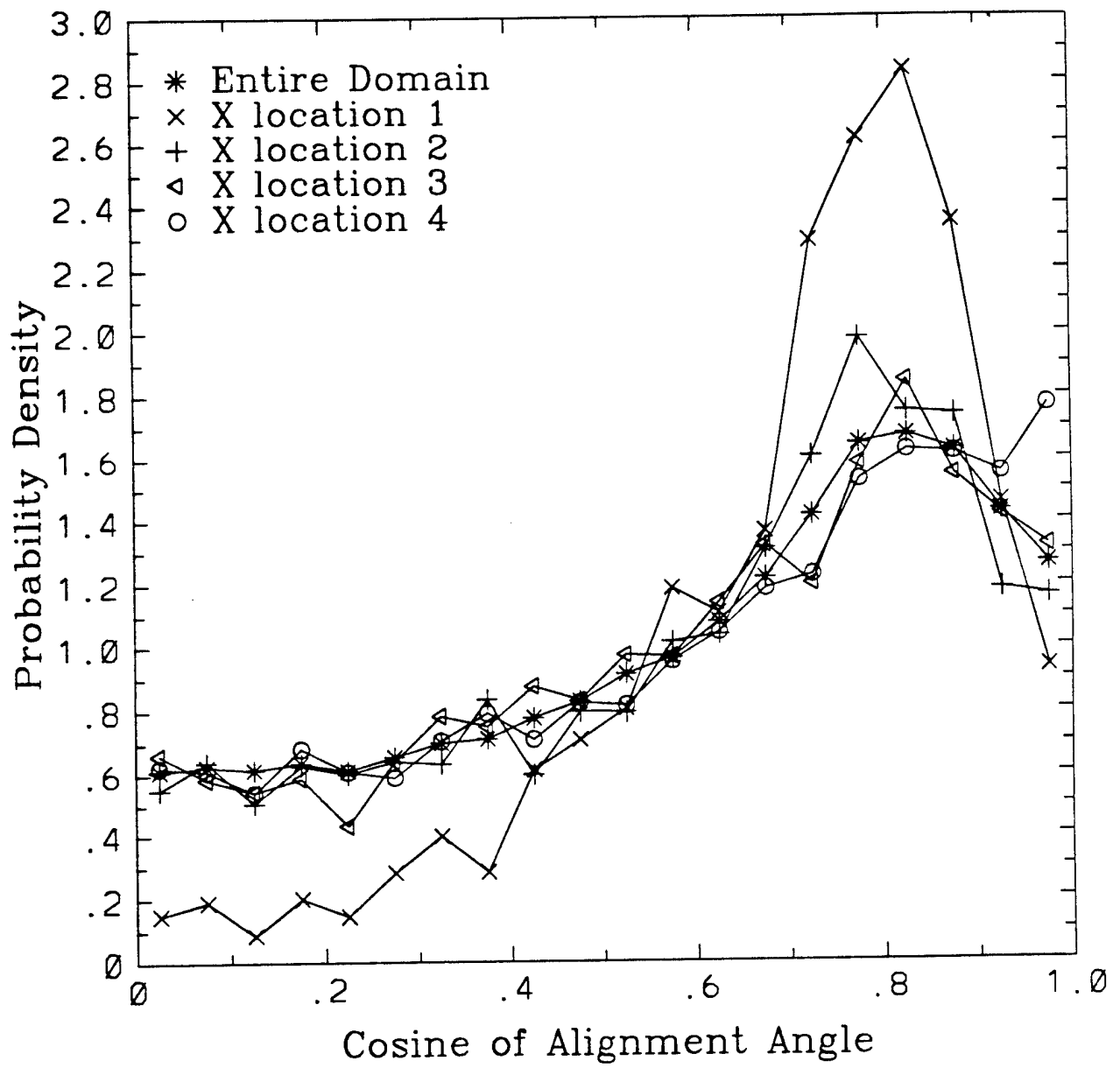


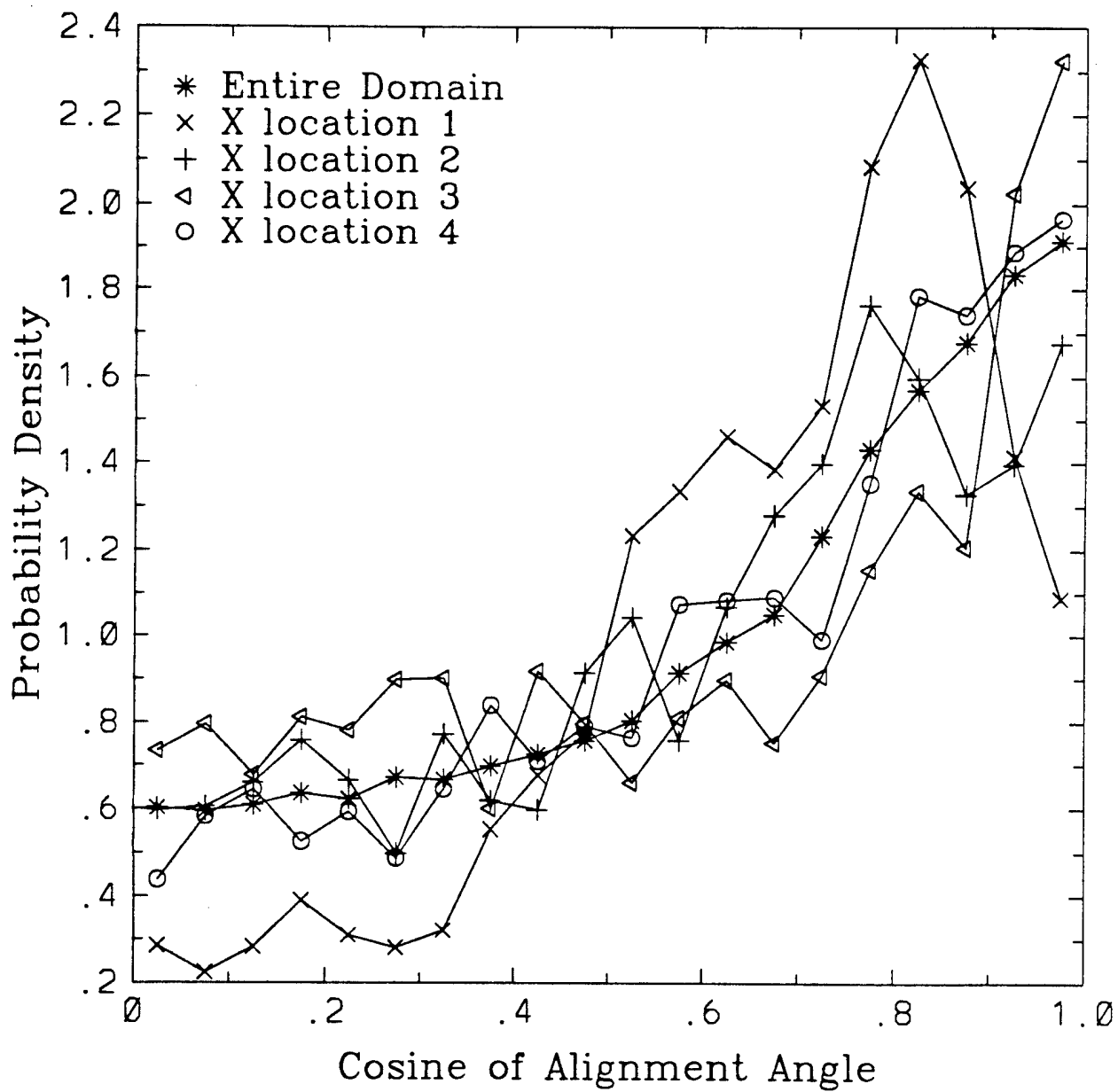




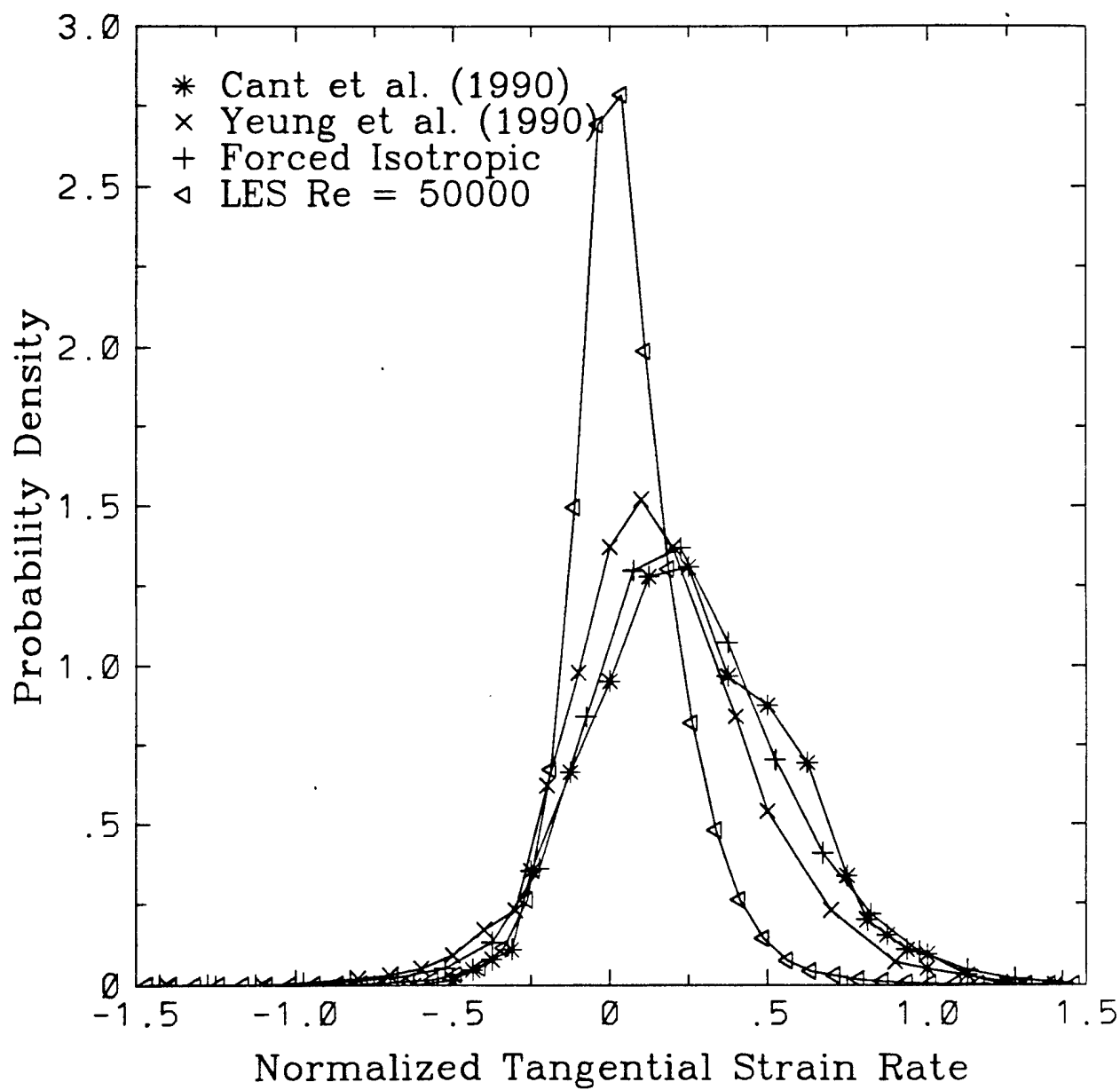


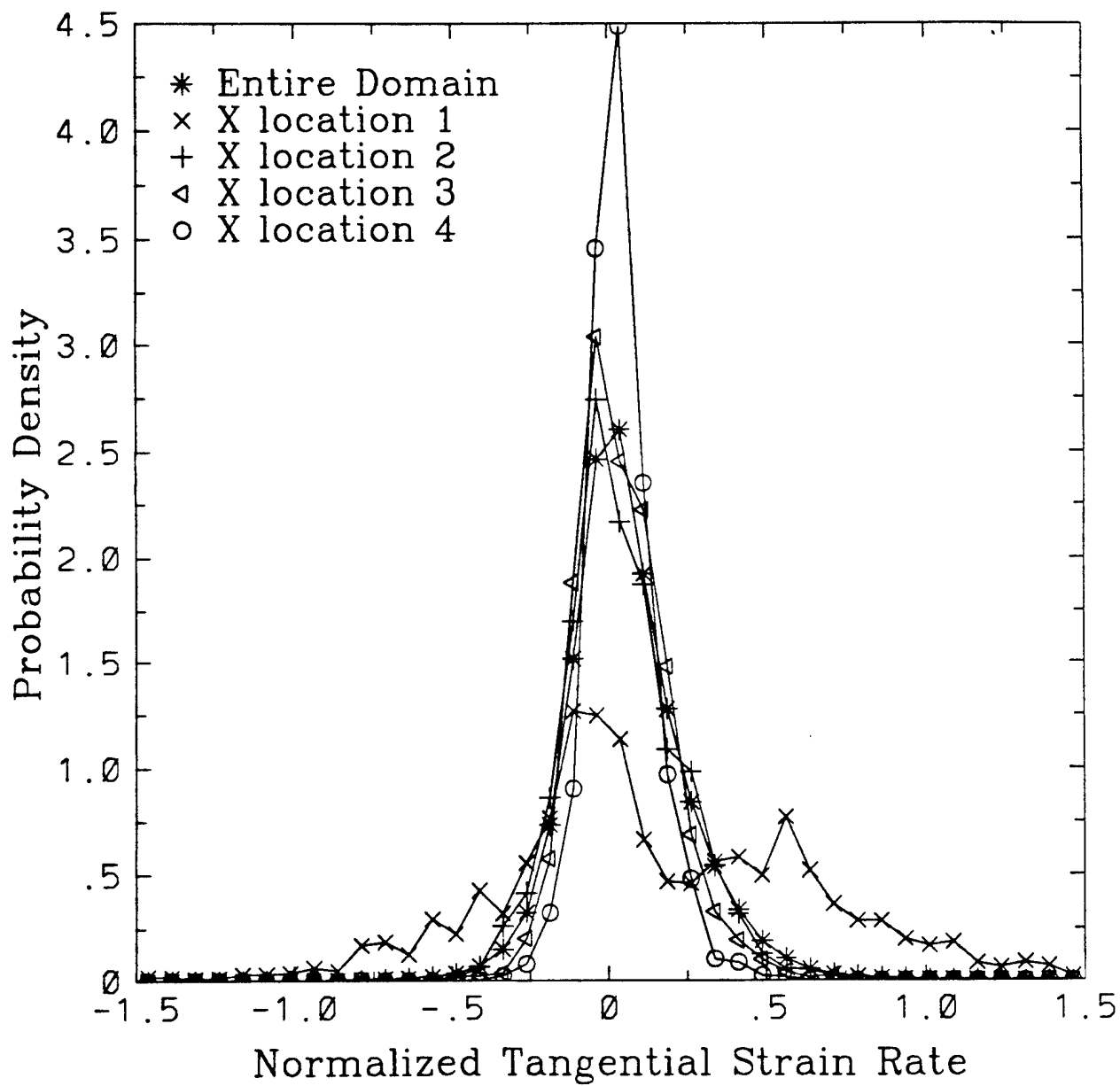


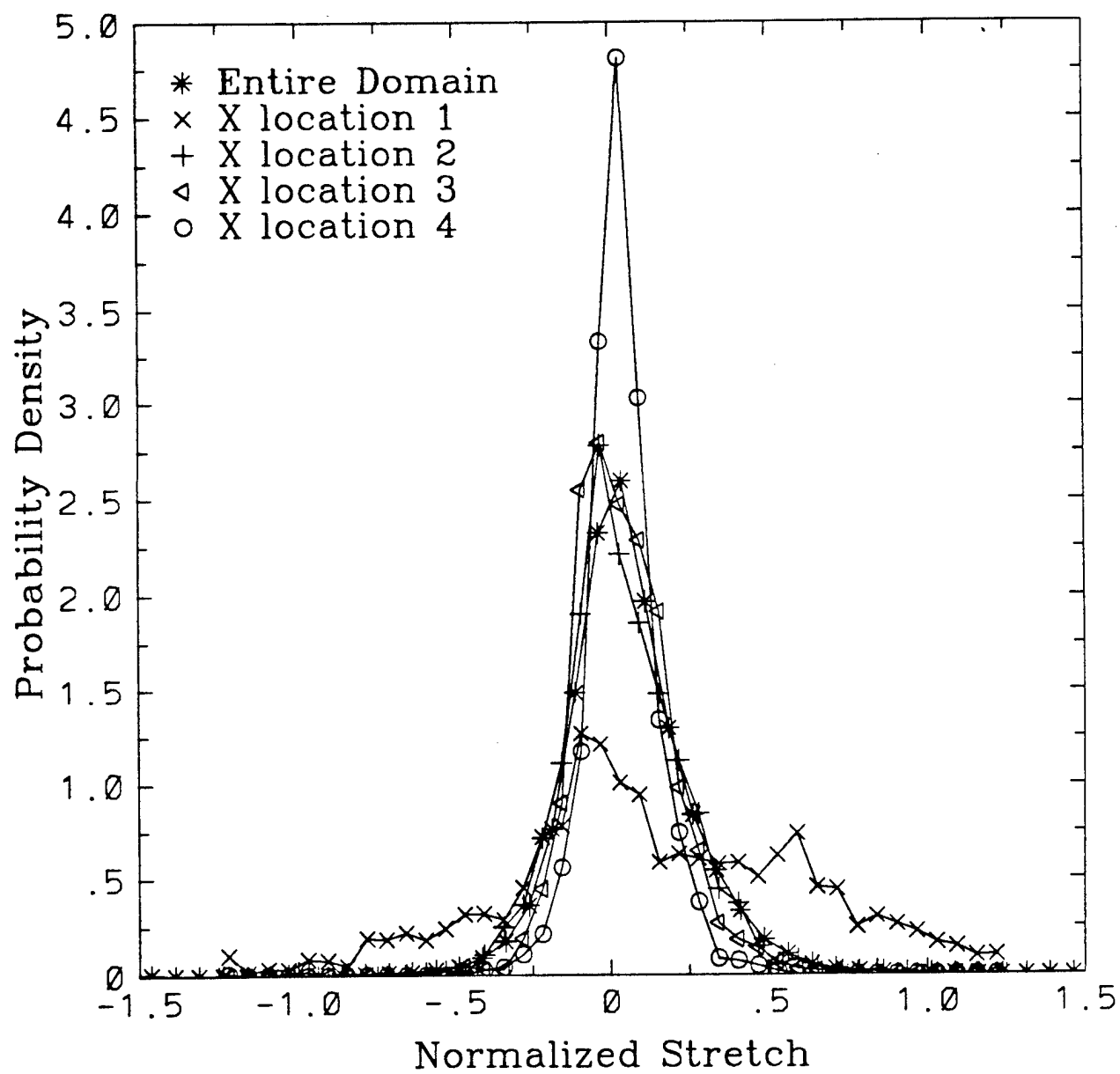












## SHORT COMMUNICATION

# Secondary Fuel Injection Control of Combustion Instability in a Ramjet

S. MENON *School of Aerospace Engineering, Georgia Institute of Technology  
Atlanta, Georgia 30332-0150*

(Received Oct. 2, 1993; in final form March 28, 1994)

**ABSTRACT**—Combustion instability in a ramjet combustor has been numerically simulated using a large-eddy simulation (LES) technique. Low frequency, large amplitude pressure oscillations characteristic of combustion instability is simulated in the combustor. Analysis of the results show that both the inlet duct acoustics and a coupled acoustic/vortex mode can excite combustion instability in the combustor. Similar observations have been made in recent experimental studies. Active control techniques that use secondary fuel injection as the controller have been investigated to suppress the instability. The results show that when the inlet duct acoustic mode is exciting the instability, active control decreases the rms fluctuation levels by around 35 percent (10 dB) but leaves the dominant frequency unchanged. When the instability is being excited by a convective mode, active control results in a similar reduction in the fluctuation level and completely suppresses the dominant frequency. However, two new frequencies, a convective mode and an inlet duct acoustic resonant mode, are excited that are not controlled. These results are consistent with recent experimental observations and suggest that, to successfully control combustion instability for a wide range of flow conditions, a dynamically adjusting controller will be required.

## 1 INTRODUCTION

Combustion instability in a ramjet engine is an extremely complex phenomenon involving nonlinear interactions among acoustic waves, vortex motion and unsteady heat release. Typically, the instability manifests itself as a large-amplitude pressure oscillation in the low-frequency range (100–800 Hz) and is very difficult to control. In recent years, both experimental (e.g., Schadow *et al.*, 1987; Smith and Zukoski, 1985; Dowling, 1989; Langhorne and Hooper, 1989; Yu *et al.*, 1991) and numerical (e.g., Menon and Jou, 1991) investigations have been conducted to determine the mechanism of the combustion instability. Attempts to control combustion instability using both passive and active control techniques have also been carried out in the past. This note summarizes the results of a numerical study of active control technique using secondary injection of the premixed fuel as the controller. More details of these results were presented earlier (Menon, 1992b).

## 2 THE SIMULATION MODEL

The simulation model used in this study was developed through a series of numerical studies described elsewhere (Menon and Jou, 1990; Jou and Menon, 1990; Menon and Jou, 1991). The equations are the full compressible Navier–Stokes equations for-

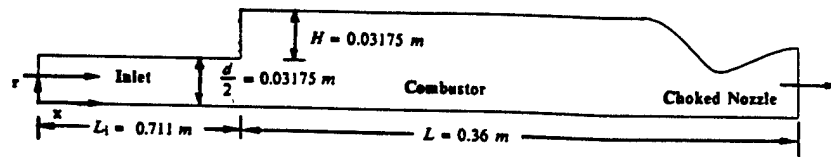


FIGURE 1 The ramjet combustor.

mulated in the axisymmetric coordinate system. The numerical technique is an unsplit, fourth-order-accurate, finite-volume scheme based on the MacCormack method. The modeled ramjet combustor consists of an axisymmetric inlet duct connected to an axisymmetric dump combustor by a sudden expansion. A convergent-divergent nozzle is attached downstream of the combustor. The flow through this nozzle is choked, and the outflow at the downstream computational boundary is supersonic. Figure 1 shows the typical ramjet configuration used in these studies.

Premixed combustion in the ramjet is modeled using the thin flame approach. This approach is valid as long as the flame thickness is much smaller than the smallest turbulent length scale (i.e., the Kolmogorov scale). The rationale for this modeling approach and the issues related to its implementation in the simulation model was discussed extensively elsewhere (Menon and Jou, 1991). Within the thin flame approximation, a model equation for premixed combustion is considered in which the local flame speed explicitly appears. If the local flame speed  $u_f$  is known, a progress variable  $G$  can be defined that is governed by the equation (Kerstein *et al.*, 1988; Menon and Jou, 1991):  $(\partial G / \partial t) + \vec{u} \cdot \nabla G = -u_f |\nabla G|$ , where  $\vec{u}$  is the fluid velocity. This equation describes the convection of the flame by the local fluid velocity and the flame propagation into the unburnt mixture through a Huygens type mechanism,  $u_f |\nabla G|$ . Here, by definition,  $G = 1$  corresponds to the premixed fuel state,  $G = 0$  corresponds to the fully burnt state, and the flame is located at a prescribed  $G = G_0$  level surface, where,  $0 < G_0 < 1$ . For laminar premixed combustion, the local flame speed  $u_f$  is the laminar flame speed  $S_L$  which contains the information on the chemical kinetics and the molecular dissipation. When applied to turbulent flows, the local flame speed  $u_f$  is taken to be the local turbulent flame speed  $u_T$ , where  $u_T$  is a prescribed function of local turbulence intensity  $u'$  and the laminar flame speed  $S_L$ . To determine the flame speed, the subgrid turbulent kinetic energy is computed explicitly using an algebraic model proposed by Squires and Zeeman (1990) and described in more details in Menon (1992b). The subgrid model is also used to determine the subgrid stresses and heat flux terms appearing in the LES equations.

The effect of heat release is included by using the heat of formation of the fuel in the definition of enthalpy as described in Menon and Jou (1991). The heat of formation of the fuel determines the amount of heat released during combustion and, thus, is a function of the equivalence ratio for a given fuel. The product temperature can then be estimated for a given heat of formation. To determine the functional relation,  $u_T = u_T(S_L, u')$  the relation developed by Yakhot (1989) is employed. This relation has been shown to reduce to the linear scaling,  $u_T/S_L \approx (1 + u'/S_L)$  when  $u'/S_L \gg 1$  limit, and to the Clavin-Williams relation  $u_T/S_L \approx (1 + (u'/S_L)^p)$ , where  $p = 2$  when  $u'/S_L < 1$  limit. However, recently (Kerstein and Ashurst, 1992) it was shown that for low  $u'/S_L$ , the

Clavin-Williams expression may be incorrect and a new scaling was proposed with  $p = 4/3$ . Therefore, in this study, the turbulent flame speed is determined by using the linear scaling, with  $p = 1$  for  $u'/S_L > 1$  and the modified Clavin-Williams relation, with  $p = 4/3$  for  $u'/S_L < 1$ .

### 3 SIMULATION OF COMBUSTION INSTABILITY

In general, combustion instability in a combustor depends upon various parameters, such as the system geometry, the flow parameters, the fuel type, and the equivalence ratio as discussed elsewhere (Menon and Jou, 1991). The results discussed here were obtained using (unless otherwise noted) identical configurations, grid resolution ( $320 \times 64$ ), heat release, and flow conditions.

Earlier (Menon, 1992b), the effect of the grid resolution and the new subgrid kinetic energy model was discussed in detail. These studies showed that the low-frequency oscillations in the combustor is relatively insensitive to the dissipation mechanism modeled by the subgrid model. This was consistent with the earlier results obtained using simple eddy viscosity model (Menon and Jou, 1991). Analysis of the subgrid kinetic energy field indicated that a significant amount of subgrid kinetic energy is associated with the large vortex. Since an increase in subgrid kinetic energy implies an increase in the turbulent flame speed (which is a measure of the turbulent reaction rate), this suggests that significant reaction processes occur around large vortices. Similar observations were made in earlier experiments (e.g., Smith and Zukoski, 1985; Yu *et al.*, 1991).

Figure 2a shows the characteristic pressure trace at the base of the step for a simulation with a reference Mach number (based on inlet conditions) of 0.32, and Figure 2b

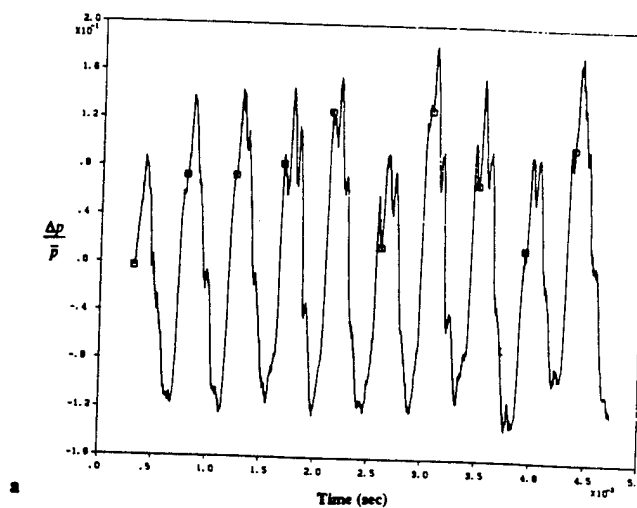


FIGURE 2 The pressure time trace and spectra at the base of the step. (a) Pressure time trace, Mach 0.32; (b) Pressure spectra, Mach 0.32; (c) Pressure spectra, Mach 0.17.

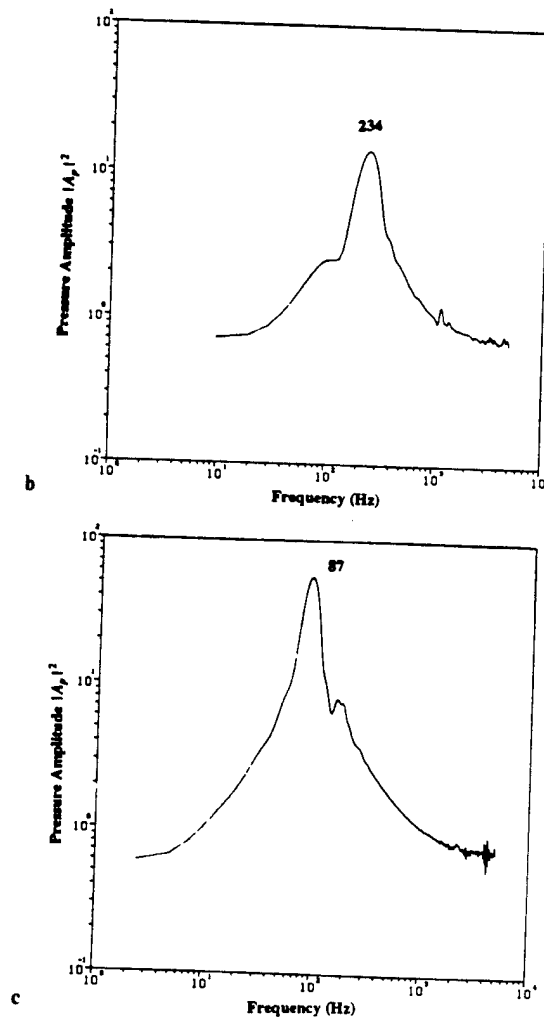


FIGURE 2 (Continued)

shows the corresponding spectra. A low frequency oscillation with a peak-to-peak level of around 30 percent of the mean pressure is seen. Recent experiments (Gutmark *et al.*, 1992) in a test rig with nearly identical dimensions observed similar fluctuation levels in the combustor. The amplitude of the 234 Hz pressure oscillation in the inlet and in the combustor was computed and the axial variation of the amplitude normalized by the pressure amplitude at the base of the step was analyzed (Menon, 1992b). The axial variation of the amplitude suggests the presence of standing half-wave acoustic mode in the combustor. A simple determination of the acoustic frequency by using the relation  $f = a/2L_i$  with  $L_i = 0.711$  m and using the speed of sound  $a$  based on the temperature at the inlet gives the same frequency. Thus, it appears that the inlet duct acts as a long-wavelength acoustic resonator. The amplitude is a maximum in the combustor

and the level is nearly unchanged in the entire combustor. The simulation results are in qualitative agreement with experimental observations of Yu *et al.* (1991).

Experiments have also suggested that the instability mechanism may not be purely acoustic in nature and there may be a convective component to the instability which is related to vortex motion in the combustor (e.g., Schadow *et al.*, 1987; Dowling, 1989; Yu *et al.*, 1991). Numerical studies of cold flows (Jou and Menon, 1990) in ramjet combustors have also shown that a coupled acoustic-vortex mode can exist in ramjet combustors. The frequency determined, based on this coupled mode oscillation, is different from that of a pure acoustic resonant mode. To determine if the instability can have a convective component, simulations at different Mach numbers of 0.17 and 0.45 were performed. Since only the axial velocity was changed to obtain different Mach numbers, only the convective component of the instability (if it exists) would be affected.

Figure 2c shows the pressure spectra at the base of the step for Mach 0.17 simulation. It can be seen that with the decrease in the Mach number the dominant frequency decreased to around 87 Hz. A higher harmonic of this oscillation at 178 Hz is also seen in the pressure spectra. The peak-to-peak pressure fluctuation level remains relatively unchanged from that seen in the Mach 0.32 simulation. Decrease in the instability frequency with the decrease in the inlet velocity has also been observed in experimental configurations (Dowling, 1989; Yu *et al.*, 1991). The acoustic oscillation at the 234 Hz frequency seen in the Mach 0.32 simulation, is no longer dominant in the combustor; however, the pressure and the axial velocity spectra in the inlet do show the presence of this frequency (not shown here, but discussed in Menon, 1992b). When the Mach number was increased to 0.45, the instability frequency remained at the inlet acoustic mode value (not shown here, but discussed in Weeratunga and Menon, 1993). These results clearly indicate that both the convective and the acoustic resonant modes are present in the flow field but, only one mode may dominate depending upon the flow conditions and the geometrical properties of the device.

Using a criterion established on the basis of experimental data (Yu *et al.*, 1991), it is possible to estimate the frequency of a coupled acoustic-convective instability. For a coupled acoustic/convective mode to exist, the instability period is the sum of two time scales: a time scale associated with the motion of the vortex/flame structure in the combustor and, a time scale associated with the time required for a pressure wave to travel from the sonic throat (which acts as a downstream acoustic boundary) to the upstream inlet duct boundary and back to the dump plane. The frequency for a coupled acoustic/vortex mode (if it exists) based on the above criterion for the Mach 0.32 case, was found to be around 115 Hz, while for the Mach 0.17 case it was around 90 Hz. Clearly, the numerically computed frequency of 234 Hz for the Mach 0.32 case is not in the range for a coupled mode; however, the frequency of 87 Hz obtained in the Mach 0.17 simulation is close to the frequency obtained from the simple model.

#### 4 ACTIVE CONTROL OF COMBUSTION INSTABILITY

In the present study, a technique that involves manipulating the unsteady heat release in the combustor to control the low-frequency oscillations is investigated. In this



technique, the control system uses additional heat release to modify the acoustic energy balance in the combustor. Although various control simulations were carried out here, we will discuss particular simulations that uncovered some interesting behavior. The secondary premixed fuel is typically introduced one step height upstream of the step. Note that, when secondary fuel is introduced in the inlet, the primary and the secondary fuel streams are both (cold) premixed fuel and the net effect of secondary injection is a modulation and an increase of the total mass flow into the combustor. The implementation of the injection conditions and its comparison with experimental approach was discussed in Menon (1992b) and, for brevity, will not be repeated here.

To develop a control strategy, we followed a technique similar to that used earlier for acoustic feedback control (Menon, 1992a). First, a cross-correlation analysis between the (earlier recorded) pressure fluctuation at the base of the step and the pressure signal at a chosen sensor location (at present, the sensor signal is the wall pressure near the downstream diffuser) is carried out to determine the time delay for peak negative correlation. Then, the time-delayed pressure signal from the sensor is used to modulate the secondary fuel flow rate. A general fuel injection controller is defined such that:  $\dot{m}_{sec} = Ga p_s(t - \tau)$ , where,  $\tau$  is a prescribed time-delay,  $\dot{m}_{sec}$  is the secondary mass flow rate,  $p_s$  is the unsteady pressure at the sensor location and  $Ga$  is a transfer function that may or may not be a constant. An estimate for  $Ga$  from linearized analysis was recently obtained (Fung *et al.*, 1991) which showed that  $Ga$  can be related to the heat content of the fuel and the mean inlet speed of sound.

Figure 3a shows the pressure spectra at the base of the step during an active control study of the Mach 0.32 instability. For this simulation, the controller was used with a time delay of 2 msec and the secondary fuel injection was carried out whenever  $p_s(t - \tau) > 0$ . Thus, the controller modeled here was a pulsed unsteady injection system and the secondary mass flow rate was estimated to be approximately 10 percent of the reference mass flow rate at the inlet. The control simulation was initiated by restarting the uncontrolled simulation (Figure 2) at an earlier time. The results show that the pressure oscillation is controlled with around a 35 percent reduction in the rms levels (around 10 dB). A recent experimental study (Gutmark *et al.*, 1992) also showed that a reduction of around 22 percent in the pressure rms level could be obtained using a fuel modulation controller. The dominant oscillation frequency seen in the controlled simulation is still present in the spectra. This suggests that the inlet duct acoustics are still controlling the combustion instability. A low frequency of around 75 Hz is also seen in the spectra. At present, the source of this mode of oscillation cannot be determined since this simulation has not been carried out long enough to obtain sufficient data to spectrally resolve this low frequency.

The same control strategy was then used to control the Mach 0.17 using a time delay of 6 msec (which was chosen based on cross-correlation analysis of the 87 Hz oscillation). Figure 3b shows the pressure spectra for this case. On comparing this data with the uncontrolled case, some interesting observations can be made. The amplitude level again was decreased by around 10 dB (Menon, 1992b). However, in this case, the dominant frequency around 87 Hz is no longer present indicating that the controller is effective in reducing the fluctuation level, as well as, in suppressing the original dominant mode of oscillation. However, the spectra shows that two new frequencies have been excited. The appearance of new modes during control was also reported in

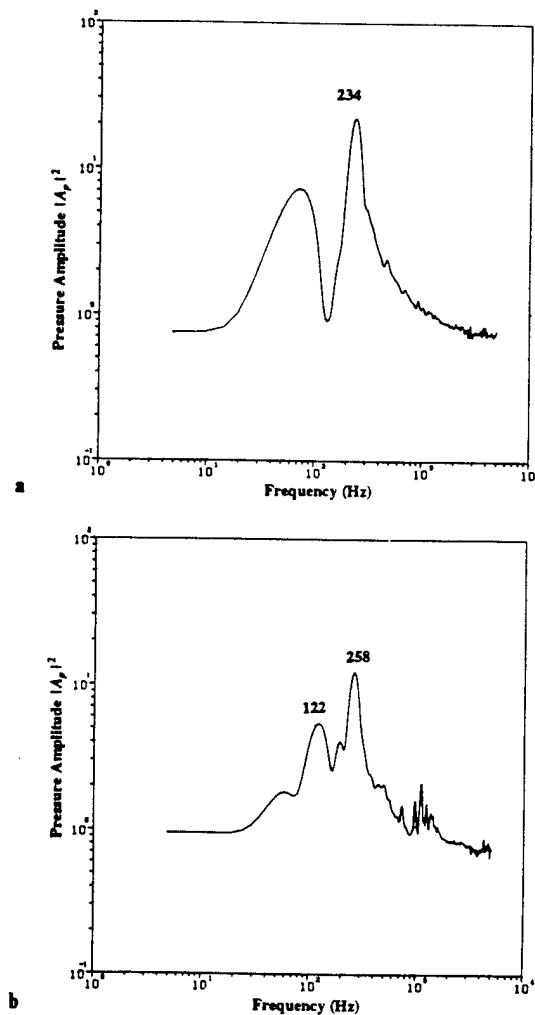


FIGURE 3 The pressure spectra at the base of the step during active control; (a) Pressure spectra, Mach 0.32; (b) Pressure spectra, Mach 0.17.

past experimental studies (Langhorne and Hooper, 1989; Gutmark *et al.*, 1992). The two new frequencies are at 122 Hz and 258 Hz. The latter value is close to the 234 Hz mode seen earlier and appears to suggest that the inlet acoustics are again starting to dominate the pressure oscillations. The introduction of the secondary fuel increases the inlet mass flow and, also, results in an increase in the axial flow velocity. It was observed earlier that for higher axial velocities, the instability mode is dominated by the inlet acoustic model. This again suggests that for a given configuration, there may be a range of flow velocities for which the coupled acoustic/convective mode may control the instability. This issue is currently being investigated in more detail and will be reported in the future.

The fact that the original frequency is controlled, but results in the excitation of new frequencies that are uncontrolled, indicates that a fixed time-delay controller cannot be used to inhibit convective/acoustic coupled mode of instability. In the experimental study (Gutmark *et al.*, 1992), a dual-channel controller capable of actively controlling multiple frequencies is being investigated. A similar controller is currently being investigated numerically, and the results will be reported in the near future.

## 5 CONCLUSIONS

A large-eddy simulation model has been employed to investigate combustion instability and secondary fuel injection controllers in a ramjet combustor. Many features of the numerically simulated combustion instability are in good agreement with experimental observations. Simulations with different reference Mach numbers were carried out to differentiate between acoustic and couple acoustic/convective modes. Analysis of the data suggests that the inlet acoustic mode determines the oscillation frequency in the combustor when the inlet Mach number exceeds 0.32. However, for a lower Mach number of 0.17, a different oscillation frequency was excited which simple analysis indicates to be a coupled acoustic-vortex mode of oscillation.

To control the observed instability, a controller that used a time-delayed pressure signal from a sensor to specify a pulsed secondary fuel flow rate was investigated in detail. When the inlet duct acoustic mode was exciting the instability in the combustor, the controller was effective with a 10 dB decrease in the rms fluctuation level but left the frequency unchanged. In the case of a convective mode of instability, the control method effectively suppressed the original dominant mode of oscillation but excited new frequencies that were not controlled. The simulated behavior of the instability and its response to the secondary fuel injection control are qualitatively similar to recent experimental observations. A more general controller that uses a dynamically adjusting time-delay is now being evaluated to determine if multiple frequencies can be controlled. The results of this study will be reported in the future.

## ACKNOWLEDGEMENT

This research is funded by the Office of Naval Research under Contract No. N00014-90-C-0089 and the computational resources were provided by the Numerical Aerodynamic Simulator (NAS) at NASA Ames Research Center and are gratefully acknowledged.

## REFERENCES

- Dowling, A. P. (1989). Reheat Buzz—An Acoustically Coupled Combustion Instability, AGARD CP-450.
- Fung, Y. T., Yang, V. and Sinha, A. (1991). Active Control of Combustion Instabilities with Distributed Actuators, *Combustion, Science and Technology*, Vol. 78, pp. 217–245.
- Gutmark, E., Wilson, K. J., Parr, T. P. and Schadow, K. C. (1992). Feedback Control of Multimode Combustion Instability, AIAA-92-0778.
- Jou, W.-H. and Menon, S. (1990). Modes of Oscillations in a Nonreacting Ramjet Combustor Flow, *J. Propulsion and Power*, Vol. 6, pp. 535–543.
- Kerstein, A. R., Ashurst, W. T. and Williams, F. A. (1988). Field Equation for Interface Propagation in an Unsteady Homogeneous Flow Field, *Physical Rev. A*, Vol. 37, No. 7, pp. 2728–2731.

- Kerstein, A. R. and Ashurst, W. T. (1992). Propagation Rate Growing Interfaces in Stirred Fluids, to appear in *J. Fluid Mech.*
- Langhorne, P. J. and Hooper, N. (1989). Attenuation of Reheat Buzz by Active Control, AGARD-Cp-450, pp. 10.1-10.16.
- Menon, S. and Jou, W.-H. (1990). Numerical Simulations of Oscillatory Cold Flows in an Axisymmetric Ramjet Combustor, *J. Propulsion and Power*, Vol. 6, No. 5, pp. 525-534.
- Menon, S. and Jou, W.-H. (1991). Large-Eddy Simulations of Combustion Instability in an Axisymmetric Ramjet Combustor, *Combustion Science and Technology*, Vol. 75, pp. 53-72.
- Menon, S. (1992a). Active Combustion Control of Combustion Instability in a Ramjet Combustor using Large Eddy Simulations, *Combustion Science and Technology*, Vol. 84, pp. 51-79.
- Menon, S. (1992b). A Numerical Study of Secondary Fuel Injection Technique for Active Control of Instability in a Ramjet, AIAA-92-0777.
- Schadow, K. C., Gutmark, E., Parr, T. P., Parr, D. M., Wilson, K. J. and Crump, J. H. (1987). Large-Scale Coherent Structures as Drivers of Combustion Instability, AIAA-87-1326.
- Smith, D. A. and Zukoski, E. E. (1985). Combustion Instability Sustained by Unsteady Vortex Combustion, AIAA-85-1248.
- Squires, K. and Zeeman, O. (1990). On the Subgrid-Scale Modeling of Compressible Turbulence, *Proc. Summer Program*, CTR, Stanford University, pp. 47-59.
- Weeraratunga, S. and Menon, S. (1993). Parallel Computations of Unsteady Combustion in a Ramjet Engine, AIAA-93-1914.
- Yakhot, V. (1989). Propagation Velocity of Premixed Turbulent Flame, *Combustion Sci. and Tech.*, Vol. 60, pp. 191-214.
- Yu, K. H., Trouve, A. and Daily, J. W. (1991). Low-Frequency Pressure Oscillations in a Model Ramjet Combustor, *J. Fluid Mech.*, Vol. 232, pp. 47-72.



**AIAA 94-0678**

**A Computational Model to Predict the  
Fractal Nature of Turbulent  
Premixed Flames**

**S. Menon**

**Georgia Institute of Technology  
Atlanta, GA**

**A. R. Kerstein**

**Sandia National Laboratories  
Livermore, CA**

**32nd Aerospace Sciences  
Meeting & Exhibit**

**January 10-13, 1994 / Reno, NV**

# A COMPUTATIONAL MODEL TO PREDICT THE FRACTAL NATURE OF TURBULENT PREMIXED FLAMES

S. Menon

School of Aerospace Engineering  
Georgia Institute of Technology  
Atlanta, Georgia

A. R. Kerstein

Combustion Research Facility  
Sandia National Laboratories  
Livermore, California

## ABSTRACT

A computational method that provides a one-dimensional stochastic representation of turbulent convection and laminar flamelet propagation in turbulent premixed flames has been used to investigate the structure and propagation characteristics of the wrinkled flame. An earlier study of the structure of the turbulent flame brush is extended and generalized to include thermal expansion (i.e., heat release). In this broader context, the issues of fractal dimension and dynamic range of fractal scaling are revisited. A new viscous length scale is identified that collapses the data and helps explain the observed dependence of the fractal dimension on  $u'/S_L$ . These and other properties of the time-varying structure of the flame brush are analyzed in order to assess the reliability of extrapolations from moderate-Re laboratory configurations to high-Re conditions.

## 1. INTRODUCTION

To understand the phenomenology of the wrinkled flamelet regime of turbulent premixed combustion (e.g., Williams, 1985), it is necessary to characterize the flame surface geometry. In recent years, various scaling laws that govern the flame geometry and its relation to the turbulent flame speed  $u_T$  have been proposed (e.g., Peters, 1986; Yakhot, 1988a, b; Kerstein, 1988b). These laws have been developed using inertial-range scaling concepts; however, these scalings do not take into account factors such as the effect of thermal expansion (heat release) on the flow field, the finite thickness of flamelets, and the dependence of the laminar flame speed  $S_L$  on flame stretch and other local properties. Despite these simplifications and additional complications such as spatial inhomogeneity of typical experimental configurations, measurements to date provide some qualitative and quantitative support for the proposed scalings.

Based on analysis of the high-turbulence-intensity regime  $u' \gg S_L$ , where  $u'$  is the turbulent velocity fluctuation, it has been proposed that  $u_T$  scales linearly with  $u'$  (Yakhot, 1988b) and that the flame surface is fractal from the turbulence integral scale  $L$  down to some lower cutoff, with a fractal dimension  $D$  of about 7/3. Specific proposals concerning the value of  $D$  and the scaling of the lower cutoff are summarized by Gulder (1990).

The proposed scalings governing flame surface geometry and turbulent flame speed are interrelated because, within the framework of the simplifying assumptions that are adopted,  $u_T/S_L$  is equal to the flame surface area per unit projected transverse area (William, 1985). Figure 1 shows the theoretical fractal behavior of a three-dimensional surface whose measured surface area  $A$  is plotted as a function of the scale of measurement  $l$  on a log-log scale. The self-similarity in the scales of various sizes (which is characteristic of the fractal regime) shows up as a straight line with slope  $(2 - D)$  within a certain range of scales bracketed by an inner cutoff ( $l_i$ ) and an outer cutoff ( $l_o$ ). The outer cutoff scale for turbulent flames is typically chosen to be the integral length scale ( $L$ ) while both the Kolmogorov scale ( $L_K$ ) and the Gibson scale ( $L_G$ ) have been proposed for the inner cutoff (see Peters, 1986). The relation between the normalized turbulent flame speed ( $u_T/S_L$ ) and the flame area ratio can be written as

$$\frac{u_T}{S_L} = \frac{A_T}{A_L} = \left[ \frac{l_i}{l_o} \right]^{2-D} \quad (1)$$

Thus, once the inner and outer cutoff length scales are known and the fractal dimension  $D$  determined, it is possible to estimate the turbulent flame speed. Fractal scaling is observed in experiments, with values of  $D$  that appear to asymptote at about 7/3 as  $u'/S_L$  increases (North and Santavice, 1990).

The objective of the present modeling study is to investigate the validity and the domain of applicability of the proposed scalings. The stochastic simulation model employed here was shown in an earlier study of premixed flames without heat release (Menon and Kerstein, 1992) to exhibit both the turbulent flame speed and the fractal geometry scalings. In this paper, the effect of heat release and thermal expansion has been included and the structure and the propagation speed of the premixed flame has been reanalyzed in a more general context.

## 2. MODEL FORMULATION

The propagation of a turbulent premixed flame through a statistically steady turbulent flow field is simulated using a formulation that regards the flame as a passive interface convected by the flow field, propagating into the unburned zone at constant laminar speed  $S_L$  relative to the local fluid element. This interface propaga-

sion problem is formally equivalent to an initial value problem for a scalar field  $G(\vec{x}, t)$  governed by the evolution equation

$$\frac{\partial G}{\partial t} + \vec{v} \cdot \nabla G = S_L |\nabla G|. \quad (2)$$

where  $\vec{v}$  is the flow velocity. Each level surface of a scalar field governed by this equation evolves as a convected, propagating interface. In particular, the source term causes any level surface to propagate with a normal velocity  $S_L \vec{n}$  relative to the local fluid element, where  $\vec{n} = -\nabla G / |\nabla G|$  is the unit vector locally normal to the surface. In the earlier study (Menon and Kerstein, 1992), without heat release effects, all level surfaces of the  $G$ -field were considered flame surfaces. Thus, each simulation corresponded to a family of simulations parameterized by  $G_0$ . However, the symmetry that leads to this interpretation (see Menon and Kerstein, 1992) is broken if heat release is included. Thus, in this study, a prescribed level surface  $G_0 = 0.5$  is initially chosen to be the initial flame location, with all  $G < G_0$  as the premixed fuel and all  $G > G_0$  as the burnt product.

The flame surface evolution as represented by the  $G$ -equation is incorporated into the framework of Kerstein's linear-eddy model (Kerstein, 1988a, 1991a,b) of turbulent mixing. The implementation of this model in this context is described elsewhere (Menon and Kerstein, 1992) and, therefore, is only summarized here.

Linear-eddy modeling is a method for simulating molecular mixing on a one-dimensional domain embedded in a turbulent flow. The method involves two concurrent processes that govern the evolution of a scalar field  $G(x, t)$  on the computational domain. In the present formulation, the flame propagation process as represented by the scalar equation  $\partial G / \partial t = S_L |\nabla G|$  is solved using a finite-difference approach within a one-dimensional domain that may be interpreted as a statistical one-dimensional slice through a three-dimensional turbulent flame brush. Figure 2 shows schematically this interpretation. The level crossing of the prespecified  $G$ -level,  $G_0$ , within the computational domain then can be interpreted as the location of the flamelets. Note that, between successive flamelets, the burnt product and fuel regions alternate and half the distance between neighboring flamelets is the linear-eddy analog of the local radius of curvature. Thus, as the neighboring flames propagate to consume the fuel, the local radius of curvature decreases (or the curvature increases) in the fuel region. On the other hand, the radius of curvature increases in the region of burnt product. In addition, when thermal expansion is included, the burnt region expands thereby further decreasing the local curvature. These issues will be discussed below.

The extent of the computational domain is determined by the requirements of a particular simulation problem. For example, in the case without heat release, the computational domain was a length of  $L$ , where  $L$  is the integral length scale. This domain was sufficient since all levels of  $G$  contributed to the flame brush statistics. However, in the present case with heat release, only statistics from one  $G$ -level can be used. In addition, the computational domain needs to be large enough to encompass the flame brush that can become quite large due to thermal (volumetric) expansion. Various sizes of computational domain were investigated and it was determined that the domain size is directly dependent on the maximum flame temperature that is to be modeled. In the present study, the maximum flame temperature studied was ten times the fuel temperature. For this case, a domain size of  $15L$  was required.

As in previous formulations, the convective term is omitted in the flame propagation part because turbulent stirring is introduced by means of the second concurrent process. The second pro-

cess consists of a stochastic sequence of instantaneous, statistically independent "rearrangement events" that punctuate the deterministic flame propagation process. Each rearrangement event may be viewed as representing the effect of an individual eddy on the scalar field. Three randomly assigned quantities govern each event. These are the location and epoch (both chosen statistically independent and uniformly within the computational domain, representing spatially homogeneous turbulence) of the event and the size of the affected segment of the one-dimensional domain. To incorporate the physics of the turbulent flow-field microstructure, the segment size is chosen according to a probability distribution based on the Kolmogorov inertial-range cascade law relating frequency to eddy size. Thus, the ensemble of rearrangements during a simulated realization simulates the ensemble of eddies in inertial-range turbulence. More details of this model for turbulent stirring is given elsewhere (Menon and Kerstein, 1992; Kerstein, 1991a, 1991b).

In essence, the rearrangement process captures the key mechanistic features of turbulent stirring despite the temporally discrete representation of a continuous-time physical process. It has been demonstrated mathematically (Kerstein, 1991a, 1991b) that many intuitive notions based on continuum flow carry over to the rearrangement process.

### 3. IMPLEMENTATION OF THE MODEL

The computational domain represents a longitudinal line through the turbulent flame brush. The scalar  $G$  field is chosen initially to be  $G(x, 0) = x/L$  for a domain  $-\infty < x < \infty$ . This configuration is simulated on a finite domain  $[0, 15L]$ . The subsequent evolution of  $G(x, t)$  is governed by the flame propagation process, thermal expansion and the mapping process representing turbulent stirring. The physical interpretation is that the evolving level set determined by  $G(x, t) = G_0$  represents the simulated propagation of a turbulent flame brush.

A transient relaxation period is required for the initially flat flame to evolve until its steady-state flame structure is achieved. As the flame propagates into the fuel region, the effect of heat release has to be included. Thermal expansion is the key result of heat release and this expansion process is implemented to maintain volume conservation, as described below. Every time a cell containing premixed fuel (at  $T_{fuel}$ ) is consumed by the flame propagation the temperature will increase to  $T_{product}$ . Since the local pressure is assumed to remain constant, by virtue of the equation of state, the density (specific volume) of the product will decrease (increase) proportionally. Thus, to maintain mass conservation, the total number of burnt cells have to be increased. For example, if the heat release parameter  $\theta = T_{product}/T_{fuel} = 5$ , then the consumption of one fuel cell (where  $G < G_0$ ) will result in the creation of five burnt cells (with  $G > G_0$ ) behind the flame location. As the number of flamelets in the flow field increases, the thermal expansion algorithm will result in a large increase in the total number of cells in the domain. To keep the computations tractable, the number of cells in the domain is kept the same by truncating the resulting  $G$ -field near the right boundary, since, at that location all cells are burnt (by virtue of the initialization, see above) and no longer contributes to the statistics. An additional feature that needs to be taken into account in the heat release algorithm is that as the flame propagates into the fuel region, more and more of the cells in the computational domain contain only burnt product. If this propagation is allowed to continue, then eventually only burnt cells are left in the entire domain and the simulation has to be terminated. Therefore, to maintain continuous (a statistically stationary) burning, a criteria is imposed whereby, a region of length  $2L$  ahead of the first flamelet is permanently maintained as a region of cells containing unburnt fuel. This is achieved by ensuring that as the lead-

ing flamelet propagates towards the left boundary and is within  $2L$  from the boundary, a finite number of burnt cells are removed from the right boundary region and an equal number of unburnt cells are added from the left boundary.

The steady state is a balance of flamelet creation by rearrangement events and pairwise annihilation of flamelets due to laminar propagation. Statistics are gathered during this statistically steady evolution. Results presented here are based on runs in which about five large-eddy turnover times (based on the turnover time  $L/u'$ ) are allocated to transient relaxation, followed by a comparable interval of data compilation. This data-gathering interval is sufficient to discriminate the qualitative structural properties of the flame brush, and to estimate quantities like  $u_T$  and  $D$  with reasonable statistical precision, as discussed in the earlier study (Menon and Kerstein, 1992).

The computations indicate that several large-eddy turnover times are required for relaxation of initial transients. In experimental studies, it is often infeasible to achieve statistically steady propagation. This is an additional complicating factor with regard to comparison of measurements to the computed results presented here or, for that matter, to the postulated scalings. The model has an additional degree of flexibility in that it may also be used to characterize the transient for purposes of comparison to specific experiments. This aspect will be addressed elsewhere.

In the earlier study (Menon and Kerstein, 1992), the computational cell size and time step were chosen small enough so that further refinement did not affect the results. Thus, the spatial structure and the time evolution are fully resolved. This reflects a key advantage of the modeling approach. Namely, the restriction to one spatial dimension allows fully resolved simulation at higher Reynolds numbers than are accessible by other methods. For  $Re = 1000$ , the highest Reynolds number considered with no heat release, the computational domain contained up to  $2^{17}$  cells per integral scale (resolution requirements also depend on  $u'/S_L$ ), and 1000 time steps per large-eddy turnover time was employed in the finite-difference solution of the evolution equation for  $G$ .

For the present study, the computational domain is much larger than the integral length scale and a similar resolution would require  $2^{21}$  cells. This is computationally prohibitive. On the other hand, the earlier study (noted above) had shown that the results become statistically independent of the grid resolution when  $2^{15}$  cells were employed for a lower Reynolds number of 100. Therefore, in the present study, the computational domain contained  $2^{16}$  cells and only low Reynolds numbers of 50 and 100 have been investigated. The issue of grid resolution and grid independence of the computed results have been studied by comparing the heat release results obtained using  $2^{15}$  and  $2^{16}$  cells. Most of the key results were found to be relatively independent of the grid in the above range. However, this issue needs further investigation and will be addressed in more detail in a future study. In addition, higher Reynolds number flows need to be studied to investigate Re-scaling of the turbulent flame structure. These aspects will also be addressed in a future study.

#### 4. RESULTS AND DISCUSSION

The results discussed here were obtained by carrying out simulations for different choices of  $u'/S_L$ ,  $\theta$  and  $Re$ . The ratio  $u'/S_L$  was varied from 1 to 16, the heat release parameter,  $\theta$  varied from 1 to 10 for two Reynolds numbers of 50 and 100.

In the present model, the scaled turbulent flame speed  $u_T/S_L$  corresponds to the mean number of crossings of the given level  $G_0$ . The fractal properties are determined by using the usual box counting method. The computational domain is partitioned into "boxes",

each containing  $r$  cells. The number of size- $r$  boxes that are occupied by one or more flamelets, represented by crossings of a level  $G_0$ , are counted. This sum is adopted as the measure of the box occupancy,  $G$ . It has the useful feature that for  $r = 1$ , it is equivalent to the expression  $u_T/S_L$ . Therefore, a plot of box occupancy versus  $r$  will roll off at small  $r$  from a fractal scaling to a constant value equal to the scaled turbulent flame speed.

The latter property suggests a plotting format that compactly exhibits all scalings of interest. Since the plateau at small  $r$  corresponds to  $u_T/S_L$ , which is expected to scale as  $u'/S_L$  for large values of that parameter, a plot of  $\alpha S_L/u'$  should exhibit collapse of the plateau values at large  $u'/S_L$ . Likewise, since the transition from fractal scaling to the plateau should occur for  $r$  in the vicinity of the lower cutoff, scaling of  $r$  by the lower cutoff (in compatible units) should collapse the transition regions for different values of  $u'/S_L$ . Fractal scaling is indicated by a linear region on the log-log plot of the scaled quantities, with the fractal dimension  $D$  equal to  $2+s$ , where  $s$  is the absolute magnitude of the slope of the linear region. (Two is added to the negative of the slope because the computations simulate a one-dimensional cut through three-dimensional space.) If  $D$  is the same for all values of  $u'/S_L$ , and if the other scalings are obeyed exactly, the curves should collapse, except where affected by the outer cutoff. Incomplete collapse indicates departures from scaling behavior.

In the previous study of constant-density flame propagation (Menon and Kerstein, 1992), two alternative lower cutoffs were considered, the Kolmogorov scale  $L_K$  and the Gibson scale  $L_G = (u'/S_L)^{-3} L$ .  $L_G$  is the scale whose characteristic eddy velocity, based on inertial-range scaling, is equal to laminar flame speed  $S_L$ . It is thus the scale at which strain-induced interface wrinkling is balanced by the smoothing effect of flame propagation, analogous to cutoff scales defined for passive scalar diffusion. Refining that analogy,  $L_G$  is the propagation analog of the Obukhov-Corrsin cutoff scale  $L_C$  governing low- $Sc$  fluids (Lesieur, 1987). For  $Sc < 1$ , i.e.,  $D_M > \nu$ , where  $D_M$  is the molecular diffusivity and  $\nu$  is the kinematic viscosity, the diffusive cutoff  $L_C$  is greater than  $L_K$ , reflecting the fact that eddy diffusivity balancing  $D_M$  exceeds  $\nu$ , and hence corresponds to a length scale larger than  $L_K$ .

For diffusive transport with  $Sc > 1$ , there is no diffusivity balance in the inertial range. Balance is obtained in the viscous range at the Batchelor scale  $L_b$ , which obeys different scalings than  $L_K$ . Analogously, there is a scaling crossover for the flame propagation problem based on the velocity ratio  $V = S_L/u_K$ , where  $u_K$  is the Kolmogorov velocity  $\nu/L_K$ . Based on  $L_K = Re^{-3/4} L$  and  $Re = u' L/\nu$ , the velocity ratio  $V = Re^{1/4} (S_L/u')$ . Gibson scaling applies for  $V > 1$ . For  $V < 1$ , considerations analogous to the derivation of  $L_G$  are applicable. Namely, the balance scale  $L_*$  is determined by  $S_L = L_*/t_K$ , where  $t_K$  is the Kolmogorov time scale  $L_K^2/\nu$ . This gives the lower cutoff scaling  $L_* = Re^{-1/2} (S_L/u') L$  for  $V < 1$ .  $V$  is less than unity for all cases considered here, so this scaling is applicable.

$V < 1$  is the regime in which the flamelet picture of turbulent premixed flame propagation is invalid because the reaction zone thickness exceeds the Kolmogorov scale. (This follows from the estimate  $D_M/S_L$  for the reaction zone thickness, where  $D_M$  can be replaced by  $\nu$  because  $Sc$  and  $Pr$  are of order unity in gases.) Thus, application of a flamelet picture for  $V < 1$  is not literally correct. Nevertheless, consideration of this regime allows the demonstration of trends and features that should carry over to  $V > 1$ , except that the lower cutoff for  $V > 1$  is  $L_*$  rather than  $L_G$ .

The reason for the limitation to  $V < 1$  is that numerical implementation of the stirring mechanism becomes costly at high  $Re$ .  $Re$  greater than  $(u'/S_L)^4$  is required to obtain  $V > 1$ . It is important to consider a wide dynamic range of  $u'/S_L$  values in



order to determine parametric trends, and to restrict  $u'/S_L$  to values greater than unity in order to obtain multiple flamelets along the streamwise line. These requirements indicate that the Re requirements for a meaningful parametric study of the regime  $V > 1$  are prohibitive. By the same token, it is difficult to perform experimental studies in this regime, hence the lack of experimental confirmation of the Gibson scaling.

In the following, the results obtained in this study are discussed. Box occupancy results for  $Re = 100$  and without heat release are plotted using the afore mentioned scaled format, that is,  $\sigma S_L/u'$  is plotted versus the normalized box size  $r/L_u$  where  $L_u$  is an appropriately chosen length scale. In Figure 3a,  $L_u$  is the lower-cutoff Gibson scale  $L_G$  and in Figure 3b it is the Kolmogorov scale  $L_K$ . The plots indicate that  $u'/S_L = u'/S_L$  is obeyed over the entire range of  $u'/S_L$  values. It is important to note that the precision of the collapse of plateau values for high  $u'/S_L$  reflects the fact that each case was simulated with the identical sequence of rearrangement events, so case-to-case variability for given Re is due solely to case-to-case variation of  $S_L$ .

A similar result is obtained when heat release is considered. Figures 4a and 4b shows the results obtained for heat release parameter  $\theta = T_{products}/T_{fuel} = 8$ . Other values of  $\theta$  also showed similar results and therefore, are not shown. These results suggest that the linear scaling between the turbulent flame speed and  $u'$  is also obeyed when thermal expansion effects are included. This is in agreement with experimental data.

Figures 3 and 4 indicate that the collapse at the lower cutoff can occur with respect to either of the two alternate lower-cutoff scalings as  $u'/S_L$  increases. However, as noted above, Gibson scaling is valid only for values of  $u'/S_L$  for which  $L_K < L_G < L$ . Based on the definition of  $L_K$  and  $L_G$ , this implies  $1 < u'/S_L < Re^{1/4}$ . For  $Re = 100$ , and for the values of  $u'/S_L$  studied here, this condition is violated (i.e.,  $V < 1$ ). This implies a deviation from Gibson scaling before its onset is fully realized.

To demonstrate the relevance of the new viscous length scale  $L_v$  as a proper lower cutoff scale for cases with  $V < 1$ , Figure 5 presents the data shown in Figure 4 replotted with the box size normalized by  $L_v$ . Figure 5a and 5b shows the results for  $Re = 50$  and 100, respectively, and, Figure 5c shows the results for  $Re = 50$  and 100 plotted together. Clearly, the new inner cutoff length scale  $L_v$  collapses the data for various  $u'/S_L$  for  $V < 1$ . The data for no heat release case (Figure 3) also collapses in like manner (not shown). The only deviation with this scaling occurs near the outer cutoff. The implication here is that when the fractal dimension is computed for each curve by computing the slope at the inflection point (see below), then the computed dependence of the fractal dimension  $D$  on  $u'/S_L$  is primarily a result of the variation of the outer cutoff with  $u'/S_L$ .

These points were raised earlier (Menon and Kerstein, 1992) where it was noted that the apparent value of  $D$  decreases as the dynamics range decreases. The lower the dynamic range, the lower the value of  $s$  (slope) at which the influence of the transition to the outer cutoff begins to be felt. The interface area per unit volume  $A_f/A_v = (l_v/l_i)^{D-2}$  (equation 1) can increase as  $u'$  increases by means of an increase in the fractal dimension  $D$  and/or an increase in the dynamic range of the fractal regime ( $l_v/l_i$ ). The results obtained here and in the earlier study suggests that the apparent fractal dimension inferred from data may be lower than the underlying physical process if the dynamic range of the fractal regime is insufficient for the fractal scaling to be fully realized.

This behavior is evident in Figures 6a and 6b which shows respectively, the computed fractal dimension for no heat release and heat release cases. These results are qualitatively consistent with

experimental observation of the dependence of  $D$  on  $u'/S_L$  (e.g., North and Santavirta, 1990). The no heat release case (Figure 6a) shows that  $D$  increases with  $u'/S_L$  and asymptotes to a value of around 2.75 which is significantly higher than the experimentally obtained value of about 2.4. Interestingly enough, with heat release (Figure 6b), the computed value of  $D$  is lower than the no heat release case and appears to reach an asymptotic value that is weakly dependent on the amount of heat release. For the largest heat release parameter  $\theta = 10$ , the asymptotic value of  $D$  is around 2.55 which is still larger than the experimental value. However, the fact that thermal expansion effects reduces the computed value of  $D$  indicates that the present heat release model is performing as expected. There are several factors that may be contributing to the observed discrepancy. First, experimental values are based on a linear fit to finite subranges of the fractal regime giving values of  $D$  that would be lower than would be obtained using the inflection-point slope method used here (see Menon and Kerstein, 1992, for further details on this aspect). Second, physical effects such as stretch effects have been omitted here, and this may effect the value of  $D$  computed from the simulation data. In addition, there are other possible reasons for the disagreement, such as the effect of grid resolution and computational domain (these issues are currently under investigation).

The simulation data can be used to obtain additional statistics on the structure of the turbulent flame brush. For example, Figure 7a shows the total number of flamelets present in the computational domain as a function of time. Around 1000 snapshots of the flow field and the flame statistics were collected during the simulation and analyzed. Figure 7b shows the mean value of the number of flamelets in the domain for different values of the heat release parameter,  $\theta$  as a function of  $u'/S_L$ . The results show that as  $u'/S_L$  increases, the number of flamelets also increases. This is consistent with an increase in the wrinkling of the flame brush with turbulence intensity and is consistent with experimental observations. There appears to be only a weak dependence on the heat release.

Figure 8a and 8b shows respectively, the time-variation of the flame brush thickness and its mean value. The flame brush width is computed by computing the distance between the two extreme flamelets (the leading and the trailing flamelets) in the computational domain. Instantaneously (Figure 8a), the flame brush can become nearly as large as the computational domain; however, in the mean (Figure 8b), the flame brush is around 2.5 times the integral length scale. The flame brush size also increases with  $u'/S_L$  and with heat release. This is physically consistent with the fact that as turbulence level increases, more flamelets are present (Figure 7) resulting in more fuel consumption and thermal expansion. This increases the flame brush width.

As noted earlier, the distance between two adjacent flamelets is the linear-eddy analog of half the radius of curvature. The instantaneous data on the radii of curvature in the computational domain gives a measure of the wrinkling of the flame brush. The various radii of curvature in the computational domain was collected and a probability density function (pdf) formed for the various cases. This result is shown in Figures 9a and 9b. Figure 9a shows the pdf for various  $u'/S_L$  for a fixed heat release parameter and Figure 9b shows the pdf for a fixed  $u'/S_L$  but for various heat release parameter. These results are consistent with the observation that with increasing  $u'/S_L$ , the flame brush is highly wrinkled resulting in a higher probability for smaller radii of curvatures (Figure 9a). On the other hand, larger heat release increases the thermal expansion effect thereby increasing the radius of curvature. This result is a higher probability for flames with larger radius of curvature with increasing heat release parameter (Figure 9b).

The distance of each flamelet from the instantaneous flame center was also determined throughout the simulation and a pdf (normalized by the computational domain) of the flamelets location relative to the center was computed. Figures 10a and 10b shows the pdf plotted against the distance normalized by the integral length scale. In general, the pdf is nearly symmetric and the distance between the leading-edge flamelet and the trailing-edge flamelet is a significant portion of the computational domain. However, as noted earlier in Figure 8, the probability drops significantly very quickly and the majority of the flamelets are typically located within a 2-5L range around the flame center. This region is not significantly changed with the changes in either  $u'/S_L$  or  $T_{product}/T_{fuel}$ .

To determine the extent of burning, a progress variable is defined which is defined equal to unity if a cell is burnt and zero if a cell contains pure fuel. Throughout the simulation, each cell in the computational domain is checked, relative to the instantaneous flame brush center, and, if it is burnt, the cumulative value of the progress variable is increased by unity. At the end of the simulation, the summed value is normalized by the total number of snapshots recorded and a pdf computed for this progress variable. Figure 10 shows this pdf plotted versus the distance relative to flame center normalized by the integral length  $L$ . There is a very high probability that the cells in the vicinity of the flame center will always contain burnt product and this probability increases with  $u'/S_L$ . Away from the flame center probability that a cell contains burnt product decreases, however, this decrease is slower when the flame is highly wrinkled. This may be understood by noting that as flame wrinkles, there are more regions in the flame brush where fuel is consumed and as a result of thermal expansion, more and more burnt cells are created.

## 6. CONCLUSIONS

In this paper, a computational model has been demonstrated that can be used to determine the characteristic properties of premixed flame propagation in a turbulent flow field. The flame structure and its propagation rate scalings proposed on the basis of inertial range scaling concepts are mutually realizable and consistent within a single modeling framework. The effect of thermal expansion has been shown to result in trends that are consistent with experimental observations. It has been shown on the basis of a new inner cutoff scaling length, that the apparent dependence of the fractal dimension on  $u'/S_L$  is due to the variation on the outer cutoff with  $u'/S_L$ . This further supports the earlier contention that the experimentally observed decrease in  $D$  at low  $u'/S_L$  reflects an insufficient dynamic range to fully resolve the fractal regime rather than an intrinsic dependence of  $D$  on  $u'/S_L$ . It is not yet clear whether definitive tests of the proposed scalings are achievable with present day technology.

## ACKNOWLEDGEMENTS

This work was supported by the Office of Naval Research under Contract No. N00014-92-J-403, and by the Division of Chemical Sciences, Office of Basic Energy Sciences, U. S. Department of Energy.

## REFERENCES

Quader, O. (1990), "Turbulent Premixed Combustion Modeling using Fractal Geometry," *Twenty-Third Symposium (International) on Combustion*, The Combustion Institute, pp. 835.

Kerstein, A. R. (1988a), "Linear-Eddy Model of Turbulent Scalar Transport and Mixing," *Combustion Science and Technology*, Vol. 60, pp. 391-421.

Kerstein, A. R. (1988b), "Fractal Dimension of Turbulent Premixed Flames," *Combustion Science and Technology*, Vol. 60, pp. 441-445.

Kerstein, A. R. (1991a) "Fractal Dimension of Propagating Interfaces in Turbulence," *Phys. Rev. A*, Vol. 44, pp. 3633-3635.

Kerstein, A. R. (1991b) "Linear-eddy Modeling of Turbulent Transport. Part 5: Geometry of Scalar Interfaces," *Physics of Fluids A*, Vol. 3, pp. 1110-1114.

Kerstein, A. R. (1991c) "Linear-Eddy Modeling of Turbulent Transport. III: Mixing and Differential Molecular Diffusion in Round Jets," *J. Fluid Mech.* hi, Vol. 231, pp. 361.

Lesieur, M. (1987) "Turbulence in Fluids," Martinus Nijhoff Publishers, Boston.

Menon, S. and Kerstein, A. R. (1992), "Stochastic Simulation of the Structure and Propagation Rate of Turbulent Premixed Flames," *24th Symposium (Intn.) on Combustion*, The Combustion Institute, pp. 443-450.

North, G. L., and Santaviceca, D. A. (1990) "The Fractal Nature of Premixed Turbulent Flames," *Combustion Science and Technology*, Vol. 72, pp. 215-223.

Peters, N. (1986) "Laminar Flamelet Concepts in Turbulent Combustion," *Twenty-First Symposium (International) on Combustion*, The Combustion Institute, pp. 1231-1238.

Williams, F. A. (1985), "Combustion Theory", 2nd Ed., Benjamin-Cummings, Menlo Park.

Yakhot, V (1988a) "Propagation Velocity of Premixed Turbulent Flames," *Combustion Science and Technology*. Vol. 60, pp. 191-214.

Yakhot, V (1988b) "Scale Invariant Solutions of the Theory of Thin Turbulent Flame Propagation," *Combustion Science and and Technology*, Vol 62, pp. 127-129.

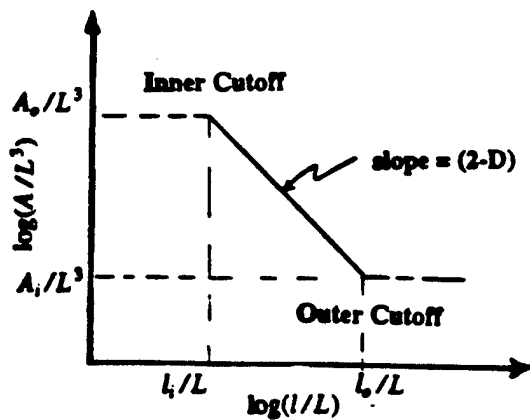


Figure 1. Theoretical representation of a surface exhibiting fractal character in a cubic volume of side  $L$

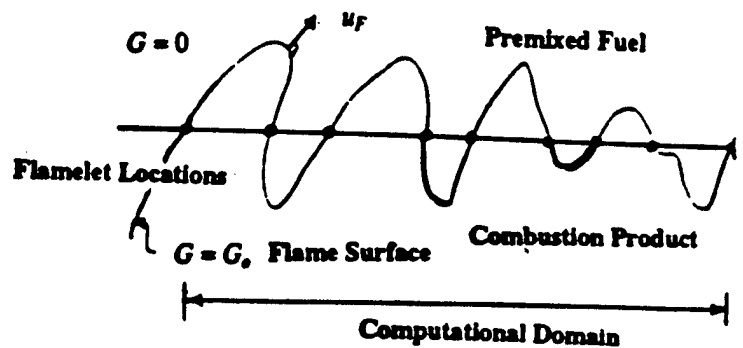


Figure 2. Schematic of a turbulent flame brush and the computational domain.

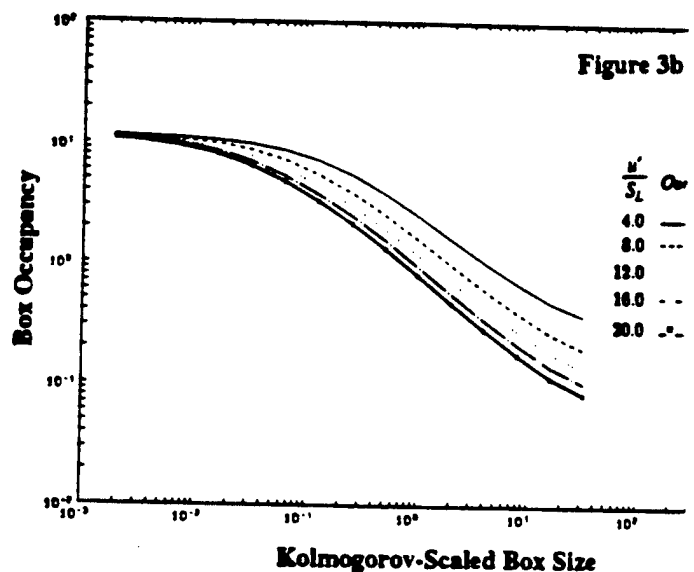
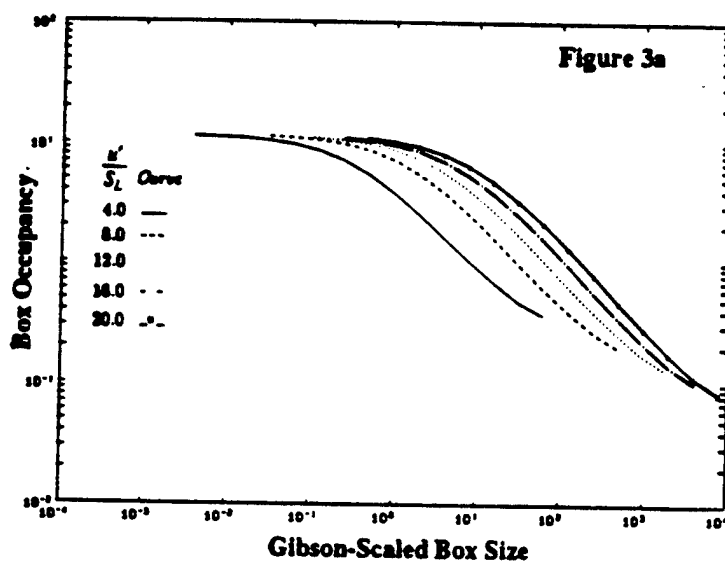


Figure 3. Box occupancy  $\sigma S_L / u'$  versus box size scaled by Gibson scale (Figure 3a) and by Kolmogorov scale (Figure 3b) for  $Re = 100$  for a range of  $u'/S_L$  values and no heat release.

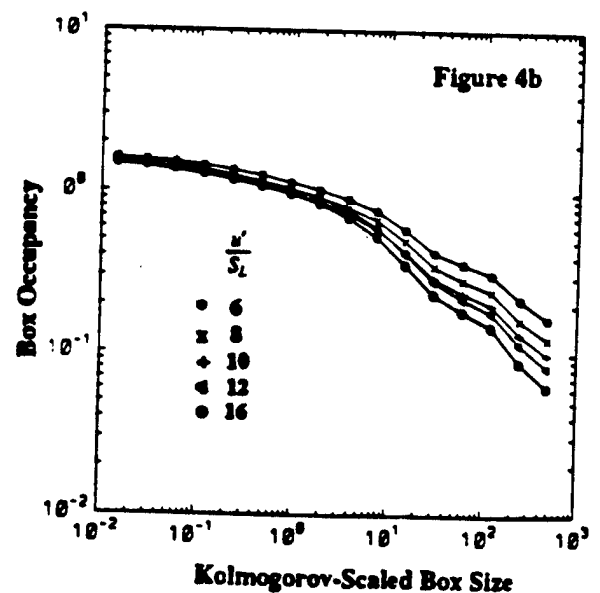
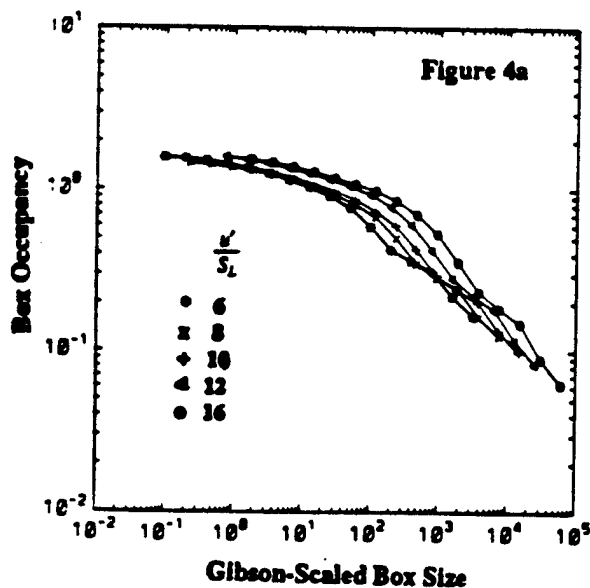


Figure 4. Box occupancy  $\sigma S_L / u'$  versus box size scaled by Gibson scale (Figure 4a) and by Kolmogorov scale (Figure 4b) for  $Re = 100$  for a range of  $u'/S_L$  values and heat release parameter  $T_{product}/T_{fuel} = 8$ .

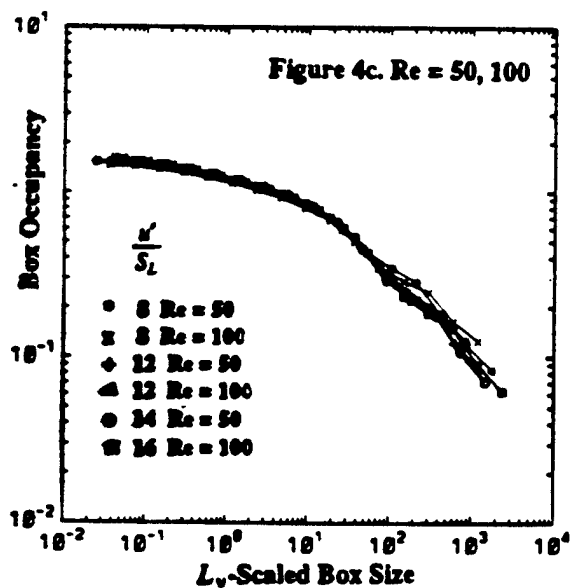
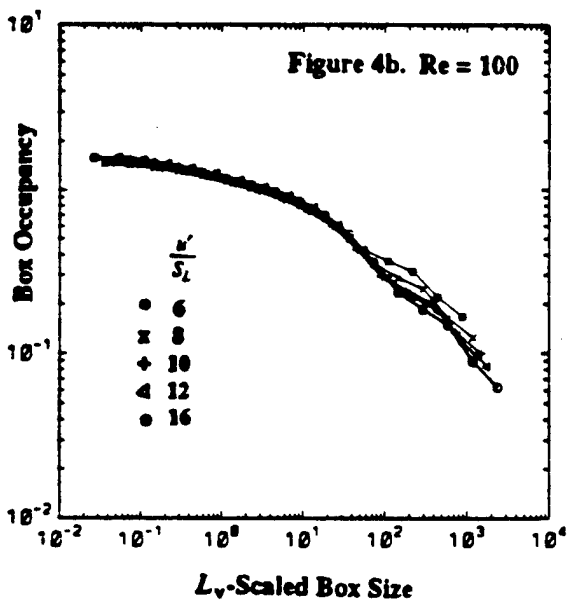
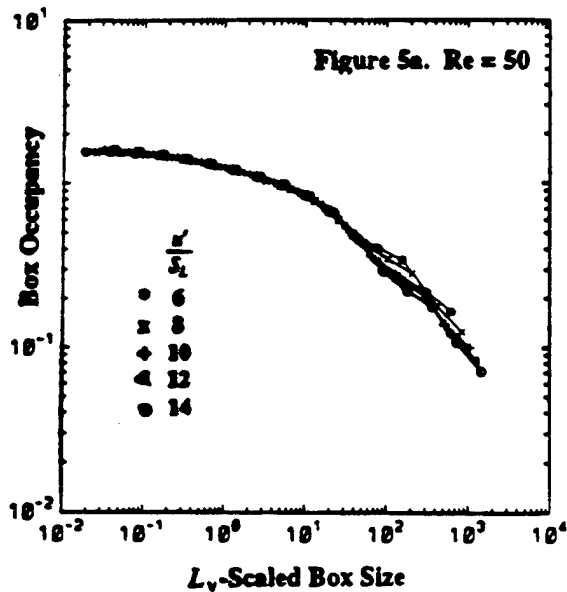


Figure 5. Box occupancy  $\sigma S_L/u'$  versus box size scaled by the new viscous scale  $L_v$  for a range of  $u'/S_L$  values and heat release parameter  $T_{product}/T_{fuel} = 8$ .

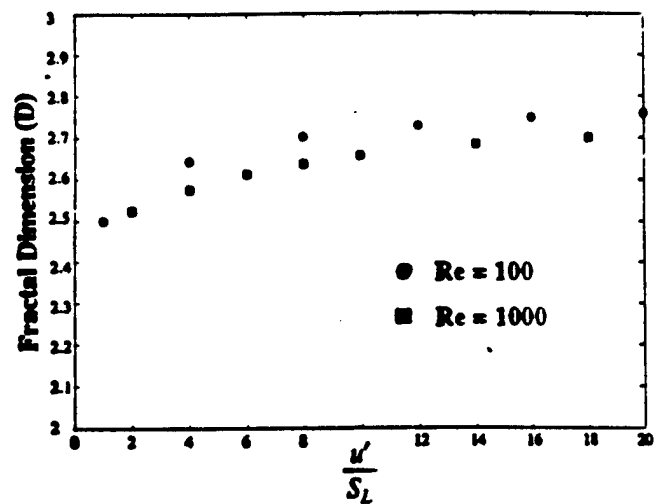


Figure 6a. No heat release case

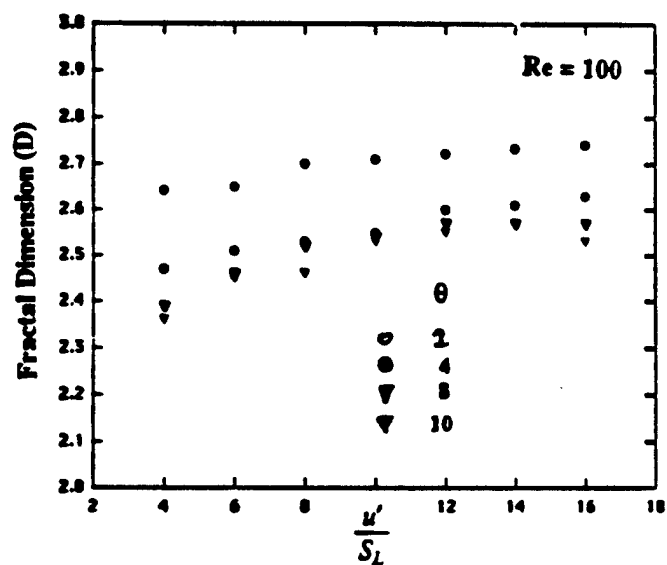


Figure 6b Heat release case

Figure 6. Fractal dimension  $D$  versus  $u'/S_L$  for various  $Re$  with and without heat release.

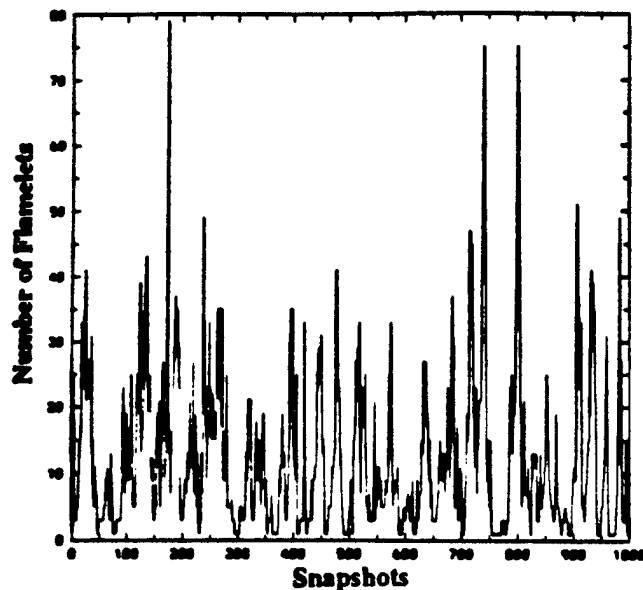


Figure 7a. Instantaneous variation

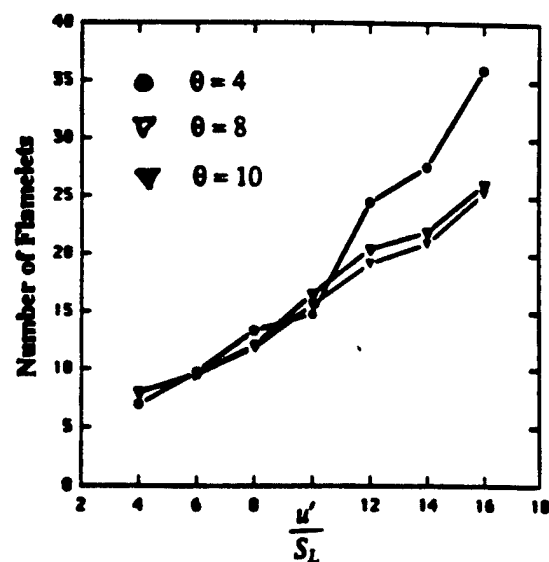


Figure 7b. Mean variation

Figure 7. The instantaneous and mean number of flamelets in the computational domain for  $Re = 100$  and for various values of  $u'/S_L$  and  $\theta$ .

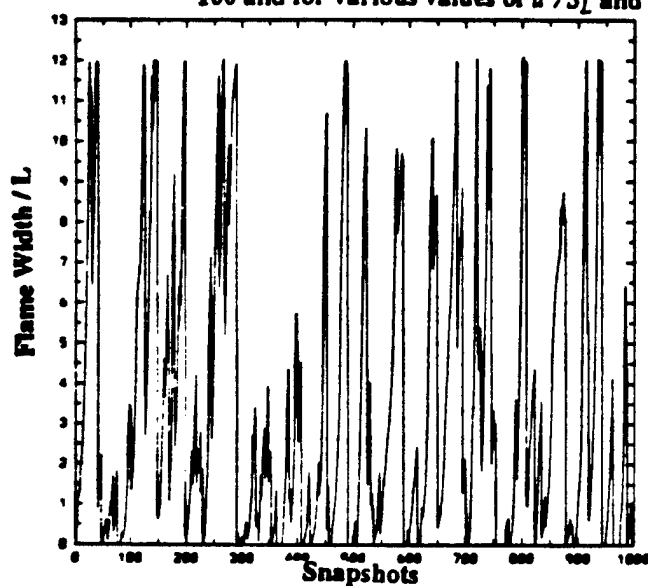


Figure 8a. Instantaneous variation

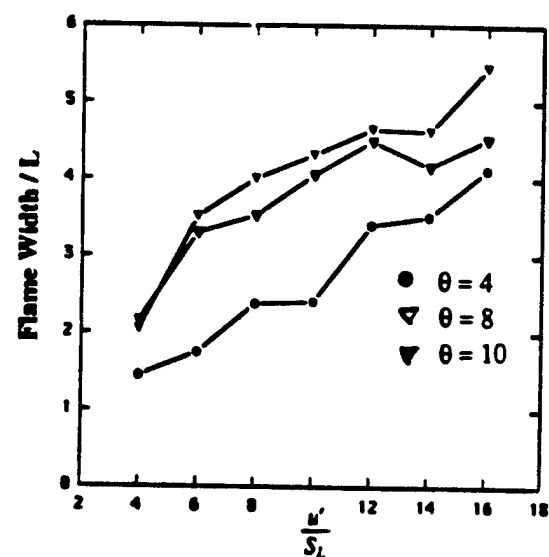


Figure 8b. Mean Variation

Figure 8. The instantaneous and mean width of the turbulent flame brush in the computational domain for  $Re = 100$  and for various values of  $u'/S_L$  and  $\theta$ .

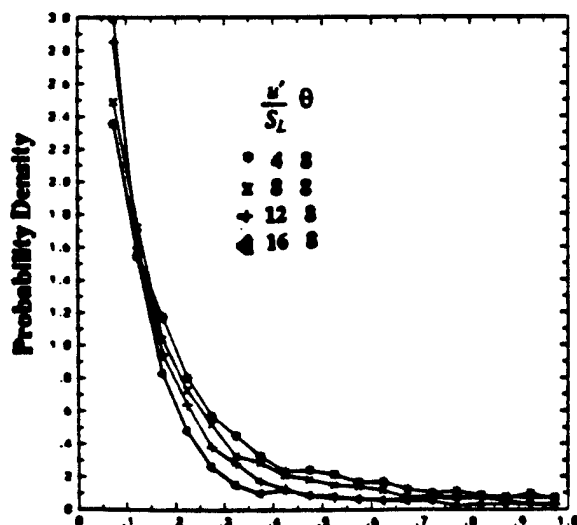


Figure 9a. Pdf as a function of  $u'/S_L$

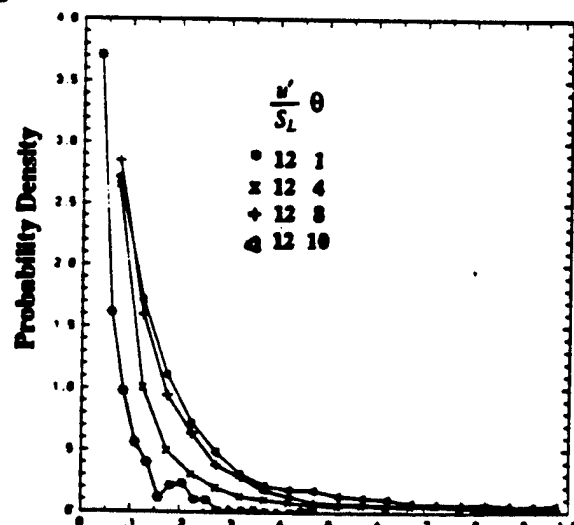


Figure 9b. Pdf as a function of  $\theta$

Figure 9. Probability density (pdf) of the radius of curvature of the flamelets.

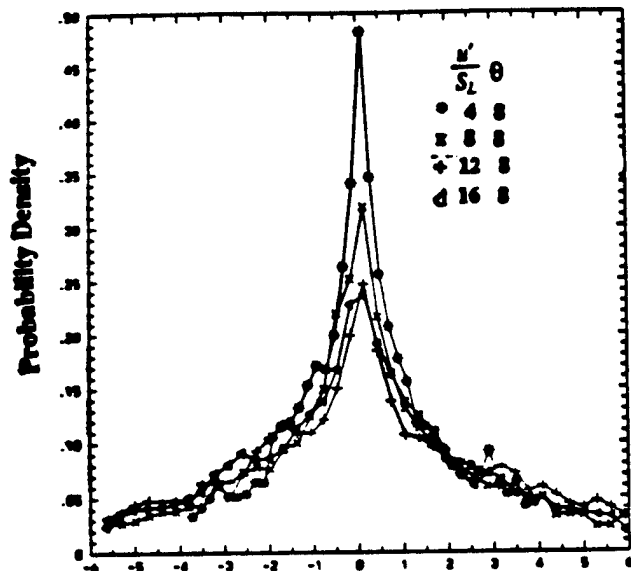


Figure 10a. Pdf as a function of  $u'/S_L$

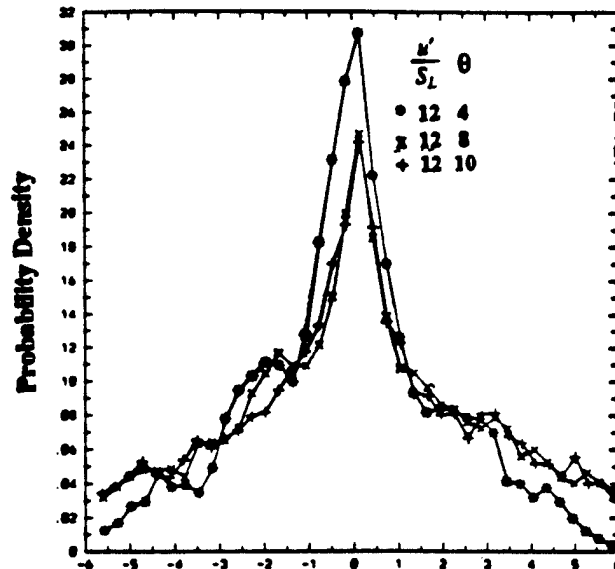


Figure 10b. Pdf as a function of  $\theta$

Figure 10. Probability density of the width of the turbulent flame brush for  $Re = 100$ . The pdf is normalized by the computational domain ( $15L$ ) and is plotted relative to the flame center. The flame width is normalized by the integral scale  $L$ .

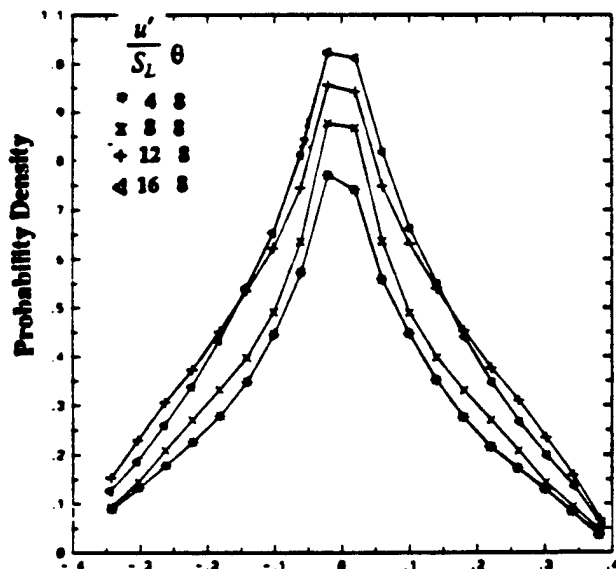


Figure 11a. Pdf as a function of  $u'/S_L$

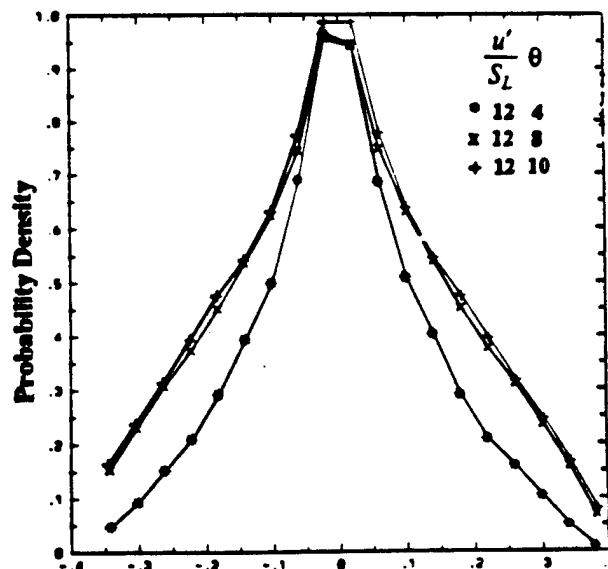


Figure 11b. Pdf as a function of  $\theta$

Figure 11. Probability density of the progress variable indicating the cells that contain only burnt product for  $Re = 100$ . The pdf of the location of the cell is plotted relative to the flame center and the distance is normalized by the integral scale  $L$ .



**AIAA-94-2391**

**THE STRUCTURE OF CONSTANT-  
PROPERTY PROPAGATING SURFACES IN A  
SPATIALLY EVOLVING TURBULENT FLOW**

**T. M. Smith**

**S. Menon**

**School of Aerospace Engineering**

**Georgia Institute of Technology**

**Atlanta, Georgia**

**25th AIAA Fluid Dynamics  
Conference**

**June 20-23, 1994 / Colorado Springs, CO**

**For permission to copy or republish, contact the American Institute of Aeronautics and Astronautics  
370 L'Enfant Promenade, S.W., Washington, D.C. 20024**

# THE STRUCTURE OF CONSTANT-PROPERTY PROPAGATING SURFACES IN A SPATIALLY EVOLVING TURBULENT FLOW

Thomas M. Smith\*

Suresh Menon\*\*

School of Aerospace Engineering  
Georgia Institute of Technology,  
Atlanta, Georgia 30332-0150

## Abstract

Large eddy simulations of spatially propagating constant-property surfaces in three-dimensional compressible turbulence have been conducted at relatively high Reynolds numbers. A thin flame model is used to simulate the propagating flame front and the propagation speed is estimated using the subgrid turbulence intensity. Analysis of the simulations show that various statistics, such as flame front shape factor, stretch effects, vorticity/strain rate, and strain rate/surface normal alignments, agree reasonably well with data from constant density, direct numerical simulations of passive scalar and premixed flame propagation in relatively simple flows (Pope et al., 1989, Ashurst et al. 1993, and Smith et al. 1994). The implications of this study are that the propagation of scalars in turbulent flows have general characteristics and that LES at high Reynolds numbers using fairly coarse grids are able to capture relevant physical characteristics of scalar propagation without the explicit knowledge of the small scale motion. A large dependence upon the spatial location at which the data are examined has been found for some statistical properties, unlike the temporal simulations. The probability density of the shape factor shows a decreased likelihood for cylindrical shaped flames moving downstream. The strain rate/flame normal alignment has been shown to transition from shear driven flow alignment to isotropic turbulence alignment in the down stream direction. Strain rate (in the plane of the flame) has been found to be highest near the step and decreasing in the downstream direction, the pdf becoming more symmetric similar to isotropic flows. The flame stretch pdf calculated apriori shows positive mean value at all locations examined and is highest near the corner of the step.

## 1. Introduction

A propagating surface is a reasonable representation of the flame sheet in premixed combustion when the flame thickness is much smaller than the smallest turbulent scale. The flame sheet is convected by the flow velocity while undergoing propagation normal to itself at the local propagation speed. The effect of turbulence is to wrinkle and stretch the propagating surface, thereby, changing its flame speed and possibly leading to local extinction. In constant density flows, a number of studies have been made aimed at characterizing the properties of the propagating surface such as its local curvature (which is a measure of local wrinkling) and its relation to the strain and vorticity fields in the turbulent flow. In temporally evolving flows, such as, isotropic and shear driven turbulence, Ashurst et al. (1987) showed that the vorticity vector tends to align itself in the direction of the intermediate strain rate even if the strain rate is compressive while the normal to the propagating surface aligns itself in the most compressive strain rate direction. Alignment of the surface normal with the most compressive strain rate implies that the surface is undergoing extension most of the time, and if this extension reaches a critical value for a long enough period of time, the flame extinguishes. Further, Ashurst et al. (1993) showed that the most likely shape of the propagating surface is cylindrical in such flows and analysis of the alignment of the surface show that it is a direct result of the modification of the propagating surface by the local vortex structure. In a related study, Smith et al. (1994) showed that similar results are obtained both in forced and decaying isotropic turbulence and in temporally evolving mixing layers. The implication of these results is that as vortices undergo stretching and the core becomes intense, the constant property surface tends to wrap around on the outside of the vortex core.

The relationship between the curvature and the strain field in the plane of the flame provides information about the effect of stretch (which is the combination of strain and curvature) on the propagating surface. What role flame stretch has in quenching the flame is an

\* Graduate Research Assistant, Student Member AIAA.

\*\* Associate Professor, Member AIAA.



important question still being addressed by the literature. It is known that the Lewis number and flame stretch effects can modify the laminar flame speed, and in severe cases, stretch can cause extinction. Curvature and strain rate affect flame propagation differently. Locally, curvature correlates with flame speed for diffusional neutral mixtures (Lewis number=1), however, the curvature is nearly symmetric in isotropic turbulence and therefore integrates to zero. Experiments have shown that curvature can increase the local laminar flame speed by a factor of 6.25 (Echekki and Mungal, 1990). Globally, the spatial average flame speed correlates with the tangential strain rate (Rutland and Trounev, 1993). At this point there is no agreed upon explanation of how flame stretch extinguishes the flame. Since flame stretch and Lewis number determine the laminar flame speed and have been shown to play a direct role in premixed flame extinction, understanding the mechanism of flame extinction in turbulent flows must first include an understanding of flame stretch.

All the above noted studies of propagating surfaces were carried out for low Reynolds number, incompressible, temporally evolving flows using periodic domains and by employing direct numerical simulations (DNS). So far, it has not been determined how the propagating surface evolves when convected spatially as opposed to temporally in a turbulent shear flow. Furthermore, the correlations of the surface curvature with the vorticity field and the strain field in such flows have not yet been determined. These studies are of direct relevance for realistic turbulent flows and for combustion problems. These issues are investigated in this paper by employing large-eddy simulations (LES) of relatively high Reynolds number flows past a rearward facing step in a rectangular channel. Since LES attempts to resolve only scales of motion larger than the grid resolution, while modeling the unresolved scales using subgrid models, it has the potential for carrying out simulations of high Reynolds number flows provided a proper representation of the subgrid terms is available. Therefore, the effect of the choice of subgrid model on the statistics of the propagating surfaces is also investigated. Only cold flows are studied here; the effects of heat release will be discussed in a future paper. The effects of compressibility, such as gas expansion from heat release, have not been determined. In this study the Mach number in the region of interest is low and we do not believe that the results will be affected by compressibility.

## 2. Simulation Model

What follows is a description of the methodology used to perform LES of a constant property surface propagating in spatially evolving turbulence.

### 2.1 Equations of LES

The Navier-Stokes equations describing the continuity of mass, momentum and total energy are given by:

$$\frac{\partial \rho}{\partial t} + \frac{\partial \rho u_i}{\partial x_i} = 0 \quad (1a)$$

$$\frac{\partial \rho u_i}{\partial t} + \frac{\partial}{\partial x_j} [\rho u_i u_j + p \delta_{ij} - \tau_{ij}] = 0 \quad (1b)$$

$$\frac{\partial \rho E}{\partial t} + \frac{\partial}{\partial x_i} [(\rho E + p) u_i + q_i - u_j \tau_{ij}] = 0 \quad (1c)$$

with the supplementary equations given by the equation of state,  $p = \rho RT$  and,

$$\tau_{ij} = \mu \left( \frac{\partial u_i}{\partial x_j} + \frac{\partial u_j}{\partial x_i} \right) - \frac{2}{3} \mu \frac{\partial u_k}{\partial x_k} \delta_{ij} \quad (1d)$$

and

$$\frac{\partial q_i}{\partial x_i} = -\lambda \frac{\partial T}{\partial x_i} \quad (1e)$$

In the above equations,  $\rho$  is the density,  $E$  is the total energy per unit mass,  $p$  is the pressure,  $u_i$  ( $i=1,3$ ) is the velocity components,  $\mu$  is the molecular viscosity coefficient,  $\lambda = C_p \mu / \text{Pr}$  is the thermal conductivity, and  $C_p$  is the specific heat at constant pressure.

In LES, the flow variables are decomposed into the resolved scale and subgrid scale components. The large scales are computed explicitly while the effects of the subgrid scales on the large scales are modeled. The large scales contain most of the energy and the small scales primarily dissipate energy transferred from the large scales. Dynamics of large scale motion is dictated by the geometry of the flow and the Reynolds number, while the small scale motion is relatively unaffected by the geometry except near the wall. The length scales and times scales are small compared to the large scales and thus, the small scales adjust faster and are more isotropic than the large scales. These concepts are used to develop subgrid models.

Following Erlebacher et al. (1987), the flow variables are decomposed into the resolved (supergrid scale) and unresolved (subgrid scale) components:

$$f = \bar{f} + f'' \quad (2)$$

The Favre average variable is defined as

$$\bar{f} = \frac{\overline{\rho f}}{\bar{\rho}} \quad (3)$$

where the tilde represents Favre average and the overbar represents a spatial filtering which is defined as

$$\overline{\rho f} = \int_D \rho f(\bar{x}) G(\bar{x} - \bar{x}', \Delta) d^3 x' \quad (4)$$

where  $D$  is the domain of the flow and  $\Delta$  is a characteristic grid size. The filtering operation is normalized by requiring that

$$\int_D G(\bar{x} - \bar{x}', \Delta) d^3 x' = 1. \quad (5)$$

Filtering reduces the high frequency content of the flow variables, separating the resolved scale component from the subgrid scales. In this study, a box filter is employed which is appropriate for finite volume schemes. Contrary to the more traditional Favre temporal averaging,  $\tilde{f} \neq \bar{f}$  and in general,  $\tilde{f}'' \neq 0$ . Applying the filtering to the Navier-Stokes equations results in

$$\frac{\partial \bar{\rho}}{\partial t} + \frac{\partial \bar{\rho} \tilde{u}_i}{\partial x_i} = 0 \quad (6a)$$

$$\frac{\partial \bar{\rho} \tilde{u}_i}{\partial t} + \frac{\partial}{\partial x_j} [\bar{\rho} \tilde{u}_i \tilde{u}_j + \bar{p} \delta_{ij} - \bar{\tau}_{ij}] + \frac{\partial \tau_{ij}^{sgs}}{\partial x_j} = 0 \quad (6b)$$

$$\frac{\partial \bar{\rho} \tilde{E}}{\partial t} + \frac{\partial}{\partial x_i} [(\bar{\rho} \tilde{E} + \bar{p}) \tilde{u}_i + \bar{q}_i - \tilde{u}_j \bar{\tau}_{ij}] + \frac{\partial H_i^{sgs}}{\partial x_i} + \frac{\partial \sigma_{ij}^{sgs}}{\partial x_j} = 0 \quad (6c)$$

Here, the subgrid closure terms are given by;

$$\tau_{ij}^{sgs} = \bar{\rho} [\tilde{u}_i \tilde{u}_j - \tilde{u}_i \tilde{u}_j] \quad (6d)$$

$$H_i^{sgs} = \bar{\rho} [\tilde{E} \tilde{u}_i - \tilde{E} \tilde{u}_i] + [\overline{p u_i} - \bar{p} \tilde{u}_i] \quad (6e)$$

$$\sigma_{ij}^{sgs} = [\overline{u_j \tau_{ij}} - \tilde{u}_j \bar{\tau}_{ij}]. \quad (6f)$$

The pressure is determined from

$$\bar{p} = \bar{\rho} R \bar{T} \quad (6g)$$

and the filtered total energy per unit volume is given by

$$\bar{\rho} \tilde{E} = \bar{\rho} \tilde{e} + \frac{1}{2} \bar{\rho} \tilde{u}_i \tilde{u}_i + \frac{1}{2} \bar{\rho} [\tilde{u}_i \tilde{u}_i - \tilde{u}_i \tilde{u}_i]. \quad (6h)$$

In order to solve this system of equations, models must be found for the subgrid terms  $\tau_{ij}^{sgs}$ ,  $H_i^{sgs}$ , and  $\sigma_{ij}^{sgs}$ . In addition, it is necessary to obtain the subgrid turbulence intensity to evaluate the flame speed model (which is

discussed in the next section). Subgrid models for compressible flows are still relatively new (Erlebacher et al. 1987, Squires and Zeman 1990, and Moin et al. 1991) and no best choice exists. In this study, we employ the one equation model for the subgrid kinetic energy proposed by Menon (1991). The equation is given by

$$\frac{\partial \bar{\rho} k}{\partial t} + \frac{\partial (\bar{\rho} \tilde{u}_i k)}{\partial x_i} = P_k - D_k + \frac{\partial}{\partial x_i} \left( \bar{\rho} \nu_i \frac{\partial k}{\partial x_i} \right). \quad (7a)$$

Here,  $k$  is the resolved subgrid kinetic energy, and the subgrid turbulence intensity is related by  $u' = \sqrt{2k}$ .  $P_k$  and  $D_k$  are the rate of production and dissipation of subgrid kinetic energy, respectively. In this model, the assumption that production and dissipation balance has been relaxed. The formulation neglects the pressure dilatation term that appears in the original exact  $k$ -equation for two reasons. First, it is still unclear how to model the pressure dilatation in terms of the resolved flow field variables, and second, at low fluctuating Mach numbers, its influence may be negligible. The production is modeled as:

$$P_k = C_k \tau_{ij}^{sgs} \frac{\partial \tilde{u}_i}{\partial x_j} \quad (7b)$$

and the dissipation has the form

$$D_k = C_\epsilon \bar{\rho} \frac{k^{3/2}}{\Delta_\epsilon} \quad (7c)$$

where  $\Delta_\epsilon$  is a characteristic grid size and  $\nu_i$  is the subgrid eddy viscosity given by

$$\nu_i = C_\nu k^{1/2} \Delta_\epsilon. \quad (7d)$$

The three constants appearing in the above equations have been prescribed as:

$$C_k = 1.0, C_\epsilon = 0.916, C_\nu = 0.0854.$$

A new dynamic  $k$ -equation model is being studied as a possible replacement to this modeling procedure. The dynamic modeling approach solves for the coefficients through the use of a double filter operation, similar to that used by Germano et al. (1991). In incompressible homogeneous isotropic turbulence, the dynamic coefficient model approach has been shown to perform better than the constant coefficient model, (Menon and Yeung, 1994). In the present study, the focus is not on optimization of the turbulence model, instead, this choice was made in order to provide a reasonable estimate of the subgrid turbulence intensity required to predict the turbulent flame speed. However, a rigorous analysis is needed to properly evaluate the model.

The  $k$ -equation is solved simultaneously with the rest of the flow equations. With  $k$  and  $\nu_t$  determined, the subgrid closure models are evaluated as:

$$\tau_{ij}^{ss} = -2\bar{\rho}\nu_t \left( \tilde{S}_{ij} - \frac{1}{3} \tilde{S}_{kk} \delta_{ij} \right) \quad (8a)$$

where

$$\tilde{S}_{ij} = \frac{1}{2} \left( \frac{\partial \tilde{u}_i}{\partial x_j} + \frac{\partial \tilde{u}_j}{\partial x_i} \right)$$

is the resolved scale stress tensor.  $H_i^{ss}$  is given by

$$H_i^{ss} = -C_e \bar{\rho} \nu_t \frac{\partial \tilde{H}}{\partial x_i} = -C_e \bar{\rho} \nu_t \left( C_p \frac{\partial \tilde{T}}{\partial x_i} + \tilde{u}_j \frac{\partial \tilde{u}_j}{\partial x_i} \right) \quad (8b)$$

and  $C_e = 1/\text{Pr}_t$ .  $\text{Pr}_t$  is the turbulent Prandtl number and  $\sigma_{ij}^{ss}$  is modeled by:

$$\sigma_{ij}^{ss} = \tilde{u}_j \tau_{ij}^{ss} \quad (8c)$$

It should be noted that third order correlations arise as a result of this modeling approach and are neglected here. Even though a stretched grid is used to cluster cells near the walls, it is necessary to apply explicit wall damping in order to properly model the subgrid kinetic energy behavior in the near wall regions of the flow. We employ Van Driest damping similar to that used by Piomelli et al. (1988)

$$\Delta_s = \left[ 1 - \exp(-y^{+3} / A^{+3}) \right]^{1/2} (\Delta_x \Delta_y \Delta_z)^{1/3} \quad (9)$$

where  $(\Delta_x \Delta_y \Delta_z)^{1/3}$  is the characteristic grid size based upon the local cell volume,  $A^+ = 26$ ,  $y^+ = y u_\tau / \nu$ , and  $u_\tau$  is the friction velocity.

## 2.2 Flame Propagation Model

To simulate the propagating surface, the thin-flame model of Kerstein et al. (1988) is used in which a progress variable  $G$  is defined that is governed by the equation (Kerstein et al., 1988 and Menon, 1991):

$$\frac{\partial G}{\partial t} + \mathbf{u} \cdot \nabla G = -u_F |\nabla G| + \frac{\nu_L}{C_G} \nabla^2 G \quad (10)$$

where  $\mathbf{u}$  is the fluid velocity and  $u_F$  is the local propagation speed. This equation is solved simultaneously with the LES equations. This equation describes the convection of a level surface, described by  $G = \text{constant}$ ,

by the fluid velocity while simultaneously undergoing propagation normal to itself at a speed  $u_F$ . In the flow field, the value of  $G$  is in the range  $[0,1]$  and in flame front modeling,  $G$  exhibits a step function like-behavior, separating the burnt region from the unburnt region.  $G$  is normally assigned the value of unity in the unburnt region and zero in the burnt region with the thin flame identified by a fixed value of  $G$  in the range  $[0,1]$ . In the present case, the same assignment of the  $G$ -field is indicated; however, since no heat release is included, any value of  $G = \text{constant}$  can be used to identify the flame front. Thus, in the present case, the physical interpretation is that an evolving  $G$ -level for any level  $G$  represents the simulated propagation of the constant property surface of that level. Thus, statistics from all values of  $G = \text{constant}$  can be combined; in effect, each simulation corresponds to a family of simulations parameterized by  $G$ .

The second term on the right hand side of equation (10) does not appear in the original equation, however it was added in order reduce the number of false minima from occurring in the flow. A false minima is not physically meaningful and results from a lack of resolution of the scalar. Ashurst (1993) and Smith et al. (1994) both added a similar term to the equation in their simulations of isotropic turbulence. The constant  $C_G = .25$  was used in all simulations reported here.

In LES of premixed combustion,  $u_F$  is considered the turbulent flame speed  $u_t$  averaged over a characteristic volume. The turbulent flame speed is not known explicitly and must be modeled. We employ the RNG model of Yakhot (1988):

$$\frac{u_t}{S_L} = \exp \left[ \frac{(u'/S_L)^2}{(u_t/S_L)^2} \right] \quad (11)$$

Yakhot (1988) found that this expression correlates quite well with various experimental observations. The laminar flame speed  $S_L$  contains information about the chemical kinetics and molecular diffusion and, once the local subgrid turbulence intensity is determined, equation (11) can be used to find  $u_F$  for a given fuel mixture.

The numerical method solves the unsteady, three-dimensional compressible filtered Navier-Stokes equations, the one-equation subgrid model, and the flame propagation model using a finite-volume scheme based on the unsplit explicit MacCormack predictor-corrector method. The scheme is formally second-order accurate in space and time. Details of the algorithm are given elsewhere (Menon and Jou, 1991).

## 3. Results and Discussion

Two simulations have been carried out for a

rearward facing step in a rectangular channel with a choked downstream nozzle. Such a configuration is characteristic of ramjet dump combustors. At the ramjet inlet the total pressure and total temperature are specified and the transverse and spanwise components of the velocity are set to zero. One-dimensional characteristic equations are solved for the remaining flow variables. At the combustor supersonic nozzle exit, all flow variables are extrapolated. Symmetry conditions are imposed on the centerline and periodic conditions are imposed in the spanwise direction. Wall boundaries are no slip and adiabatic. Figure 1a shows the computational domain and Figure 1b shows the  $96 \times 48 \times 16$  grid used for these simulations. The simulations carried out correspond to an inlet Mach number of .32 and a Reynolds number based on step half height of 5000 and 50000. The average velocity in the chamber (between the step corner and beginning of the nozzle) is roughly half the inlet velocity and the Mach number is approximately .16. These conditions were chosen because both axisymmetric and two-dimensional LES for these conditions have been performed in the past. Thus, the current 3D LES data can be compared to these earlier 2D data, however no comparisons are made in this paper.

The shear layer separating from the step rolls up into spanwise coherent vortices due to shear layer instability. This is shown in figure 2a. These vortices undergo a pair/merging process as they propagate downstream and also undergo vortex stretching effects due to the 3D nature of the flow. Once the spanwise vortices have completed their roll up, secondary instability effects cause the formation of coherent streamwise vortices. These counter-rotating vortices form typically in the braid region between adjacent spanwise vortices and are highly coherent rod-like structures as shown in figure 2b. Secondary instability effects seen here are very similar to results obtained in low-Re DNS of temporal mixing layers (Metcalfe et al, 1987). Further downstream, vortex stretching effects break down the coherent spanwise structures. Interestingly, the streamwise vortices maintain their coherence, and the braid-like structures persist all the way into the choked nozzle. The acceleration in the nozzle further stretches these structures. Compression of the x-vortices near the step and near the diffuser show that these vortices start to orient more randomly as the diffuser is approached. This picture is highly reminiscent of the randomly oriented vortex-tubes seen in DNS of homogeneous isotropic turbulence (Smith et al., 1994).

The effect of this intense vorticity on the propagating scalar surface is to wrinkle the surface and as a result, the surface develops regions of high curvature. This is shown in figure 2c. The influence of both spanwise and streamwise vorticity can be seen on the curvature of the surface. This natural evolution of the flow and flame sheet structure do not occur in temporally simulations of mixing layers and isotropic homogeneous

turbulence.

Figure 3a shows a 2D plane of z-vorticity magnitude, and figure 3b, the subgrid kinetic energy, in the combustor region for the  $Re = 50000$  simulation. These figures are taken from the same snapshot as in the previous figures, 2a-c. A single  $G$  contour that is in the range  $.45 < G < .55$  is also plotted in the figures. These figures show how the curvature in the streamwise direction is changing. Initially, spanwise vorticity shed at the corner of the step is intense and creates a highly wrinkled flame. As the flame convects downstream, two effects are at work. First, is the propagation effect, due to the flame burning normal to itself at the local flame speed  $u_f$ , which causes negative curvature to decrease and positive curvature (concave to the fresh mixture) to increase. The second effect is due to the changing flow field. The reduction in z-vorticity allows the flame curvature to relax tending toward a planar shape in the  $z$  plane.

Figures 3c-e demonstrate how the x-vorticity influences the curvature of the flow. Counter-rotating vortices are shown along with the  $G$  contour in the same range as before. The flame is drawn up between two vortex cores and the curvature is greatly increased. In figure 3d, the propagation effect is seen by the positive curvature becoming larger than the negative curvature. Propagation by the flame, normal to itself, increases the possibility of pockets of fuel tearing away from the rest of the fresh mixture. Further downstream, the vorticity becomes more diffused and randomly oriented and the curvature of the flame sheet is in general smaller than in the near field region.

The subgrid kinetic energy contours, figures 3b, and 3f, are shown in order to qualitatively demonstrate the subgrid model behavior. The model predicts  $k$  to be large in the shear flow region and there also remain large regions where  $k$  is essentially zero. This variation in  $k$  combines with the vorticity to effect the curvature and overall flame propagation by the coupling of the local flame speed to the subgrid kinetic energy, equation (11).

In order to quantify observations made from the flow visualizations, probability densities (pdf's) have been calculated from a series of instantaneous snapshots. Each pdf is an ensemble of twenty snapshots at time intervals of roughly 1/3 of the flow through time, beginning after the flow field has reached a quasi stationary state. The spatial locations for the pdf's start a small distance downstream of the step corner and end at the point where the convergent nozzle begins. This region will be referred to as the entire domain of interest in the following discussions. All statistics have been volume weighted due to the fact that cell volumes vary greatly over the domain of interest. Volume weighting simply means that equal cell volumes

contribute equally to the statistical quantities.

One measure of the structural shape of the surface is the ratio of the smaller principle radius of curvature to the larger one. The radii of curvature of the scalar are determined from the eigenvalues of the curvature tensor (Ashurst, 1993):

$$h_i = -\frac{\partial^2 G}{\partial x_i \partial x_j} \frac{1}{g} + \frac{1}{g^3} \sum_{k=1}^3 \frac{\partial G}{\partial x_i} \frac{\partial G}{\partial x_k} \frac{\partial^2 G}{\partial x_j \partial x_k} \quad (12)$$

where  $g = |\nabla G|$ . This nine element tensor has two real eigenvalues  $h_1$  and  $h_2$  and one eigenvalue equal to zero. The ratio of the smaller radius divided by the larger, hereafter referred to as the shape factor is bounded by  $\pm 1$ . Pope et al. (1989) used this definition to determine the shape of material surfaces in isotropic turbulence. The value -1 corresponds to a saddle point, 0 corresponds to cylindrical and +1 to spherical. The probability density of the shape factor from each of the twenty realizations, encompassing the entire combustion chamber and over a range of  $G$ ,  $.2 \leq G \leq .8$ , was calculated and an ensemble pdf was obtained. Figure 4a shows this pdf. The maximum occurs very near zero indicating a high probability of cylindrical shapes with vanishing probability for spherical or saddle points. Data from incompressible direct simulations by Ashurst et al. (1993), Pope et al. (1989), and Smith et al. (1994), obtained earlier using simpler flow fields such as isotropic turbulence and temporally evolving mixing layers are also shown in this figure. There is very good agreement between all these widely different simulated flow fields indicating that even in the spatially evolving shear layer studied here, the probability density indicates that the propagating surface tends to be a cylindrical shaped surface. The shape factor also tells us that in general one radius of curvature is much larger than the other.

Figures 1a and b show that the curvature was dominated by the spanwise and streamwise vorticity and that these two components are interacting in such a way as to develop the streamwise vorticity while diminishing the spanwise component downstream. It was also shown that the curvature in the near field was higher than the curvature further downstream. For this reason it is reasonable to suspect that a spatial dependence of the shape factor of the propagating surface exists. This is the case and can be shown by plotting the probability density for different streamwise locations. In figure 4b the shape factor for the entire domain and at four streamwise locations, starting near the step and increasing in  $x$  by increments of twice the step length, has been plotted. The spatial probability densities include data from a single  $x$  plane only, from the same twenty snapshots used for the pdf of the entire domain of interest. The probability for cylindrical shape decreases in the downstream direction and increases for saddle point, while the probability for

spherical shape remains nearly zero. This seems to indicate that the ratio of curvatures (which equals the ratio of radii) is increasing in the downstream direction. From the  $Re = 5000$  simulation, not shown, the same prediction can be made.

The mean curvature is defined as  $\bar{C} = \frac{1}{2}(h_1 + h_2)$ . The mean curvature pdf for the entire domain and the four  $x$  locations is presented figure 5. In order to be consistent with published data, the negative of the mean curvature is plotted. The negative sign is due to the definition that curvature concave with respect to the unburnt fuel is positive. The data has been normalized by the Kolmogorov length scale. The pdf's are nearly symmetric having very small mean values, however, the mean value is decreasing in the downstream direction.

The cylindrical shape of the flame sheet is due to intense vorticity that wraps the flame around it, creating curvature and tangential strain in the plane of the flame. Ashurst et al. (1987) showed that the vorticity aligns with the intermediate principle strain rate while the normal to the flame aligns with the most compressive strain rate. The principle strain rate directions are the eigenvectors obtained from the strain rate tensor. The dot product of all three principle strain rate vectors with the vorticity vector shows a statistical tendency for alignment with the intermediate direction. Figure 6a shows the alignment for the data from incompressible DNS by Ashurst et al. (1987), a 3D mixing layer, and forced isotropic turbulence simulation by (Smith et al., 1994) and the  $Re = 50000$  LES simulation. A similar trend of alignment exists in all four cases, though the mixing layer having a higher degree of coherence has a much higher probability of alignment. Because the vorticity field and flame sheet are evolving, there is reason to suspect that a spatial dependence exists for the alignment data as in the case of the shape factor. In figure 6b the alignment is plotted over the entire domain and at the same four locations as before. There is a large difference between the near field and far field alignment which suggests that the vorticity is more intense and coherent in the near field.

Ashurst et al. (1987) examined the alignment between the most compressive strain rate and the flame normal for shear driven turbulence and isotropic turbulence. In the case of shear driven turbulence, the alignment peaked at an angle of roughly 30 degrees, while the peak for the isotropic case was at an angle nearly zero. Figure 6c shows these results along with the LES data for  $Re = 5000$ . Figure 6d shows the isotropic case, data from forced isotropic turbulence, and the  $Re = 50000$  simulation over the entire domain. The low  $Re$  simulation compares well with the shear driven turbulence results of Ashurst et al. (1987) while the  $Re = 50000$  case compares with the isotropic turbulence results. In figure 6e, the alignment pdf's over the entire domain and at the four streamwise

locations are shown for the  $Re = 5000$  case. These results suggest that the alignment evolves in the downstream flow direction. The alignment resembles the shear driven pdf of Ashurst et al. (1987) in the near field, however there is a transition to isotropic-like alignment moving downstream. This is evidence that the vortex stretching is causing a breakdown of the vorticity, moving from ordered to disordered. A similar trend occurs for the  $Re = 50000$  case, however the transition occurs at a faster rate. At the first  $x$  location, just downstream of the step corner, the alignment resembles shear flow, however, at the fourth  $x$  location, the alignment resembles the isotropic flow.

The tangential strain rate (in the plane of the flame) is found by solving the relation  $\mathbf{t}_1 \cdot \bar{\mathbf{e}} \cdot \mathbf{t}_2 = \nabla \cdot \mathbf{u} - \mathbf{n} \cdot \bar{\mathbf{e}} \cdot \mathbf{n}$ , where  $\mathbf{t}_1$  and  $\mathbf{t}_2$  are two orthogonal vectors in the plane of the scalar surface,  $\bar{\mathbf{e}} = \frac{1}{2}[\nabla \mathbf{u} + \nabla \mathbf{u}^T]$  is the resolved scale strain rate tensor, and  $\mathbf{n}$  is the unit normal,  $\mathbf{n} = \nabla G / |\nabla G|$ , in the direction of the surface propagation. The pdf of the tangential strain rate in the plane of the surface is presented in Figure 7a. The tangential strain rate is normalized by the Kolmogorov time-scale and the pdf data indicates that the mean strain is slightly positive. The data are in good qualitative agreement with the laminar flamelet modeling of Cant et al. (1990) and the material surface curvature analysis of Yeung et al. (1990). Mean positive straining indicates that on the whole the flame is being stretched but the data also show that compression of the flame surface can occur as indicated by a non-zero probability of negative tangential strain rate shown in figure 7a. The probability density, for the entire domain and the spatial variation at the four locations, of the tangential strain rate for the  $Re = 50000$  simulation is shown in figure 7b. The probability density becomes more symmetric downstream, similar to isotropic flow, and the probability for high strain rates is decreased. This suggests that the flame experiences much higher strain rates near the the step and the strain rate decreases downstream.

The flame stretch  $\kappa$ , is defined as the rate of change of a Lagrangian flame surface element  $\delta A$  and can be expressed in terms of the local tangential strain rate, curvature and flame speed (Candel and Poinso, 1990):

$$\kappa = \frac{1}{\delta A} \frac{d(\delta A)}{dt} = \left[ \nabla \cdot \mathbf{u} - \mathbf{n} \cdot \bar{\mathbf{e}} \cdot \mathbf{n} + \frac{S_L}{R} \right]. \quad (13)$$

where  $R = 1/h_1 + 1/h_2$ , is the sum of the principle radii of curvature. Positive stretch tends to reduce the flame speed while negative tends to increase it. Though the effect of flame stretch is not included in these calculations, examination of the flame stretch apriori may provide useful information. Figure 8 is a plot of the probability density of flame stretch from the  $Re = 50000$  simulation for the entire domain and the four  $x$  locations. From the

figure, it is shown that a spatial dependence does exist, which is no surprise having examined the strain rate spatial dependence. The mean probability in all cases is slightly positive. This means that on average, the laminar flame speed will be reduced by the effects of flow field. The flame stretch is expected to be highest in the step region and decrease in the downstream direction. Therefore, possibility of flame extinction is highest near the step.

#### 4. Conclusions

A study of scalar propagation in three-dimensional compressible spatially evolving turbulence at two different Reynolds numbers has been conducted using LES. Statistics of the entire flow for shape factor, curvature, vorticity/strain rate alignment, strain rate/surface normal alignment, and strain rate have been compared with data from constant density direct numerical simulations of passive scalar and premixed flame propagation in relatively simple flows (Pope et al., 1989, Ashurst et al. 1993, and Smith et al. 1994).

A large dependence upon the spatial location at which the data are examined has been found for some statistical properties, unlike the temporal simulations.

The probability density of the shape factor shows a decreased likelihood for cylindrical shaped flames moving downstream.

The curvature pdf, for all regions of the flow, remains symmetric and the mean is nearly zero.

The strain rate/flame normal alignment has been shown to transition from shear driven flow alignment to isotropic turbulence alignment in the down stream direction.

Strain rate (in the plane of the flame) has been found to be highest near the step and decreasing in the downstream direction, the pdf becoming more symmetric, similar to isotropic flows.

The flame stretch pdf calculated apriori shows positive mean value at all locations examined and is highest near the corner of the step. This may have important implications in flamelet modeling, for it is known that the flame stretch together with the Lewis number can greatly affect the laminar flame speed and in extreme cases may cause local extinction.

#### Acknowledgment

This research is funded by the Office of Naval Research under Contract No. N00014-92-J-403. The computational resources were provided by the Numerical Aerodynamic Simulation (NAS) at NASA Ames Research

Center and are gratefully acknowledged.

### References

- Ashurst, Wm.T., Kerstein, A.R., Kerr, R.M., and Gibson, C.H. (1987) "Alignment of vorticity and scalar gradient with strain rate in simulated Navier-Stokes turbulence," *Phys. Fluids A*, Vol. 30, No. 8, pp. 2343-2353.
- Ashurst, Wm.T., (1993) "Constant-Density Markstein Flamelet in Navier-Stokes Turbulence", to appear in *Combustion, Science and Technology*.
- Candel, S.M. and Poinot, T.J. (1990) "Flame Stretch and the Balance Equation for the Flame Area," *Combust. Sci. and Tech.*, Vol. 70, pp. 1-15.
- Cant, R.S., Rutland, C.J., and Trouve, A. (1990) "Statistics for laminar flamelet modeling," Center for Turbulent Research, Proceedings of the Summer Program pp. 271-279.
- Echekki, T. and Mungal, M.G. (1990) "Flame Speed Measurements at the Tip of a Slot Burner: Effects of Flame Curvature and Hydrodynamic Stretch," Twenty-Third Symposium (International) on Combustion, The Combustion Institute, pp. 451-461.
- Erlebacher, G. Hussaini, M.Y. Speziale, C.G. and Zang, T.A. (1987) "Toward the Large-Eddy Simulation of Compressible Turbulent Flows," Institute for Computer Applications in Science and Engineering, Hampton, VA, ICASE 87-20.
- Germano, M., Piomelli, U., Moin, P., and Cabot, W.H. (1991) "A Dynamic Subgrid-Scale Eddy viscosity Model," *Phys. Fluids A*, No. 3, pp. 1760-1765.
- Kerstein, A.R., Ashurst, W.T., and Williams, F.A., (1988) "The Field Equation for Interface Propagation in an Unsteady Homogeneous Flow field," *Phys. Rev. A*, 37, 2728.
- Menon, S. (1991) "Active Control of Combustion Instability in a Ramjet Using Large-Eddy Simulations," AIAA-91-0411, 29th Aerospace Sciences Meeting, Reno, Nevada, January 7-10.
- Menon, S. and Jou, W.-H. (1991) "Large-Eddy Simulations of Combustion Instability in an Axisymmetric Ramjet Combustor," *Combustion Science and Technology*, Vol. 75., pp. 53-72.
- Menon, S., and Yeung, P.K. (1994) "Effect of Subgrid Models on the Computed Interscale Energy Transfer in Compressible and Incompressible Isotropic Turbulence," AIAA-94-2387 Presented at the AIAA 25th Fluid Dynamics Conference, Colorado Springs, CO, June 20-23.
- Metcalfe, R.W., Orszag, S.A., Brachet, M.E., Menon, S., and Riley, J.J. (1987) "Secondary Instability of a Temporally Growing Mixing Layer," *J. Fluid Mech.*, vol. 184, pp. 207-243.
- Moin, P., Squires, K., Cabot, W., and Lee, S. (1991) "A Dynamic Subgrid-Scale Model for Compressible Turbulence and Scalar Transport," *Phys. Fluids A*, No. 3, Vol. 11.
- Piomelli, U., Moin, P., and Ferziger, J.H. (1988) "Model Consistency in Large Eddy Simulation of Turbulent Channel Flows," *Phys. Fluids*, Vol. 31, pp. 1884-1891.
- Pope, S.B., Yeung, P.K., and Girimaji, S.S., (1989) "The curvature of material surfaces in isotropic turbulence," *Phys. Fluids*, Vol. 1, No.12, pp. 2110-2018.
- Rutland, C.J. and Trouvé, A. (1993) "Direct Simulations of Premixed Turbulent Flames with Nonunity Lewis Numbers," *Combustion and Flame*, 94, pp. 41-57.
- Smith, T.M., Menon, S., and McMurtry, P.A. (1994) "The Structure of Premixed Flames in Isotropic and Shear Driven Turbulent Flows," AIAA 94-0677, 32nd Aerospace Sciences Meeting, Reno, Nevada, Jan. 10-13.
- Squires, K. and Zeman, O. (1990) "On the Subgrid-Scale Modeling of Compressible Turbulence," Center for Turbulence Research, Proceedings of the Summer Program.
- Yeung, P.K., Girimaji, S.S., and Pope, S.B. (1990) "Staining and Scalar Dissipation on Material Surfaces in Turbulence: Implications for Flamelets," *Combustion and Flame*, Vol. 79 pp. 340-365.
- Yakhot, V. (1988) "Propagation Velocity of Premixed Turbulent Flame," *Comb. Sci. Tech.*, Vol. 60.

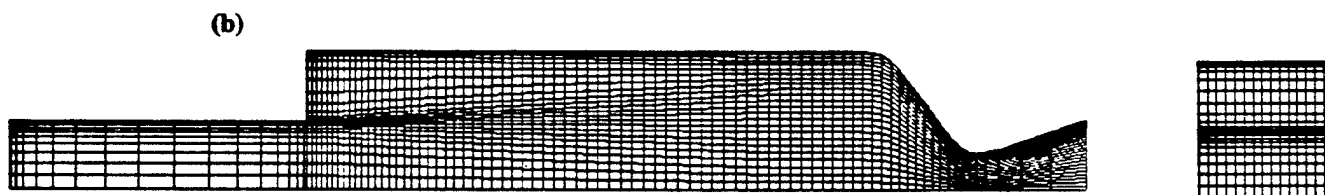
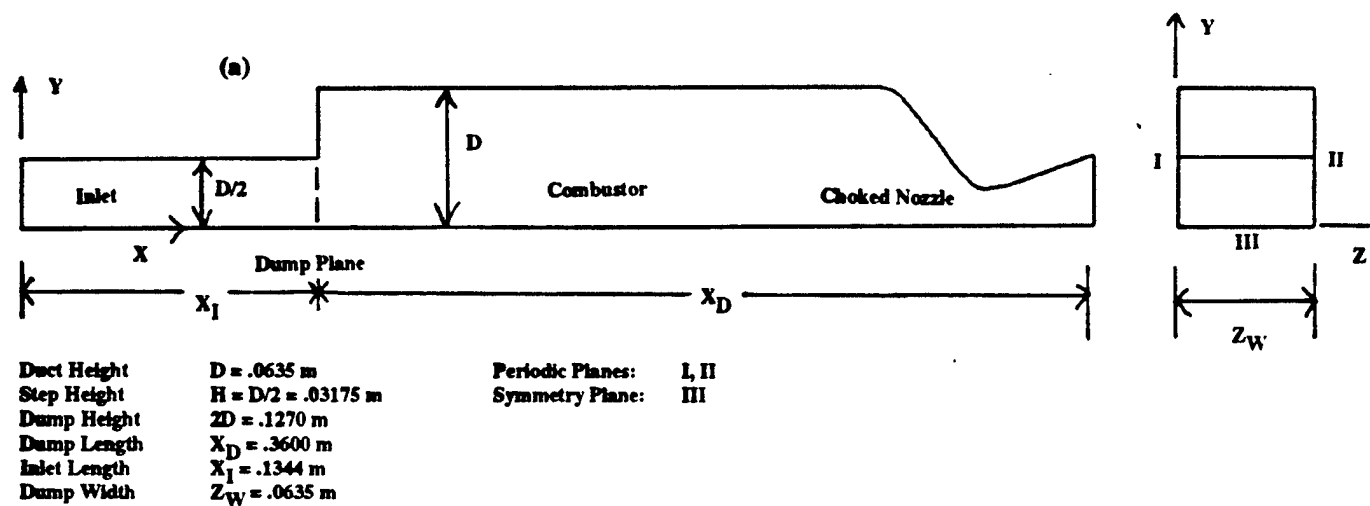
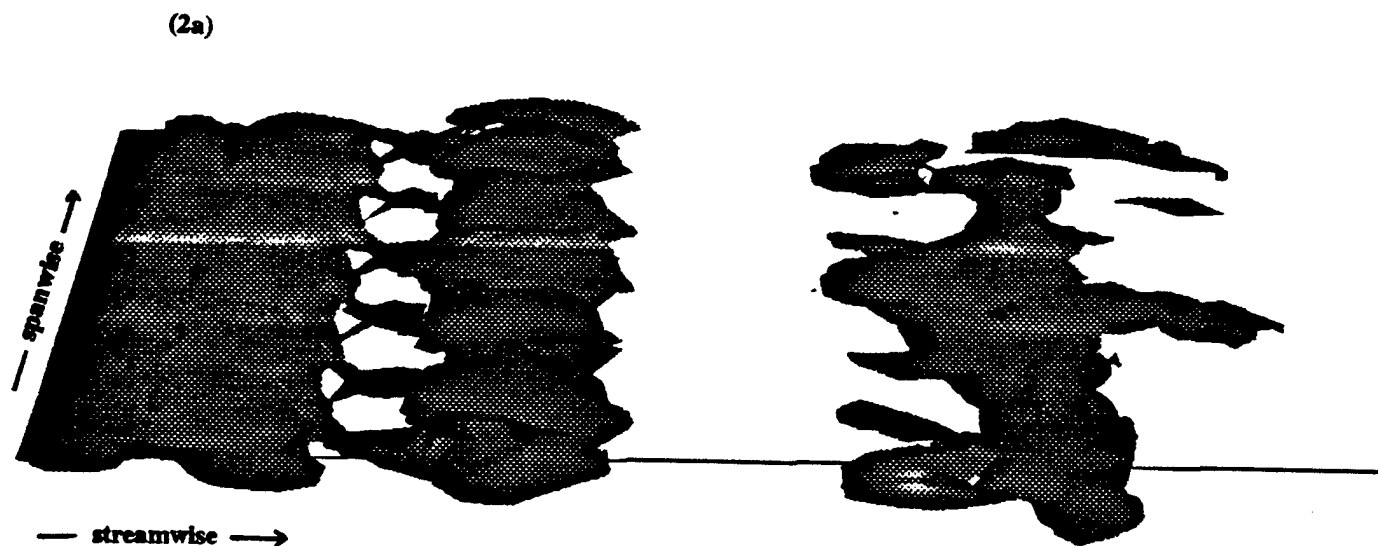
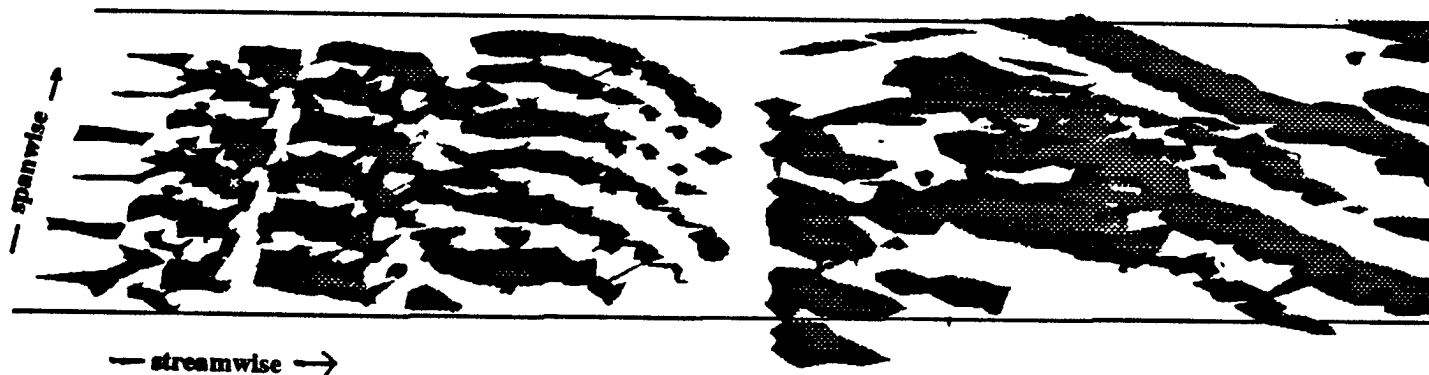


Figure 1. Three-dimensional dump combustor; a) characteristic geometry and dimensions, b) two planes of the  $96 \times 48 \times 16$  grid (every other  $y$  line shown).





(2b)



(2c)

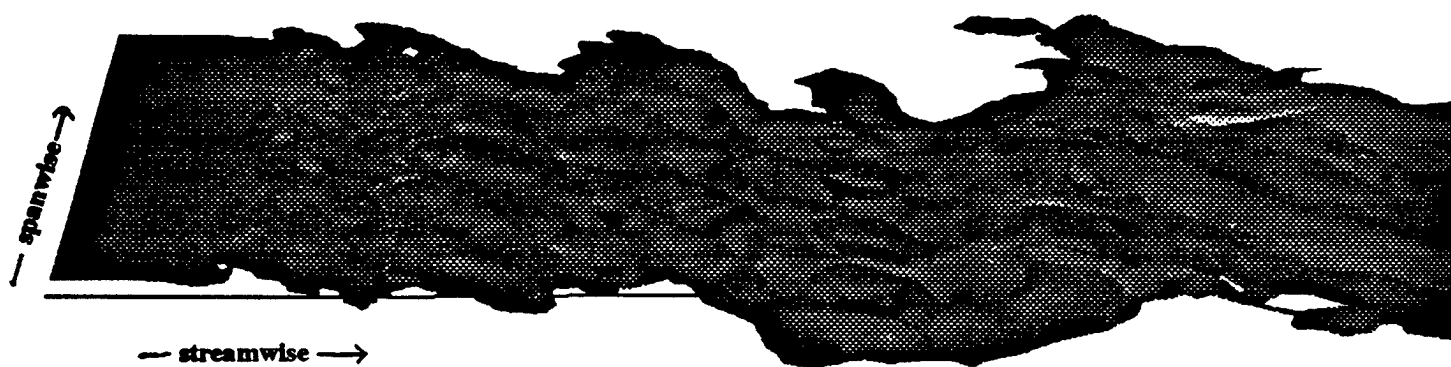
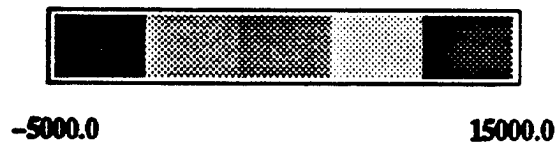


Figure 2. Three-dimensional views from a snapshot of the flow field; a) spanwise vorticity, b) streamwise vorticity, and c)  $G$ -field.

(3a)



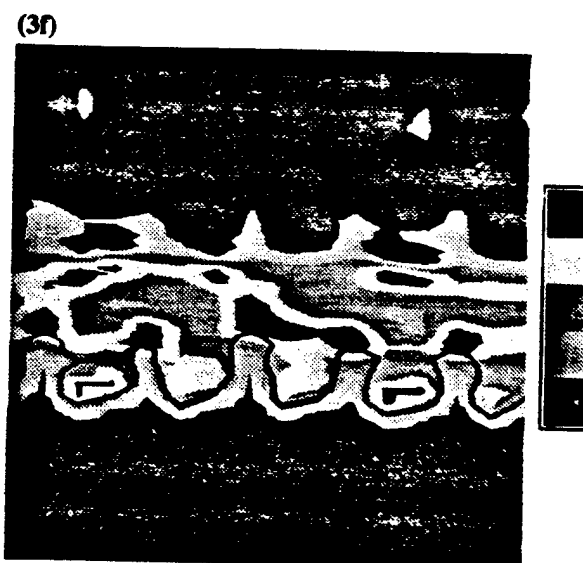
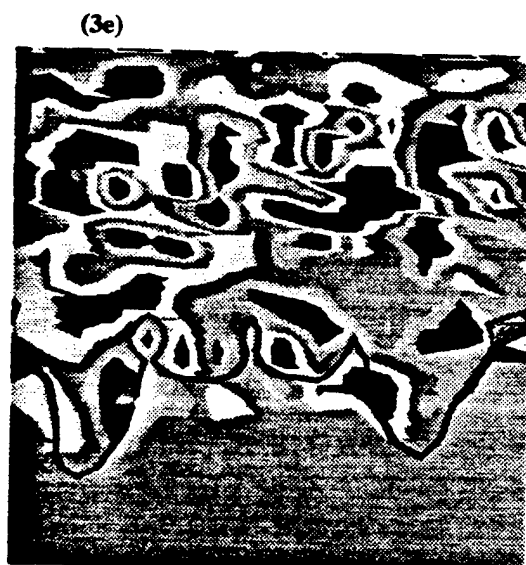
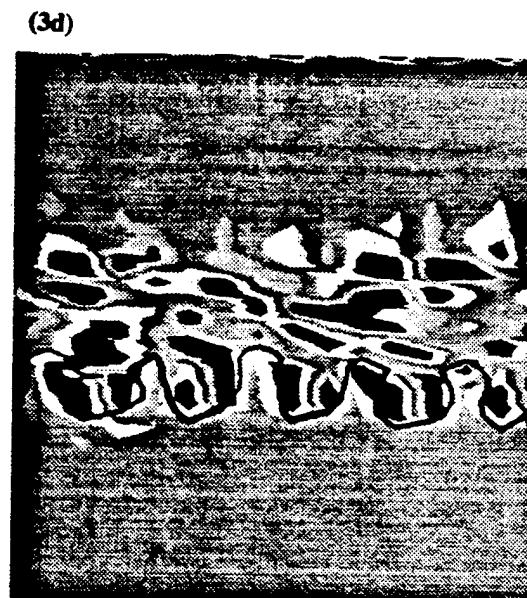
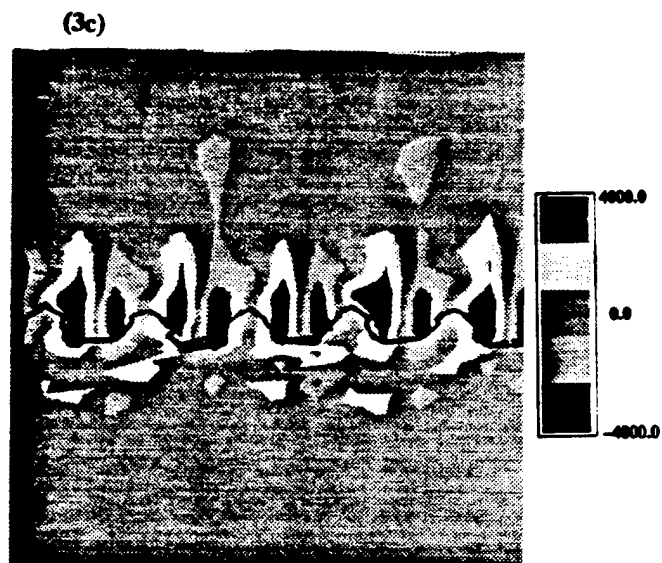
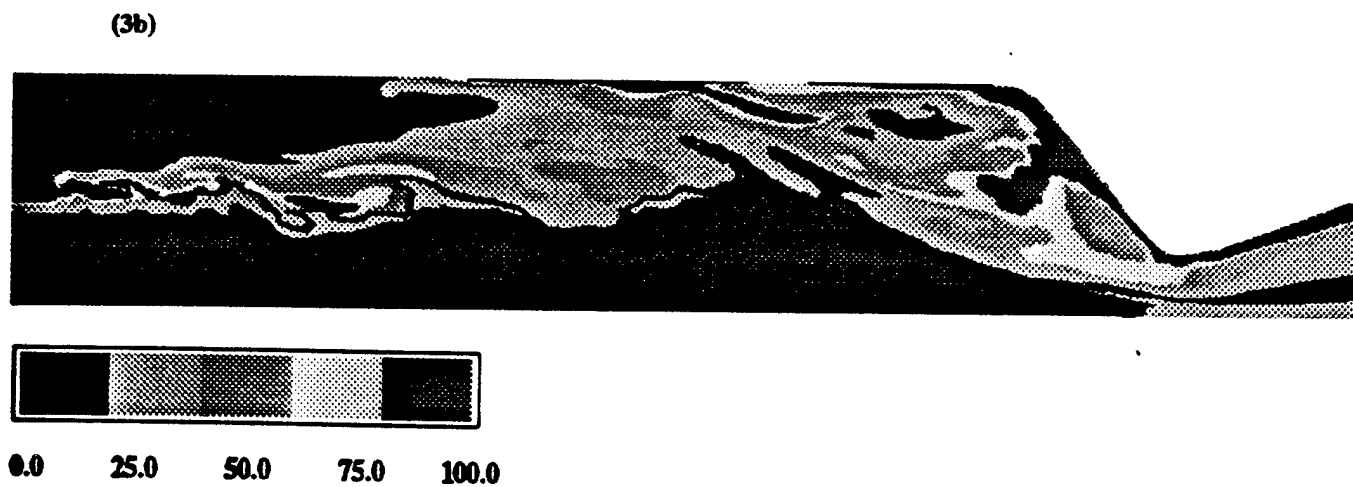


Figure 3. Vorticity, subgrid kinetic energy and  $G$ -field; a) spanwise vorticity and  $G$ -field in a  $z$ -plane, b) subgrid kinetic energy and  $G$ -field in a  $z$ -plane, c) streamwise vorticity and  $G$ -field in  $x$ -plane 1, d) streamwise vorticity and  $G$ -field in a  $x$ -plane 2, e) streamwise vorticity and  $G$ -field in a  $x$ -plane 3, and f) subgrid kinetic energy and  $G$ -field in  $x$ -plane 2.

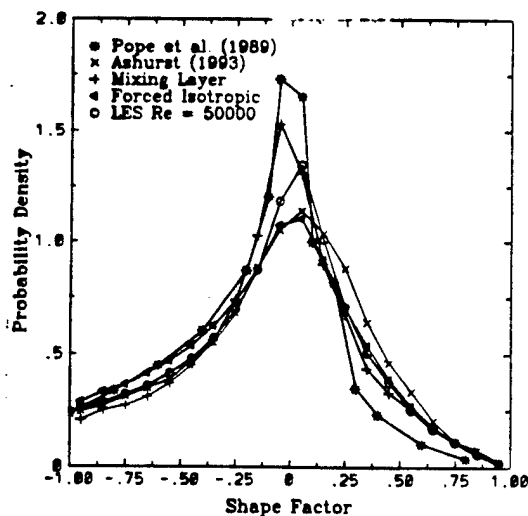


Figure 4a. Probability density of the shape factor for data by Pope et al. (1989), Ashurst (1993), Smith et al. (1994), and LES at  $Re = 50000$ .

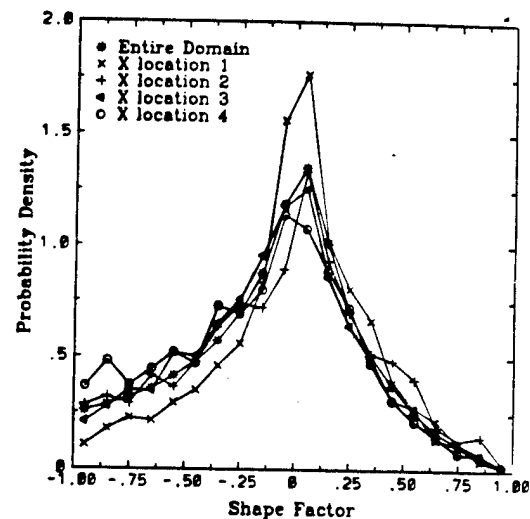


Figure 4b. Probability density of the shape factor for LES at  $Re = 50000$  over the entire domain and four  $x$  locations.

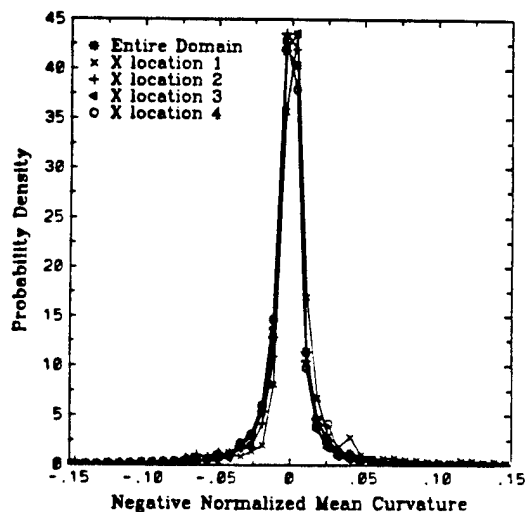


Figure 5. Probability density of negative mean curvature for LES at  $Re = 50000$  over the entire domain and four  $x$  locations.

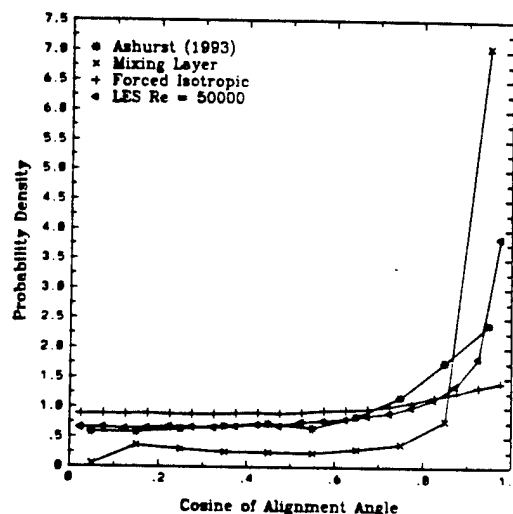


Figure 6a. Probability density of the alignment between the intermediate strain rate and vorticity for data by Ashurst (1993), Smith et al. (1994) and LES at  $Re = 50000$ .

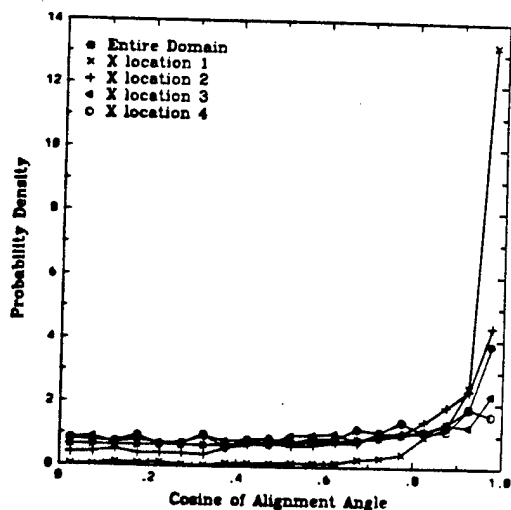


Figure 6b. Probability density of the alignment between the intermediate strain rate and vorticity for LES at  $Re = 50000$  over the entire domain and four  $x$  locations.

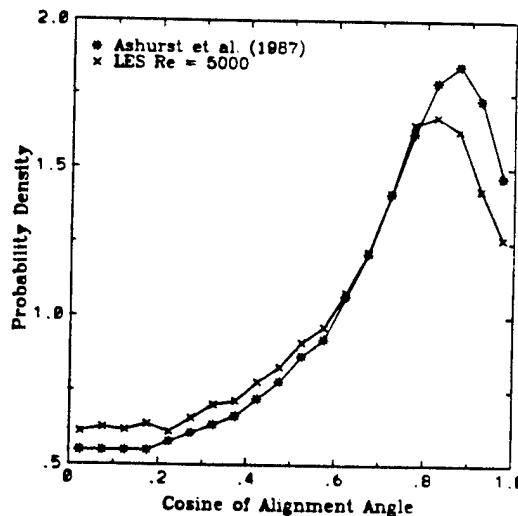


Figure 6c. Probability density of the alignment between strain rate and the flame normal for data by Ashurst et al. (1987) and LES at  $Re = 5000$  over the entire domain.

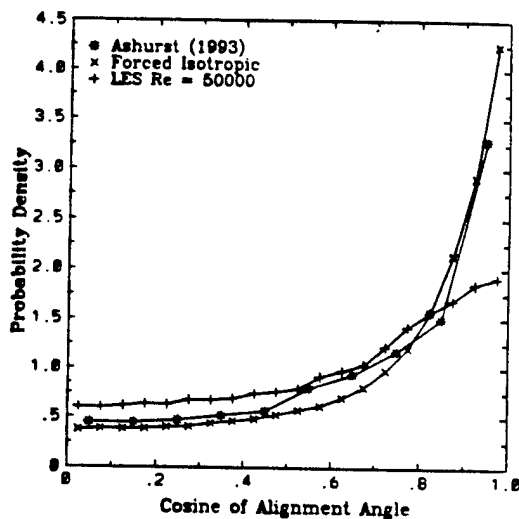


Figure 6d. Probability density of the alignment between strain rate and the flame normal for data by Ashurst et al. (1993) and LES at  $Re = 50000$  over the entire domain.

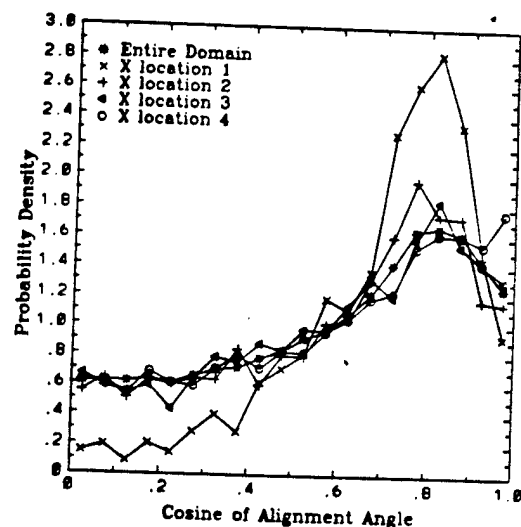


Figure 6e. Probability density of the alignment between strain rate and the flame normal for LES at  $Re = 5000$  over the entire domain and four  $x$  locations.

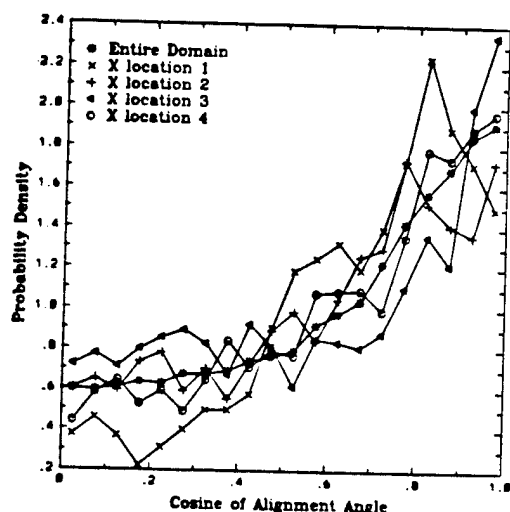


Figure 6f. Probability density of the alignment between strain rate and the flame normal for LES at  $Re = 50000$  over the entire domain and four  $x$  locations.

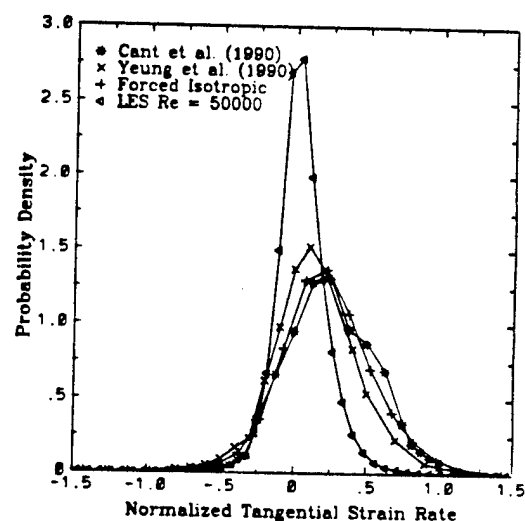


Figure 7a. Probability density for the tangential strain rate for data by Cant et al. (1990), Yeung et al. (1990) and Smith et al. (1994) and LES at  $Re = 50000$ .

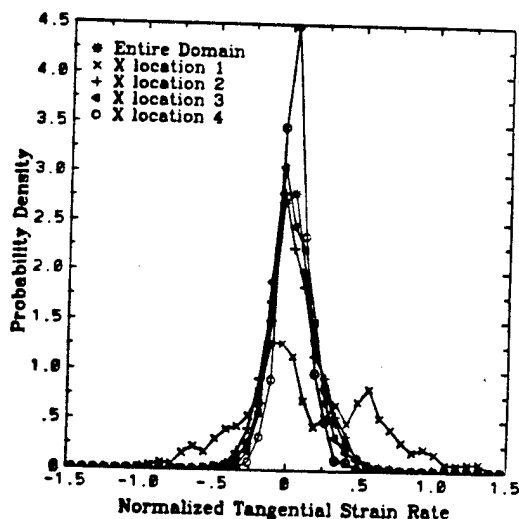


Figure 7b. Probability density of the tangential strain rate for LES at  $Re = 50000$  over the entire domain and four  $x$  locations.

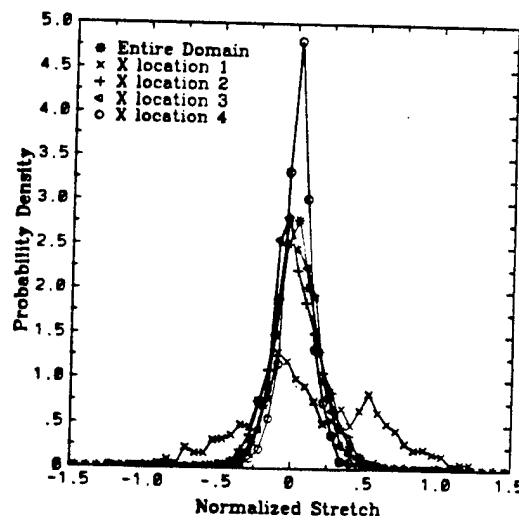


Figure 8. Probability density of flame stretch for LES at  $Re = 50000$  over the entire domain and four  $x$  locations.



**AIAA 94-0677**

**The Structure of Premixed Flames in  
Isotropic and Shear Driven Turbulent  
Flows**

**T. M. Smith**

**S. Menon**

**School of Aerospace Engineering**

**Georgia Institute of Technology**

**Atlanta, Georgia**

**and**

**P. A. McMurtry**

**Department of Mechanical Engineering**

**University of Utah**

**Salt Lake City, Utah**

**32nd Aerospace Sciences**

**Meeting & Exhibit**

**January 10-13, 1994 / Reno, NV**

# THE STRUCTURE OF PREMIXED FLAMES IN ISOTROPIC AND SHEAR DRIVEN TURBULENT FLOWS

Thomas M. Smith\*

Suresh Menon\*\*

School of Aerospace Engineering  
Georgia Institute of Technology  
Atlanta, Georgia

and

Patrick A. McMurtry\*\*\*

Department of Mechanical Engineering  
University of Utah  
Salt Lake City, Utah

## Abstract

The characteristic properties of constant density flames in turbulent flows have been analyzed using the results from direct simulations. A thin flame model incorporating the effects of flame stretch has been implemented into a pseudo spectral Navier-Stokes solver to simulate the propagation of the flame sheet in forced/decaying isotropic turbulence, and in a temporal mixing layer with three-dimensional instability. The study concentrates on curvature, alignment, and strain rate statistics, and turbulent flame speed estimations. The most probable shape of the flame, regardless of the flow configuration is found to be cylindrical. This agrees with Pope et al. (1989) and Ashurst (1992). The probability is decreased slightly by stretch effects. The flame normal has a large probability of aligning with the most compressive strain rate direction for both flow configurations, agreeing with Ashurst (1992). Again, the probability is slightly decreased by stretch effects. The mean tangential strain rate is found to be positive, for the isotropic forced/decaying turbulence simulations. This agrees with Cant et al. (1990) and Yeung et al. (1990). The turbulent flame speed as a function of  $u'/S_L$  including stretch effects is in reasonable agreement with recently published analytical, numerical, and experimental data. The flame stretch reduces the turbulent flame speed by reducing the amount of flame wrinkling.

## 1. Introduction

The direct numerical simulation (DNS) of premixed flames in turbulent flows is extremely difficult due to the existence of length and time scales differing by many orders of magnitude. Very small grid spacing is required to resolve the

smallest turbulent structures thereby severely limiting the overall size of the domain and the number of large scale structures that can be captured making the adequate resolution at both small and large scales almost impossible. In premixed combustion, if an appropriately defined Damköhler number is sufficiently high, the flame thickness will be much smaller than the smallest length scale of turbulence (the Kolmogorov scale). The computational requirement for resolution of the inner flame structure makes direct simulation impractical for large Reynolds number flows. The problem is further compounded by the numerous stiff chemical reaction equations that must be solved simultaneously. Therefore, direct simulations of turbulent combustion including finite rate kinetics cannot be considered as a method for practical engineering applications. To carry out DNS studies of reacting flows, recent studies (e.g. Trounev and Poinso, 1993) have artificially adjusted the chemical kinetics to thicken the flame structure so that it can be resolved. Such studies have provided a new understanding of the effect of small scale structures on propagating flame surfaces; however, the resolved flame structure is much larger than the Kolmogorov scale.

It is well known that the propagation speed of a laminar flamelet can be significantly modified by the flow strain and curvature (the so-called stretch effects). Preferential diffusion effects, (Lewis number effects) when combined with stretch, have also been shown to greatly affect the flame speed (Asato et al., 1988). Exactly how the flame speed depends on the flame curvature, the strain field in the plane of the flame, and the Lewis number is a matter of intense research in recent years. Recent results suggest that in the presence of large curvature, the flame speed can increase by a factor of six when compared to the unstrained speed (Echekki and Mungal, 1990). Rutland et al. (1993) reported that in three-dimensional (3D) DNS of premixed flames with constant density and single-step Arrhenius kinetics, the local flame speed depends upon curvature, whereas globally, curvatures cancel out and the strain becomes the dominant factor in determining the turbulent flame speed. This agrees with the earlier study by Cant and Bray (1988) where it was shown that the overall effect of curvature on

\* Graduate Research Assistant, Student Member AIAA.

\*\* Associate Professor, Member AIAA.

\*\*\* Associate Professor, Member AIAA.

the flame speed integrates to zero if the curvature distribution is symmetric. However, more recently, Poinso et al. (1991) characterized flame quenching based on strain and curvature in two-dimensional (2D) compressible DNS of a premixed flame impinging on a vortex pair. For large vortex pairs, greater than five times the flame thickness, quenching was attributed to strain effects, while for vortex pairs smaller than five times, flame curvature was considered responsible. Thus, it is still not clear what role flame stretch plays in determining the structure of the flame, turbulent flame speed, and flame quenching. These issues are important because the strain and curvature information can be obtained without solving the chemistry, thereby making flamelet models a promising alternative to study premixed combustion.

Using DNS data, the effects of stretch (defined in this study as the combination of tangential strain rate, in the plane of the flame surface, and the sum of the two principle curvatures), can be statistically analyzed since the state variables are known at every grid point. Stretch is much more difficult to determine in experiments due to the difficulty in evaluating velocity gradients and flame surface curvature, although recent studies have made significant progress in directly measuring curvature (Lee et al., 1992).

In this study, the flame is assumed an infinitely thin flame sheet and a governing propagation equation is solved along with the Navier-Stokes equations (e.g. Ashurst, 1992). No attempt is made to resolve a flame structure and the effects of gas expansion due to heat release are neglected so that the flow equations are decoupled from the propagation equation. However, the propagation of the flame sheet is influenced by the velocity field. Neglecting gas expansion is not considered to be a serious drawback. For example, Clavin and Williams (1982) reported no new quantitative effects of flamelet motion when gas expansion effects were included in an analysis of premixed flame propagation in low intensity turbulence. In isotropic turbulence and using single-step Arrhenius chemical kinetics, Rutland et al. (1990) reported that correlations between turbulent flame speed and root mean square (r.m.s.) velocity agreed well with experiment despite neglecting gas expansion in the simulations. A future study will address the significance of heat release and gas expansion.

In this study, we will investigate the structure of premixed flames in turbulent flows by studying how stretch effects the flame structure and the turbulent flame speed. A description of the flow simulation model is presented in the next section followed by the flame propagation model. The results that follow are arranged into the two topics mentioned above. Conclusions and suggestions for further work complete the remainder of the paper.

## 2. Simulation Models

What follows is a brief description of the numerical method used to study the propagation of premixed flamelets in isotropic and shear driven turbulent flows. We begin with the flow solver and then discuss the premixed flame propagation model.

### 2.1 Direct Simulations of Turbulent Flows

The numerical scheme used here is well known and is based on the pseudo-spectral (collocation) method developed by McMurtry et al. (1986, 1989). In this method, the incompressible Navier-Stokes equations are solved explicitly by

computing the spatial derivatives in spectral space and marching in time using Adams-Bashforth time stepping in the physical domain. The flow equations can be written as

$$\nabla \cdot \mathbf{u} = 0 \quad (1)$$

$$\frac{\partial \mathbf{u}}{\partial t} + \nabla \cdot (\mathbf{u}\mathbf{u}) + \nabla \frac{p}{\rho} = \nu \nabla^2 \mathbf{u} \quad (2)$$

where  $\mathbf{u}$  is the velocity vector,  $p$  is the pressure, and  $\rho$  is the density assumed to be unity. The momentum equation is rewritten with the convection and viscous terms grouped together,

$$\frac{\partial \mathbf{u}}{\partial t} = -\nabla p + \mathbf{A}(\mathbf{x}) \quad (3)$$

and equation (3) is advanced to an intermediate time step by first neglecting the pressure term

$$\mathbf{u}^* = \mathbf{u}^n + \Delta t \left[ \frac{3}{2} \mathbf{A}^n(\mathbf{x}) - \frac{1}{2} \mathbf{A}^{n-1}(\mathbf{x}) \right] \quad (4)$$

where  $\mathbf{A}^n(\mathbf{x})$  and  $\mathbf{A}^{n-1}(\mathbf{x})$  are the convection and the viscous terms computed in spectral space for the  $n$  and  $n-1$  time levels. The pressure term becomes

$$\frac{\mathbf{u}^{n+1} - \mathbf{u}^*}{\Delta t} = -\Delta p^{n+1/2} \quad (5)$$

The addition of (4) and (5) results in a second order accurate approximation for the time derivative. Taking the divergence of (5) and noting that

$$\nabla \cdot \mathbf{u}^{n+1} = 0 \quad (6)$$

results in a Poisson equation for the pressure,

$$-\nabla^2 p^{n+1/2} = \frac{1}{\Delta t} \nabla \cdot \mathbf{u}^* \quad (7)$$

In the absence of boundaries the pressure can be computed efficiently by transforming equation (7) into spectral space, solving for the pressure, and transforming back to the physical domain. Finally the velocity at the  $n+1$  time level is found by solving equation (5). More details of this method are given elsewhere (McMurtry et al., 1986, 1989).

### 2.2 Flame Model

To simulate the flame, we employ the thin-flame model of Kerstein et al. (1988). In this model, it is assumed that the flame thickness is small compared to the smallest turbulent length scale and if the changes in the reaction-diffusion structure due to turbulent straining are also small, then the reaction zone can be considered to be asymptotically thin. Within the thin flame approximation, a model equation for premixed combustion is considered in which the local flame speed explicitly appears. If the local flame speed  $u_f$  is known, a progress variable  $G$  can be defined that is governed by the equation (Kerstein et al., 1988, Menon and Jou, 1991)

$$\frac{\partial G}{\partial t} + \mathbf{u} \cdot \nabla G = -u_f |\nabla G| + \nu \nabla^2 G \quad (8)$$

where  $u$  is the fluid velocity,  $u_F$  is the local flame speed, and  $v'$  is a dissipation coefficient. The flame is located along a specified isosurface  $G$ , separating the fuel mixture  $G > G_0$  and the fully burnt combustion product  $G < G_0$ . Equation (8) describes the convection of the flame by the local fluid velocity and the flame propagation into the unburnt mixture through a Huygens type mechanism,  $\frac{\partial G}{\partial t} = -u_F |\nabla G|$ . For laminar premixed combustion, the local flame speed  $u_F$  is the laminar flame speed  $S_L$  which contains the information on the chemical kinetics and the molecular dissipation.

If equation (8) is applied to turbulent flows without the use of a sub-grid model that explicitly represents the fine scales, the local flame speed is taken to be the local turbulent flame speed  $u_F$ , where  $u_F$  is a function of local turbulence intensity  $u'$  and the laminar flame speed  $S_L$ . In the present study, the effect of using a constant  $S_L$  and a  $S_L$  modified by stretch effects will be investigated using DNS. The resulting turbulent flame speed will be determined as a part of this study, as discussed below.

In equation (8), a dissipation term is added to prevent pockets of burnt fuel, which are not physically possible, from arising due to the discrete numerics. A similar approach was used by Ashurst (1992). Another reason this term is needed is due to the nature of spectral methods which cannot resolve thin discontinuities. Earlier, Ashurst (1990) showed that this addition does not affect the statistics of the flame geometry since  $v'$  is typically small (relative to the molecular viscosity). A similar result is also obtained in the present study.

Typical flame structure characteristics have been investigated using the data on the local flame curvature and the strain field in the plane of the flame. Both these properties contribute to the flame stretch,  $\kappa$ , which can be shown to be (Clavin, 1985, Ashurst, 1992)

$$\kappa = L_M \left[ -(\bar{n} \cdot \bar{e} \cdot \bar{n}) / S_L - \left( \frac{1}{R_1} + \frac{1}{R_2} \right) \right] \quad (9)$$

where,  $\bar{n} = \nabla G / |\nabla G|$  is the outward (local) normal to the flame surface,  $\bar{e} = [(\nabla u) + (\nabla u)^T]$  is the rate of strain tensor,  $R_1$ ,  $R_2$  are the two principle radii of curvature, and  $L_M$  is the Markstein length. The Markstein length depends on the diffusional properties of the mixture and its magnitude is of the order of the flame thickness. Curvature concave with respect to the unburnt fuel is defined as positive in this study.

The radii of curvature of the scalar are determined by finding the eigenvalues of the curvature tensor

$$h_{ij} = -\frac{\partial^2 G}{\partial x_i \partial x_j} \frac{1}{g} + \frac{1}{g^3} \sum_{k=1}^3 \frac{\partial G}{\partial x_i} \frac{\partial G}{\partial x_k} \frac{\partial^2 G}{\partial x_j \partial x_k} \quad (10)$$

where  $g = |\nabla G|$ . This nine element tensor has two real eigenvalues  $h_1$ ,  $h_2$  and one eigenvalue equal to zero. The real eigenvalues give the radii of curvature,  $R_1 = 1/h_1$  and  $R_2 = 1/h_2$ . The ratio of the smaller radius divided by the larger,  $(R_{\min}/R_{\max})$ , called the shape factor, is bounded by  $\pm 1$ . The value -1 corresponds to a saddle point (or pseudospherical, Pope et al., 1989), 0 is cylindrical and +1 is spherical. Pope et al. (1989) used this definition to define the structure of material

surfaces and Ashurst (1992) extended this technique to study flame fronts.

The stretch effect has been incorporated in this study using a variant of Markstein's approach as done earlier by Ashurst (1992). Thus, the stretch-modified flame speed is given by  $u_F = S_L(1 - \kappa)$ , where  $S_L$  is the planar constant laminar flame speed. Instead of this expression a slightly different expression is used,  $u_F = S_L \exp(-\kappa)$ . The use of the exponential prevents the flame speed from becoming negative. Another modification added was to restrict the maximum stretched flame speed to  $4S_L$ . This upper limit is necessary to enhance stability of the flame propagation due to the effect of finite time marching (Ashurst, 1992). Lewis numbers effects are included in the Markstein length, however, in this study the Lewis number is assumed to be unity.

### 3. Results and Discussion

A discussion of the results is presented here on the geometrical characteristics of the constant property surfaces that evolve in simulated 3D turbulent flows. Simulations of the flame propagation in both shear driven and decaying isotropic turbulent flows were carried out and the statistics of flame structure, flame normal/strain rate alignment, and vorticity/strain rate alignment were evaluated. Estimations of the turbulent flame speed based on the increased area of the flame front as a function of the ratio  $u'/S_L$ , where  $u'$  is the r.m.s. velocity fluctuation and  $S_L$  is the laminar flame speed is also discussed.

Temporally evolving mixing layers and forced/decaying isotropic turbulence were studied. Both studies were conducted using  $64^3$  grid points in a  $(2\pi)^3$  domain. The scalar transport equation was solved along with the momentum equations. For the constant density case, the momentum equations are decoupled from the scalar equations, however, the convective transport of the flame surface occurs due to the evolving turbulent velocity field. The physical interpretation is that an evolving  $G$ -level for any level  $G$  represents the simulated propagation of a turbulent flame brush. Furthermore, for constant density flames, an added simplification occurs whereby any level  $G$  can be identified with a flamelet. Thus, statistics for all levels  $G$  can be combined. In effect, each simulation corresponds to a family of simulations parameterized by  $G$ . It is important to note that the symmetry that leads to this interpretation is broken if heat release is included, in which case only a pre specified  $G$  level can be identified with the flame.

#### 3.1 Flamelet Structures

Simulations were first carried out using a temporal mixing layer flow configuration. The mixing layer was initialized in the usual manner with a tangent hyperbolic mean velocity and a perturbation velocity field based on linear stability (McMurtry et al., 1986, 1989). The perturbation velocity included the fundamental spanwise mode and a streamwise mode similar to the approach used earlier to study secondary instability in mixing layers (Metcalf et al., 1987). The Reynolds number based on the initial vorticity thickness, mean velocity difference, and kinematic viscosity was 50. The  $G$ -field was initialized as an error function with  $G = 0$  in the lower half plane and  $G = 1$  in the upper half plane. As the flow evolves in time, the mixing layer rolls up into one spanwise vortex. At the same time, due to the 3D mode, streamwise vorticity develops into pairs of counter rotating braid-like structures (see Metcalfe



et al., 1987, for more details). Figure 1a shows a 3D perspective plot of the vorticity magnitude at an instant where spanwise structure has completed its rollup and the streamwise structures are clearly visible. The level shown is 18% of the maximum. The influence of the vorticity on the flame sheet can be observed in Figure 1b, which shows the flame surface is wrapped around the vortex structures.

In the second flow configuration, isotropic turbulence was simulated. The flow was initialized by a randomly generated divergence-free field that conformed to a specified energy spectrum (e.g., Lee and Reynolds, 1985). The vorticity/strain field alignment as discussed by Ashurst et al. (1987) does not exist in the initial random velocity field. The alignment evolves as the flow turbulence evolves and coherent vortex structures emerge, forming tube-like structures. One difficulty in running these simulations was that by the time the vorticity-strain field became aligned, the integral length scale was of the order of half the size of the domain, making flame simulations impossible. On the other hand, flame simulations starting with the random initialization did not contain the proper turbulent statistics for reasons just mentioned. For these reasons, a velocity forcing procedure was implemented (McMurtry, 1993). In this procedure, the low wave number components of velocity are frozen such that a constant energy system is produced. This forcing procedure is similar to that employed in an earlier study of forced isotropic turbulence (e.g., Kerr, 1985). The Taylor Reynolds number  $Re_\lambda$ , Taylor microscale  $\lambda$ , and  $u'$  remain constant as well. By holding the energy in the low wave numbers constant, the integral length is held constant as well. Parameters used for this set of runs are summarized in Table 1. The Prandtl number, chosen to be  $Pr = .72$ , will be required later in order to estimate the Markstein length. Decaying isotropic turbulence cases were also studied; however, the turbulence was allowed to relax after reaching a stationary state. Thus, the effects of initial flow conditions were not present in the decaying cases. Figure 2a shows  $u'$  and  $Re_\lambda/100$  for the forced and unforced isotropic simulations. The vorticity alignment is shown in Figure 2b. Forced and unforced alignment for the duration of a typical simulation are in close agreement. Figure 3a shows the vorticity at a chosen constant at a magnitude 40% of the maximum, demonstrating the tubular nature of the vorticity.

To carry out flame propagation simulations, additional parameters such as the Markstein length have to be defined. Determination of the Markstein length  $L_M = M_K \delta$  requires an estimation of the Markstein number  $M_K$  and the flame thickness,  $\delta$ . From two experimental studies (Searby and Quinard, 1990, and Deshaies and Cambray, 1990) where the Markstein number was experimentally measured for common hydrocarbon fuels, we choose  $M_K = 4.1$ . The flame thickness was estimated based on one-dimensional steady laminar flame propagation (Williams 1985),  $\delta = \nu / S_L Pr$ .

To simulate the propagation of flamelets in a periodic domain, two flames are necessary. These flames are initialized perpendicular to the  $x$  direction by setting the value of  $G = 0$  in the interior  $y$ - $z$  planes and  $G = 1$  at the  $y$ - $z$  planes on either side. Here,  $G = 0$  denotes burnt product and  $G = 1$  denotes premixed fuel. The interface between 0 and 1 is a steep linear gradient in the  $x$  direction. There is approximately 1.5 integral lengths between the two flamelets. As the simulation evolves, the two flames burn outward in opposite directions. As the edge of the domain is reached, the two flames begin to influence one another, the  $G$  field is no longer periodic, and the simulation is

halted. Figure 3b shows the flames in a typical isotropic turbulence simulation. This snapshot, taken at  $t = 1$ , and  $G = .5$ , shows a highly wrinkled, 3D flame shape. The choice of  $G$  is arbitrary and statistically identical to other levels.

The shape factor (which is the ratio of the smaller to the larger radius of curvature) pdfs, for the mixing layer and forced isotropic turbulence are compared with the data from Ashurst (1992) and the material surface statistics of Pope et al. (1989) in Figure 4a. The pdfs for all four cases agree with a peak near zero which indicates that the scalar statistics tend to a cylindrical shape. The agreement with Pope et al. (1989) suggests that the propagating flame has properties similar to that of a material surface. In fact, the flame surface is a material surface in the limit of vanishingly small flame speed. This data along with the data shown for the mixing layer suggest that the flame shape has a tendency to achieve a cylindrical shape regardless of the type of flow field. In addition, since the pdfs have a broad peak around the value of zero, this indicates that in most of the samples the flame shapes have one curvature significantly larger than the other. The data also clearly shows that there is zero probability for a spherical flame shape (shape factor equal +1) and a small finite probability for a pseudo-spherical (Pope et al., 1989) flame shape (shape factor equal -1). This is, again, in agreement with earlier observations.

The simulation data clearly show that the flame tends toward a cylindrical shape. The practical significance of this data is that it may be possible to study realistic premixed combustion in 2D flows. In fact, past 2D (or axisymmetric) simulations of realistic combustion instability in ramjet engines using the  $G$ -equation model has shown remarkable agreement with experimental data (Menon and Jou, 1991). However, the effect of 3D vortex stretching must be modeled in some manner so that the 2D simulations are representative of the full 3D flows. This aspect is under study at present.

Strain alignment pdfs are formed by first evaluating the eigenvalues and unit eigenvectors of the strain tensor. The three eigenvalues describe the normal strain rate in the vector direction. The three eigenvalues are denoted by  $\alpha$ ,  $\beta$ , and  $\gamma$ , where  $\alpha \geq \beta \geq \gamma$  by convention. For incompressible flows  $\alpha + \beta + \gamma = 0$  and for isotropic turbulence the mean values of these three strain rates are approximately  $\alpha:\beta:\gamma = 3:1:-4$  (Ashurst et al., 1987 and Yeung et al., 1990). Earlier studies showed that whereas vorticity aligns with the intermediate strain direction, a passive scalar aligns with the most compressive strain direction, (Ashurst et al., 1987). The vorticity/strain rate alignment is then formed by evaluating the absolute value of the dot product between the normalized vorticity vector and the normalized intermediate strain rate vector (which is the cosine of the angle between the two vectors). Similarly, the flame normal/strain rate alignment is found by evaluating the dot product between the unit flame normal,  $\mathbf{n}$ , and the normalized most compressive strain rate vector.

Figure 4b shows a plot of the probability of the alignment of the vorticity vector and the intermediate strain rate vector and Figure 4c shows the probability of the alignment of the flame surface normal with the most compressive (i.e., negative) strain direction. The vorticity alignment probability is much larger for the mixing layer due to the higher level of coherence of the vortex structure when compared with forced isotropic turbulence. The alignment of the flame propagation direction (as indicated by  $\mathbf{n}$ ) with the most compressive strain direction is similar in all the cases, as seen in Figure 4c. This suggests that the cylindrical nature of the constant scalar surface

and its alignment characteristics are nearly independent of the background turbulent flow.

The tangential strain rate normalized by the Kolmogorov time scale,  $\tau = (\nu/\epsilon)^{1/2}$ , where  $\epsilon$  is the energy dissipation rate, is presented in Figure 4d for the present forced isotropic case along with the data of Cant et al. (1990) which was obtained from a data base of DNS of premixed combustion with single-step Arrhenius chemistry, a similar geometric flamelet initialization, and the data from DNS of propagating material surfaces in isotropic turbulence (Yeung et al., 1990). Yeung et al. reported the mean strain rate of the area weighted pdf  $\sim .28$  and the mean for the unweighted pdf  $\sim .15$ . Cant et al. reported the mean for the weighted pdf to be  $\sim .28$ . The present study indicated that the unweighted pdf mean is  $\sim .11$ . This is significant because results from three independent turbulence simulations and three different scalar models produced the average strain rate in the plane of the constant scalar surface that is almost the same. In other words, the volume averaged strain rate seems to be independent of the model being used. The mean tangential strain rate is positive in all the cases shown in Figure 4d. Positive strain indicates that the surface is stretched most of the time, but there is a non-zero probability that the flame surface can experience negative strain. It can also be seen that the pdf is definitely not Gaussian. This agrees with the observations by Yeung et al. (1990).

Next, we present results from simulations chosen to illustrate differences between the pdfs of flamelet shape factor and flame alignment for stretched and unstretched flames, propagating in both forced and decaying isotropic turbulence. Table 2 contains a summary of the parameters used for these calculations. Data in Table 2 for the decaying case give parameters ranging from the beginning to the end of the simulation. The duration of the simulations was  $\sim 2.42$  eddy turnover times. Data for the pdfs was taken over four instances, each  $t = 0.5$  apart, early in the runs to be consistent. Edge effects were encountered in all runs, but at different times in each run depending on whether the laminar flame speed was constant or stretched. Therefore, beyond an upper time limit, the flame was no longer a continuous sheet over the entire domain. Initial transients, caused by the planar flame sheet initialization, created a lower time limit for collecting data. Data for all pdfs were collected between these time limits, roughly  $t = 1$  to  $t = 4$  for all cases. In Figure 5a, the shape factor pdfs is presented. The data for the forced/stretched case are the same data used to compare with the mixing layer results and published results appearing in Figures 4a-d. There exists very little difference between the forced cases and the decaying cases. There are two reasons for this. First, the initial field for the decaying case has already evolved into isotropic turbulence from a random field. Therefore, the vorticity alignment already exists albeit the probability is not nearly as high as in Ashurst's (1992) results (see Figure 2b). The alignment is evidence of rodlike vorticity filaments containing intense vorticity that warps the flame into a locally cylindrical shape (Figures 1b and 3a). The second reason that the flame structures in decaying isotropic turbulence are very similar to the forced case is based on observations of the pdfs, the flames align very quickly compared to the vorticity. Therefore, relative to the vorticity, the flamelets adjust to the changing turbulence very quickly.

Differences between stretched and unstretched cases are significant. Both unstretched cases have a higher peak and narrower band in the pdf. The damping effect of positive stretch, which tends to reduce the curvature of the flamelet,

resists the warping due to vorticity. Figure 5b shows the alignment pdf between the flame and the most compressive strain rate. As seen in Figure 5a, decaying turbulence does not alter the alignment with strain. Again it may be reasoned that the flame response to changing flow conditions is much faster than the changes in flow conditions. The Damköhler number ( $D_K$ ), which is the ratio of a characteristic flow time by a characteristic chemical time, gives a measure of how the flamelet is effected by the turbulence. A high  $D_K$  means the flame is relatively unaware of the turbulence and therefore, behaves more like a planar laminar flame. Following Linán and Williams (1993), and combining expressions in terms of known quantities, the Damköhler number is estimated as

$$D_K = S_L^2 \beta \text{Pr} \sqrt{\nu/(\epsilon')^3} / \nu, \text{ where } \beta \text{ is the Zel'dovich number.}$$

The authors argue that  $D_K \gg 1$  is a sufficient criteria for the flame to be considered a thin reaction sheet (i.e., flamelet). We estimate that  $D_K \sim 15$  for these forced runs and slightly higher for the decaying cases. This is reasonably high, therefore, the alignment does not seem to be affected by a slowly changing flow field. On the other hand, positive stretch tends to reduce the laminar flame speed effectively reducing the speed at which the flame can adjust to the changing vorticity so that the effect of stretch may tend to misalign the flamelet.

To obtain the sensitivity of the flame structure to the parameter  $u'/S_L$ , four runs were carried out with the stretched flame speed in forced isotropic turbulence. Table 3 summarizes the parameters used in these runs. The flow field for each of these runs is identical. The laminar flame speed was adjusted and  $u'$  remained constant. For this analysis,  $\delta = \nu / S_L \text{Pr}$  and so the Markstein length was adjusted to reflect the different  $\delta$ 's. Figure 6a is a plot of the shape factor pdfs. Again, as seen earlier, there is a very high probability for the cylindrical flame shape and this probability increases with  $u'/S_L$ . There is still a finite probability for the shape factor -1 (pseudo spherical shape) but zero probability for the spherical shape. The increase in probability for cylindrical shape with  $u'/S_L$  can be understood by noting that as  $u'/S_L$  increases the flame surface wrinkling increases thereby increasing the curvature. The probability for cylindrical shape also increases with increasing Markstein Length and decreasing Damköhler number. These results seem to suggest that  $u'/S_L$  and Damköhler number have a strong influence on the flame structure. These results are not in agreement with Ashurst's results, where he found very little change in the shape factor for different  $u'/S_L$  cases. The reason that the probability differs may be due to the much higher Markstein length used in these simulations. Ashurst reported using  $L_M = .0125$  and  $.05$  for  $u'/S_L = 0.5$  and  $2$ , respectively, and with  $u' = 1$  (for his simulations) the flame speeds are  $S_L = 2$  and  $0.5$  for  $u'/S_L = 0.5$  and  $2$ , respectively. In the present case, the flame speeds are  $.513$  and  $.128$  for the same  $u'/S_L$  values.

Figure 6b shows the flamelet alignment with strain rate. While the curvature was affected by  $u'/S_L$ , the flame alignment is only slightly affected. This can be understood by remembering that the strain rate is a fluid dynamic property independent of the flame propagation and since  $u'$  is fixed for these simulations, this alignment is not significantly effected by changes in the flame propagation speed  $S_L$ . Figure 6c shows the tangential strain normalized by the Kolmogorov time scale. Again, the mean tangential strain is positive and shows a weak dependence on the  $u'/S_L$  (especially with  $u'/S_L < 1$ ). The cases

with  $u'/S_L \geq 1$  shows nearly identical variation. Figure 6d presents the stretch probability density. In all four cases the mean is positive, therefore the average local flame speed is reduced by the stretch. The band width increases with Markstein length. Two cases,  $u'/S_L = 2$  and 4, have significant probability of high stretch. This is primarily due to the increase in the Markstein length. The assumption of small stretch (on which the model is based) is certainly called into question for these two cases, though it is not clear how it has manifested itself in the solutions.

### 3.2 Turbulent Flame Speed Estimations

When estimating the turbulent flame speed, it is useful to classify the premixed burning regime. Two parameters were calculated for different  $u'/S_L$  cases. Damköhler numbers, discussed earlier, for these runs are listed in Table 3. Three cases presented here meet the criteria for thin reaction sheet, the fourth,  $u'/S_L = 4$ , where  $D_K = 3.84$ , may not. Another parameter used to classify premixed combustion is the Karlovitz number ( $K_{ar}$ ) which is a dimensionless stretch factor. Using the definition given by Abdel-Gayed and Bradley (1985,1989),  $K_{ar} = (u'/\lambda)(\delta/S_L)$ . The Karlovitz numbers are also presented in Table 3. Three cases, with  $u'/S_L = 0.5, 1$ , and 2 lie in the continuous laminar flame sheet region defined by Abdel-Gayed and Bradley and the  $u'/S_L = 4$  case crosses over into the region where break-up of continuous flame sheet occurs.

Turbulent flame speeds were estimated by two methods. Both methods assume that the ratio of turbulent flame speed to unstretched laminar flame speed is equal to the area ratio of the wrinkled flame to planar flame, that is,  $u_t/S_L = A_F/A_L$ . The  $G$  field provides a convenient means for approximating the wrinkled flame area. The first method makes use of the definition,  $\frac{A_F}{A_L} = \frac{1}{\cos(\theta)} = \frac{\partial G/\partial x}{|\nabla G|}$ , Williams (1985).

This method uses the gradients already calculated for the curvature terms in the stretch and samples all levels of  $G$  and then compiles a volume average. However, this method does not require a continuous sheet to span the entire  $y$ - $z$  planes of the domain, and therefore, becomes inaccurate as the flames approach the ends of the domain (in the  $x$  direction). A second method was adopted that counts the number of flame crossings for a given  $G$ -level and compares this number to that of a planar flame. The ratio is again an approximation to  $A_F/A_L$ . Experiments were performed to ensure that the number of crossings is independent of the  $G$ -level chosen. As long as the flame has not reached the edge of the domain this condition is satisfied. One advantage of this method over the gradient method is that it can be determined exactly when the computational boundaries are reached. Figure 7a shows the evolution of the turbulent flame speed from a planar front for four  $u'/S_L$  cases with stretch effects. The  $u'/S_L = 0.5$  reaches the computational domain edge first, as expected, and the turbulent flame speed goes to zero as the fuel is depleted. The rate of increase in area for all four cases is identical initially, however, as the flame sheets begin to wrinkle, the effects of the Damköhler number becomes discernible. The  $u'/S_L = 0.5$  case has the highest  $D_K$  while the  $u'/S_L = 4$  case has the lowest  $D_K$ . The flame having the higher  $D_K$  is less aware of the background turbulence and remains more planar. Therefore, the rate of increase of turbulent flame speed is less for the  $u'/S_L = 0.5$  case.

Next, we compare the normalized flame speeds obtained in these simulations to three other published results (Yakhot, 1989, Wirth and Peters, 1992, and Gülder, 1990). Yakhot employed renormalization group theory to the propagating equation (8) resulting in a nonlinear expression for

the turbulent flame speed,  $\frac{u_t}{S_L} = \exp\left[\frac{(u'/S_L)^2}{(u_t/S_L)^2}\right]$ . Wirth and

Peters used a spectral closure method to derive a steady turbulent flame speed for the propagation equation (8) including an expression for the stretch similar to (9). They assumed a Markstein number  $M_A = 4$  and  $L_M/\ell = 0.08$ . From our data, this ratio is .028, .055, .110, .220 for  $u'/S_L = 0.5, 1, 2$ , and 4, respectively. Gülder correlated available experimental data and presented a curve fit which is a function of  $u'/S_L$  and a Reynolds number based on the Kolmogorov length. He defined boundaries of the wrinkled flame regime as  $Re_\eta \geq 1.5(u'/S_L)$  and  $Re_L \leq 3200$ . The functional form of the curve fit is  $u_t/S_L = 1 + 0.62(u'/S_L)^{1/2} Re_\eta$ . For our forced turbulence calculations,  $\eta = .041$  and  $Re_\eta = 3.5$  and  $Re_L = 60$ . This is greater than  $1.5u'/S_L$  for  $u'/S_L = 0.5, 1, 2$  but smaller for  $u'/S_L = 4$ . Figure 7b presents the results of our comparison. A single data point for the unstretched case is plotted to show how the stretch effects smooth the flame wrinkling and reduce the turbulent flame speed. The present simulation data lies between Yakhot's prediction and Wirth and Peter's and Gülder's data. Further analysis showed that the decrease in  $u_t/S_L$  is primarily due to the relatively large Markstein Length used in these simulations which results in increasing the stretch effect and thereby decreasing the turbulent flame speed.

### 4. Conclusions

Constant density premixed flames have been simulated in two distinctly different flow configurations; forced/decaying isotropic turbulence and a temporal mixing layer with three-dimensional instability in order to study their characteristic properties. A thin flame propagation model that incorporates flame stretch has been used to simulate thin flames. Data was analyzed mainly in the form of probability density functions and mean quantities. The turbulent flame speed for different  $u'/S_L$  values was also estimated. From this analysis, we make the following conclusions about the flame structures and turbulent flame speeds:

1. The most probable shape of the flame, regardless of the flow configuration is cylindrical. This agrees with Pope et al. (1989) and Ashurst (1992). The practical significance is that it may be possible to study realistic premixed combustion in 2D flows. The probability is decreased slightly due to stretch effects.
2. The flame normal has a large probability of alignment with the most compressive strain rate direction for both flow configurations. Again, this agrees with Ashurst (1992). The probability is slightly decreased by stretch effects. This may be caused by positive stretch which reduces the flames ability to adjust to changing flow conditions.
3. The mean tangential strain rate (in the plane of the flame) is positive, for the isotropic forced/decaying turbulence simulations. This agrees with Cant et al. (1990) and Yeung et al. (1990). This means that most of the time the flame is being pulled apart by the flow, however, there is still a finite probability for the flame to be compressed.

4. The turbulent flame speed as a function of  $u/S_L$  including stretch effects is in reasonable agreement with recently published analytical, numerical, and experimental data. The flame stretch reduces the turbulent flame speed by reducing the degree to which the flame wrinkles.

Topics for further study include the effects of expansion due to heat release, Lewis number effects which enter into the formulation through the Markstein length, and the role stretch plays in flame extinction.

#### Acknowledgment

This research is funded by the Office of Naval Research under Contract No. N00014-92-J-403. The computational resources were provided by the Numerical Aerodynamic Simulation (NAS) at NASA Ames Research Center and are gratefully acknowledged.

#### References

- Abdel-Gayed, R.G. and Bradley, D. (1985) "Criteria for Turbulent Propagation Limits of Premixed Flames," *Combustion and Flame*, 62, pp. 61-68.
- Abdel-Gayed, R.G. and Bradley, D. (1989) "Combustion Regimes and the Straining of Turbulent Premixed Flames," *Combustion and Flame*, 76, pp. 213-218.
- Ashurst, Wm.T., Kerstein, A.R., Kerr, R.M., and Gibson, C.H. (1987) "Alignment of vorticity and scalar gradient with strain rate in simulated Navier-Stokes turbulence," *Phys. Fluids A* Vol. 30, No. 8, August.
- Ashurst, Wm.T., (1990), "Geometry of Premixed Flames in Three-Dimensional Turbulence," Center for Turbulence Research, Proceedings of the Summer Program.
- Ashurst, Wm.T., (1992), "Constant-Density Markstein Flamelet in Navier-Stokes Turbulence," Accepted for Publication *Comb. Sci. Tech.*, Aug.
- Asato, K., Kawamura, T., and Ban, T. (1988) "Effects of Curvature on Extinction of Premixed Flames Stabilized in Stagnation Flow," Twenty-Second Symposium (International) on Combustion, The Combustion Institute, p. 1509.
- Cant, R.S., Rutland, C.J., and Trounev, A. (1990) "Statistics for laminar flamelet modeling," CTR Proceedings of the Summer Program, pp. 271-279.
- Clavin, P. (1985) "Dynamic Behavior of Premixed Flame Fronts in Laminar and Turbulent Flows," *Prog. Energy Combust. Sci.*, Vol. 11, pp. 1-59.
- Clavin, P. and Williams, F.A. (1982) "Effects of molecular diffusion and of thermal expansion on the structure and dynamics of premixed flames in turbulent flows of large scale and low intensity," *J. Fluid Mech.*, vol. 116, pp. 251-282.
- Deshaies, B. and Cambray, P. (1990) "The Velocity of a Premixed Flame as a Function of the Flame Stretch: An Experimental Study," *Combustion and Flame*, 82, pp. 361-375.
- Echekki, T. and Mungal, M.G. (1990) "Flame Speed Measurements at the Tip of a Slot Burner: Effects of Flame Curvature and Hydrodynamic Stretch," Twenty-Second Symposium (International) on Combustion, The Combustion Institute, p. 771.
- Gülder, Ö. L., (1990) "Turbulent Premixed Flame Propagation Models for Different Combustion Regimes," Twenty-Third Symposium (International) on Combustion, The Combustion Institute, pp. 743-750.
- Kerr, R.M. (1985) "Higher-order derivative correlations and the alignment of small-scale structures in isotropic numerical turbulence," *J. Fluid Mech.* vol. 53, pp. 31-58.
- Kerstein, A.R., Ashurst, W.T., and Williams, F.A., (1988), "The Field Equation for Interface Propagation in an Unsteady Homogeneous Flow field", *Phys. Rev. A*. 37, 2728.
- Lee, M.J. and Reynolds, W.C., (1985) "Numerical Experiments on the Structure of Homogeneous Turbulence," Report no.TF-24, Dept. of Mechanical Engineering, Stanford University, Stanford, CA.
- Lee, T.W., North, G.L. and Santaviceca, D.A. (1992) "Curvature and Orientation Statistics of Turbulent Premixed Flame Fronts," *Combustion Science and Technology*, Vol. 84, pp. 121-132.
- Linán and Williams, F.A. (1993) Fundamental Aspects of Combustion, Oxford University Press.
- McMurtry, P.A. (1993) Private communications.
- McMurtry, P.A., Jou, W.-H., Riley, J.J., and Metcalfe, R.W., (1986), "Direct Numerical Simulations of a Reacting Mixing Layer with Chemical Heat Release", *AIAA J.*, vol. 24, No. 6, p. 962.
- McMurtry, P.A., Riley, J.J., and Metcalfe, R.W., "Effects of Heat Release on the Large-Scale Structure in Turbulent Mixing Layers", (1989), *J. Fluid Mech.*, vol. 199, pp. 297-332.
- Menon, S., and Jou, W.H., (1991), "Large-Eddy Simulations of Combustion Instability in an Axisymmetric Ramjet Combustor," *Combustion Science and Technology*, Vol. 75, pp. 53-72.
- Metcalfe, R.W., Orszag, S.A., Branchet, M.E., Menon, S., and Riley, J.J., (1987), "Secondary Instability of a Temporally Growing Mixing Layer," *J. Fluid Mech.*, Vol. 184, pp. 207-243.
- Pope, S.B., Yeung, P.K., and Girimaji, S.S., (1989), "The Curvature of Material Surfaces in Isotropic Turbulence," *Physics of Fluids*, Vol. 1, No.12, pp. 2110-2018.
- Poinsot, T. Veynante, D. and Candel, S. (1991) "Quenching processes and premixed turbulent combustion diagrams," *J. Fluid Mech.*, vol. 228, pp. 561-606.
- Rutland, C.J. and Trounev, A. (1993) "Direct Simulations of Premixed Turbulent Flames with Nonunity Lewis Numbers," *Combustion and Flame*, 94, pp. 41-57.
- Rutland, C.J. Ferziger, J.H. and El Tahry, S.H. (1990) "Full Numerical Simulations and Modeling of Turbulent Premixed

Flames." Twenty-Third Symposium (International) on Combustion, The Combustion Institute, pp. 621-627.

Searby, G. and Quinard, J. (1990) "Direct and Indirect Measurements of Markstein Numbers of Premixed Flames," *Combustion and Flame*, 82, pp. 298-311.

Trounev, A. and Poinso, T. (1993) "The evolution for the flame surface density in turbulent premixed combustion," Submitted to *J. Fluid Mech.*

Williams, F.A. (1985) Combustion Theory. 2nd ed. The Benjamin/Cummings Publishing Company, Inc.

Wirth, M. and Peters, N. (1992) "Turbulent Premixed Combustion: A Flamelet Formulation and Spectral Analysis in Theory and IC-Engine experiments," Twenty-Fourth Symposium (International) on Combustion, The Combustion Institute, pp. 493-501.

Yakhot, V. (1988) "Propagation Velocity of Premixed Turbulent Flame," *Comb. Sci. Tech.*, Vol. 60.

Yeung, P.K., Girimaji, S.S., and Pope, S.B. (1990) "Straining and Scalar Dissipation on Material Surfaces in Turbulence: Implications for Flamelets," *Combustion and Flame*, Vol. 79, pp. 340-365.



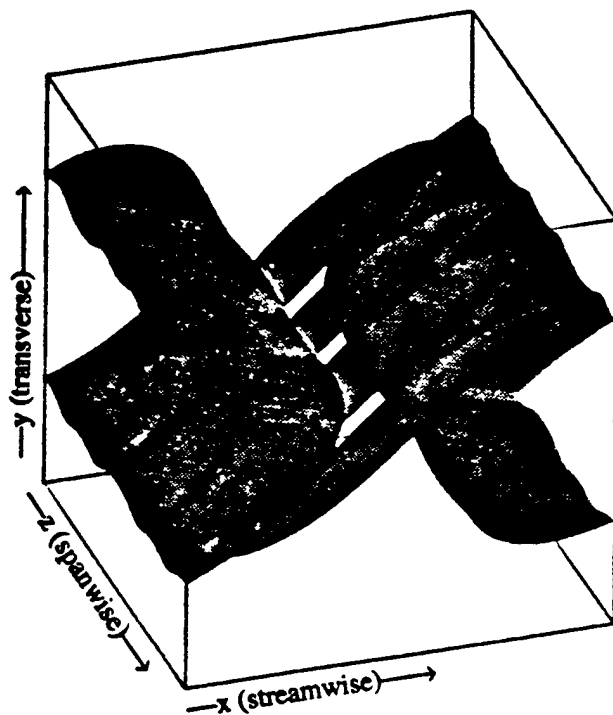


Figure 1a. Three-dimensional perspective of constant vorticity magnitude in a 3D mixing layer, showing the main spanwise vortex and pairs of counter-rotating streamwise vortices.

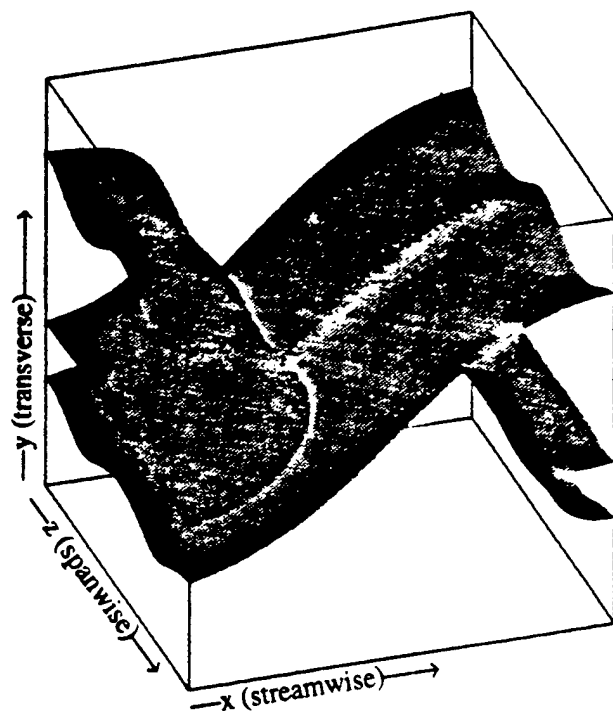


Figure 1b. Three-dimensional perspective of a flame sheet (at the instant shown in Figure 1a), in a 3D mixing layer, at a constant value of  $G$ . Warping by the vorticity is evident.

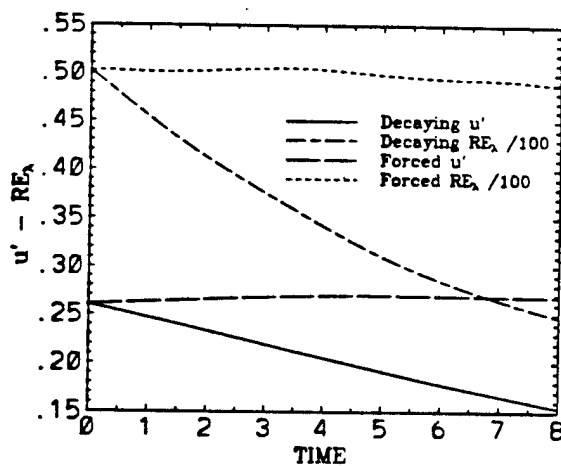


Figure 2a. Time evolution of the r.m.s. velocity fluctuation and Taylor Reynolds number in forced and decaying isotropic turbulence.

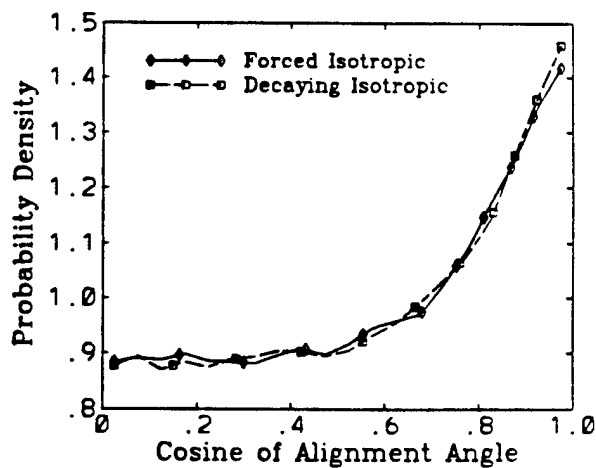


Figure 2b. Probability density of the alignment between the vorticity and intermediate strain rate direction for forced and decaying isotropic turbulence.



Figure 3a. Three-dimensional perspective plot of constant vorticity magnitude in isotropic turbulence, showing tube like coherent vortical structures.

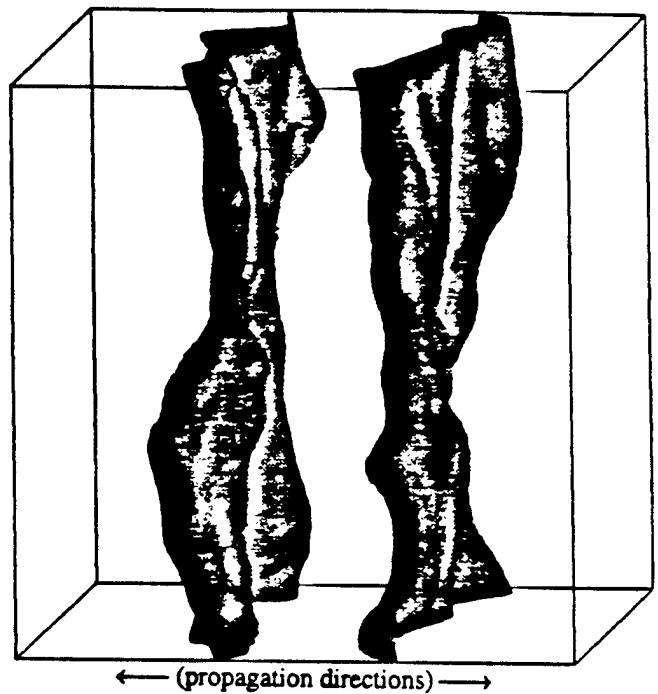


Figure 3b. Three-dimensional perspective of twin flame sheets propagating through isotropic turbulence in opposite directions.

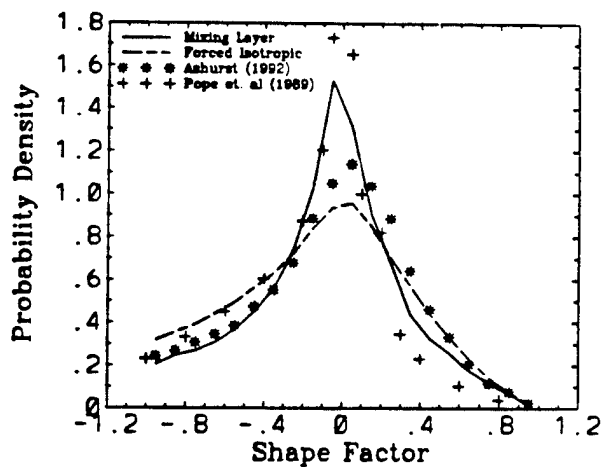


Figure 4a. Probability density of the shape factor in a 3D mixing layer, forced isotropic turbulence, and data from Ashurst (1992) and Pope et al. (1989).

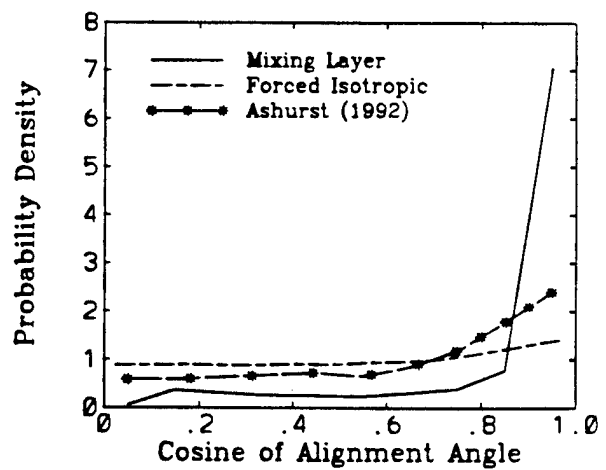


Figure 4b. Probability density of the vorticity/strain rate alignment for the 3D mixing layer, forced isotropic turbulence, and data from Ashurst (1992).



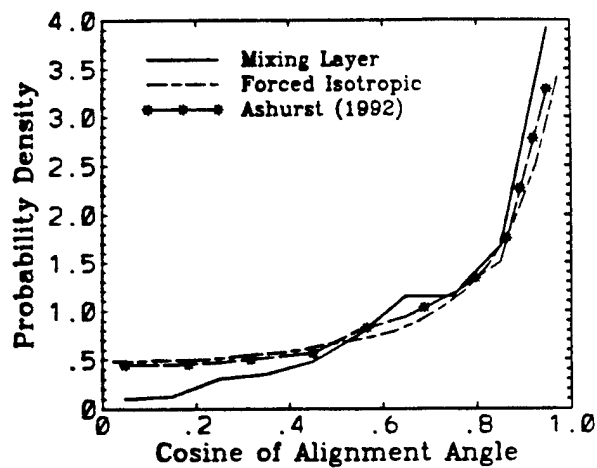


Figure 4c. Probability density of the flame normal/strain rate alignment for the 3D mixing layer, forced isotropic turbulence, and data from Ashurst (1992).

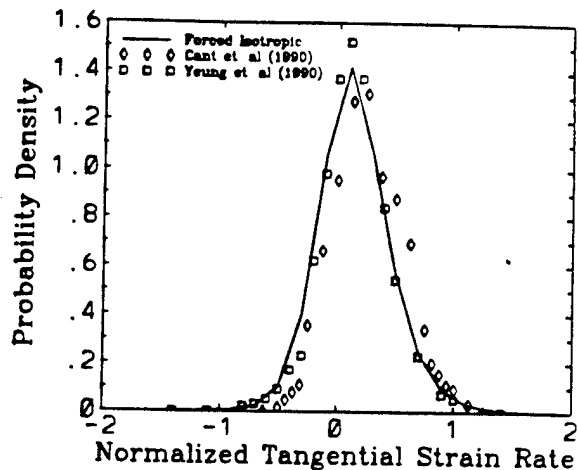


Figure 4d. Probability density of the normalized tangential strain rate for forced isotropic turbulence, data from Cant et al. (1990) and Yeung et al. (1990).

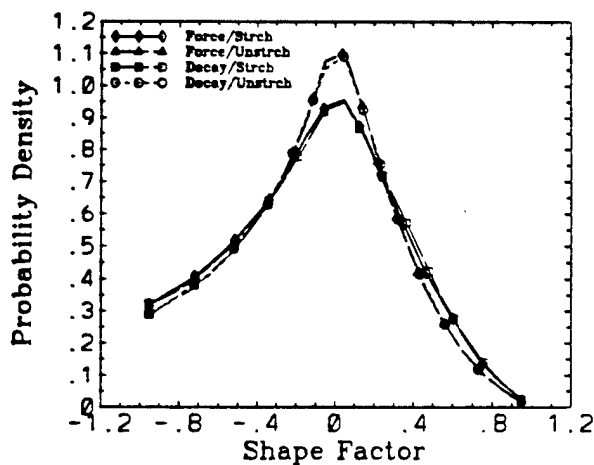


Figure 5a. Probability density of the shape factor of flame sheets propagating in forced/decaying isotropic turbulence, with/without stretch effects.

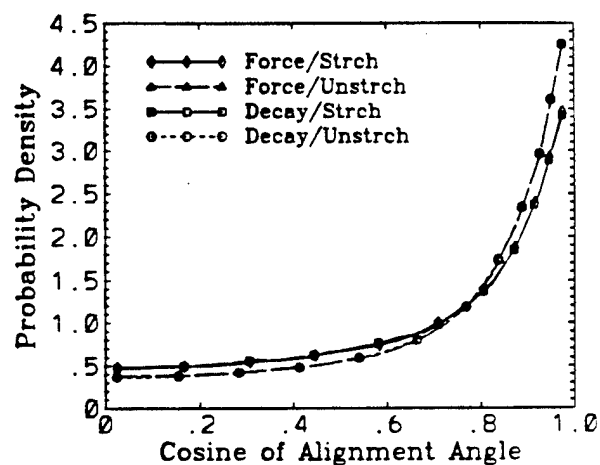


Figure 5b. Probability density of the flame normal/strain rate alignment of flame sheets in forced/decaying isotropic turbulence, with/without stretch effects.

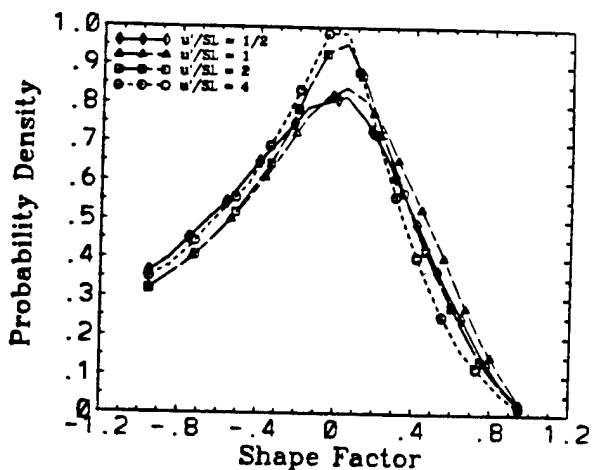


Figure 6a. Probability density of the shape factor of the flame sheets propagating through forced isotropic turbulence for different values of  $u'/S_L$ .

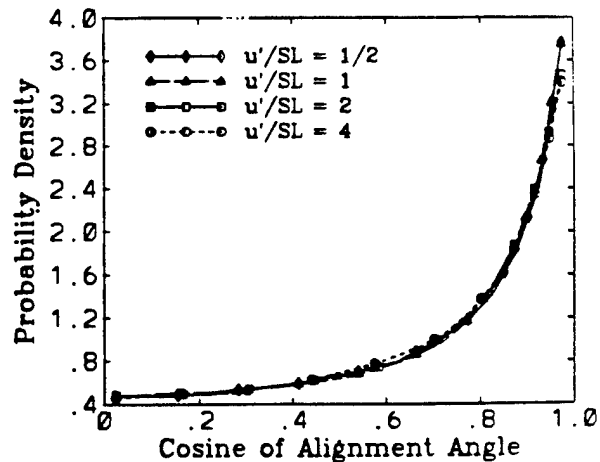


Figure 6b. Probability density of the flame normal/strain rate alignment of flame sheets propagating through forced isotropic turbulence for different values of  $u'/S_L$ .

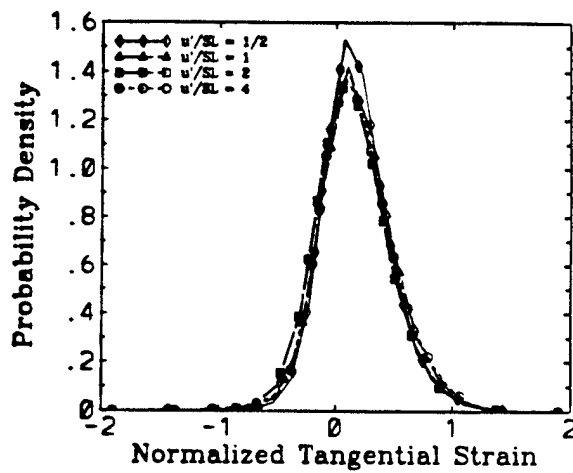


Figure 6c. Probability density of the normalized strain rate of flame sheets propagating through forced isotropic turbulence for different values of  $u'/S_L$ .

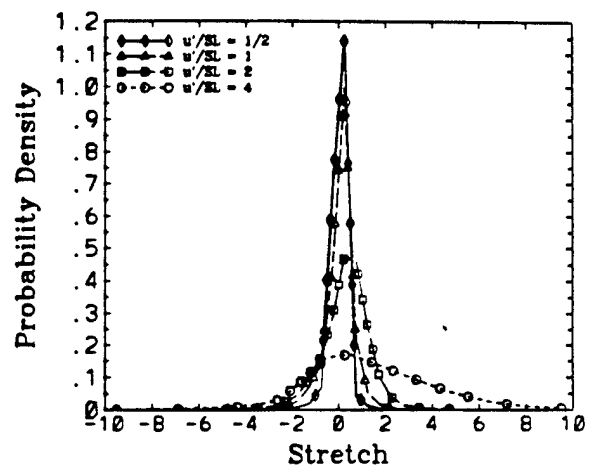


Figure 6d. Probability density of the stretch experienced by flame sheets propagating through forced isotropic turbulence for different values of  $u'/S_L$ .

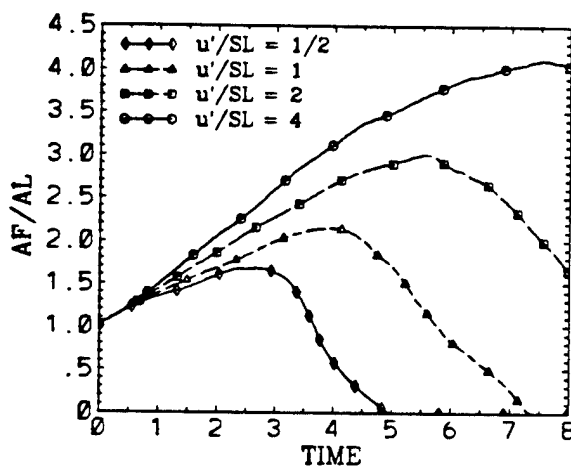


Figure 7a. Time evolution of the turbulent flame speed for flame sheets propagating through forced isotropic turbulence for different values of  $u'/S_L$ .

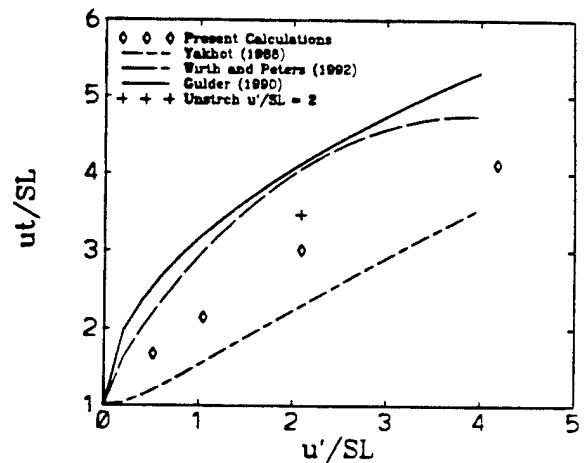


Figure 7b. Normalized turbulent flame speed as a function of  $u'/S_L$  compared with models of Yakhot (1988), Wirth and Peters (1992), and Gülder (1990).



AIAA 93-1914

Parallel Computations of  
Unsteady Combustion in a Ramjet Engine

S. Weeratunga, NASA Ames Research  
Center, CA

S. Menon, Georgia Institute of Technology,  
Atlanta, GA

**AIAA/SAE/ASME/ASEE  
29th Joint Propulsion  
Conference and Exhibit  
June 28-30, 1993 / Monterey, CA**

# PARALLEL COMPUTATIONS OF UNSTEADY COMBUSTION IN A RAMJET ENGINE

Sisira Weeratunga  
NASA Ames Research Center  
Moffett Field, California

and

Suresh Menon  
School of Aerospace Engineering  
Georgia Institute of Technology  
Atlanta, Georgia

## ABSTRACT

Combustion instability in ramjets is a complex phenomenon that involve nonlinear interaction between acoustic waves, vortex motion and unsteady heat release in the combustor. To numerically simulate this phenomenon, very large computer resources (both time and memory) are required. Although current vector supercomputers are capable of providing adequate resources for simulations of this nature, the high cost and their limited availability, makes practical use of such machines less than satisfactory. To investigate the use of massively parallel systems for unsteady simulations, a large-eddy simulation model for combustion instability was implemented on the Intel iPSC/860 and a careful investigation was carried out to determine the benefits and problems associated with the use of highly parallel distributed processing machines for unsteady simulations. Results of this study along with some of the results of the simulations carried out on the iPSC/860 are discussed in this paper.

## 1. INTRODUCTION

Ramjet combustors exhibit combustion instability under certain operating conditions, which manifests itself as highly unsteady combustion accompanied by large amplitude pressure oscillations. Such combustion instabilities tend to have an adverse effect on the performance of ramjet combustors and limit the practical utility of such devices. These combustion instabilities are a result of highly complex nonlinear interactions among acoustic waves, vortex motion and heat release involving a multitude of temporal and spatial scales. Among the instabilities that are most difficult to control are those associated with the low frequency (100-800 Hz.), longitudinal pressure waves. When the amplitude of these acoustic waves reaches a critical level, it can lead to an engine unstart as a result of the shock in the inlet duct being expelled to form a bow shock ahead of the inlet, and/or to structural damage caused by metal fatigue. Due to the serious nature of the engine unstart on the operation of ramjet engines, a major research effort involving both experimental (e.g., Schadow et al., 1987; Smith and Zukoski, 1985; Sterling and Zukoski, 1987; Hedge et al., 1987; Dowling, 1989; Yu et al., 1991) and numerical simulations (e.g., Menon and Jou, 1987, 1990; Menon and Jou, 1991; Jou and Menon, 1990; Kailasanath et al., 1989) were undertaken to identify the mechanisms responsible in the combustion instability and to devise ways to control it.

This paper concerns with the numerical simulation of combustion instability in ramjet combustors. In previous research work, a finite-volume based simulation model was developed to compute the unsteady compressible flow field associated with an axisymmetric ramjet combustor (Menon and Jou, 1987, 1991). The scheme uses a thin-flame combustion model developed by (Williams, 1985; Kerstein et al., 1988), based on the ideas of flame front tracking, to represent the temporally and spatially evolving combustion process and the associated heat release inside the combustor. This approach does away with the high computational complexity associated with the combustion models based on finite-rate chemical kinetics as well as their other related computational difficulties. The combustion model is supplemented by a large-eddy simulation (LES) methodology to treat the relatively high Reynolds number turbulent flow field of the ramjet combustor. The numerical realization of this mathematical model was carried out in a way that maintains the requisite temporal and spatial accuracy based on an explicit time integration using MacCormack's unsplit scheme. The resultant code implemented on a single processor of Cray-YMP was used to study the combustion instabilities associated with ramjet combustors, including the aspects of their active control (Menon, 1991, 1992a, 1992b, 1993). Some of the results obtained from the numerical simulations have been validated against experimental data.

Computation of the unsteady, turbulent flow field associated with ramjet combustor instability is currently limited to axisymmetric geometries at low to moderate Reynolds numbers. These computations are characterized by barely adequate mesh resolution and simplified subgrid scale turbulence models. Even with such simplifications, the number of configuration and parameter space studies that can be carried out is rather limited. One of the primary reasons for this state of affairs with regard to unsteady flow simulations is their very large computer resource requirements both in terms of CPU time and computer memory. Although some of the current generation of vector supercomputers such as Cray-YMP-C90 and NEC SX-3, are fully capable of providing adequate resources for simulations of this nature, the high cost of such machines and consequently their limited availability, makes the use of such machines less than satisfactory for 3-D, moderate to high Reynolds number simulations with appropriate mesh resolutions and meaningful subgrid turbulence models.

From a computer hardware point of view, single processor machines are rapidly approaching fundamental limitations on performance due to limits on signal transmission speed, switching delays etc. making their continued development a risky and expensive process. At the same time, the explicit time integration algorithms used in unsteady flow simulations often possess a very high degree of parallelism, making them very amenable to efficient implementation on large-scale parallel computers. Under these circumstances, distributed memory parallel computers offer an excellent near-term solution for greatly increased computational speed and memory, at a cost that may render the combustor simulations of the type discussed above more feasible and affordable. Among the recent advances in computer hardware technologies that lend credibility to such expectations are the 64-bit, high-performance Reduced Instruction Set Computing (RISC) microprocessor chips, high density Dynamic Random Access Memory (DRAM) chips and high-speed interconnect networks that are easily scalable to the level of hundreds of nodes. The essential remaining ingredient for this mode of computing is the development and implementation of numerical algorithms that are capable of retaining high parallel efficiencies on distributed memory parallel architectures, when the number of processors used range in the hundreds.

The programming environment that is provided for majority of the current generation distributed memory, Multiple Instruction Multiple Data (MIMD) machines lacks advanced software engineering tools comparable to those found in vector supercomputers to aid in program development. As a result, an extra implementation effort involving a complete top down analysis of the entire numerical scheme in search of exploitable parallelism and data dependencies is often required. In addition, an in-depth knowledge of the underlying computer hardware is also needed. Nevertheless, once an efficient implementation is realized, the current generation of distributed memory MIMD parallel computers can provide performance comparable to vector supercomputers in many areas of unsteady fluid flow simulation. In this paper, we discuss these issues in the context of numerical simulation of combustion instability of a ramjet combustor on Intel iPSC/860, a distributed memory MIMD machine with 128 processors.

The primary goals of this investigation are: a) to investigate the benefits and problems associated with the use of highly parallel distributed memory MIMD computers in carrying out unsteady flow simulations, and, b) to verify and extend the range of applicability of the results from previous ramjet combustor simulation efforts by performing configuration, mesh refinement and parameter space studies. The emphasis of this paper is on the first objective, although some results of the unsteady combustion simulations are also shown and discussed.

## 2. MATHEMATICAL MODEL

In this section, for completeness, we provide an abbreviated description of the mathematical model used for the ramjet combustor instability study. A more detailed description of the mathematical model along with the underlying justifications for various simplifying assumptions can be found in (Menon and Jou, 1987, 1990, Menon and Jou, 1991). The flow field is modeled using the unsteady, compressible Navier-Stokes equations:

$$\frac{\partial \rho}{\partial t} + \nabla \cdot (\rho \mathbf{v}) = 0 \quad (1)$$

$$\frac{\partial (\rho \mathbf{v})}{\partial t} + \nabla \cdot (\rho \mathbf{v} \mathbf{v} + p \mathbf{I}) = \nabla \cdot \boldsymbol{\sigma}, \quad (2)$$

$$\frac{\partial (\rho E)}{\partial t} + \nabla \cdot (\rho \mathbf{v} H + \mathbf{q} - \mathbf{v} \cdot \boldsymbol{\sigma}) = 0 \quad (3)$$

where  $\rho$ ,  $p$  and  $\mathbf{v}$  are the fluid density, pressure and velocity vector respectively.  $\mathbf{I}$  is the identity tensor,  $\boldsymbol{\sigma}$  is the shear stress tensor,  $\mathbf{q}$  is the heat flux vector,  $E$  is the total energy and  $H$  is the total enthalpy. These quantities are defined as follows:

$$\boldsymbol{\sigma} = \mu (\nabla \mathbf{v} + \nabla' \mathbf{v}) + \lambda (\nabla \cdot \mathbf{v}) \mathbf{I}$$

$$\mathbf{q} = -\kappa \nabla T,$$

$$E = C_v T + \frac{1}{2} \mathbf{v} \cdot \mathbf{v}, \quad H = E + (p/\rho), \quad p = \rho R T$$

### 2.1. Combustion Model

Following the work of (Williams, 1985; Kerstein et al., 1988), the premixed, turbulent combustion process occurring in the ramjet combustor was previously modeled as a thin, wrinkled interface that separates the burnt from the unburnt regions (Menon and Jou, 1991). This interface, while being convected by the surrounding unsteady flow field, also undergoes propagation normal to itself toward the unburnt region at a rate that depends on the local curvature of the interface and the local strain field. Propagation of the interface into the unburnt region is accompanied by heat release at the interface, which in turn causes volumetric expansion of the surrounding fluid. This induces global as well as local distortions of the strain field.

Mathematically, this interface propagation problem is cast as an initial value problem for a scalar field  $G(\mathbf{x}, t)$ , one of whose level surfaces represent the interface. Then, the propagation of the interface is governed by the following non-linear scalar field equation:

$$\frac{\partial G}{\partial t} + \mathbf{v} \cdot \nabla G = -u_f |\nabla G|. \quad (4)$$

If a particular value of this scalar field, say  $G_c$ , is chosen to be associated with the flame front, then it can be tracked over the time steps by simply plotting the level surface for  $G_c$  at each time step. As a result, no discrete parameterization of the flame front itself is necessary. Therefore, the model can easily cope with the complex shape changes of the evolving flame front including such effects as development of cusps and spikes, both in two and three space dimensions. In flame front modeling,  $G$  exhibits a step function like behavior, separating the burnt region from the unburnt region.  $G$  is normally assigned the value of unity in the unburnt region and zero in the burnt region. To avoid numerical difficulties associated with propagating a step function,  $G$  is assumed to be a continuous function, which results in the capturing of the flame front as a smeared discontinuity. The value of  $G(\mathbf{x}, t) = 0.50 = G_c$  is chosen to mark the flame front, while  $1.0 \geq G(\mathbf{x}, t) > 0.50$  indicates the unburnt region and  $0.0 \leq G(\mathbf{x}, t) < 0.50$  indicates the burnt region. The implications of this numerical artifact on the simulation integrity are discussed in greater detail elsewhere (Menon and Jou, 1991). The description of the model is completed by prescribing the local turbulent flame speed,  $u_f$ , which is assumed to be a function of the laminar flame speed  $S_L$  and the local sub-grid scale turbulence intensity  $u'$ . The laminar flame speed contains the information associated with the chemical reaction kinetics of the flame and the molecular diffusion. The following functional relationship between  $u_f$ ,  $S_L$  and the subgrid turbulence intensity has been

obtained by Yakhot (1988) through renormalization group theory:

$$\frac{u_F}{S_L} = \exp \left[ \frac{u'^2}{u_F^2} \right] \quad (5)$$

The chemical heat release associated with the propagation of the flame front is a function of  $G$  and the specific chemical energy of the fuel mixture. Consequently, the specific enthalpy of the mixture is defined as:  $h = C_p T + h_f G$ , where  $h_f$  is the heat of formation of the premixed fuel,  $C_p$  is the specific heat of the mixture at constant pressure and  $T$  is the temperature of the mixture. At present, the burnt and unburnt gases are assumed to have the same fluid properties, such as  $\gamma$ ,  $C_p$  and  $C_v$ .

## 2.2. Subgrid Model

In order to close the combustion model, the subgrid turbulence intensity must be determined. Due to the absence of well-proven subgrid models for high Reynolds number compressible flows, the following one-equation model for the subgrid turbulent kinetic energy (Menon, 1991) is currently implemented for further evaluation in future studies:

$$\frac{\partial k}{\partial t} + \nabla \cdot (\rho \mathbf{v} k) = P_k - D_k + \frac{\partial}{\partial x_i} \left[ \rho v_i \frac{\partial k}{\partial x_i} \right] \quad (6)$$

Here,  $\rho$ , and  $u_i$  are the filtered, large-scale density and velocities respectively and  $k = \frac{1}{2} \langle u'^2 \rangle$  is the subgrid turbulent kinetic energy.

Also,  $P_k$  and  $D_k$  are respectively the production and dissipation of  $k$ , and they are being modeled as:

$$P_k = C_k \rho v_i \left( 2 S_{ij} S_{ij} \right) \quad (7)$$

and

$$D_k = C_\epsilon \rho \frac{k^{3/2}}{\Delta_t} \quad (8)$$

where the strain tensor  $S_{ij}$  and the subgrid eddy viscosity  $\nu$ , are defined as:

$$S_{ij} = \frac{1}{2} \left( \frac{\partial u_i}{\partial x_j} + \frac{\partial u_j}{\partial x_i} \right) \quad (9)$$

$$\nu = C_\nu k^{1/2} \Delta_t \quad (10)$$

Here,  $\Delta_t$  is the characteristic grid size and  $C_k$ ,  $C_\epsilon$  and  $C_\nu$  are constants to be prescribed. Once  $k$  is known, the subgrid turbulence intensity  $u'$  appearing in Equation (5) can be easily determined ( $u' = \sqrt{2k}$ ). This  $k$  equation model is also used to determine the turbulent subgrid fluxes appearing in the momentum and energy equations (Menon, 1992b).

## 2.3. Ramjet Combustor Geometry and Computational Mesh

The geometry of the ramjet combustor, as depicted in Figure 1a, consists of a circular inlet duct of diameter  $D_i$  followed by a sudden expansion into a larger circular dump combustor of diameter  $D_c$ . Downstream of the combustor is a convergent-divergent nozzle which is used to accelerate the low subsonic flow in the combustor to supersonic flow at the nozzle outlet. The flow field inside the ramjet is extremely complex and highly unsteady. However, as elaborated in Menon and Jou (1987, 1990), the primary aspects of the flow physics of interest to this investigation may be represented by

an axisymmetric flow field to a sufficient degree of accuracy. Invocation of the axisymmetric approximation to the flow field leads to a significant reduction in the computational complexity as well as the overall cost of the simulations. A body-conforming, tensor product mesh of quadrilateral cells is used to discretize the combustor geometry, which is now reduced to a single circumferential plane. Algebraic interpolation with a stretching function based on hyperbolic tangent (Thompson et al., 1985) is used to generate the body-conforming tensor product mesh in the physical space with appropriate mesh line clustering in regions where strong gradients are likely to exist. A typical grid distribution used to model the combustor is shown in Figure 1b. The regions where the mesh is clustered and the accompanying justifications can be found in Menon and Jou (1987). This results in a  $L$ -shaped computational domain  $G$  with a logically-structured rectangular mesh in the computational space, as shown in Figure 2.

## 2.4. Boundary Conditions

On  $\Gamma_1$  (see Figure 2), which is a subsonic inflow boundary, the stagnation pressure, the stagnation temperature and the local flow direction is specified. The characteristic variable carried by the outgoing characteristic is determined by solving the pertinent decoupled interior characteristic equation. Along the centerline of the device, represented by  $\Gamma_2$ , relevant symmetry conditions are applied to all flow variables. The flow at the nozzle exit  $\Gamma_3$  is assumed to be supersonic and all flow variables are set by extrapolation from the interior. The solid walls denoted by  $\Gamma_4$  are assumed to be adiabatic and no-slip condition with pressure extrapolation is applied. Again, a more detailed discussion on the type of boundary conditions applied at the numerical boundaries and their impact on the simulation can be found in Menon and Jou (1987).

## 2.5. Numerical Algorithm

In this section, we present a brief overview of the well known numerical algorithm used in this study to facilitate the subsequent discussion of issues pertaining to the parallel implementation. The governing partial differential equations are integrated explicitly in time using the unsplit MacCormack predictor-corrector scheme, based on the standard cell-centered finite volume formulation (Peyret and Taylor, 1983). The composite numerical scheme is second-order accurate in both time and space and, being an explicit scheme, is conditionally restricted by the Courant and viscous stability limits of the system of governing equations. The governing Equations (1)-(6) are combined to form a system of partial differential equations, that can be written in the following familiar form, under the assumption of an axisymmetric flow field:

$$\frac{\partial U}{\partial t} + \frac{\partial F}{\partial x} + \frac{1}{y} \frac{\partial (yG)}{\partial y} = \frac{Q}{y}, \quad (11)$$

where,  $U = [\rho, \rho u, \rho v, \rho E, \rho G, \rho k]^T$  is the vector of conserved (resolved) variables,  $F' = [\rho u, \rho u^2 + p, \rho u v, \rho u H, \rho u G, \rho u k]^T$  and  $G' = [\rho v, \rho u v, \rho v^2 + p, \rho v H, \rho v G, \rho v k]^T$  are the inviscid flux vectors,  $F^V = [0, \bar{\tau}_{xx}, \bar{\tau}_{xy}, u \bar{\tau}_{xx} + v \bar{\tau}_{xy} - \bar{q}_x, 0, \rho v k_x]^T$  and  $G^V = [0, \bar{\tau}_{xy}, \bar{\tau}_{yy}, u \bar{\tau}_{xy} + v \bar{\tau}_{yy} - \bar{q}_y, 0, \rho v k_y]^T$  are the viscous flux vectors. Here,  $F = F' - F^V$  and  $G = G' - G^V$ , and  $Q = [0, 0, p + \bar{\tau}_{xx}, 0, -(\rho u_f) |\nabla G|, P_k - D_k]^T$  is the vector of source terms. Also,  $\bar{\tau}_{ij} = \tau_{ij} - \pi_{ij}$  is the total stress tensor and  $q_i = q_i - \epsilon_i$  is the total heat flux such that  $\tau_{ij}$  and  $q_i$  are the components of the resolved-scale viscous stress tensor while  $\pi_{ij}$  are components of the subgrid (modeled) stresses and  $\epsilon_i$  are components of the subgrid (modeled) heat flux. The subgrid contribution to the governing equations can be obtained using simplified closure methods in terms of an algebraic subgrid eddy viscosity model and the resolved rate-of-strain tensor  $S_{ij}$  (e.g. Erlebacher et al., 1987) or by using a model

for the subgrid kinetic energy as proposed here.

The finite-volume method is based upon an integral form of the Equation (11):

$$\frac{\partial U^h_{ij}}{\partial t} + \frac{1}{V_h} \int_{\Gamma_h} (y F dy - y G dx) = \frac{A_h}{V_h} Q_{ij} \quad (12)$$

where  $\Omega_h$  is a typical quadrilateral cell with a boundary  $\Gamma_h$  as shown in Figure 3a and  $U^h$  is the cell-averaged vector of conserved variables associated with cell centers. The line integrals in Equation (12) are approximated by midpoint rule, resulting in the following semi-discrete equation:

$$\frac{\partial U^h_{ij}}{\partial t} + \frac{1}{V_h} (R_{AB} + R_{BC} + R_{CD} + R_{DA}) = \frac{A_h}{V_h} Q_{ij} \quad (13)$$

in which the fluxes through the cell edges are given by expressions similar to the following:

$$R_{CD} = y_{CD} F_{CD} (y_C - y_D) - y_{CD} G_{CD} (x_C - x_D)$$

where  $y_{CD}$ ,  $F_{CD}$  and  $G_{CD}$  are the mean values of  $y$ ,  $F$  and  $G$  on the edge CD. The inviscid flux vectors  $F'$  and  $G'$  that depend only on  $U$  are defined as:

$$F'_{CD} = \alpha_i F'(U^h_{ij}) + (1 - \alpha_i) F'(U^h_{i+1,j})$$

and,

$$G'_{CD} = \alpha_i G'(U^h_{ij}) + (1 - \alpha_i) G'(U^h_{i+1,j})$$

where  $\alpha_i = 0$  or 1. Similar expressions are used along the remaining cell edges, to obtain  $F'_{BC}$  and  $G'_{BC}$  using  $\alpha_j$  instead of  $\alpha_i$ . The viscous flux vectors  $F^v$  and  $G^v$  involve the first derivatives, so that it is necessary to define the mean values of these at cell edges. These are obtained through finite-difference approximations by assuming the center of the cell  $(i, j)$  belongs to a curvilinear coordinate system  $\xi(x, y) = \text{const}$  and  $\eta(x, y) = \text{const}$  as shown in Fig. 3b.

In the final form, the geometry of the mesh appears only as coordinates of the cell vertices and the cell center. The first derivatives in source vector  $Q$  are similarly evaluated at the cell centers. The semi-discretized system of equations can be written as:

$$\frac{dU^h_{ij}}{dt} + \left[ \frac{1}{V_{ij}} \right] S_{ij} = 0$$

where  $S_{ij} = R_{AB} + R_{BC} + R_{CD} + R_{DA} - A^h Q^h_{ij}$  is a function of vectors  $U^h_{i,j,k}$  and  $\beta$ ,  $\delta = -1, 0, 1$ . The solution is advanced from  $U^h_{ij}$  to  $U^{n+1}_{ij}$  through the well known MacCormack's explicit, two-step predictor-corrector scheme.

The values of  $\alpha_i$  and  $\alpha_j$  alternate between 0 and 1 through the predictor and corrector steps as well as between the successive time steps in a prescribed manner. Thus, the algorithm proceeds from one time step to the next by repeatedly computing the corrections to the flow variables associated with each cell, based on the summation of the flux vectors through all its edges and the source term vector at its center. Since these flux and source term vectors are computed using the cell-center variables already computed during the previous stage, the corrections to any cell in a given stage can be computed completely independent of those of other cells. Also, for a given cell, the computation of these flux and source term vectors depends at most on the values at eight neighboring cell-centers, as depicted in Figure 4a. Thus, the algorithm has a highly localized spatial data dependency. The cell-vertex coordinates needed for this computation are shown in Figure 4b.

### 3. THE INTEL iPSC/860 SYSTEM ARCHITECTURE

The performance data for the parallel implementation discussed in this paper were obtained on a 128 processor Intel iPSC/860 at the NASA Ames Research Center. In the following sections, we provide a brief overview of the specific hardware and software characteristics of this machine.

#### 3.1. Hardware

The iPSC/860 system is an aggregate of computing nodes that are interconnected with a communication network having a hypercube topology. Each computing node consists of three main components; the i860 microprocessor, the local memory and the inter-node communication hardware. The iPSC/860 at the NASA Ames Research Center consists of 128 such computational nodes, each with 8 Mbytes of memory. The i860 is a 40 MHz. reduced instruction set (RISC) microprocessor that features multiple pipelined processing units, on-chip data and instruction caches, large register sets and an internal 128-bit wide data path. As a result of its ability to operate upto three processing units concurrently, the i860 is capable of delivering a theoretical peak performance of 60 Mflops in 64-bit computations. The 128 node iPSC/860 delivers an aggregate peak performance of 7.6 Gflops on 64-bit data and supports a total of one Gbyte of random access memory. This peak performance rate is based on ideal conditions with regard to mix of instructions, cache utilization, pipelining, data alignment etc. which are seldom realized in practical CFD computations.

The 128 processors in the iPSC/860 are interconnected by a circuit-switched, 7-dimensional hypercube communication network. Each computational node interfaces with the network through a dedicated communication processor called the Direct-Connect Module (DCM). The DCM can supervise upto 8 bi-directional, bit-serial channels with a peak data transfer rate of 2.8 Mbytes per second per channel. Seven of these channels are used for connecting to the direct neighbors in the hypercube and the remaining channel is reserved for the I/O. A communication request between any two nodes is fulfilled by dynamically building a path between the two nodes involved using free channels belonging to intermediate nodes. The path is determined by a special router algorithm, and if a free path can be constructed, it is reserved until the communication request between the two nodes is completed. All activities involved in the communication path set-up and message routing are handled by the DCM without any intervention from the i860. As a result, messages can pass equally quickly between adjacent nodes and nodes at the opposite corners of the interconnection network, provided there is no channel contention. Thus, it effectively emulates a fully connected network with very little penalty for non-neighbor communications.

Attached to the communication network over the 8-th DCM channel are 10 I/O-nodes, each of which is an Intel 80386 processor with approximately 700 Mbytes of disk space. These I/O nodes form the Concurrent File System (CFS) with a total capacity of 7 Gbytes. The I/O-nodes are directly accessible to the computational nodes over the interconnection network. The peak data transfer rate between a single computational node and the CFS is about 1.5 Mbytes per second. This translates into a peak transfer rate of approximately 15 Mbytes/sec. However, the actual transfer rates realized in practical computations are much lower due to contention for I/O nodes, network congestion and inefficient file cache utilization.

#### 3.2. System Software

The iPSC/860 is controlled by an attached host computer, referred to as the System Resource Manager (SRM). The SRM serves as the machine's interface to outside world by providing

such functions as system resource management and external network access. Each of the computational nodes in the iPSC/860 runs a simplified operating system known as NX/2 that supervises process execution and supports buffered, queued message passing over the interconnection network with other computational nodes, I/O nodes and the SRM. All interprocessor communication on the iPSC/860 is asynchronous. NX/2 buffers all incoming and outgoing messages in such a way that no rendezvous is necessary between two communicating processes. In addition to sharing of information, this mechanism is also the primary means of synchronization between processors. The messages passed between processors are given a label, i.e., typed, which provides the destination node with a means of distinguishing between different messages awaiting receipt. The communication primitives are available for both blocking and non-blocking message passing. In the blocking case, the sending or receiving processor is halted until the message has been sent or received. In the non-blocking operation, the programs merely informs the operating system that a message should be sent or received. The processor is allowed to proceed with the computations while the DCM handles the message request. In addition to these node-to-node communication primitives, the iPSC/860 also supports a variety of reduction operations requiring global communications. These communication primitives operate at a very low level, which presents the programmer with a very flexible environment. Coincidentally, the programmer is also responsible for building buffers to be sent and reassembling data items from buffers received.

### 3.3. The iPSC/860 Programming Model

In distributed memory machines such as the iPSC/860, there is no globally shared, directly addressable memory. Instead, each processor has a private address space in a private memory, out of which it's own version of the program is run. Consequently, as a first step, an appropriate scheme for data and/or task partitioning and assignment to processors must be decided upon. Then, a program must be derived for each processor that respects this partitioning. This implies that when non-local data is needed, the appropriate blocking or non-blocking send-receive protocol explicitly coded in the program is used to establish the data communication. In addition, this data communication must be accomplished in such a manner that satisfies the data dependency constraints of the underlying numerical algorithms. As a result, in addition to managing the parallelism, the programmer is required to have a clear understanding of all the inherent data dependencies as well as the relevant task barriers and ensure that these requirements are satisfied through appropriately labeled inter-processor communication. The messages exchanged have relatively high communication latencies (approximately 65-150 microseconds) and low communication bandwidths. Hence, there is a significant performance penalty for moving data between processors frequently and/or in large quantities.

## 4. PARALLEL IMPLEMENTATION ISSUES

In the following sections, we describe, in some detail the issues arising in the parallel implementation of the numerical scheme used to simulate the unsteady flow field in the ramjet combustor on the iPSC/860.

### 4.1. Characterization of computational tasks

There are two well-known techniques for exploiting inherent parallelism of an algorithm on a distributed memory machine; concurrency and pipelining. In some instances, a combination of the two is used. While concurrency is designed to extract the available spatial parallelism, pipelining deals with temporal

parallelism. There are two modes of concurrency; functional and data. Under functional concurrency, the overall application is decomposed into several distinct computational tasks that can be executed simultaneously on multiple processors. In data concurrency, the primary data space of the application is partitioned and distributed among the processors. In this mode, the processors may be running the same program but operating on different subsets of data. Algorithms exploiting the data concurrency are commonly referred to as data parallel algorithms. Which technique and mode that is best suited to a given application is primarily dependent on the type and degree of parallelism inherent in the underlying algorithms. Therefore, as a first step towards an efficient parallel implementation, it is essential to perform a careful analysis of the application to identify: 1) various distinct algorithmic phases, 2) the inter-dependencies of the algorithmic phases, 3) the inherent degree of parallelism and its granularity for each algorithmic phase, 4) the type of data dependencies associated with each algorithmic phase. In this discussion, the degree of parallelism refers to the order of magnitude of the number of finest granularity concurrent subtasks within a given algorithmic phase. Also, the degree of parallelism and the type of data dependencies associated with each of these phases can vary widely.

We restrict our characterization of the computational tasks to those within a single time step, as there is no exploitable parallelism across multiple time steps. A single time step of the unsplit MacCormack predictor-corrector explicit time integration scheme used in this investigation can be viewed as consisting of two primary subtasks: a predictor step followed by a corrector step. Each of these primary subtasks can be further subdivided into following computational phases: a) Evaluation of inviscid and viscous flux vector contributions associated with all four edges of the quadrilateral cells, b) Evaluation of the contribution from the vector of source terms at the cell centers, c) Summation of the contributions from the four cell edges and the cell center to form the cell based flux balance and the update of cell-center flow variables, and d) Update the cell-center flow variables of ghost cells bordering physical boundaries based on the enforcement of the appropriate physical/numerical boundary conditions. It should be noted that for each cell, flux vectors through only two of the edges need be computed, for example north and east, due to the the sharing of edges by adjoining cells.

The data dependencies across the predictor and corrector steps are such that they are required to occur in strict sequence and there is no exploitable functional concurrency across these two subtasks. The subtasks (a), (b) and (c) all involve only independent cell based computations and their data dependencies are restricted to those associated with the 8 nearest neighbor cells. Therefore, these subtasks are characterized by  $O(N^2)$  degree of extractable parallelism with homogeneous spatial distribution of the computational load. In this discussion,  $N$  refers to a typical number of computational cells in either of the coordinate directions. The degree of extractable parallelism associated with the subtask (d) is  $O(N)$ . In addition, since the enforcement of boundary conditions occurs only along the physical boundaries, the spatial distribution of the computational load is not homogeneous. Hence, there exists the potential for creating load imbalances. The severity of this load imbalance is dependent on the amount of computations associated with the mix of boundary condition types used. The only mitigating factor is that in most realistic simulations, the ratio of boundary cells to interior cells tends to be small. However, the spatial data dependencies associated with the boundary conditions are still confined to those of nearest neighbor cells.



#### 4.2. Data partitioning

The above analysis clearly indicates that the application under consideration is best suited for a data parallel implementation. In developing applications for distributed memory machines based on data parallelism, a first step is to decide exactly how the data space will be partitioned and distributed to the processors. Since the analysis of the previous section indicates that the finest level of subtask granularity is at the level of individual cells, it is natural to partition the tensor-product data space of the numerical scheme at the level of group of cells in each coordinate direction. The group size may be as small as one. This concept is commonly referred to as mesh partitioning and is based on the geometric substructuring of the computational domain. The idea is to assign or map the subdomains (i.e., processes) so created onto the processors of the distributed memory multiprocessor in such a way that; 1) the distribution of cells to the computational nodes leads to a nearly balanced load of computation and communication among all nodes, 2) the inherent spatial data locality of the underlying tensor-product cell structure is maintained so as to minimize the amount of inter-processor data communication.

In the case of tensor product computational meshes, this is easily achieved by partitioning the computational domain into logically congruent, nearly equal-sized, rectangular subdomains. Since the subgrids created by this partitioning are themselves logically structured, the nodal programs written for the individual processors of the distributed memory machine will bear a close resemblance to the program structure of a sequential implementation. The parallel implementations based on such partitioning schemes possess the following characteristics; 1) the underlying numerical algorithms are not changed, i.e., the parallel implementation give exactly the same results as the sequential version, 2) Single Program Multiple Data (SPMD) model of programming the processors, 3) implementations are independent from the topology of the interconnection network and the number of computational nodes (provided the local memory capacity is sufficient for a problem of given size), 4) simplified communication patterns for data exchange among processors, 5) equi-distribution of computational and communication load among processors for concurrent tasks that are spatially homogeneous. It should be noted that the homogeneous programming of processors implied in the SPMD model does not preclude fact that each processor can have a different execution path through this program.

The cell partitioning schemes used in this study statically decomposes the 2-dimensional tensor product computational domain into logically congruent, nearly equal-sized rectangles. In addition, exactly one such domain is assigned to each of the processors and consequently such a partitioning scheme is referred to as a uni-partitioning scheme. The simplest and most commonly used structured mesh partitioning scheme slices the computational domain along planes normal to each of the coordinate directions. As a result, the maximum number of partitions in a given coordinate direction is limited to the number of cells in that direction. When the computational domain is sliced only along one coordinate direction, it is referred to as a 1-D partitioning. Similarly, when it is sliced in two directions, the resulting partitioning scheme is known as a 2-D partitioning. These two cases are depicted in Figure 5.

The highest dimensionality of the partitioning scheme that can be used for a given cell oriented algorithm depends on the degree of extractable parallelism of that algorithm. In the case of current application, where most of the subtasks possess  $O(N^2)$  degree of parallelism, both 1-D and 2-D uni-partitioning can be used without excessive processor idling. When both the problem size and the number of processors are fixed, the granularity of the subdomains does not change with the dimensionality of the parti-

tioning. It is only the shape of the subdomain that is changed along with the area-to-perimeter ratio. This in turn affects the computation-to-communication ratio of the algorithm which may impact the performance depending on; 1) algorithm's computational and communication requirements, 2) machine architectural features such as interconnection network topology, interprocessor communication latency and bandwidth. In any case, for a problem of fixed size, use of higher dimensional partitioning, if feasible, may allow the use of larger number of processors than would be possible with a lower dimensional partitioning.

#### 4.3. Implementation details

The goal of the current parallel implementation is the extraction of maximum concurrency to minimize the execution time of the application on a given number of processors. However, there are several different types of overheads associated with a parallel implementation on a distributed memory MIMD architecture. They are: (1) inter-processor communication overhead, (2) data dependency delays, (3) load imbalance, (4) arithmetic overhead and (5) memory overhead. In the current context, the arithmetic and memory overheads refer to the extra arithmetic operations and memory needed by the parallel implementation when compared with the equivalent best serial implementation. While the first four types of overheads lead to performance degradation, the memory overhead may limit the size of the problem that can be run on a system with a fixed number of processors. In practice, the task of simultaneously minimizing all these overheads proves to be a difficult one. Consequently, most parallel implementations require compromises to be made with regard to different types of overheads with the overall goal of achieving a near-minimum execution time, subject to a reasonable programming effort. In making such implementation decisions, sufficient attention must be paid to the attributes of the underlying hardware. In the following sections, we describe some of the implementation details along with the techniques used to optimize the overall performance.

##### 4.3.1. Partitioning and Message Passing

Either 1-D or 2-D partitioning of the finite-volume cells as shown in Figure 5 where the entire L-shaped computational domain is treated as a single entity can lead to an uneven distribution of useful computational load among processors and complete idling of some processors. In order to avoid the inefficiencies associated with the above cell partitioning scheme, we resort to a two-level approach that is specifically tailored to the underlying geometry of the computational domain. In this scheme, the L-shaped computational domain  $\Omega$  is first split into two subdomains  $\Omega_1$  and  $\Omega_2$ , with an interdomain boundary  $\Gamma_0$ , as shown in Figure 2. Then, each of these rectangular subdomains are further subdivided, completely independent of each other, either using 1-D or 2-D partitioning schemes discussed above. Such a method is referred to as a geometry tailored partitioning scheme and is shown in Figure 6. Although this scheme may ensure a good load balance among all processors, there are two added complications: 1) the implementation requires a minimum of two processors, 2) complex interprocessors communication patterns across the subdomain boundary  $\Gamma_0$ . The second issue will be discussed in greater detail in a later section.

In the discussion below, we assume a fixed problem size with  $NC$  finite-volume cells and a fixed number of processors  $P$ . To ensure a good load balance under this two-level partitioning scheme, the fraction of processors assigned to each subdomain should be nearly proportional to the total fraction of the cells belonging to that subdomain. Let,  $NC_1$  = No. of cells in  $\Omega_1$ ,  $NC_2$  = No. of cells in  $\Omega_2$ , and  $NC = NC_1 + NC_2$  = No. of cells in

$\Omega = \Omega_1 \cup \Omega_2$ . Then,  $P_1 = (NC_1/NC)P$ , and  $P_2 = (NC_2/NC)P$ , subject to the constraint that  $P = P_1 + P_2$ , where  $P_1$  and  $P_2$  are the number of processors assigned to  $\Omega_1$  and  $\Omega_2$  respectively. Assumptions implicit in this partitioning scheme are: a) the number of processors is substantially greater than two, b) the number of finite-volume cells in each of the two primary subdomains is much greater than the number of processors assigned to them. If neither of these are true, our ability to achieve a good load balance is significantly diminished.

The cell partitioning scheme discussed above is carried out on the basis of cell centers. During this process, each cell center is paired with the cell vertex at the lower left-hand corner. This results in simultaneous distribution of cell centers and cell vertices among processors. A typical partition resulting from this process is shown in Figure 7. The current implementation is based on two level, 2-D uni-partitioning of the computational domain. However, two-level, 1-D uni-partitioning is a subset of this implementation. Here, each partition is assigned to a computational node of the iPSC/860 in an algebraic manner, i.e., the  $i$ -th partition to the  $i$ -th processor. As a result, all the logically neighboring partitions are not directly connected via the hypercube communication network. In general, the hypercube topology allows the embedding of rings and 2-D meshes through the binary reflected gray code mapping (Chan and Saad, 1986) such that logical neighbors end up being physical neighbors as well. As a result of two-level partitioning scheme adapted here, such an embedding is no longer possible. Therefore, the distances traveled by messages during data exchanges between partitions that are logically adjacent may be longer and there is also the potential for encountering network link contention during such exchanges. However, as discussed in the section under iPSC/860 hardware, due to the ability of DCM to mimic the appearance of a nearly fully connected network, any adverse effects resulting from this simple process-to-processor mapping is assumed to be minor.

Under this statically determined uni-partitioning scheme, each processor is responsible for performing the computations associated with the finite-volume cells that belong to the subdomain held by it. As discussed under algorithm characterization, the underlying data dependencies are such that the computation of flux and source term vectors associated with a cell lying next to an inter-partition boundary requires data held by a minimum of one and a maximum of eight adjacent partitions. Due to high message start-up cost, it will be inefficient to resort to communication each time such data items are required by such a cell. Instead, following a well-known practice, we modify our subdomain data structures to hold one extra layer of cell based data along all boundaries of a partition. This is a process analogous to the creation of ghost cells along physical boundaries, for the convenience of imposing boundary conditions. This extra layer of cells, which forms a halo around the partition is commonly referred to as an overlap area (Figure 7). The presence of such overlap areas allows the exchange of data required by boundary cells to be carried out via a few, relatively long messages. As a result, the high cost of latency associated with message passing is minimized, resulting in a reduced communication overhead. However, the allocation of storage for such overlap areas and the need for using several equally long message buffers during the data exchange process results in increased memory overhead. This serves as an example where a memory overhead penalty is taken to reduce the high cost of communication overhead and data dependency delays.

The exchange of data needed for overlap areas should be such that a strict coherency is maintained between values held by cells in the overlap areas and the corresponding values held by the cells along inter-partition boundaries. This requires that such data

exchanges be carried out at the end of both the predictor and the corrector stages. In order to gain a better understanding of the inter-processor communication pattern involved in the exchange of data for the overlap areas, we consider a typical partition that is surrounded on all sides by other partitions. It is clear from the data dependency considerations that we require data for the overlap cells at the four corners of the rectangular partition. At first glance, it appears as if that data exchanges are needed with the four partitions occupying the diagonally opposite corners, in addition to those with the four lying along the partition edges. However, this can be avoided by resorting to a two stage communication process as shown in Figure 8. In the first stage (Figure 8a), data exchanges with the two partitions to the east and the west are performed, only involving data that belongs to the partition's interior cells. In the next stage (Figure 8b), exchanges with the partitions to the north and south are carried out, involving not only data belonging to the interior cells, but also those belonging to two overlap area cells at the east and west ends of the partition. These values have been obtained in the first stage of the data exchange, whose completion is required before the second stage can begin. This reduces the total number of message exchanges from eight to four.

It is evident from the above discussion that the computation to communication ratio associated with a processor level subdomain is directly proportional to the area-to-perimeter ratio of that subdomain. It is a well known fact that maximizing the computation-to-communication ratio leads to higher parallel execution efficiencies. Hence, the second level partitioning should be carried out in a manner that maximizes the area-to-perimeter ratio of the resultant partitions. This favors the 2-D partitioning strategy.

As mentioned previously, due to the use of a two-level partitioning scheme, the first stage of the data communication process is somewhat more complicated for partitions along the primary inter-domain boundary  $\Gamma_0$ . For these partitions, it is now necessary to identify: 1) the adjacent partitions lying across  $\Gamma_0$  that require data held by the partition under consideration, 2) the segments of the partition edge to be exchanged with each such adjacent partitions, as shown in Figure 9. As a result, some of these partitions may end up exchanging data with several other adjacent partitions, as opposed to the typical value of one per partition edge. It is evident that geometry tailored cell partitioning involves increased number of message exchanges for some processors. However, in most cases, this increased communication cost is more than offset by the overwhelming benefits of a superior load balance.

In addition to message passing complications, the two-level cell partitioning scheme also eliminates some aspects of symmetry and homogeneity from the individual node programs, generally found under one-level partitioning schemes. In certain sections of the program, partitions belonging to subdomain  $\Omega_1$  need to have execution paths that are different from those belonging to subdomain  $\Omega_2$ . This results in somewhat complicated program logic and longer codes.

In exchanging the data belonging to the cells in overlap areas, only the values of conservative variables stored at the cell centers are exchanged to reduce the number of messages and the amount of data communicated. This results in the redundant computation of: 1) the flux vectors through cell edges coincident with partition boundaries, 2) the values of the primitive variables associated with the overlap area cell centers. This results in added arithmetic overhead and is an example where redundant but relatively inexpensive floating-point computations are performed to minimize the relatively expensive inter-processor communications. Also, when the conservative variables are exchanged, all the relevant variables along the entire partition edge or a relevant portion of it is packed into a single buffer and sent as one message instead of send-

ing separate messages for each variable. This reduces the cost of data communication latencies at the expense of increased buffer space requirements.

In carrying out the data exchanges for overlap area cells, each partition posts the appropriate number of non-blocking receive calls for messages expected from adjacent partitions, before proceeding to send the data needed by adjacent processors. This requires the reservation of extra buffer space from the program's address space. However, this eliminates the need for the NX/2 (i.e., the node operating system) to dynamically allocate buffers for receiving messages that are longer than 100 bytes out of its own address space as well as the requirement to subsequently copy the received message to the buffer allocated from the program's address space. This results in a reduction of the communication overhead and is yet another instance where an added memory overhead is tolerated to reduce the costs associated with message passing.

Under the uni-partitioning schemes, subdomains containing physical boundary edges are held only by a subset of the processors. Therefore, while the subtask (d) (see Section 4.1) is being processed by these nodes, others may be idle, primarily due to data dependency delays. This load imbalance can only be eliminated by redistributing the data associated with the boundary cells and their ghost cells among all available processors. This will undoubtedly incur a significant communication overhead. Not only that data has to be redistributed at the beginning of subtask (d), they also has to be sent back to the originating processors at the completion of the subtask. In addition, the computational costs associated with subtask (d) is not necessarily homogeneous across all boundary cells, due to the variation of the types of boundary conditions imposed. As a result, if a redistribution is to be attempted, it is necessary to balance the load not only with regard to the number of boundary cells but also the associated boundary condition type. Given the following facts; 1) the inter-processor data communication on the iPSC/860 is relatively expensive, 2) for most problem sizes, the number of boundary cells is only a small fraction of the total number of cells and 3) programming complexity of equi-distributing the computational load associated with boundary cells, we came to the conclusion that a redistribution of data during subtask (d) would not bring about tangible performance improvements. Most likely, it will result in degradation of overall performance due to increased communication requirements. Hence, computations associated with subtask (d) are carried out by the processors holding the subdomains with physical boundary edges, with no additional communication costs. However, the program logic should reflect the fact that the execution path associated with subtask (d) is taken only by the relevant subset of processors with further branching to reflect the different types of boundary edges.

#### 4.3.2. Grid Generation

Conceptually, the grid generation process for the global body-fitted grid begins by decomposing the ramjet combustor geometry into a few primary regions based on the underlying geometry and the grid clustering requirements. Then it proceeds to generate the algebraically interpolated grid in each region, subject to the constraint that grid lines are continuous across inter-region boundaries. The properties of the hyperbolic stretching function used for clustering grid points along a line segment depends only on the total length of the line segment, number of grid points spanning the segment and the grid spacing at one or both ends of the segment. As a result, the algebraic grid generation process can be implemented using the data parallel model, wherein each processor level subdomain generates its own portion of the global grid, independently of others. This is based on each processor's knowledge of the number of grid points that belongs to it in each

coordinate direction and the global index ranges of these grid points, which in turn determines the region of the physical space covered by that processor's grid.

#### 4.3.3. I/O Considerations

Simulation of an unsteady flow field requires periodic writing of the field related data files to a secondary storage device such as the CFS. Due to the high frequency and the relatively large quantity of data associated with such output operations, the I/O capabilities of the computer used deserves considerable attention. In addition, the I/O operations associated with a distributed memory machine such as the iPSC/860 differs significantly from the rather straightforward process found in conventional supercomputers. Due to the cell partitioning required for data parallel implementation, the field data is fragmented across the processors. In contrast, for convenience during restart and post-processing operations, the CFS files are required to contain the logically-structured data for the entire solution domain. This implies that when data is being written to the CFS files, each processor is required to appropriately position the segment of data it is writing to respect the Fortran column-major ordering dictated by the logically-structured global grid. As a result, the program must now contain all the logic necessary to manage this ordered assembly process, based on each subdomain's relative position with respect to the global index space. An immediate outcome of this process is that each processor is now allowed to write only a small segment of the data associated with its grid at a time. This results in a large number of messages to I/O nodes over the inter-connection network, with its attendant price for high startup costs and delays associated with contentions for network links and the limited number of I/O nodes. Recall that there are only 10 I/O nodes for the 128 computational nodes. In addition, due to small quantity of data associated with each write operation, I/O nodes are unable to efficiently utilize their file caching capability and are required to reposition the attached disks frequently. Most of these factors are likely to have an adverse effect on the machine's overall I/O performance with their severity increasing almost directly with the number of processors used for a given problem size.

### 5. RESULTS AND DISCUSSION

In this section, we describe in some details the results of our study of the capability of the parallel large-eddy simulation code on the i860. The results of the scaling studies (as function of both grid resolution and the number of processors) and the parallelism efficiency analysis is first discussed followed by analysis of the results of some preliminary simulations.

#### 5.1. Parallel Performance Data

The integrity of the parallel implementation was verified by comparing the L-2 norms of the cell-centered conservative variables after 500 time steps with those produced by the serial version of the code running a test case with identical combustor geometry and flow conditions. The L-2 norms were found to agree upto 12 significant digits. The code was run using double precision accuracy and using between 16 and 128 processors (on iPSC/860 the total number of processors allocated to a job must be a power of 2), with a variety of subdomain partitioning combinations to assure the accuracy of the implementation. In order to evaluate the scalability of the parallel implementation with regard to the overall computational and I/O performance, six different test cases representing a range of grid sizes that are likely to be encountered in combustor instability simulations with a typical ramjet geometry were chosen. These grid sizes range from relatively coarse grids used in low to moderate Reynolds number simulations to those that are fine

enough for resolving a significant fraction of the relevant length-scales at higher Reynolds numbers. The grid sizes associated with the six test cases are shown in Table 1.

Two different categories of performance tests were run for each test case. The first set of results, shown in Table 2 were obtained by running the code with the solution of the scalar field equation for the subgrid kinetic energy disabled. The second set of results were obtained when the complete set of governing conservation laws were being solved and are shown in Table 3. The results were obtained for runs with four different processor numbers, i.e., 16, 32, 64 and 128. The two-level data partitioning used for the different test cases are also shown in Table 1. All performance data reported are for 64-bit computations with an implementation based entirely on Fortran. We also report timing data for the same test cases obtained by running a highly vectorized version of the serial code on a single processor of the Cray-YMP and the Cray-C90, for the purpose of performance comparison with modern vector supercomputers. In addition, Table 4 presents the results obtained by measuring the time required to write a typical field data file used for post-processing to the CFS.

The most favorable way of measuring scalability of a parallel implementation is to assume that the problem size will scale up with increasing number of processors. Given 8 Mb. of memory per processor, the current implementation is capable of holding upto 14400 cells in each processor. However, in this study we have opted for more realistic grid sizes in lieu of the scaled-speedup data. This is based on the premise that the grid size for a problem should be determined only by the spatial resolution requirements of the underlying physical problem. In addition to the CPU time per step (in seconds), reported in Tables 2 and 3, we also report the Cray-YMP equivalent MFLOPS, both for iPSC/860 and Cray-C90. These were computed using the MFLOPS rate reported by the hardware performance monitor on the Cray-YMP. The efficiency data reported in Tables 3 and 4 were obtained based on an estimated uniprocessor CPU time/step, assuming the same test cases were run on a single processor of the iPSC/860. In order to compute these time estimates, the serial code was run on a single node of the iPSC/860 for several different grid sizes, chosen to fit within 8 Mb. of memory. Based on these timing data, an average CPU time per step per cell was computed. This number was multiplied by the total number of cells in each of the six different test cases to obtain their estimated uniprocessor CPU time per step. Then the multiprocessor efficiency is defined as:  $\eta = T_{1p} / (N_p T_{mp})$  where  $T_{1p}$  is the estimated time/step on a uniprocessor,  $T_{mp}$  is the measured time on a multiprocessor and  $N_p$  is the number processors used. The effective I/O bandwidth reported in Table 4 was obtained based on the total number of bytes written to the CFS and the time required for all the processors to complete the write operation.

It is clear from the results that the sustained MFLOPS rate for a single i860 processor is in the range of 3.75-5, with the values at the higher end of the range being reported for the second category of tests. These values are far from being close to the 60 MFLOPS theoretical peak of the i860. The primary cause of this performance degradation is the inadequate bandwidth and high latency for data movement between the on-chip data cache and the external memory. An equally important contributing factor is the high cost of floating point divide operations and intrinsic functions such as square roots. The higher rate for the second category of tests are attributed to the enhanced temporal locality of cached data afforded by the additional computations associated with the subgrid model at each cell. The number of floating point divisions required per step can be further reduced at the cost of extra storage requirements. However, we did not pursue this approach in the current implementation.

The multiprocessor efficiency data reported in Tables 2 and 3 shows some values greater than unity. This is a well-known behavior associated with parallel computers built using processors with multilevel memory hierarchies such as the i860. For a given problem size, as the number of processors are increased, the size of the data partition associated with each processor is reduced. This results in increased temporal locality at the lower levels of the memory hierarchy, which is accompanied by performance improvements. However, counteracting this behavior is the fact that as the number of processors is increased, some of the overheads associated with the parallel implementation tend to increase and leads to performance degradations. The overall performance is based on the balance between these two opposing effects and eventually results in lower efficiencies as the number of processors is increased beyond a certain value for a fixed problem size. For a fixed number of processors, as the problem size is increased, the multiprocessor efficiency tend to increase. This is because the size of data partition associated with a processor increases resulting in a higher computation to communication ratio and a reduction in the inter-processor communication overhead. Also, the efficiency data for the second category of tests indicate somewhat higher values, again brought about by the increased computation to communication ratio associated with extra computations pertaining to the subgrid model.

The Tables 2 and 3 indicate that the 64 nodes of the iPSC/860 achieves performance equal to or better than a single processor of the Cray-YMP for both categories of test data, with significantly better performance for the tests in second category. One processor of the Cray-C90 is always faster than 128 nodes of the iPSC/860 for the first category of test cases, but the situation is completely reversed for the tests in the second category. The results in Table 4 confirms that the effective I/O bandwidth decreases with increasing number of processors, for reasons outlined in the section under I/O considerations. The sustained effective bandwidth achieved as a fraction of the theoretical peak range from less 1 % for 128 processors with a small grid size and upto 30 % for 16 processors with a large grid size.

## 5.2. Simulation Results

We began our simulation studies by verifying that the parallel simulation code is reproducing results identical to those obtained using the serial (Cray) version of the code. Subsequently, it was decided to carry out a study of the grid resolution and subgrid modeling effects. In the past (e.g., Menon and Jou, 1987; Menon, 1992b), the effect of grid resolution on the low frequency pressure oscillation was evaluated by carrying out simulations with grid resolution of 128 x 48, 256 x 64 and 320 x 64 in the Reynolds number (based on the inlet duct diameter) range of 10,000 - 20,000. It was determined in those studies that the low frequency oscillation was relatively unaffected in the chosen dissipation range. Simulations using higher grid resolution were not possible on the Cray due to the limited availability of the machine. Now, using the i860 version of the code, it was decided to revisit the issue of grid resolution by carrying out two simulations with grid resolution of 320 x 64 and 640 x 120. The computational domain chosen for these simulations is shown in Figure 1a and a typical grid (only every other grid point is plotted) is shown in Figure 1b. The test conditions for this study were chosen (based on our previous study, Menon and Jou, 1991) so that the combustion will occur in a 'stable' manner (that is, the low frequency oscillation will have relatively low amplitude levels. The Reynolds number for the simulation was 16,000 and the reference Mach number at the inlet was 0.45. A constant eddy viscosity model was used to characterize the subgrid processes in a manner similar to an earlier study (Menon and Jou, 1991) and the turbulent flame speed was chosen to be a constant, about 4 percent of the mean inlet velocity.

In the following, we will discuss the results using the spectra of the pressure, axial velocity and the vorticity at chosen locations. Figure 10 shows the pressure spectra at the base of the rearward facing step for the 320 x 64 grid (Figure 10a) and the 640 x 120 grid (Figure 10b). It can be seen that both simulations show nearly identical spectral peaks in the low frequency range. There are, however, some differences in the high frequency peaks (in the KHz range) specially in the amplitude levels. Analysis of the time traces showed that the peak-to-peak level of the low frequency pressure oscillation was in the range of 6-8 percent of the mean pressure in both cases. Figure 11 shows the pressure spectra further downstream at the entrance to the diffuser. Again, both grid resolution simulations show similar low frequency spectral peaks.

Using the data from these simulations and our past simulations (discussed in Menon, 1992b and 1993), it is possible to identify the source of the low frequency oscillation at around 200 Hz. In the earlier study, (using the same inlet duct as here, but with a slightly smaller combustor) it was determined that low frequency pressure oscillations in the combustor could be driven by either an acoustic resonant mode in the inlet duct or by a coupled acoustic-vortex mode. The acoustic mode was shown to be a standing half wave in the inlet while the coupled mode has a frequency that is determined by the sum of the time for the shed vortex to travel from the step to the impinging region at the diffuser and the time for an acoustic wave to travel from the vortex impinging region back to the inlet and then forward to the separation point of the shear layer at the step. The method for determining the coupled mode frequency is described in Menon (1993) and was experimentally determined by Yu et al. (1991).

Correcting for the relatively large Mach number, the inlet duct mode frequency is given by  $a(1-M^2)/2L_i$ , where  $a$  is the speed of sound at the inlet. This gives a frequency of around 192 Hz for the present simulation which is close to the low frequency seen in the present simulation. In the earlier study (Menon, 1992b, 1993), using a Mach 0.32 flow, a low frequency of around 240 Hz was observed and it was shown that this value was close to the inlet duct acoustic mode. Further, an analysis of the amplitude of the pressure oscillation in the inlet showed that this mode is a standing half-wave (Menon, 1993). Although a similar analysis has not yet been performed on the data from the present simulation, the acoustic mode frequency estimation noted above and a preliminary examination of the pressure signature at various locations in the duct shows that the low frequency oscillation at around 200 Hz is due to the acoustic resonant mode in the inlet duct. It is also interesting to observe that the present simulation data shows the presence of higher harmonics of the low frequency oscillation. Analysis of the present data using the criteria for estimating the frequency of the coupled acoustic/vortex mode indicates that the coupled mode (if it exists) should have a frequency of around 100 Hz. Such a frequency is clearly absent in the present data.

Figure 12 shows the comparison of the axial velocity spectra at the dump plane measured at the centerline. The low frequency modes seen in the pressure spectra is again present in these figures. The velocity fluctuation level was found to be around 16 percent of the mean velocity. Figure 13 shows the spanwise vorticity spectra for the same two grid cases measured in the shear layer just downstream of the step. The low frequency peak is again present in these spectra clearly indicating that both the pressure field and the vortex motion in the shear layer are correlated. Analysis of the various flow properties downstream in the diffuser showed that the low frequency is present everywhere. In contrast, the high frequency peaks are dominant only in the coarse grid data. This may suggest that the source of the high frequency may not be physical and may be related to the noise in the numerical code.

Further study is planned to address this issue.

Finally, it was decided to study the effect of replacing the constant eddy viscosity model with a more appropriate subgrid model. As a first step towards evaluating subgrid models for such complex flows, an algebraic subgrid model similar to the compressible eddy viscosity model of Erlebacher et al. (1987) was employed to model the subgrid Reynolds stresses and the subgrid heat flux. The scalar field was allowed to evolve as before (i.e., with a constant flame propagation). The same test conditions were used and the simulation with the grid 320 x 64 was repeated with the subgrid model. Figure 14a through 14c show respectively, the pressure spectrum at the base of the step, the axial velocity spectrum at the dump plane and the vorticity spectrum in the shear layer. The low frequency of around 200 Hz seen in the earlier simulations (with constant eddy viscosity) is again present, except that the frequency is slightly higher, at around 225 Hz. The higher harmonics of this frequency are also still present in the spectra. The peak-to-peak level in the pressure field was again around 6 percent of the mean pressure. It is interesting to note that the intermediate high frequency at around 1350 Hz has now disappeared but that the higher frequency at around 2 KHz is still present. This high frequency is clearly dominant in the vorticity spectrum and may suggest that the source of this frequency may be related to the vortex shedding frequency. However, the high resolution data did not show this frequency and therefore, its source is still not clear. Further analysis is planned to resolve this issue by repeating the high resolution simulation with the subgrid model.

## 6. CONCLUSIONS

We have demonstrated that it is possible to realize a highly scalable, distributed memory, data parallel implementation for a class of explicit time integration schemes used in unsteady combustion simulations. The geometry-tailored, two-level data partitioning strategy adapted to deal with L-shaped computational space appears to have resulted in an efficient implementation, in spite of its added complexity. The implementation is general enough to be portable to any MIMD parallel computer that supports processor-to-processor communication primitives. This includes most of the current and emerging highly parallel MIMD computers as well as networks of workstations supporting distributed computing software such as the Parallel Virtual Machine (PVM). The MIMD parallel computers such as the Intel iPSC/860 appears to provide a scalable, yet reasonably low-cost alternative to traditional vector supercomputers for simulation of unsteady flow phenomena, except in the crucial area of external I/O performance. Further improvements in the computational and the inter-processor communication performance envisaged for the future generations of the highly parallel computers will make them attractive tools for carrying out 3-D unsteady flow simulations. The additional computations associated with computing fluxes for hexahedral cells is likely to improve the computation to communication ratio over that encountered in 2-D computations and lead to enhanced scalability. However, to realize this promise, the above mentioned hardware performance improvements will have to be accompanied by rapid improvements in the external I/O performance to produce systems that are well-balanced in all relevant aspects of performance.

The analysis of the high resolution simulation data further demonstrated that the earlier relatively coarse grid simulations were capable of capturing the low frequency pressure oscillation characteristic of combustion instability. The study using the algebraic subgrid model also showed that the low frequency oscillation is unaffected by the dissipation mechanism in the modeled equations. Therefore, these studies lend further credibility to the earlier simulation results that were obtained using relatively coarse grids and

crude subgrid models.

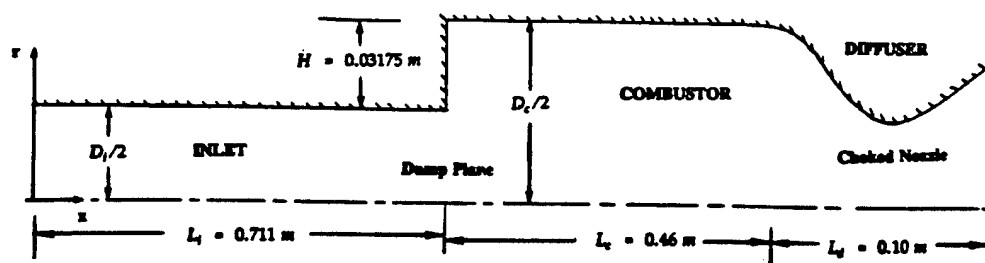
The development of the parallel simulation model allows us to further explore unsteady combustion in a parameter space that was uneconomical and difficult to accomplish with the available resources on the Cray YMP. Further study of combustion instability using the full  $k$ -equation subgrid model and using a new approach to model the premixed flame within the subgrid (Menon et al., 1993a, 1993b) is planned in the next phase of this research.

#### ACKNOWLEDGEMENT

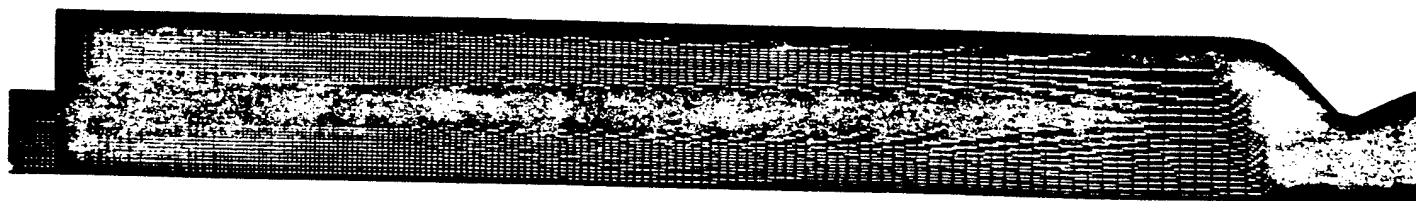
This research (by the second author) is funded by the Office of Naval Research under Contract No. N00014-92-J-403. The computational resources were provided by the Numerical Aerodynamic Simulation (NAS) at NASA Ames Research Center and are gratefully acknowledged.

#### REFERENCES

- Chan, T. F. and Saad, Y. (1986), "Multigrid Algorithms on the Hypercube Multiprocessors," IEEE Transactions on Computers, Vol. C-35, No. 11, pp. 969-977.
- Dowling, A. P. (1989) "Reheat Buzz - An Acoustically Coupled Combustion Instability," AGARD CP-450.
- Erlebacher, G., Hussaini, M. Y., Speziale, C. G., and Zang, T. A. (1987), "Toward the Large-Eddy Simulations of Compressible Turbulent Flows," ICASE Report No. 87-20.
- Hedge, U. G., Reuter, D., Zinn, B. T., and Daniel B. R. (1987) "Fluid Mechanically Coupled Combustion Instabilities in Ramjet Combustors," AIAA-87-0216.
- Jou, W.-H., and Menon, S. (1990) "Modes of Oscillations in a Non-reacting Ramjet Combustor Flow," *J. Propulsion and Power*, Vol. 6, pp. 535-543.
- Kailasanath, K., Gardner, J. H., Oran, E. S., and Boris, J. P. (1989) "Effects of Energy Release on High Speed Flows in an Axisymmetric Combustor," AIAA-89-0385.
- Kerstein, A. R., Ashurst, W. T., and Williams, F. A. (1988) "Field Equation for Interface Propagation in an Unsteady Homogeneous Flow Field," *Physical Rev. A*, Vol. 37, No. 7, pp. 2728-2731.
- Menon, S. and Jou, W.-H. (1987) "Simulations of Ramjet Combustor Flow Fields Part I - Numerical Model, Large-Scale and Mean Motions," AIAA-87-1421.
- Menon, S., and Jou, W.-H. (1990) "Numerical Simulations of Oscillatory Cold Flows in an Axisymmetric Ramjet Combustor," *J. Propulsion and Power*, Vol. 6, No. 5, pp. 525-534.
- Menon, S., and Jou, W.-H. (1991) "Large-Eddy Simulations of Combustion Instability in an Axisymmetric Ramjet Combustor," *Combustion Science and Technology*, Vol. 75, pp. 53-72.
- Menon, S. (1991) "Active Control of Combustion Instability in a Ramjet Combustor using Large-Eddy Simulation," AIAA Paper No. 91-0411.
- Menon, S. (1992a) "Active Combustion Control of Combustion Instability in a Ramjet Combustor using Large Eddy Simulations," *Combustion, Science and Technology*, Vol. 84, pp. 51-79.
- Menon, S. (1992b) "A Numerical Study of Secondary Fuel Injection Technique for Active Control of Instability in a Ramjet," AIAA-92-0777.
- Menon, S., McMurtry, P.A., and Kerstein, A. R. (1993a) "Linear Eddy Subgrid Model for Turbulent Combustion: Application to Premixed Combustion," AIAA Paper No. 93-0107.
- Menon, S., McMurtry, P.A., and Kerstein, A.R. (1993b) "A Linear-Eddy Mixing Model for LES of Turbulent Combustion", to appear in *LES of Complex Engineering and Geophysical Flows*, ed. B. Galperin and S. A. Orszag, Cambridge University Press.
- Menon, S. (1993) "Secondary Fuel Injection Control of Combustion Instability in a Ramjet", submitted to *Combustion, Science and Technology*.
- Peyret, R. and Taylor, T.D., "Computational Methods for Fluid Flow", Springer-Verlag, 1983.
- Schadow, K. C., Gutmark, E., Parr, T. P., Parr, D. M., Wilson, K. J., and Crump, J. H. (1987) "Large-Scale Coherent Structures as Drivers of Combustion Instability," AIAA-87-1326.
- Smith, D. A., and Zukoski, E. E. (1985) "Combustion Instability Sustained by Unsteady Vortex Combustion," AIAA-85-1248.
- Sterling, J. D. and Zukoski, E. E. (1987) "Longitudinal Mode Combustion Instabilities in a Dump Combustor," AIAA-87-0220.
- Thompson, J.F., Warsi, Z.U.A. and Mastin, C.W. (1985), "Numerical Grid Generation", Nort\_Holland, 1985.
- Williams, F. A. (1985) "Combustion Theory", 2nd Ed. Benjamin-Cummings, Menlo Park, 1985.
- Yakhot, V. (1989) "Propagation Velocity of Premixed Turbulent Flame," *Combustion Sci. and Tech.*, Vol. 60.
- Yu, K. H., Troune, A., and Daily, J. W. (1991) "Low-Frequency Pressure Oscillations in a Model Ramjet Combustor," *J. Fluid Mech.*, Vol. 232, pp. 47-72.



(a) The ramjet geometry



(b) The computational grid

Figure 1. The ramjet geometry and the computational grid.

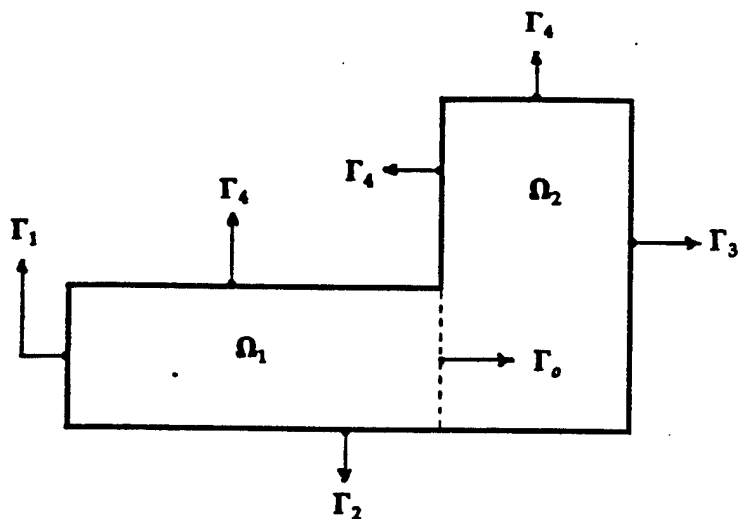
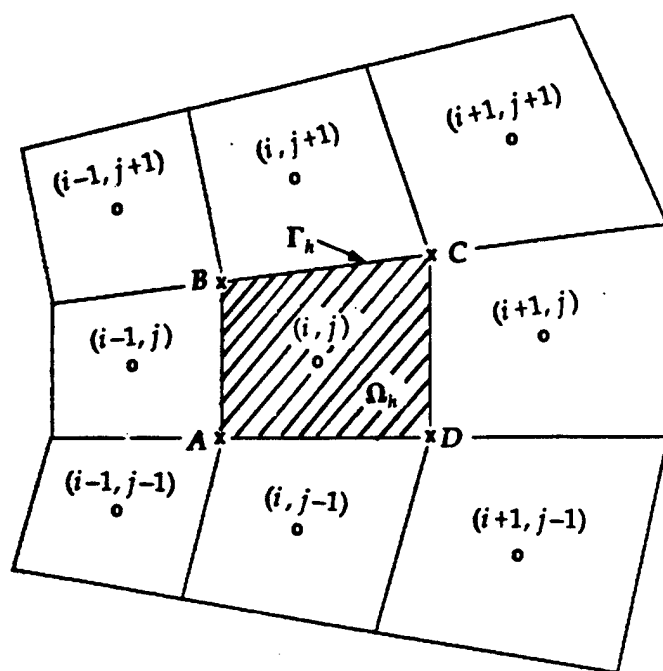
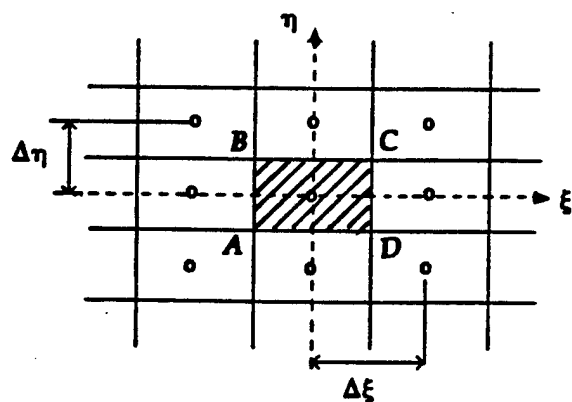


Figure 2. Schematic of the computational domain.

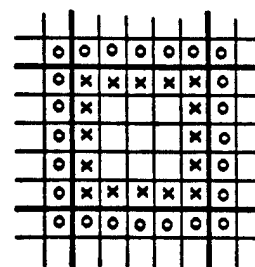


(a) Finite-volume cell in the physical space

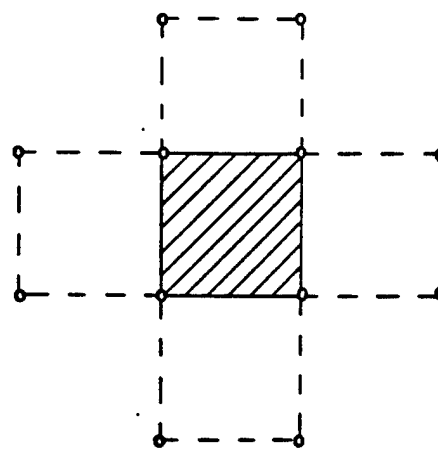


(b) Finite-volume cell in the computational space

Figure 3. Discretized finite-volume grid in physical and computational space.

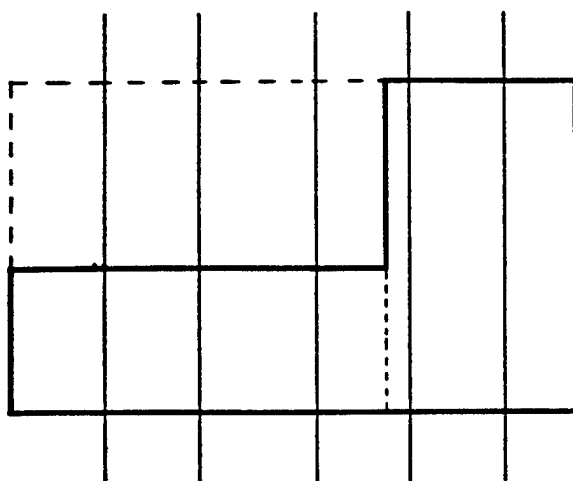


(a) cell-centered case

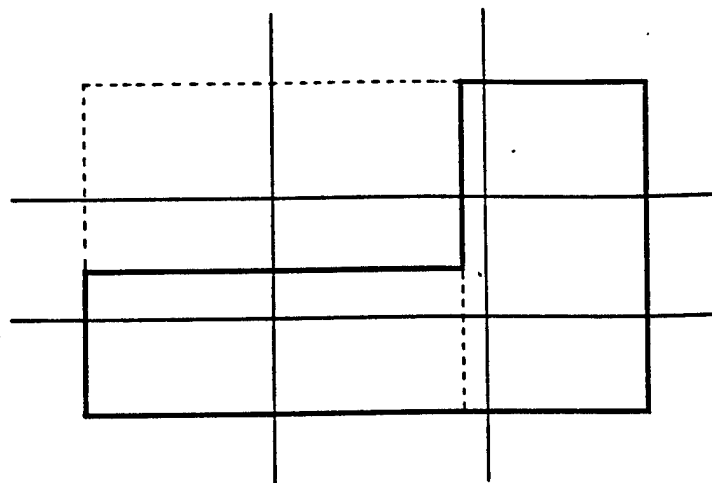


(b) cell vertex case

Figure 4. Spatial data dependency in the computational gri

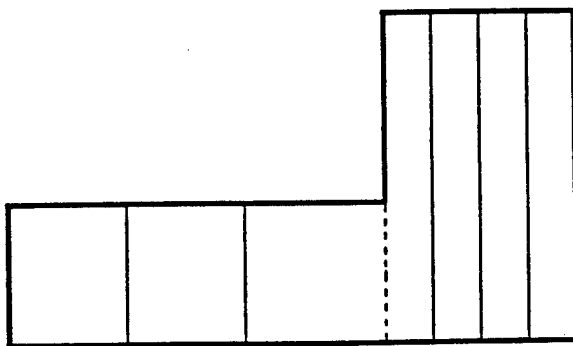


(a) One-dimensional partitioning

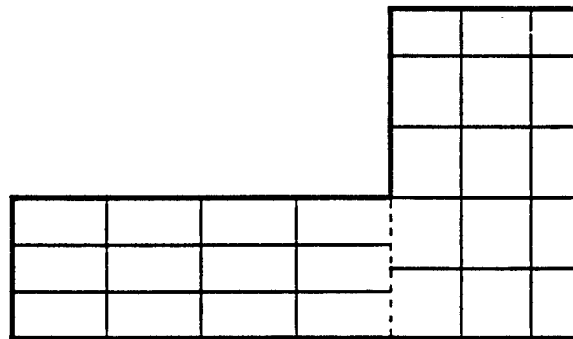


(b) Two-dimensional partitioning

Figure 5. Partitioning schemes for i860 based on spatial dimensions.



(a) Geometry tailored one-dimensional partitioning



(b) Geometry tailored two-dimensional partitioning

Figure 6. Partitioning schemes for i860 based on problem geometry.

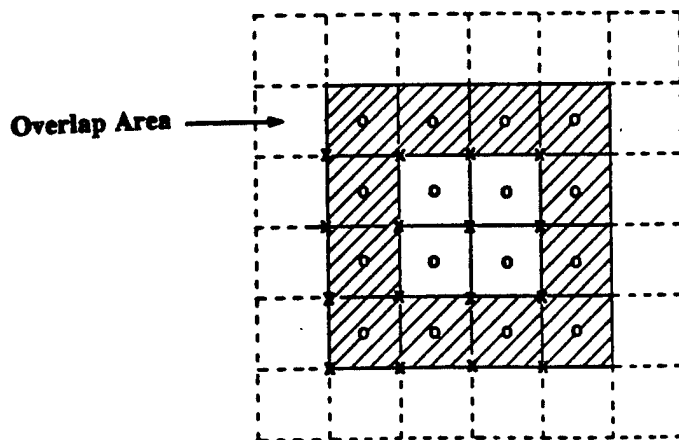


Figure 7. Processor specific subdomain.



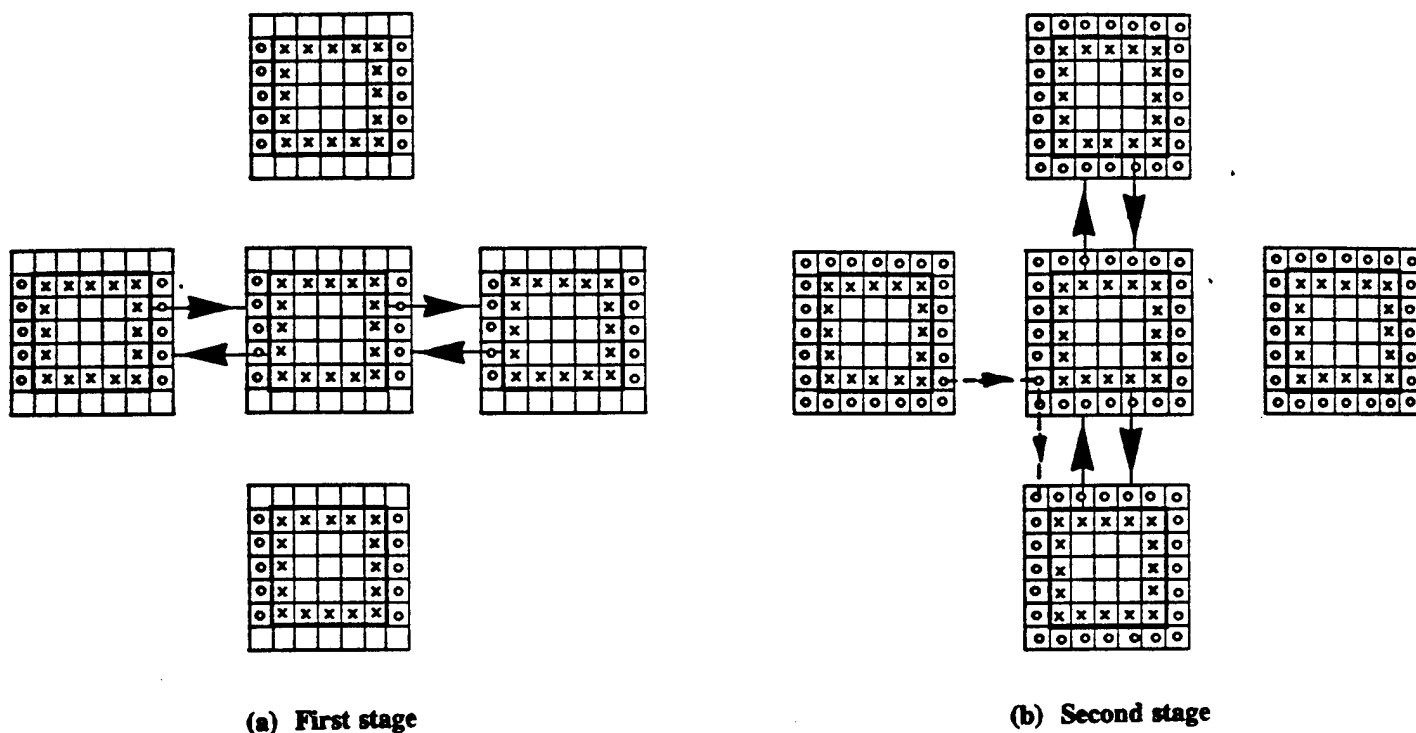


Figure 8. Different stages of inter-processor communication.

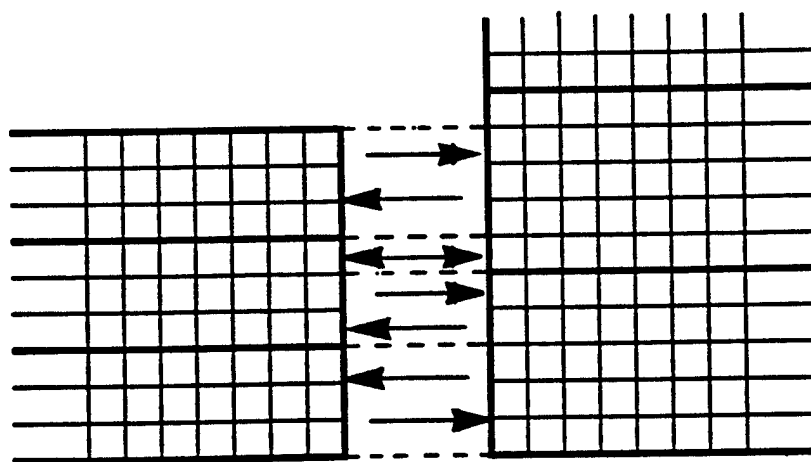


Figure 9. Inter-processor communications along the boundary  $\Gamma_0$ .

Prob. No.	Grid Size		Logical Data Partitioning							
	Domain $\Omega_1$	Domain $\Omega_2$	No. of Processors							
			16		32		64		128	
1	(125X32)	(196X64)	(4,1)	(6,2)	(4,2)	(8,3)	(8,2)	(12,4)	(8,4)	(12,8)
2	(195X32)	(286X64)	(4,1)	(6,2)	(8,1)	(8,3)	(8,2)	(16,3)	(16,2)	(24,4)
3	(225X48)	(336X96)	(4,1)	(6,2)	(8,1)	(8,3)	(8,2)	(16,3)	(16,2)	(24,4)
4	(225X60)	(336X120)	(4,1)	(6,2)	(4,2)	(8,3)	(8,2)	(16,3)	(16,2)	(24,4)
5	(345X60)	(516X120)	(4,1)	(6,2)	(8,1)	(8,3)	(8,2)	(16,3)	(16,2)	(24,4)
6	(340X90)	(521X180)	(4,1)	(6,2)	(8,1)	(8,3)	(8,2)	(12,4)	(8,4)	(24,4)

Table 1. Grid sizes and logical data partitioning used for the Intel i860.

Prob. No.		Intel iPSC/860				Cray-YMP	Cray-C90
		No. of Proc.					
		16	32	64	128		
1	Time/Step	0.2356	0.1275	0.0751	0.0460	0.0802	0.0338
	Mflops	60	111	189	308	177	419
	Efficiency	1.05	0.97	0.83	0.68	-	-
2	Time/Step	0.3390	0.1779	0.0994	0.0601	0.1119	0.0456
	Mflops	60	115	206	340	183	449
	Efficiency	1.09	1.04	0.93	0.77	-	-
3	Time/Step	0.5717	0.2981	0.1603	0.0900	0.1903	0.0750
	Mflops	62	118	220	391	185	469
	Efficiency	1.14	1.09	1.02	0.91	-	-
4	Time/Step	0.7203	0.3739	0.1959	0.1088	0.2405	0.0918
	Mflops	62	119	227	409	185	485
	Efficiency	1.14	1.09	1.04	0.94	-	-
5	Time/Step	1.1022	0.5623	0.2931	0.1580	0.3598	0.1374
	Mflops	61	120	230	426	187	489
	Efficiency	1.14	1.12	1.07	0.99	-	-
6	Time/Step	1.6423	0.8371	0.4307	0.2271	0.5382	0.2044
	Mflops	62	121	235	446	188	494
	Efficiency	1.16	1.13	1.10	1.04	-	-

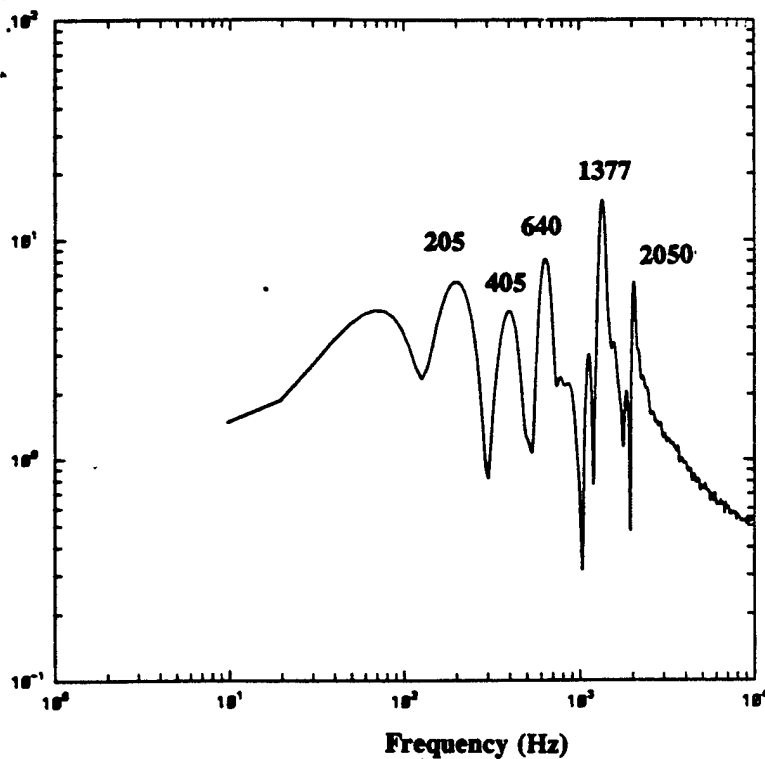
Table 2. Comparison of the CPU timing and efficiency of the Intel iPSC/860, Cray YMP and Cray C90 for various grid resolutions with combustion and no subgrid model.

Prob. No.		Intel iPSC/860				Cray-YMP	Cray-C90
		No. of Proc.					
		16	32	64	128		
1	Time/Step	0.3137	0.1691	0.0998	0.0598	0.1380	0.0606
	Mflops	79	147	249	415	180	409
	Efficiency	1.08	1.00	0.85	0.71	-	-
2	Time/Step	0.4519	0.2382	0.1324	0.0795	0.1984	0.0845
	Mflops	81	154	277	462	185	434
	Efficiency	1.09	1.04	0.93	0.77	-	-
3	Time/Step	0.7653	0.3981	0.2137	0.1189	0.3406	0.1429
	Mflops	83	160	298	536	187	445
	Efficiency	1.16	1.12	1.04	0.93	-	-
4	Time/Step	0.9663	0.5013	0.2594	0.1447	0.4230	0.1757
	Mflops	82	159	307	550	188	453
	Efficiency	1.15	1.11	1.07	0.96	-	-
5	Time/Step	1.4769	0.7515	0.3913	0.2113	0.6430	0.2626
	Mflops	83	163	314	581	191	467
	Efficiency	1.16	1.14	1.09	1.01	-	-
6	Time/Step	2.2172	1.1230	0.5742	0.3018	0.9612	0.3927
	Mflops	83	163	320	608	191	467
	Efficiency	1.17	1.15	1.13	1.07	-	-

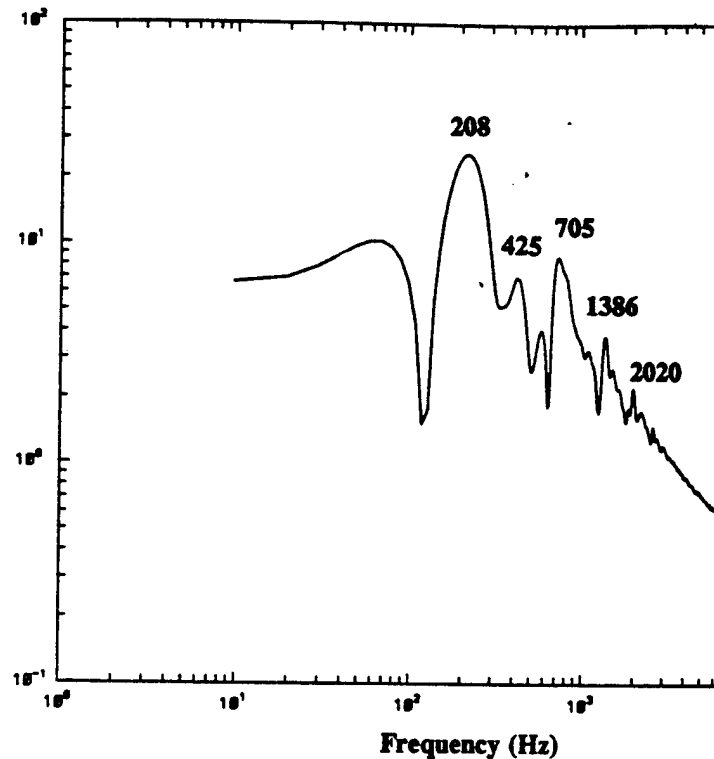
**Table 3. Comparison of the CPU timing and efficiency of the Intel iPSC/860, Cray YMP and Cray C90 for various grid resolutions with combustion and one-equation subgrid model.**

Prob. No.		Intel iPSC/860			
		No. of Proc.			
		16	32	64	128
1	I/O Time (Sec.)	0.3756	0.6537	1.2611	2.2479
	Eff. Bw. (Mb./Sec.)	0.69	0.39	0.20	0.11
2	I/O Time (Sec.)	0.4017	0.6809	1.1429	2.4427
	Eff. Bw. (Mb./Sec.)	0.95	0.56	0.34	0.16
3	I/O Time (Sec.)	0.5343	0.7532	1.3799	2.6998
	Eff. Bw. (Mb./Sec.)	1.27	0.90	0.49	0.25
4	I/O Time (Sec.)	0.4826	0.7936	1.5070	2.5996
	Eff. Bw. (Mb./Sec.)	1.76	1.07	0.56	0.33
5	I/O Time (Sec.)	0.5106	0.8711	1.5407	2.8831
	Eff. Bw. (Mb./Sec.)	2.56	1.50	0.85	0.45
6	I/O Time (Sec.)	0.6138	1.1413	1.8574	3.2726
	Eff. Bw. (Mb./Sec.)	3.21	1.73	1.06	0.60

**Table 4. The I/O time and effective bandwidth on the Intel i860 for different problem sizes.**

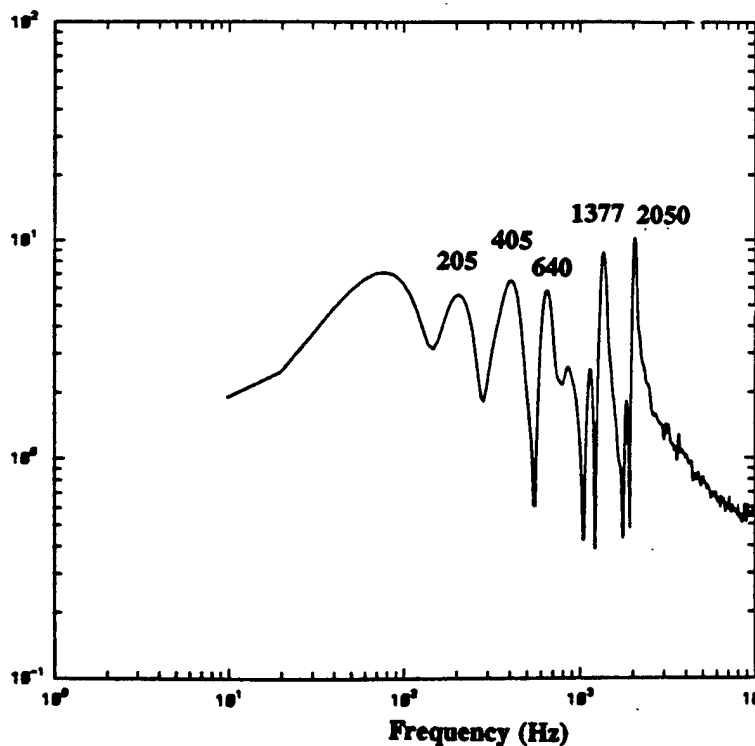


(a) 320 x 64 grid

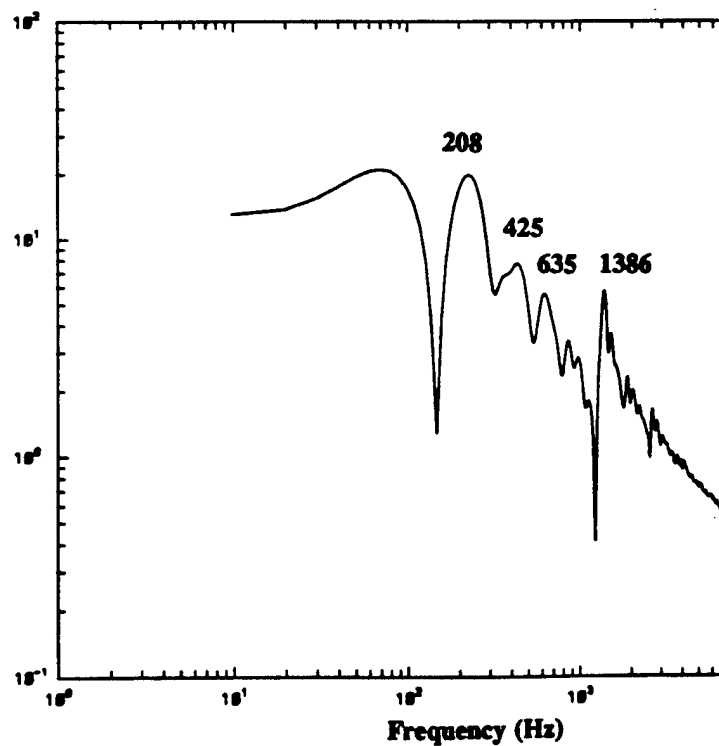


(b) 640 x 120 grid

Figure 10. Comparison of pressure spectra at the base of the step for different grid resolutions using a constant eddy viscosity subgrid model.

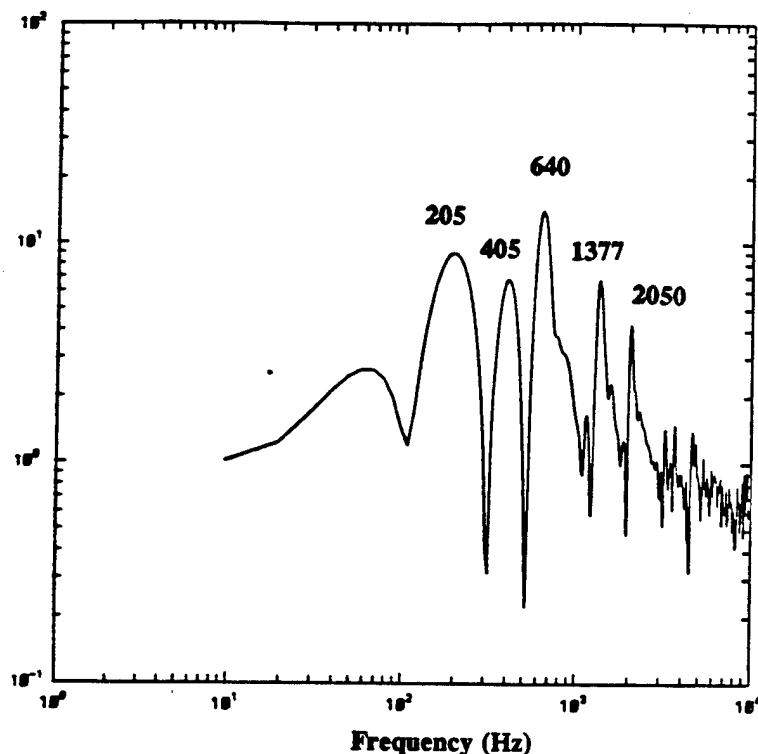


(a) 320 x 64 grid

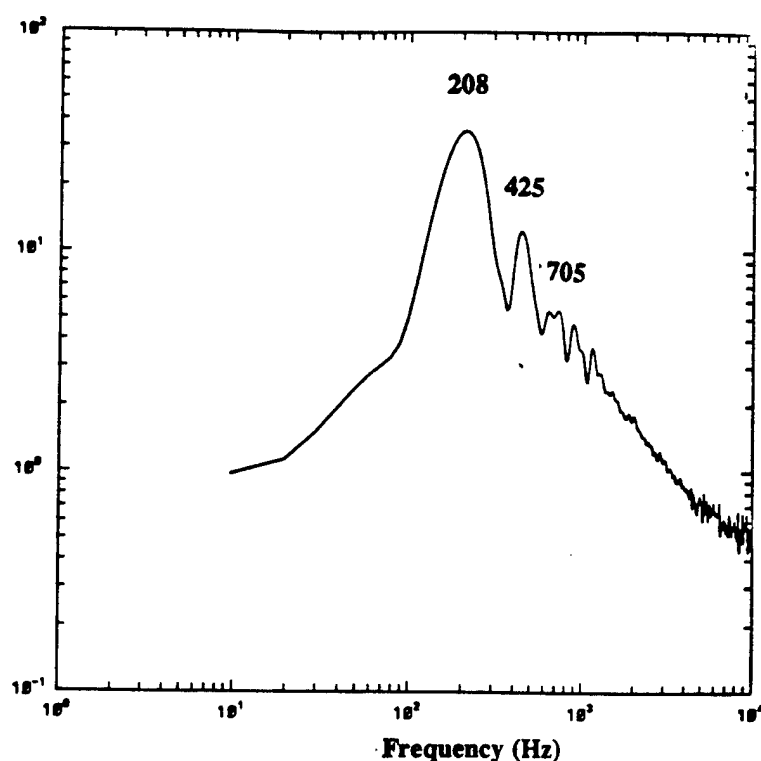


(b) 640 x 120 grid

Figure 11. Comparison of pressure spectra at the entrance to the diffuser for different grid resolutions using a constant eddy viscosity subgrid model.

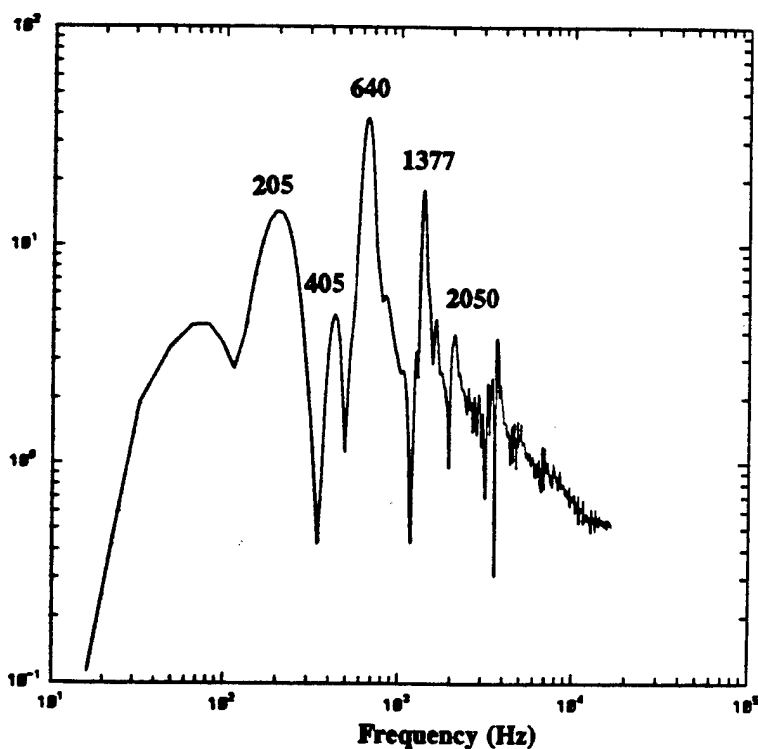


(a) 320 x 64 grid

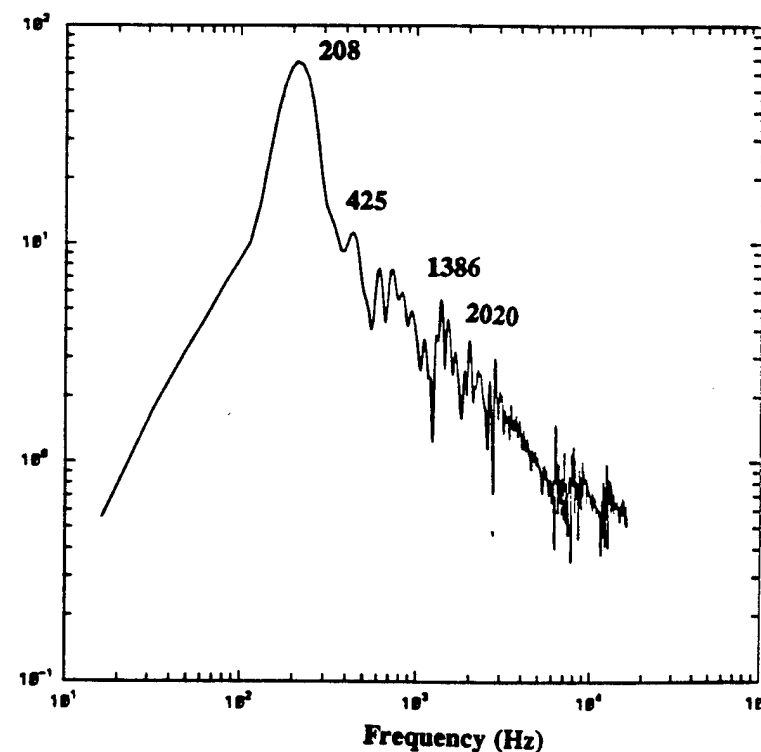


(b) 640 x 120 grid

Figure 12. Comparison of axial velocity spectra at the dump plane for different grid resolution using a constant eddy viscosity subgrid model.

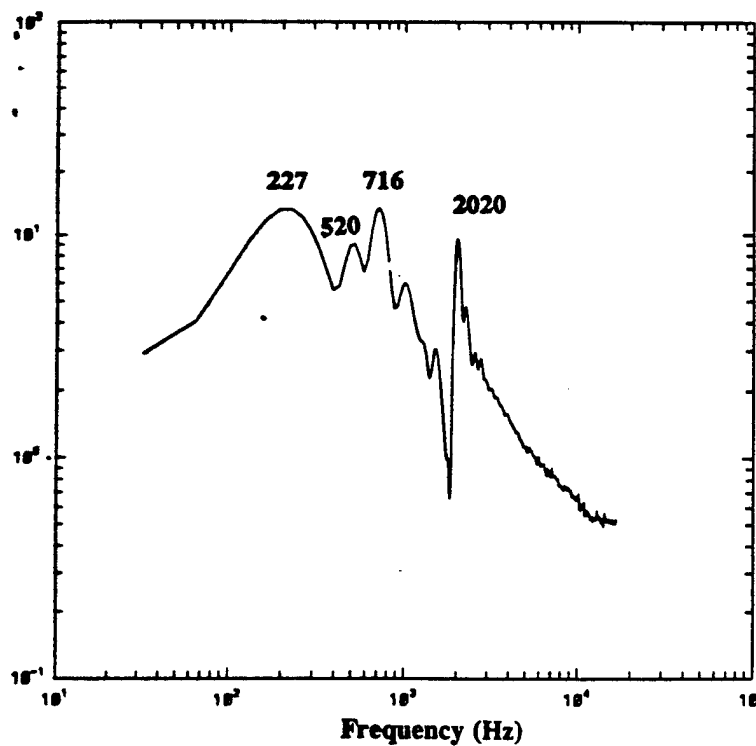


(a) 320 x 64 grid

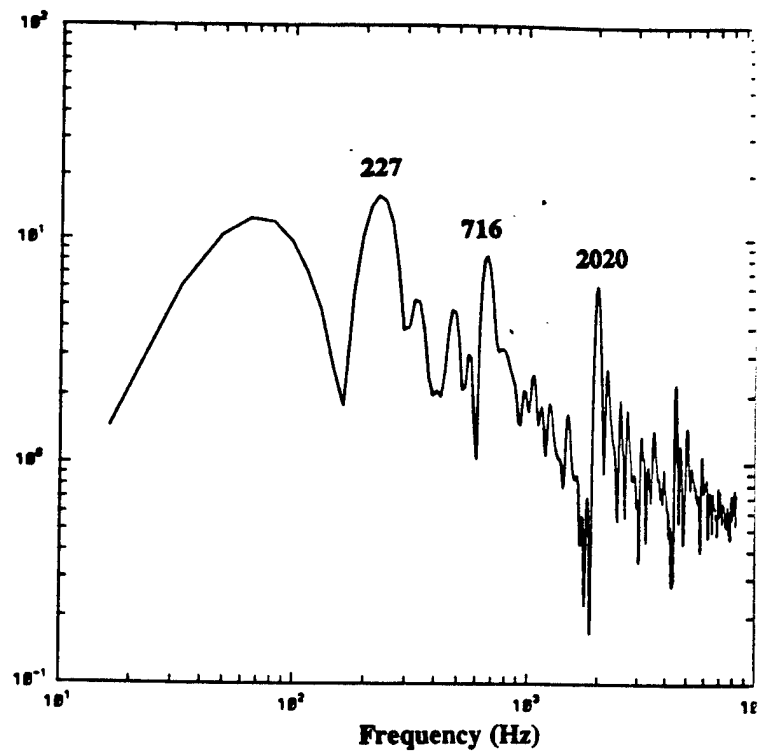


(b) 640 x 120 grid

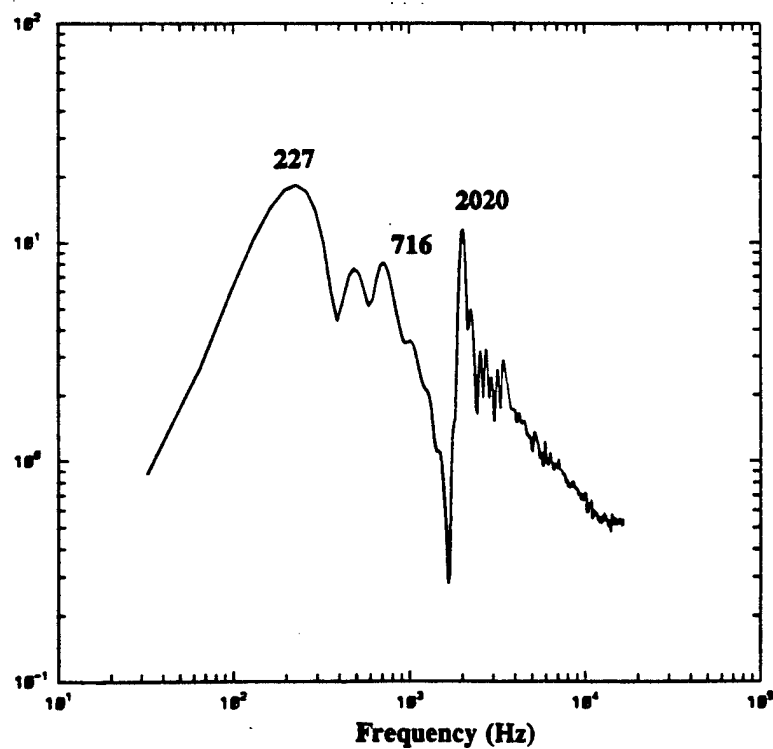
Figure 13. Comparison of vorticity spectra in the shear layer for different grid resolution using a constant eddy viscosity subgrid model.



(a) Pressure spectra at the base of the step



(b) Axial velocity spectra at the dump plane



(c) Vorticity spectra in the shear layer

Figure 14. Pressure, axial velocity and vorticity spectra using a 320 x 64 grid and an algebraic subgrid model.



**AIAA 93-0116**

**Some Issues Concerning Active Control of  
Combustion Instability in a Ramjet**

**S. Menon**

**Georgia Institute of Technology**

**Atlanta, GA**

**and**

**V. Yang**

**The Pennsylvania State University**

**University Park, PA**

**31st Aerospace Sciences  
Meeting & Exhibit  
January 11-14, 1993 / Reno, NV**

# **SOME ISSUES CONCERNING ACTIVE CONTROL OF COMBUSTION INSTABILITY IN A RAMJET**

**Suresh Menon**  
School of Aerospace Engineering  
Georgia Institute of Technology  
Atlanta, Georgia

and  
**Vigor Yang**  
Department of Mechanical Engineering  
The Pennsylvania State University  
University Park, Pennsylvania

## **ABSTRACT**

Active control of combustion instability in a ramjet has been numerically investigated using a large-eddy simulation technique. Various types of secondary fuel injection controllers have been investigated. The results of the study show that, in some cases, even when the amplitude of instability frequency is reduced, additional new frequencies can be excited which are not controlled. This phenomenon has been observed in the experiments, and has led to the investigation of advanced adaptive controllers that employ neural net algorithms. Numerically, such controllers are computationally very expensive to train and therefore, an alternate approach is sought. The approach proposed here employs a theoretical model for the dynamic behavior of nonlinear oscillations with distributed feedback actions. The theoretical model is used to analyze the simulation data (without control) and an optimization procedure is used to establish a criteria for selecting controller gains in terms of time-delays and locations of sensors and actuators. The theoretical analysis show that the limit cycle behavior of the LES-computed pressure oscillation during combustion instability can be reproduced quite well and further, that the theoretically devised controller can successfully suppress the amplitude of the oscillation. This demonstration provides the basis for the next step, which is to implement the theoretical model in the numerical simulation code to develop an adaptive secondary fuel injection controller that will automatically produce an optimum control response to the growth of the pressure oscillations.

## **1. INTRODUCTION**

Combustion instability in a ramjet engine is an extremely complex phenomenon involving nonlinear interactions among acoustic waves, vortex motion and unsteady heat release. Typically, the instability manifests itself as a large-amplitude pressure oscillation in the low-frequency range (100-800 Hz) and is very difficult to control. When the amplitude of the pressure oscillation reaches some critical limit, it can cause structural damage due to fatigue or can cause an engine "unstart," which occurs when

the shock in the inlet duct is expelled to form a bow shock ahead of the inlet. This phenomenon of engine unstart is one of the most serious technical problems encountered in developing an operational ramjet engine.

In recent years, both experimental (e.g., Schadow et al., 1987; Smith and Zukoski, 1985) and numerical (e.g., Menon and Jou, 1991) investigations have been conducted to determine the mechanism of the combustion instability. Results of both experimental and numerical studies show that the pressure fluctuations in the combustor grow to large-amplitude, low-frequency oscillations when the unsteady heat release in the combustor is in phase with the pressure fluctuation (the so-called Rayleigh criteria). These studies also showed that a large-scale vortex/flame structure propagates through the combustor at the same frequency suggesting a complex nonlinear coupling between the shear flow, the pressure oscillation and the unsteady heat release in the combustor.

Attempts to control combustion instability using both passive and active control techniques have also been carried out in the past. Passive control methods that typically involve structural (i.e., geometrical) modifications have proven insufficient for controlling the low-frequency instability (Culick, 1989). Recent experimental studies (e.g., Langhorne and Hooper, 1989; Wilson et al, 1991; Gutmark et al., 1992) suggest that active control techniques may be more effective in controlling the combustion instability in a ramjet. In parallel to the experimental studies, a numerical study of active control methods is also being carried out (Menon, 1991, 1992a, 1992b, 1992c). The results of the simulations are in good agreement with experimental observation. However, both experimental and numerical studies indicate that the development of a general-purpose active controller (i.e., controllers that work over a wide operating regime) to suppress the instability will require further investigation. In this paper, the various issues involved in carrying out numerical studies of active control are first discussed and then an approach that will be used to develop an adaptive numerical controller is introduced.



## 2. ACTIVE CONTROL OF COMBUSTION INSTABILITY - UNRESOLVED ISSUES

Experimentally, two active control techniques have been demonstrated successfully in the laboratory. These techniques involve acoustic feedback control and secondary fuel injection control. Both techniques have successfully suppressed the instability in small-scale dump combustor. Acoustic feedback control involves sensing the pressure signature at some chosen location (using a microphone), amplifying and phase shifting (or time delaying) the signal and then driving the acoustic driver (typically, a loudspeaker) at another chosen location (e.g., Lang et al., 1987). This type of controller changes the phase relationship between the pressure fluctuation and the unsteady heat release in the combustor, thereby damping the oscillation. Acoustic drivers have also been used to modulate the fuel flow rate at the frequency of the combustion instability with varying phase shift relative to the instability (Wilson et al., 1991). Results show that the instability level can be suppressed by nearly 50% using this approach; however, the control effectiveness was limited to a certain range of phase shift angles. Furthermore, the effectiveness of this type of control system was limited to low flow rates, for which a single mode instability occurs.

Numerical studies have essentially confirmed these results. For example, simulations using an acoustic feedback controller showed that the controller is effective only as long as the cross-correlation between the recorded pressure signature and the driving pressure signal was negative (Menon, 1991; 1992a). Although, these experimental and numerical results were encouraging, in realistic ramjet combustors, acoustic drivers are not practical due to the hostile (hot) environment in the combustor. In addition, realistic combustors operate in the MW range and the large power requirements for the acoustic drivers makes acoustic feedback control an impractical means for controlling instability.

Active control techniques which use secondary injection of the fuel as the controller have shown to be more practical in controlling combustion instability, at least in laboratory dump combustors (e.g., Langhorne and Hooper, 1989). This approach achieves control of the instability by directly manipulating the unsteady heat release in the combustor using a controlled supply of secondary fuel flow into the combustor. Since this approach also has the potential for increasing the net thrust of the engine while controlling the low-frequency instability (Langhorne and Hooper, 1989), this method appears to be the most promising one for full-scale ramjet engines.

Practical application of such a controller in a full-scale combustor has yet to be demonstrated. Studies using laboratory combustors show that control using secondary fuel injection can be quite complicated, in part due to the fact that in high flow rate combustors, combustion is irregular, and, multiple frequencies are amplified. In this case, the dominant instability mode can shift in frequency depending upon operating conditions. When active control is attempted using secondary heat release, even when the dominant oscillation amplitude is suppressed, additional new frequencies can be excited that are not controlled. This phenomena has been observed in both the experiments (Gutmark et al., 1992) and recent numerical simulations (Menon, 1992b, 1992c). The switching of the dominant mode of instability from one frequency to another during

active control makes development of a general purpose controller quite difficult.

The limited success of single frequency controllers has led to development of more complex controllers such as the dual-loop feedback control system to suppress bi-model instabilities (Gutmark et al., 1992). The results were somewhat successful; when the two frequencies were harmonic, the controller succeeded in suppressing the amplitudes of both the frequencies, however, when the frequencies were anharmonic, suppression of one frequency resulted in amplification of the other. More complex systems currently under development involve application of neural nets algorithms (e.g. Bowman and Powell, 1992). This method has the potential for application to realistic combustors but requires that the neural net be trained on a particular combustor before it can become effective. The training process itself requires a series of experiments (without control) varying one parameter at a time while recording the combustor response. Typically, the nature of the pressure oscillation (frequency and amplitude) and the energy output from the combustor is recorded as a function of various operating parameters such as fuel flow rate, flow velocity, equivalence ratio, and inflow air temperature. The neural net algorithm then attempts to minimize (or maximize) a prespecified cost function (for example, minimize pressure amplitude and maximize energy output) by introducing appropriate control signal (e.g., acoustic waves or secondary fuel) into the combustor.

Although such a training process has been demonstrated in the laboratory, from the computational standpoint, it is clearly impractical due to the extensive computational resources that will be required to develop the operating map. Therefore, it is necessary to seek an alternate approach that can be used economically in a numerical simulation.

In recent studies, a theoretical analysis of active control of nonlinear combustion instabilities in combustion chamber has been developed (Fung and Yang, 1992; Fung et al., 1991, Yang et al., 1992). This approach involves application of the generalized wave equation which describes the dynamic behavior of nonlinear oscillations with distributed feedback actions. Control studies using secondary fuel injection, with its instantaneous mass flow rate modulated by a proportional-plus-integral controller has been studied. Analytical studies using this theoretical model has demonstrated a capability to study the behavior of nonlinear oscillations and has enabled a systematic examination of various characteristics associated with secondary fuel injection control in dump combustors. More importantly, these studies demonstrated an optimization procedure to establish a criteria for selecting controller gains in terms of time-delays and locations of sensors and actuators.

It is the eventual goal of this collaborative research to utilize this theoretical framework to both analyze the simulation results and to develop a numerical secondary fuel injection controller that can be coupled to the simulation model so that when the instability begins to manifest itself, the controller will automatically develop an optimum response and suppress the instability. In the following, the pertinent features of the theoretical and simulation models are summarized and then some of the results obtained so far are discussed.

### 3. THE THEORETICAL MODEL

The theoretical analysis of combustion instabilities under active control actions follows the general formulation described by Fung and Yang (1992). Briefly stated, a wave equation for the acoustic pressure is first derived with expansion of the dependent variables in two small parameters which measure the Mach number of the mean flow and the amplitude of the wave motion. The wave equation with its boundary condition can be written as

$$\nabla^2 p' - \frac{1}{a^2} \frac{\partial^2 p'}{\partial t^2} = h + h_c \quad (1)$$

$$\mathbf{n} \cdot \nabla p' = -f - f_c \quad (2)$$

where  $h$  and  $f$  accommodate all influences of acoustic motions, mean flow, and combustion response, under conditions without external forcing. The functions  $h_c$  and  $f_c$  represent the effects arising from the control inputs. Their explicit expressions depend on the specific controller under investigation.

To establish a closed-loop control system, the source term  $h_c$  is related to the mass flow rate of the injected fuel by means of a generalized time-lag theory (Fung et al., 1991). If the multiplicative effects of the acoustic field on the control input are ignored,  $h_c$  takes the form

$$h_c(\mathbf{r}, t) = -\frac{\bar{R}\Delta H_c}{a^2 C_v} \left[ \frac{\partial \dot{m}_{in}(t-\tau)}{\partial t} R(\mathbf{r}(\tau), t-\tau) \right] \quad (3)$$

where  $\dot{m}_{in}(t)$  is the injection rate of the control fuel at time  $t$ ,  $a$  is speed of sound,  $\Delta H_c$  is the heat of formation of the fuel (per unit mass),  $\bar{R}$  is the gas constant, and  $C_v$  is the specific heat at constant volume. Further,  $R(\mathbf{r}(\tau), t)$  is a spatial distribution function characterizing the fraction of the fuel element burned at position  $\mathbf{r}$  with a time delay  $\tau$  in respect to the moment of injection. For the convenience of formulation, the distributed control action is approximated by an assembly of  $M$  point actuators; each supplies a control excitation  $b_k u_{in}(t-\tau_k)$  at a position  $\mathbf{r}_k$ . Thus, the above equation leads to

$$h_c(\mathbf{r}, t) = -\sum_{k=1}^M \left[ b_k u_{in}(t-\tau_k) \right] \delta(\mathbf{r}-\mathbf{r}_k) \quad (4)$$

with

$$u_{in}(t-\tau_k) = \frac{\bar{R}\Delta H_c}{a^2 C_v} \left[ \frac{\partial \dot{m}_{in}(t-\tau_k)}{\partial t} \right] \quad (5)$$

and

$$b_k = R(\mathbf{r}_k(\tau_k), t-\tau_k) \Delta V(\mathbf{r}_k) \quad (6)$$

where  $\Delta V(\mathbf{r}_k)$  denotes the volume of the discretized element at position  $\mathbf{r}_k$ ,  $\delta(\mathbf{r}-\mathbf{r}_k)$  the Dirac delta function, and  $\tau_k$  the time delay associated with the  $k$ th point actuator.

Since the source terms in Eqs. (1) and (2) are treated as small perturbations to the acoustic field, within second-order accuracy, the solution of the wave equation (1) can be legitimately approximated by a synthesis of the normal modes of the chamber. Thus,

$$p'(\mathbf{r}, t) = \bar{p} \sum_{n=1}^{\infty} \eta_n(t) \psi_n(\mathbf{r}) \quad (7)$$

where  $\eta_n$  are the amplitudes of the  $n$ th mode and  $\psi_n$  are the normal mode function satisfying

$$\nabla^2 \psi_n + k_n^2 \psi_n = 0 \quad (8)$$

with  $\mathbf{n} \cdot \nabla \psi_n = 0$  along the boundary. Substituting Eq. (7) into Eq. (1), multiplying the result by  $\psi_n$ , and integrating over the entire volume, we obtain the set of ordinary differential equations for the amplitude of each mode.

$$\ddot{\eta}_n + \omega_n^2 \eta_n = F_n \quad (9)$$

If the nonlinear contributions arise only from acoustic wave motions, the forcing function  $F_n$  can be expressed more conveniently as follows (Fung, 1991):

$$F_n = -\sum_{i=1}^{\infty} \left[ D_{ni} \dot{\eta}_i + E_{ni} \eta_i \right] - \sum_{i=1}^{\infty} \sum_{j=1}^{\infty} \left[ A_{nij} \dot{\eta}_i \dot{\eta}_j + B_{nij} \eta_i \eta_j \right] + U_n(t) \quad (10)$$

where the coefficients  $D_{ni}$  and  $E_{ni}$  represent the influences of linear processes, and  $A_{nij}$  and  $B_{nij}$  result from the nonlinear coupling of acoustic modes. The control input to the  $n$ th mode,  $U_n(t)$ , can be shown to be (Fung et al., 1991):

$$U_n(t) = \frac{a^2}{\bar{p} E_n^2} \sum_{k=1}^M \left[ b_k u_{in}(t-\tau_k) \right] \psi_n(\mathbf{r}_k) \quad (11)$$

where  $E_n$  denotes the Euclidean norm of the mode function.

To complete the formulation, the state of the acoustic field must be determined. In the numerical simulation, the instantaneous pressure signature is monitored at a fixed location, for example, at the wall near the downstream diffuser (Menon, 1991). Mathematically, this can be interpreted as a point sensor, located at position  $\mathbf{r}$ , and having an amplification factor  $c$ . Thus, the sensor output  $y(t)$  becomes

$$y(t) = c p'(\mathbf{r}, t) = \bar{p} \sum_{n=1}^{\infty} \eta_n(t) \psi_n(\mathbf{r}) \quad (12)$$

Following the idea discussed in Fung et al. (1991), a proportional-plus-integral (PI) controller is proposed for modulating the mass injection rate of the secondary fuel. Because it is the time derivative of the fuel injection rate that exerts direct influence on the acoustic field, the PI control law is equivalent to introducing a proportional-plus-derivative (PD) control action to the feedback system. Thus, from Eq. (5), the total acoustic pressure input produced by the combustion of the injected fuel becomes

$$u_{in}(t) = \frac{\bar{R}\Delta H_c}{a^2 C_v} \left[ \frac{\partial \dot{m}_{in}(t)}{\partial t} \right] \quad (13a)$$

$$= K_P e(t-\tau_c) + K_D \dot{e}(t-\tau_c) \quad (13b)$$

where  $e(t)$  is the error signal between the desired system

response  $r(t)$  and the measured pressure output  $y(t)$ . The time delay between the sensor output and fuel injection  $\tau_c$ , accounts for the actual time required for data acquisition, signal processing, and dynamic response of the fuel injection mechanism. The coefficients  $K_P$  and  $K_D$  are defined as the effective proportional and derivative gains of the feedback control loop, respectively. The above equations (Eqs. 11-13), in conjunction with the system equation (7), provide a complete description of the nonlinear acoustic flow field in the combustion chamber under distributed PD control actions.

### 3.1. Selection of Controller Parameters

The goal of the controller design is to determine the actuator inputs so that the amplitude of the pressure oscillation can be modulated within a desired range according to the prespecified requirements for control-input energy and actuating duration. From the aspect of hardware implementation, the only major parameter to be determined is the instantaneous injection rate of the control fuel. However, for the distributed-control system treated here, the effectiveness of the control actions depends not only on the controller gains  $K_P$  and  $K_D$ , but also on the time delay and the spatial distribution of the external forcing associated with the burning of the injected fuel. Thus, strategies must be established to optimize the controller parameters, under constraints imposed by the distributed combustion of the control fuel.

For a distributed-input system, the integrated effects of all the constituent actuators must be taken into account in determining the controller gains. Unfortunately, the spatial variation of time delays associated with these actuators,  $\tau_k (k = 1, \dots, M)$ , prohibits the use of simple formula to satisfy the following criteria: (1) the performance of the controller is least sensitive to the variation of the actuator time delay; and (2) the energy of the control input is minimized. Since the optimization procedure intrinsically involves contributions from all the point actuators, an arithmetic average of the optimization condition for individual point actuators can be carried out (Fung and Yang, 1992). Thus, the optimized controller gain ratio for a distributed-input system becomes:

$$\frac{K_P}{K_D} = - \frac{\omega_n \sum_{k=1}^M [U_{nk} \sin(\omega_n \tau_k)]}{\sum_{k=1}^M [U_{nk} \cos(\omega_n \tau_k)]} \quad (14)$$

Using this relation along with the assumption that the acoustic mode amplitudes are of the form

$$\eta_n(t) = e^{\alpha_n t} \sin[(\omega_n + \theta_n)t + \xi_n] \quad (15)$$

the gain parameters  $K_P$  and  $K_D$  can be determined in terms of  $\alpha_n$  and  $\omega_n$ . Here,  $\alpha_n$  and  $\theta_n$  are the linear growth constant and the frequency shift for the corresponding open-loop system (i.e., without control) and can be determined in terms of the linear terms  $D_{ni}$  and  $E_{ni}$ . Once the gain parameters,  $K_P$  and  $K_D$  are known, the secondary fuel injection strategy for active control can be determined from equation (13b) in terms of the sensor output.

## 4. THE SIMULATION MODEL

The eventual goal of this research is to utilize the theoretical model described above in a numerical simulation model to analyze and devise appropriate active control algorithm to suppress combustion instability. The simulation model used to simulate combustion instability has been described in details elsewhere (Menon and Jou, 1990; 1991). Briefly, the full, unsteady, compressible Navier-Stokes equations are formulated in the axisymmetric coordinate system. The numerical technique is an unsplit fourth-order-accurate, finite-volume scheme based on the MacCormack's method. The modeled ramjet combustor consists of an axisymmetric inlet duct connected to an axisymmetric dump combustor by a sudden expansion. A convergent-divergent nozzle is attached downstream of the combustor. Figure 1 shows the typical ramjet configuration used in these studies. This configuration is similar to an experimental test rig currently being used for active control studies at the Naval Weapons Center, China Lake (Wilson et al., 1991; Gutmark et al., 1992) except that in the simulations, a convergent-divergent nozzle is attached downstream of the combustor. This is more representative of a real operating ramjet configuration. The flow through this nozzle is choked, and the outflow at the downstream computational boundary is supersonic.

The combustion model in the simulation code employs the thin flame approximation and a model equation for premixed combustion in terms of a progress variable  $G$  (Kerstein et al., 1988; Menon and Jou, 1991):

$$\frac{\partial \rho G}{\partial t} + \frac{\partial}{\partial x_i} \rho u_i G = -\rho u_F |\nabla G| \quad (16)$$

where  $\rho$  is the density and  $u_i$  is the fluid velocity. Equation (15) describes the convection of the flame by the local fluid velocity and the flame propagation into the unburnt mixture through a Huygens type mechanism,  $u_F |\nabla G|$ . Here, by definition,  $G = 1$  corresponds to the premixed fuel state,  $G = 0$  corresponds to the fully burnt state and the flame is located at a prescribed  $G = G_0$  level surface, where,  $0 < G_0 < 1$ . For laminar premixed combustion, the local flame speed  $u_F$  is the laminar flame speed  $S_L$  which contains the information on the chemical kinetics and the molecular dissipation. When Equation (15) is applied to turbulent flows, the local flame speed  $u_F$  is taken to be the local turbulent flame speed  $u_T$ , where  $u_T$  is a prescribed function of local turbulence intensity  $u'$  and the laminar flame speed  $S_L$ . The implementation of the thin flame model as a part of the LES transport equations, therefore, explicitly requires the specification of the subgrid turbulent kinetic energy to determine the turbulent flame speed. This is accomplished by explicitly computing the subgrid turbulent kinetic energy. The details of the implementation of the combustion model and the subgrid kinetic energy equation is given elsewhere (Menon and Jou, 1991; Menon, 1992b), and will not be repeated here.

## 5. SIMULATION OF COMBUSTION INSTABILITY

The theoretical model for combustion instability control formulated in Section 3 is applicable only for situations when the instability is caused by the acoustic modes in the combustor. Combustion instability due to the acoustic resonant modes in the combustion chamber have been seen in both the experiments and numerical studies. Therefore,

the theoretical model can be applied to study and control such types of combustion instability.

However, experiments have shown that, in some cases, the instability mechanism is not purely acoustic in nature and may include a convective component which is related to vortex motion in the combustor (e.g., Schadow et al., 1987; Yu et al., 1991). Numerical studies of both cold (Jou and Menon, 1990) and reacting flows (Menon, 1992b) in ramjet combustors have also shown that a coupled acoustic-vortex mode can exist in ramjet combustors. The frequency of this coupled mode oscillation is different from that of a pure acoustic resonant mode. The theoretical model does not include the convective effect and thus, may not be appropriate for developing active control strategies when coupled-mode instability occurs in the combustor. Further research is required to extend the current formulation to account for convective effects.

In the following, we briefly describe the pertinent characteristics of both types of combustion instability that were recently numerically computed. More detailed analysis of these simulations was reported recently (Menon, 1992c).

Figure 2a shows the characteristics pressure trace at the base of the step for a simulation with a reference Mach number of 0.32 and Figure 2b shows the computed pressure spectra. A low frequency oscillation with a peak-to-peak level of around 30 percent of the mean pressure is seen. The pressure spectra shows a dominant frequency of around 234 Hz and also shows its higher harmonic at around 458 Hz. The amplitude of the dominant frequency in the inlet and in the combustor was computed and the axial variation of the amplitude showed the presence of a standing half-wave acoustic mode in the combustor (Menon, 1992c). A simple determination of the acoustic frequency by using the relation  $f = a/2L_i$  with  $L_i = 0.711$  m and using the speed of sound  $a$  based on the temperature at the inlet gives nearly the same frequency. Thus, it appears that the inlet duct acts as a long-wavelength acoustic resonator. The theoretical model described earlier can, therefore, be used for developing a controller for this instability. This is described in the later sections.

The convective mode instability was seen in another simulation with a lower Mach number of 0.17 (obtained by decreasing the inlet velocity). All other conditions were maintained the same as in the earlier Mach 0.32 simulation. Figure 3a shows the pressure trace at the same location as in Figure 2a and Figure 3b shows the computed pressure spectra. It can be seen that with the decrease in the Mach number the dominant frequency shifts down to around 87 Hz. A higher harmonic of this oscillation at 178 Hz is also seen in the pressure spectra. The peak-to-peak pressure fluctuation level remains relatively unchanged from that seen in the earlier simulation (Figure 2). Since the acoustic mode frequency should remain unaffected by the change in the flow velocity, this indicates that this type of instability has a convective component. Decrease in the instability frequency with the decrease in the inlet velocity has also been observed in experimental configurations (e.g., Yu et al., 1991). The acoustic oscillation at the 244 Hz frequency seen in the earlier simulation is no longer dominant in the combustor; however, the pressure and the axial velocity spectra in the inlet do show the presence of this frequency (Menon, 1992c). These results indicate that both the convective and the acoustic resonant modes are present in the

flow field but that only one mode may dominate at any given situation.

A simple criterion developed by Yu et al. (1991) can be used to demonstrate the nature of the instability. They suggested that for a coupled acoustic/convective mode to exist, the instability period is the sum of two time scales: a time scale associated with the motion of the vortex/flame structure in the combustor ( $\tau_v$ ) and a time scale associated with the time required for a pressure wave to travel from the sonic throat (which acts as a downstream acoustic boundary) to the upstream inlet duct boundary and back to the dump plane ( $\tau_a$ ). Here, we choose  $\tau_v = L_c/u_{ref}$ , where,  $L_c$  the distance from the dump plane to the sonic throat and  $u_{ref}$  as the characteristic axial velocity at the inlet boundary. The acoustic time scale is determined as

$$\tau_a = \left\{ 2 \frac{L_i}{a} \frac{1}{1-M^2} + \frac{L_c}{a-u_{ref}} \right\}. \quad \text{The instability period}$$

$T_i = \tau_v + \tau_a$  was computed for both the Mach 0.32 and 0.17 cases. The frequency for a coupled acoustic/vortex mode (if it exists) for the Mach 0.32 case was found to be around 115 Hz while for the Mach 0.17 case it was around 90 Hz. Clearly, the numerically computed frequency of 244 Hz for the Mach 0.32 case is not in the range for a coupled mode; however, the frequency of 87 Hz obtained in the Mach 0.17 simulation is close to the frequency obtained from the simple model.

The theoretical model is now used to analyze the simulated results (the acoustic mode instability) and to determine if a controller can be developed to suppress the instability. A more simplified control algorithm has also been used in the numerical simulation to evaluate its effect on the pressure oscillation. These results are summarized below.

## 6. THEORETICAL ANALYSIS OF THE SIMULATED COMBUSTION INSTABILITY

The theoretical model summarized in Section 3 is implemented to analyze the calculated pressure fluctuation in the combustor. The simulated instability shown in Figure 2 was used for this purpose. Emphasis is placed on the non-linear coupling of acoustic oscillations. With the aid of the method of time averaging, the time-varying amplitude  $\eta_n(t)$  is split into two variables:  $r_n(t)$  and  $\phi_n(t)$  representing the amplitude and phase of the  $n$ th mode, respectively. Then, using a functional form:  $\eta_n(t) = r_n(t) \sin[\omega_n t + \phi_n]$ . Equation (9) reduces to a system of ordinary differential equations characterizing the amplitude and phase of each mode (Fung et al., 1991):

$$\frac{dr_n}{dt} = \alpha_n r_n \quad (17)$$

$$- \frac{n\beta}{2} \sum_{i=1}^{\infty} [\gamma_{in} \cos \Phi_1 + \sigma_{in} \cos \Phi_2 - \xi_{in} \cos \Phi_3]$$

and

$$\frac{d\phi_n}{dt} = \theta_n \quad (18)$$

$$- \frac{n\beta}{2r_n} \sum_{i=1}^{\infty} [\gamma_{in} \sin \Phi_1 + \sigma_{in} \sin \Phi_2 - \xi_{in} \sin \Phi_3]$$

Here,  $\gamma_{in} = r_i r_{i-n}$ ,  $\sigma_{in} = r_i r_{i+n}$ ,  $\xi_{in} = r_i r_{n-i}$ ,  $\Phi_1 = \phi_n - \phi_i - \phi_{i-n}$ ,  $\Phi_2 = \phi_n + \phi_i - \phi_{i+n}$ , and  $\Phi_3 = \phi_n - \phi_i - \phi_{n-i}$ . The coefficient  $\beta$  arises from the

second-order nonlinear acoustic interactions among modes. Since the simulation results show only two modes (Figure 2), only the first two modes are used from these relations. Rewriting Equations (17) and (18) for the first two modes and setting the time derivatives to zero, the result can be rearranged to obtain the explicit expressions for the amplitudes of limit cycles:

$$r_{10} = \frac{1}{\beta \cos \Phi_0} \sqrt{-\alpha_1 \alpha_2} \quad (19)$$

$$r_{20} = \frac{1}{\beta \cos \Phi_0} \alpha_1 \quad (20)$$

$$\Phi_0 = \tan^{-1} \left[ \frac{2\theta_1 - \theta_2}{2\alpha_1 + \alpha_2} \right] \quad (21)$$

The subscript 0 denotes values in the limit cycles. Because the amplitude  $r_{10}$  is real, we must have  $\alpha_1 \alpha_2 < 0$ . This is the necessary and sufficient condition for the existence of limit cycles in a two-mode system. If one mode is linearly stable, then the second mode must be unstable. Examination of the simulation data suggests that the first mode (234 Hz) is clearly unstable.

With a judicious selection of the linear parameters, the calculated pressure oscillations presented in Figure 2 can be faithfully simulated. Figure 4(a) shows the amplitude of both the computed modes showing the existence of a stable limit cycle. To obtain this result the amplitude of the pressure fluctuation, the dimensions of the combustor and the fuel inlet temperature (needed to compute  $a$ ) from the simulation were used to inversely solve Equations (19)-(21) to obtain the linear growth parameters  $\alpha_1$  and  $\alpha_2$ . Then the amplitude equations for the first two modes, Equation (17) are solved to obtain the growth of linear disturbance into the finite-amplitude limit cycle.

Once the conditions (i.e., the linear parameters) for the limit cycle behavior are determined, they can then be used to calculate the controller gain parameters,  $K_P$  and  $K_D$ . The ability of the derived controller to suppress the instability can then be investigated. This is described in the next section along with the results of the numerical studies.

## 7. ACTIVE CONTROL OF COMBUSTION INSTABILITY

Active control of combustion instability using secondary fuel injection has been studied using both theoretical and numerical methods separately. So far, the eventual goal of coupling the theoretical model with the simulation model has not been achieved; however, research in that direction is currently underway. It is worthwhile noting that the process used to obtain the parameters (in Section 6) is essentially what needs to be implemented in the code. Here, we describe the results of the theoretical and the numerical studies that were carried out without direct coupling.

### 7.1. Theoretical Results

The theoretical model has been used to determine the parameters that reproduce the limit cycle behavior seen in the numerical simulation (Figure 4a). Subsequently, the gain parameters for the proportional-plus-integral controller were computed and the behavior of the pressure oscillation

under the influence of this controller studied. This involves using Equation (13) in (11) and then solving Equation (9) for the first two modes. Figure 4b compares the amplitude of the pressure oscillation of the two acoustic modes with and without control. The results show that with control, the dominant mode amplitude is decreased by around 35 percent clearly suggesting that this type of controller should be successful.

Further work is planned in the theoretical study to investigate and fine-tune the secondary fuel injection parameters, such as, the time-delay, the location of the fuel injection and the gain parameters to understand the behavior of the controller. This would help in understanding the behavior of the controller when it is implemented in the simulation model.

### 7.2. Numerical Results

The numerical implementation of the secondary fuel injection controller involved some simplifications. The secondary fuel is introduced one step height upstream of the step in the inlet and normal injection is modeled. Thus, when secondary fuel is introduced in the inlet, the primary and the secondary fuel streams are both (cold) premixed fuel and the net effect of secondary injection is a modulation and an increase of the total mass flow into the combustor. This makes it difficult to interpret the time delay  $\tau$  or  $\tau_c'$  used in the theoretical model to represent the time between the injection and the actual combustion process.

To determine the time delay  $\tau_c$  (see Equation 13b) associated with the time between the sensor output and fuel injection, a cross-correlation between the sensor signal (the sensor is the wall pressure near the downstream diffuser) and the pressure signature at the base of the step was carried out to determine the time delay for peak negative correlation. (The use of such a time delay was quite successful in the study of acoustic feedback control, Menon, 1991).

A proportional fuel injection controller was chosen for the simulation:

$$\dot{m}_{sc} = Ga_1 p_s'(t - \tau_c) \quad (22)$$

where,  $\tau_c$  is a prescribed time-delay,  $\dot{m}_{sc}$  is the secondary mass flow rate and  $p_s'$  is the unsteady sensor output.  $Ga$  is a transfer function can be related to the heat content of the fuel and the mean inlet speed of sound using the theoretical model in Section 3. This controller was simpler to implement numerically than the PI controller (Equation 13), and was therefore, first investigated. A PI controller of the form:

$$\dot{m}_{sc} = Ga_2 \frac{\partial p_s'(t - \tau_c)}{\partial t} \quad (23)$$

is currently being implemented. The gain parameter  $Ga_2$  will be determined in terms of the theoretically derived coefficients  $K_P$  and  $K_D$ . The results of this approach will be reported later.

In addition to prescribing the secondary fuel flow rate, additional conditions are necessary to implement the injection boundary conditions. Details of the injection boundary conditions were described earlier (Menon, 1992a, 1992b).

Figure 5a shows the pressure signature at the base of the step during an active control study of the Mach 0.32 simulated instability. For this simulation, the controller, equation (21) was used with a time delay of 2 msec and the secondary fuel injection was carried out whenever  $p_s'(t - \tau) > 0$ . When the sensor signal showed a negative value, the injection was turned off. Thus, the controller modeled here was a pulsed unsteady injection system. For these values, the secondary mass flow rate was approximately 10 percent of the reference mass flow rate at the inlet. The control simulation was initiated by restarting the previous (uncontrolled) simulation (Figure 2) at an earlier time. The results show that the pressure oscillation is controlled with around a 50 percent drop in the peak-to-peak pressure fluctuation level (or around 35 percent reduction in the rms levels). This is similar to the level reduction obtained in the theoretical analysis and also similar to the experimental results of Gutmark et al. (1992).

The spectral analysis of the pressure fluctuation at the base of the step is shown in Figure 5b. The dominant oscillation frequency seen in the uncontrolled simulation is still present in this spectra. This suggests that the inlet duct acoustics is still controlling the combustion instability. A low frequency of around 75 Hz is also seen in the spectra. At present, the source of this mode of oscillation cannot be determined since this simulation has not been carried out long enough to obtain sufficient data to spectrally resolve this low frequency.

## 8. CONCLUSIONS

In this paper, the formulation of a theoretical model to study combustion instability and active control is described. The primary focus has been to develop the theoretical model so that it can be implemented within a unsteady simulation model. This would allow the use of the theoretical model during the simulation to determine the parameters that govern the behavior of limit cycles. This has been demonstrated by using the numerical simulation data to obtain the growth parameters in Section 7. Subsequently, the controller gains will be determined and used to control the introduction of the secondary fuel into the combustor. Preliminary analysis of the controller shows that it can reduce the amplitude of the limit cycle.

Numerical simulations using a simpler version of the proportional-plus-integral controller (investigated theoretically) has been carried out to control combustion instability in a ramjet. The results show that the instability amplitude can be reduced by around 35 percent using a proportional controller.

There are a few parameters, such as, the proper time delay, the sensor and fuel injection locations, etc., that will have to be optimized using numerical simulations. However, it is hoped that this combined approach will prove to be computationally more efficient than the neural net training process (being used experimentally) for the development of adaptive controls.

## ACKNOWLEDGEMENT

This research is funded by the Office of Naval Research under Contract No. N00014-92-J-4030 and monitored by Dr. Eric Hendricks of the Applied Research and Technology Directorate. The computational resources were provided by the Numerical Aerodynamic Simulator (NAS) at NASA Ames Research Center and are gratefully acknowledged.

nowledged.

## REFERENCES

- Bowman, C. T. and Powell, J. D. (1992) "Investigation of Adaptive Optimal Control of Performance of Air-Breathing Combustors," Proceeding of the ONR Active Control Research Initiative Review, pp. 6-15.
- Culick, F. E. C. (1989) "Combustion Instabilities in Liquid-Fueled Propulsion Systems - An Overview," AGARD CP-450, pp. 1.1-1.73.
- Fung, Y. T. (1991), "Active Control of Linear and Nonlinear Pressure Oscillations in Combustion Chambers," Ph.D. Thesis, The Pennsylvania State University, University Park, PA.
- Fung, Y. T., Yang, V., and Sinha A. (1991), "Active Control of Combustion Instabilities with Distributed Actuators," *Combustion Science and Technology*, Vol. 78, pp. 217-245.
- Fung, Y. T., Yang, V. (1992), "Active Control of Nonlinear Pressure Oscillations in Combustion Chambers," *Journal of Propulsion and Power*, Vol. 8, pp. 1282-1289.
- Gutmark, E., Wilson, K. J., Parr, T. P., and Schadow, K. C. (1992) "Feedback Control of Multimode Combustion Instability," AIAA-92-0778.
- Jou, W.-H., and Menon, S. (1990) "Modes of Oscillations in a Nonreacting Ramjet Combustor Flow," *J. Propulsion and Power*, Vol. 6, pp. 535-543.
- Kerstein, A. R., Ashurst, W. T., and Williams, F. A. (1988) "Field Equation for Interface Propagation in an Unsteady Homogeneous Flow Field," *Physical Rev. A*, Vol. 37, No. 7, pp. 2728-2731.
- Lang, W., Poinot, T., and Candel, S. (1987), "Active Control of Combustion Instability," *Comb. and Flame*, Vol. 70, pp. 281-289.
- Langhorne, P. J., and Hooper, N. (1989) "Attenuation of Reheat Buzz by Active Control," AGARD-CP-450, pp. 10.1-10.16.
- Menon, S., and Jou, W.-H. (1990) "Numerical Simulations of Oscillatory Cold Flows in an Axisymmetric Ramjet Combustor," *J. Propulsion and Power*, Vol. 6, No. 5, pp. 525-534.
- Menon, S., and Jou, W.-H. (1991) "Large-Eddy Simulations of Combustion Instability in an Axisymmetric Ramjet Combustor," *Combustion Science and Technology*, Vol. 75, pp. 53-72.
- Menon, S. (1991) "Active Control of Combustion Instability in a Ramjet Combustor using Large-Eddy Simulation," AIAA Paper No. 91-0411.
- Menon, S. (1992a) "Active Combustion Control of Combustion Instability in a Ramjet Combustor using Large Eddy Simulations," *Combustion, Science and Technology*, Vol. 84, pp. 51-79.
- Menon, S. (1992b) "A Numerical Study of Secondary Fuel Injection Technique for Active Control of Instability in a Ramjet," AIAA-92-0777.
- Menon, S. (1992c) "Secondary Fuel Injection Control of Combustion Instability in a Ramjet", submitted to *Combustion, Science and Technology*.

Schadow, K. C., Gutmark, E., Parr, T. P., Parr, D. M., Wilson, K. J., and Crump, J. H. (1987) "Large-Scale Coherent Structures as Drivers of Combustion Instability," AIAA-87-1326.

Smith, D. A., and Zukoski, E. E. (1985) "Combustion Instability Sustained by Unsteady Vortex Combustion," AIAA-85-1248.

Wilson, K. J., Gutmark, E., Schadow, K. C., and Smith, R. A. (1991) "Active Control of a Dump Combustor with Fuel Modulation," AIAA-91-0368.

Yang, V., Sinha A., and Fung, Y. T. (1992), "State-Feedback Control of Longitudinal Combustion Instabilities," *Journal of Propulsion and Power*, Vol. 8, pp. 66-73.

Yu, K. H., Trouve, A., and Daily, J. W. (1991) "Low-Frequency Pressure Oscillations in a Model Ramjet Combustor," *J. Fluid Mech.*, Vol. 232, pp. 47-72.

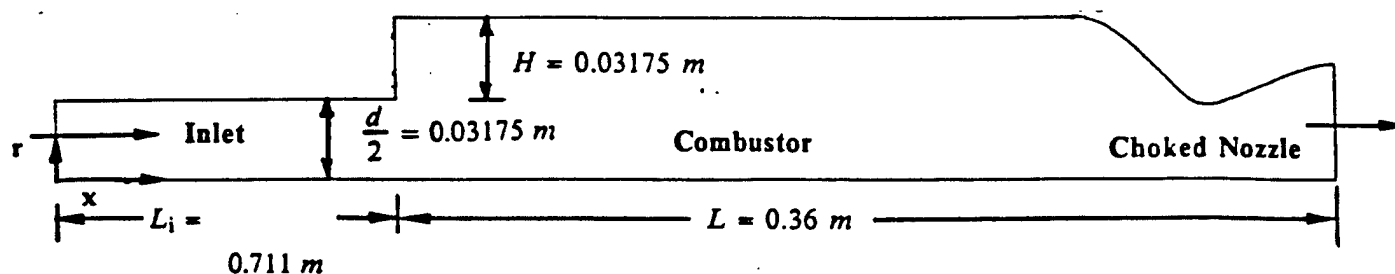
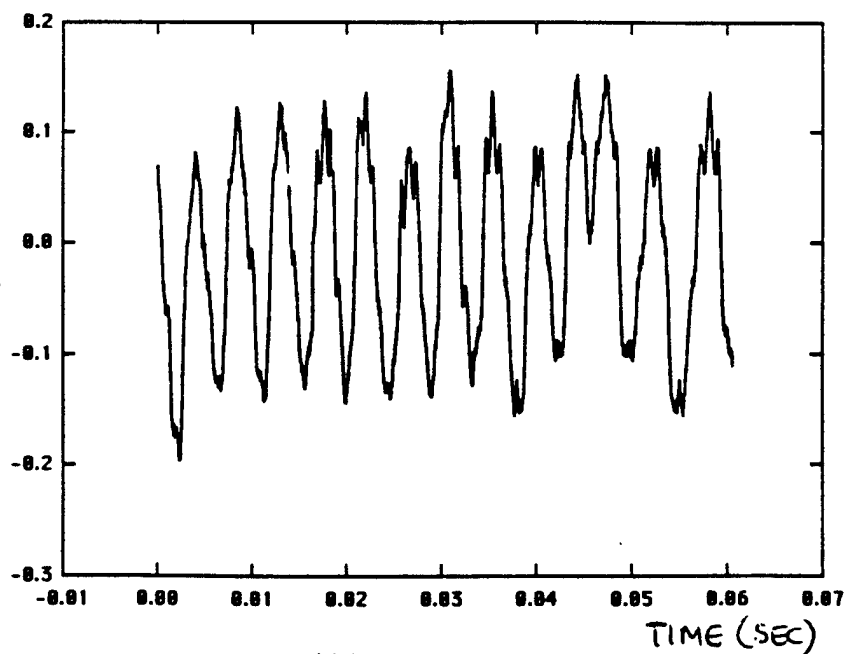
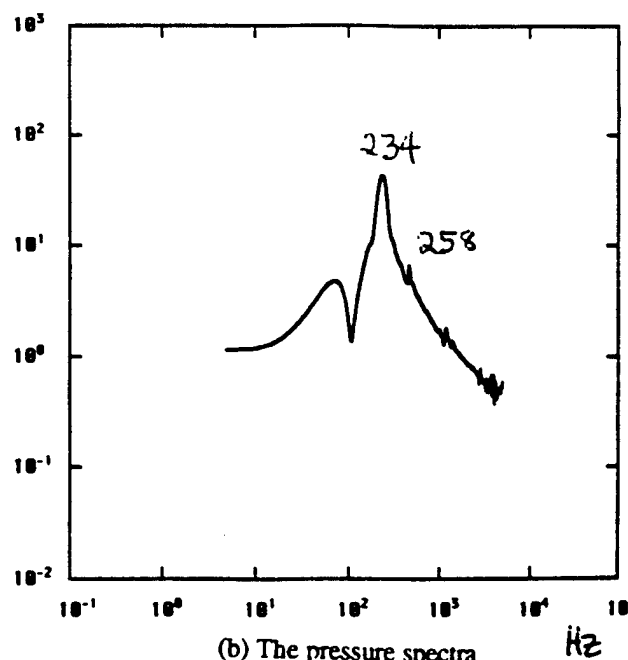


Figure 1. The Ramjet Combustor

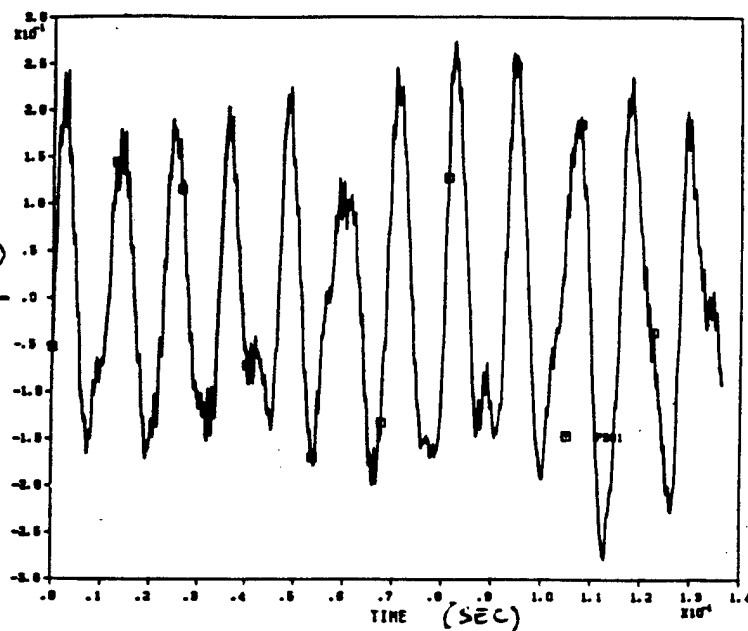


(a) The pressure time trace

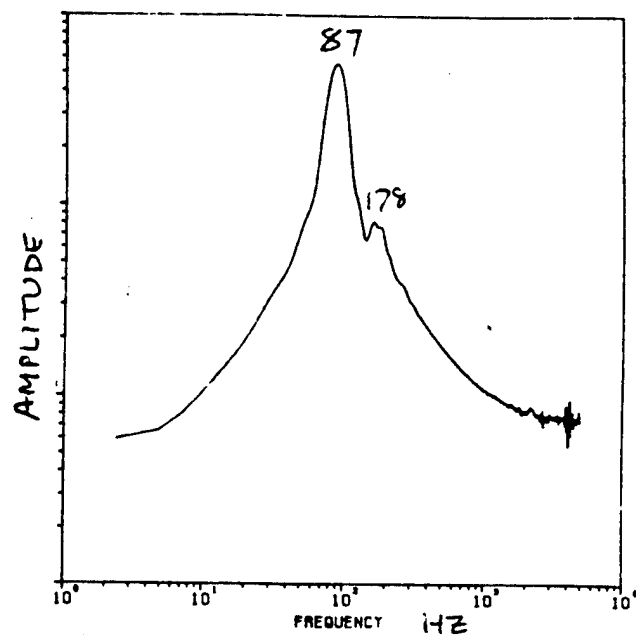


(b) The pressure spectra

Figure 2. The pressure oscillation signature and the spectra at the base of the step for the Mach 0.32 simulation. Combustion instability is caused by the acoustic resonant mode in the combustor.

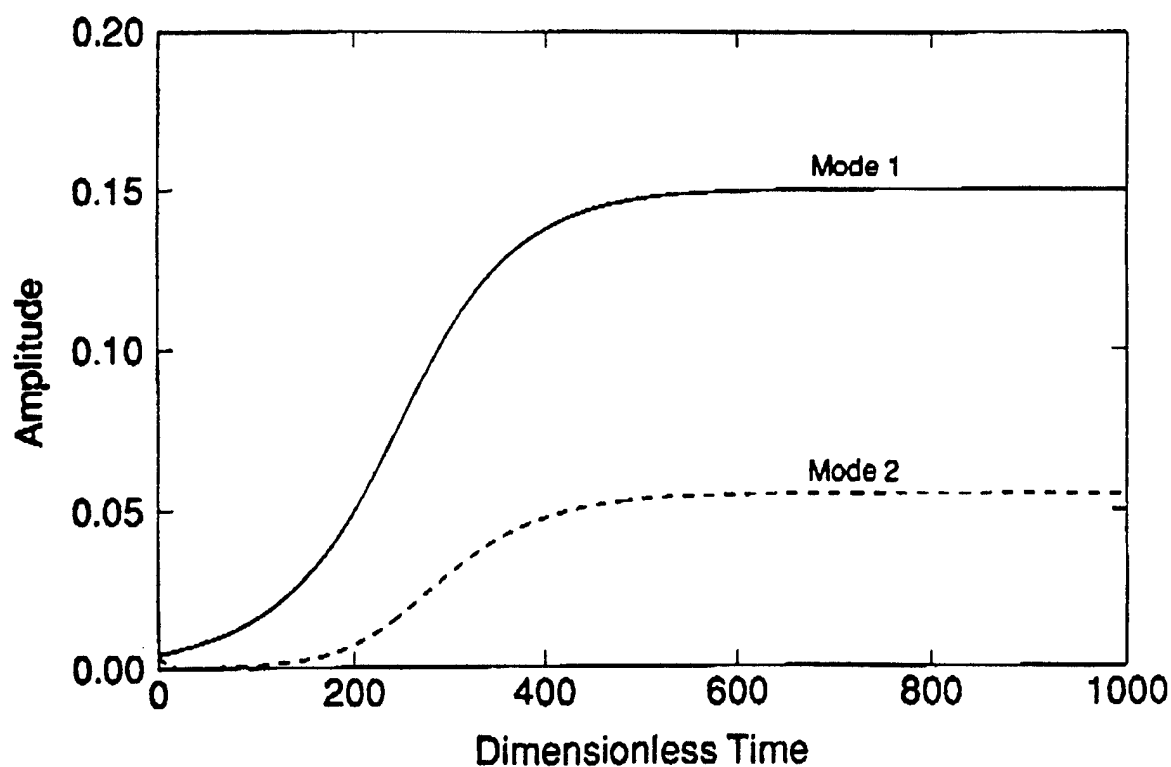


(a) The pressure time trace



(b) The pressure spectra

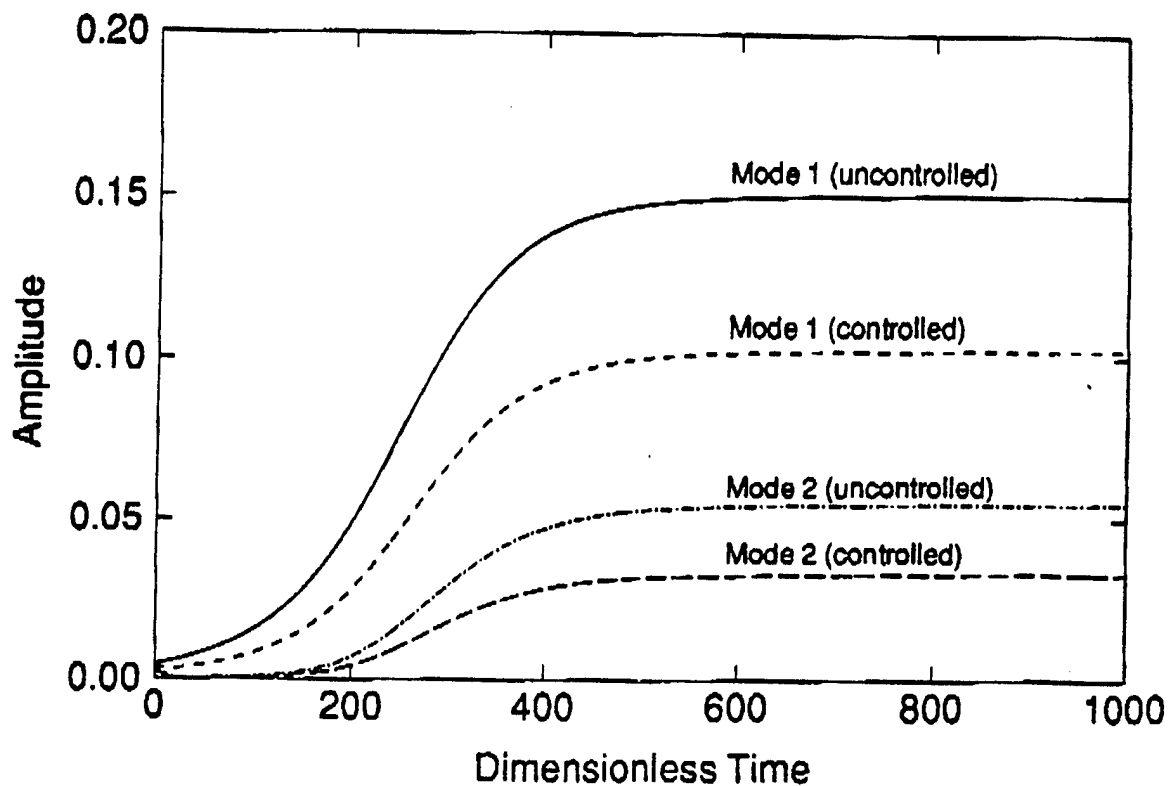
Figure 3. The pressure oscillation signature and the spectra at the base of the step for the Mach 0.17 simulation. Combustion instability is caused by a coupled acoustic/vortex mode in the combustor.



(a) The existence of a stable limit cycle for the Mach 0.32 simulation

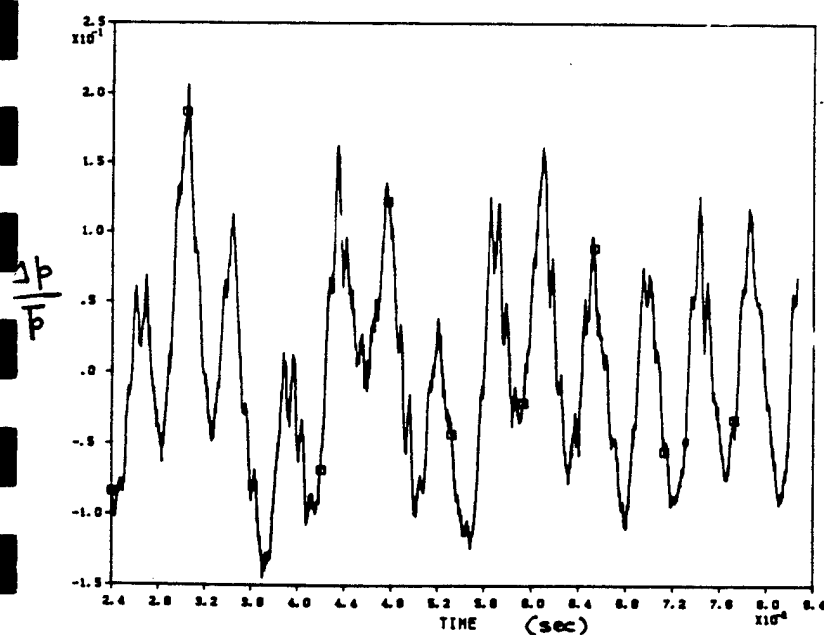
Figure 4. The stable limit cycle behavior and its control as predicted by the theoretical model.



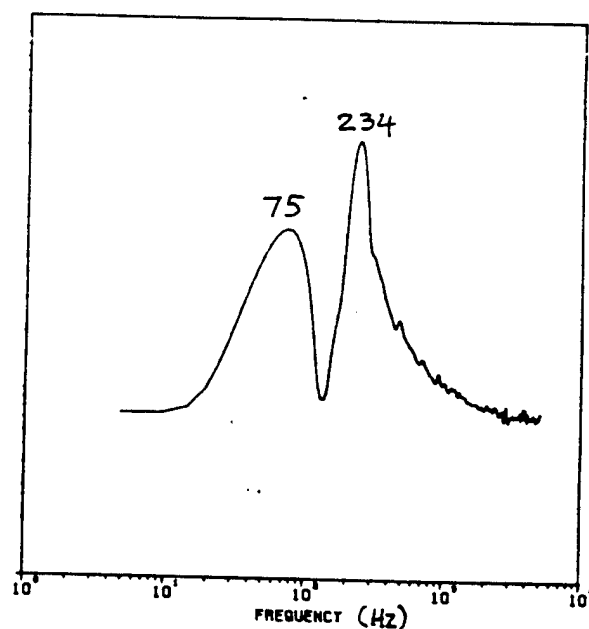


(b) Amplitudes of the pressure oscillations with and without fuel injection control using a proportional-plus-integral controller

Figure 4. The stable limit cycle behavior and its control as predicted by the theoretical model.



(a) The pressure time trace



(b) The pressure spectra

Figure 5. The pressure time trace and spectra for the Mach 0.32 simulation with secondary fuel injection control using a proportional controller.